

**A STUDY OF FLUCTUATIONS IN
ULTRA-RELATIVISTIC HEAVY ION
COLLISIONS**

A THESIS

Submitted to the

FACULTY OF SCIENCE

PANJAB UNIVERSITY, CHANDIGARH

for the degree of

DOCTOR OF PHILOSOPHY

2007

MONIKA SHARMA

CENTRE OF ADVANCED STUDY IN PHYSICS

PANJAB UNIVERSITY,

CHANDIGARH, INDIA

Dedicated
to
My Beloved Parents
and
My Beloved Sister, Manjari

Acknowledgements

This research would not have been possible without tremendous support of Prof. M. M. Aggarwal and Prof. A. K. Bhati, my thesis advisers at the Department of Physics, Panjab University, Chandigarh. I thank them for their valuable guidance, patience and encouragement. Most of all I thank Prof. M. M. Aggarwal for agreeing to review my thesis and sending his comments by email. I fumble with words to thank both my advisers. They always gave me opportunities to travel and work with various people in the STAR Collaboration. Thank you for helping me always.

I would like to express my heartfelt thanks to Dr. Y. P. Viyogi, PMD Project Manager, for giving me all the opportunities during my research career.

My sincere thanks are due to Prof. M. M. Gupta, present Chairperson, Prof. Nir-mal Singh, Prof. J. M. Kohli and Prof. T. S. Cheema, former Chairpersons, Department of Physics, Panjab University, Chandigarh, for providing me necessary research facilities.

I would like to take this opportunity to thank Dr. Tapan K. Nayak, Variable Energy Cyclotron Center, Kolkata, with whom I started the PMD analysis and Dr. S. Chattopadhyay, Variable Energy Cyclotron Center, Kolkata, with whom I did the PMD analysis. Thank you Subhasisda for teaching me PMD & STAR related software. You were always patient with me for all my C++ and ROOT related questions.

Its my pleasure to thank Dr. Bedangadas Mohanty, Variable Energy Cyclotron Center, Kolkata, who provided me student fellowship for QM '06. This enabled me to present the PMD results (in the form of a poster) at the Quark Matter conference at Shanghai, China. Thank you Bedanga bhai for the wonderful opportunity.

I express my deep sense of gratitude to Prof. Claude Pruneau, Wayne State University, Detroit, USA, for inviting me to work with him on dynamical net charge fluctuation analysis. During my stay at Wayne State University I learnt a lot about the Physics behind the analysis, C++ and of course ROOT. Constant discussions with him guided me to have better understanding of the subject. The dynamical net charge fluctuation analysis is now ready to be reviewed by a STAR God Parent Committee. Prof. Pruneau was extremely kind to understand my problems related to the US visa and did his best to help me out of the situation. Thank you Prof. Pruneau for your constant support and encouragement.

I am thankful to our spokes-person, Dr. T. Hallman for his financial support to my trips to the Brookhaven National Laboratory. My sincere thanks are also due to

Dr. W. Christie, Dr. R. Brown, Dr. B. Stringfellow, Dr. A. Lebedev and Dr. T. Ljubicic for their valuable help during the STAR data taking period. I would like to especially thank Dr. B. Stringfellow for believing in my capabilities and giving me a chance to serve as STAR Shift Leader during the data taking period. I would also like to thank Dr. J. Lauret for providing me computing facilities at BNL. Thank you Dr. Jerome for always answering my emails.

Among the group at Wayne State University I would like to express my sincere thanks to Dr. Sergei Voloshin, Dr. Rene Belleweid, Dr. Sean Gavin, Dr. Ilya Seluzhenkov, Ms. Sarah Lapointe, Mr. C. De Silva, Mr. L. Tarini and Mr. Muhammad El-nimr for being extremely nice to me during my stay there. I would especially like to thank Dr. Sergei Voloshin for his interest in my work and many interesting discussions with him.

I am extremely grateful to Prof. Ratna Naik, Chairperson, Department of Physics and Astronomy, Wayne State University, Detroit, for being so helpful to me. Thank you so much Prof. Naik for being so affectionate and helpful.

Within the group at Panjab University, I would like to thank my colleagues: Mr. Ajay Kumar, Mr. Lokesh Kumar and Ms. Natasha Sharma for their voluntary support. It was extremely nice working with you guys.

I am thankful to Mr. Ajit Singh, Mr. Satish Sharma, Mr. Dinesh Kumar Gupta and Mr. Daljit Singh, Department of Physics, Panjab University, Chandigarh, for their technical support.

I would like to express my sincere thanks to Dr. Z. Ahammed, Dr. P Ghosh, Mr. G. S. N. Murthy, Mr. M. Duttamazumdar, Mr. S. Pal, Mr. S. Ramnarayan, Mr. V. Singhal, Mr. J. Saini and Mr. P. Ghosh of the PMD group at Variable Energy Cyclotron Center, Kolkata.

I would like to take this opportunity to thank my fellow collaborator, Dr. Pawan Kumar Netrakanti, Purdue University, U.S.A., who was always approachable whenever needed. Thank you Pawan for all your help during my thesis writing stage.

I would also like to express my sincere thanks to my colleagues, Ms. Gagan Gupta, Panjab University, Chandigarh, Dr. Dipak Mishra, GSI, Germany, Dr. Supriya Das, GSI, Germany, Mr. Sunil Dogra, Ms. Renu Datta, Dr. Ramni Gupta, Dr. Anita Sharma from the University of Jammu, Jammu, Mr. Sudhir Bhardwaj and Mr. Pawan Jain from Jaipur. Thank you so much for your help and co-operation.

I admire my friends, Ms. Rupa Chatterjee, Variable Energy Cyclotron Center, Kolkata, Mr. Michal Bystersky and Mr. Pavel Jakel, Nuclear Physics Institute, Academy

of Sciences, Czech Republic, for their cordial and cooperative attitude. I spent very good time with you guys abroad.

It gives me immense pleasure to thank Dr. Anupam Kumar, without whom I would not have completed this arduous task. His constant motivation and never-say-die attitude helped me kept going in my research. Thank you Anupam for always being there for me during the ups and downs of my research career.

I cannot graduate without expressing my sincere thanks to my friend, Ms. Manmeet Kaur Juneja. Thank you Manmeet for listening to me patiently every time I wanted to speak my heart out. You were always there for me whenever I needed you the most. Thank you so much Manmeet. May God bless you!

I find it extremely difficult to verbalize my deepest sense of indebtedness to my parents and my beloved sister for being my role models. Their constant encouragement, support and love gave me strength to successfully complete this tremendous task.

Date :
Chandigarh.

(Monika Sharma)

List of Publications

- *✓ **Energy and System Size Dependence of Photon Production at Forward Rapidities at RHIC,**
M. Sharma *et. al.*,
Inter. Jour. of Mod. Phys. E (IJMPE) **16** (2007) 1845-1851

- *✓ **Beam Energy and System Size Dependence of Dynamical Net Charge Fluctuations,**
STAR Collaboration, B. I. Abelev *et. al.*,
In preparation, to be submitted to Phy. Rev. C

- ✓ **Forward Lambda Production and Nuclear Stopping Power in $d+Au$ Collisions at $\sqrt{s_{NN}} = 200$ GeV,**
arXiv:nucl-ex/0706.0472

- ✓ **Measurement of Transverse Single-Spin Asymmetries for Di-jet Production in Proton-Proton Collisions at $\sqrt{s_{NN}} = 200$ GeV,**
arXiv:nucl-ex/0705.4629

- ✓ **Enhanced Strange Baryon Production in Au+Au Collisions Compared to $p+p$ at $\sqrt{s_{NN}} = 200$ GeV,**
arXiv:nucl-ex/0705.2511

- ✓ **Global Polarization Measurement in Au+Au Collisions,**
STAR Collaboration, B. I. Abelev *et. al.*,
Phys. Rev. C **76** (2007) 024915.

- ✓ **Energy Dependence of Charged Pion, Proton and Anti-Proton Transverse Momentum Spectra for Au+Au Collisions at $\sqrt{s_{NN}} = 62.4$ and 200 GeV,**
arXiv:nucl-ex/0703040

- ✓ **Partonic Flow and Phi Meson Production in Au+Au Collisions at $\sqrt{s_{NN}} = 200$ GeV,**
arXiv:nucl-ex/0703033

- ✓ **Charged Particle Distributions and Nuclear Modifications at High Rapidities in $d+Au$ Collisions at $\sqrt{s_{NN}} = 200$ GeV,**
arxiv:nucl-ex/0703016

- ✓ **Mass, Quark-Number, and $\sqrt{s_{NN}}$ Dependence of the Second and Fourth Flow Harmonics in Ultra-Relativistic Nucleus-Nucleus Collisions,**
STAR Collaboration, B. I. Abelev *et. al.*,
Phys. Rev. C **75** (2007) 054906

- ✓ **The Energy Dependence of p_T Angular Correlations Inferred from Mean- p_T Fluctuation Scale Dependence in Heavy Ion Collisions at the SPS and RHIC,**
STAR Collaboration, J. Adams *et. al.*,
J. Phys. G. **34** (2007) 451

- ✓ **Rapidity and Species Dependence of Particle Production at Large Transverse Momentum for d +Au Collisions at $\sqrt{s_{NN}} = 200$ GeV,**
arXiv:nucl-ex/0609021

- ✓ **Longitudinal Double-Spin Asymmetry and Cross Section for Inclusive Jet Production in Polarized Proton Proton Collisions at $\sqrt{s_{NN}} = 200$ GeV,**
STAR Collaboration, J. Adams *et. al.*,
Phys. Rev. Lett. **97** (2006) 252001

- ✓ **Neutral Kaon Interferometry in Au+Au Collisions at $\sqrt{s_{NN}} = 200$ GeV,**
STAR Collaboration, J. Adams *et. al.*,
Phys. Rev. C **74** (2006) 054902

- ✓ **Strange Particle Production in $p+p$ Collisions at $\sqrt{s_{NN}} = 200$ GeV,**
STAR Collaboration, J. Adams *et. al.*,
Phys. Rev. C **75** (2007) 064901

- ✓ **Transverse Momentum and Centrality Dependence of High- p_T Non-Photonic Electron Suppression in Au+Au Collisions at $\sqrt{s_{NN}} = 200$ GeV,**
STAR Collaboration, J. Adams *et. al.*,
Phys. Rev. Lett. **98** (2007) 192301

- ✓ **Delta-phi Delta-eta Correlations in Central Au+Au Collisions at $\sqrt{s_{NN}} = 200$ GeV,**
STAR Collaboration, J. Adams *et. al.*,
Phys. Rev. C **75** (2007) 034901

- ✓ **The Multiplicity Dependence of Inclusive p_T Spectra from $p+p$ Collisions at $\sqrt{s_{NN}} = 200$ GeV,**
STAR Collaboration, J. Adams *et. al.*,
Phys. Rev. D **74** (2006) 032006

- ✓ **Scaling Properties of Hyperon Production in Au+Au Collisions at $\sqrt{s_{NN}} = 200$ GeV,**
STAR Collaboration, J. Adams *et. al.*,
Phys. Rev. Lett. **98** (2007) 062301

- ✓ **Identified Baryon and Meson Distributions at Large Transverse Momenta from Au+Au Collisions at $\sqrt{s_{NN}} = 200$ GeV,**
STAR Collaboration, J. Adams *et. al.*,
Phys. Rev. Lett. **97** (2006) 152301

- ✓ **Strange Baryon Resonance Production in $\sqrt{s_{NN}} = 200$ GeV $p+p$ and Au+Au Collisions,**
STAR Collaboration, J. Adams *et. al.*,
Phys. Rev. Lett. **97** (2006) 132301

- ✓ **Direct Observation of Dijets in Central Au+Au Collisions at $\sqrt{s_{NN}} = 200$ GeV,**
STAR Collaboration, J. Adams *et. al.*,
Phys. Rev. Lett. **97** (2006) 162301

- ✓ **Forward Neutral Pion Production in $p+p$ and $d+Au$ Collisions at $\sqrt{s_{NN}} = 200$ GeV,**
STAR Collaboration, J. Adams *et. al.*,
Phys. Rev. Lett. **97** (2006) 152302

- ✓ **Measurements of Identified Particles at Intermediate Transverse Momentum in the STAR Experiment from Au+Au Collisions at $\sqrt{s_{NN}} = 200$ GeV,**
arXiv:nucl-ex/0601042.

- ✓ **Identified Hadron Spectra at Large Transverse Momentum in $p+p$ and $d+Au$ Collisions at $\sqrt{s_{NN}} = 200$ GeV,**
STAR Collaboration, J. Adams *et. al.*,
Phys. Lett. B **637** (2006) 161.

- ✓ **Multiplicity and Pseudorapidity Distributions of Charged Particles and Photons at Forward Pseudorapidity in Au+Au Collisions at**

$\sqrt{s_{NN}} = 62.4 \text{ GeV}$,
STAR Collaboration, J. Adams *et. al.*,
Phys. Rev. C **73** (2006) 034906.

✓ **Directed Flow in Au+Au Collisions** $\sqrt{s_{NN}} = 62.4 \text{ GeV}$,
STAR Collaboration, J. Adams *et. al.*,
Phys. Rev. C **73** (2006) 034903.

✓ **Incident Energy Dependence of p_T Correlations at RHIC**,
STAR Collaboration, J. Adams *et. al.*,
Phys. Rev. C **72** (2005) 044902.

✓ **Multi-Strange Baryon Elliptic Flow in Au+Au Collisions at**
 $\sqrt{s_{NN}} = 200 \text{ GeV}$,
STAR Collaboration, J. Adams *et. al.*,
Phys. Rev. Lett. **95** (2005) 122301.

✓ **Distributions of Charged Hadrons Associated with High Transverse Mo-**
mentum Particles in pp and Au+Au Collisions at $\sqrt{s_{NN}} = 200 \text{ GeV}$,
STAR Collaboration, J. Adams *et. al.*,
Phys. Rev. Lett. **95** (2005) 152301.

✓ **Multiplicity and Pseudorapidity Distributions of Photons in Au+Au Col-**
lisions at $\sqrt{s_{NN}} = 62.4 \text{ GeV}$,
STAR Collaboration, J. Adams *et. al.*,
Phys. Rev. Lett. **95** (2005) 062301.

**Results from these publications are included in this thesis.*

Contents

1	Introduction	1
1.1	Heavy Ion Collisions	4
1.1.1	The Space-Time Picture	6
1.2	The QCD Phase Diagram	7
1.3	Signals of Phase Transition	8
1.3.1	Strangeness Enhancement	8
1.3.2	Collective Flow (v_1, v_2)	9
1.3.3	J/ψ Suppression	10
1.3.4	High p_T Suppression of Hadrons	15
1.3.5	Nonstatistical Event-by-Event Fluctuations and Correlations	18
1.4	Particle Multiplicities	24
1.5	Organization of the Thesis	27
	Bibliography	28
2	Experimental Facility	36
2.1	Relativistic Heavy Ion Collider (RHIC)	36
2.1.1	The Accelerator	36
2.2	The STAR Experiment in Year 2006	40
2.2.1	The Magnet	40
2.2.2	The Time Projection Chamber	41
2.2.3	The Endcap Electromagnetic Calorimeter	46
2.2.4	The Barrel Electromagnetic Calorimeter (BEMC)	46
2.2.5	The Forward Time Projection Chamber (FTPC)	49
2.2.6	The Silicon Vertex Tracker (SVT)	50
2.2.7	The Silicon Strip Detector (SSD)	52
2.2.8	The STAR Trigger	52
2.2.9	The Central Trigger Barrel (CTB)	53

2.2.10	The Zero Degree Calorimeter (ZDC)	54
2.2.11	The Multi Wire Counter (MWC)	54
	Bibliography	58
3	The Photon Multiplicity Detector (PMD)	60
3.1	History and Future of the PMD	61
3.2	Physics Goals of the PMD	61
3.3	Principle of a Pre-shower Detector	62
3.4	Design of the PMD	64
3.5	Characteristics of Charged Particle Detection	65
3.6	Description of the PMD	67
3.6.1	Mechanical Design and Construction	67
3.6.2	Fabrication of Honeycomb Array	67
3.6.3	Honeycomb Chambers	69
3.6.4	Assembly of a Unit Module	69
3.6.5	Assembly of a Supermodule	69
3.6.6	Gas Flow within a Supermodule	74
3.6.7	The CPV and the PMD Numbering Scheme	74
3.6.8	Converter Plates	75
3.6.9	Support Assembly	76
3.7	Gas System for the PMD	76
3.8	Front End Electronics	79
3.8.1	Use of Gassiplex Chips in the PMD	79
3.8.2	Electronic Noise/Pedestal	82
3.8.3	Experimental Results	82
3.8.4	Electronic Chains	82
3.9	Trigger Logic for the PMD	85
	Bibliography	86
4	Simulation of the PMD	88
4.1	Simulation Framework	89
4.2	Data Selection in Simulation	89
4.3	Photons Distribution in the PMD Acceptance	90
4.4	Implementation of Dead Cells	92
4.5	Simulation of the Expected Signal in a Cell	93

4.6	Hit Level Characteristics	93
4.7	Results from Clustering	94
4.7.1	Photon Hadron Discrimination	96
4.7.2	Optimization of Discrimination Threshold	98
4.8	Effect of Upstream Material	99
4.9	Photon Counting Efficiency	101
4.10	Purity of Photon Samples	101
4.11	PMD Acceptance Factors	103
4.11.1	Consistency Checks	106
	Bibliography	109
5	Data Analysis of the PMD	110
5.1	Data Selection	110
5.2	Data Cleanup	112
5.3	Hit Level Information	114
5.4	Data After Cleanup	114
5.5	Single Cell Response	117
5.6	Calibration of Data	120
5.7	Event Generator: (HIJING)	125
5.8	Photon Pseudo-rapidity Distribution Results from the PMD	125
5.8.1	Photon Pseudo-rapidity Distribution	127
5.8.2	Centrality Dependence of Photon Production	128
5.8.3	Scaling of Photon Production with N_{coll}	128
5.8.4	Centrality and System Size Dependence of Longitudinal Scaling of Photon Production	129
5.9	Photon Multiplicity Fluctuations	130
5.9.1	Estimation of Fluctuation in a Participant Model	134
5.9.2	Comparison of Data with Results from Model Calculations	137
	Bibliography	139
6	Dynamical Net Charge Fluctuations	142
6.1	Data Selection	146
6.1.1	Analysis Cuts	147
6.2	Net Charge Fluctuation Results	166
6.2.1	Systematic Error Studies	168

6.2.2	Beam Energy Dependence	174
6.2.3	Collision Centrality Dependence	176
6.2.4	Longitudinal and Azimuthal Dependences of the Dynamical Fluctuations	178
	Bibliography	185
7	Conclusions	188

List of Figures

1.1	Figure depicting a micro-bang taking place in a laboratory.	2
1.2	Particle energy (temperature) as a function of time in the early Universe. Different evolutionary epochs are shown along with the accessible range of accelerator laboratory experiments.	3
1.3	Time sequence of a central (head-on) Au-Au collision at RHIC.	4
1.4	The space-time picture of a nucleus-nucleus collision.	6
1.5	The QCD Phase Diagram. See text for details.	7
1.6	Pattern of enhancement of strange and multi-strange baryons at the top SPS energy (NA57).	9
1.7	Directed flow of charged particles as a function of pseudorapidity, for centrality 10-70%. Lower panel shows the midrapidity region in more detail. Figure is taken from Ref. [71].	11
1.8	(Color online). Charged hadron v_2 vs. p_T for the centrality bins (bottom to top) 5 to 10% and in steps of 10% starting at 10, 20, 30, 40, 50, 60, and 70 up to 80%. Solid lines are Blast Wave fits. Figure is taken from Ref. [72].	12
1.9	Measured J/ψ production yields, normalized to the yields expected assuming that the only source of suppression is ordinary absorption by the nuclear medium. The data is shown as a function of the energy density reached in the several collision system. Figure taken from Ref. [78].	14
1.10	$R_{AB}(p_T)$ from Eq. 1.9 for minimum bias and central $d + Au$ collisions, and central $Au + Au$ collisions [83]. The minimum bias $d + Au$ data are displayed 100 MeV/c to the right for clarity. The bands show normalization uncertainties, which are highly correlated point-to-point and between the two $d + Au$ distributions.	16

1.11	(a) Efficiency corrected two-particle azimuthal distributions for minimum bias and central $d + Au$ collisions, and for $p + p$ collisions [84]. (b) Comparison of two-particle azimuthal distributions for central $d + Au$ collisions to those seen in $p + p$ and central $Au + Au$ collisions [84].	17
1.12	Azimuthal correlation histograms of high p_T charged hadron pairs for 0-5% $Au + Au$ events, for various $p_T^{trig.}$ and $p_T^{assoc.}$ ranges. In the lower left panel the yield is suppressed due to the constraint $p_T^{assoc.} < p_T^{trig.}$	18
1.13	(Left panel) Results of PHOBOS measurement of charged particle density near mid rapidity in central $Au + Au$ collisions at $\sqrt{s_{NN}} = 200$ GeV (shown by vertical line with the dashed lines denoting the systematic uncertainty) compared to theoretical prediction. (Right panel) Charged particle multiplicity density per participant near mid rapidity for central nucleus-nucleus collisions as a function of $\sqrt{s_{NN}}$	25
1.14	(Left panel) Pseudorapidity density distributions of charged particles in $p(\bar{p}) + p$ collisions at a range of energies versus the $\eta - y_{beam}$. (Right panel) Similar data for particles emitted along the jet axis in an $e^+ + e^-$ collision versus $y_T - y_{jet}$	26
2.1	Schematic view of the RHIC complex. The figure highlights various stages in the acceleration of heavy ions or pp collisions.	38
2.2	Position of four experiments around the RHIC ring. The STAR experiment is at 6 o'clock position and other experiments, PHENIX, PHOBOS and BRAHMS are located at 8 o'clock, 10 o'clock and 2 o'clock positions, respectively.	38
2.3	Experimental setup of the STAR detector.	40
2.4	Schematic view of the Time projection chamber.	41
2.5	End view of the STAR TPC. 12 sectors on each end cover the full azimuth range. Inner and outer sectors can be seen in the figure.	42
2.6	Detailed view of a single sector of the TPC showing inner and outer sub-sector. The inner sub-sector is on the right side and has small pads arranged in widely spaced rows. The outer sector which is seen on the left has densely packed pads.	43
2.7	The readout chamber region of the STAR TPC. The gating grid and ground plane wires are on a 1 mm pitch, while the anode wires are spaced every 4 mm.	44

2.8	The energy loss distribution for the primary and secondary particles in the STAR TPC as a function of p_T . The magnetic field was set at 0.25 T. . . .	44
2.9	Schematic diagram of the EEMC tower structure. See text for details. . . .	47
2.10	Data flow through the trigger.	53
3.1	Cross-sectional view of the STAR experiment. The PMD is shown with thick black lines on the East side.	61
3.2	Principle of a preshower detector. Single cell hit is due to a MIP, whereas signal deposited in continuous cells is due to a photon.	63
3.3	Cross-sectional view of the PMD.	64
3.4	Schematic design of the honeycomb chamber and wire readout.	65
3.5	Cross-sectional view of an extended cathode cell.	66
3.6	ADC distribution of an isolated cell in the CPV plane.	66
3.7	A close-up view of a small region of the cells in a unit module showing studs and notches in detail.	68
3.8	Rhombus shaped unit module containing an array of 24×24 hexagonal cells.	68
3.9	Schematic view showing the junction of two unit modules. The cell walls at the boundaries are half as thick as those inside and make a seamless joint with cells from adjoining unit module.	70
3.10	Components of the unit module : (1) bottom PCB, (2) honeycomb cathode, (3) moulded frame, (4) SAMTEC connectors, (5) top PCB, (6) shielding PCB, and (7) slot for connector.	70
3.11	Wire scheme for an array of 64 cells to 70 pin connector.	71
3.12	Jig used for wire insertion during assembly of the unit module.	71
3.13	Schematic of a section of the supermodule showing different components.	72
3.14	Unit modules assembled in a supermodule.	73
3.15	Gas feed sub-assembly placed at the top of the supermodule.	74
3.16	The CPV SM numbering scheme and row, column scheme. “i” and “j” represent the direction of row and column for every supermodule.	75
3.17	The PMD SM numbering scheme and row, column scheme. “i” and “j” represent the direction of row and column for every supermodule.	76
3.18	Suspension mechanism of the PMD showing movement along the x-direction. The two halves of the PMD are shown separated.	77
3.19	Rear view of the PMD gas system.	78
3.20	Front view of the PMD gas system.	78

3.21	Block diagram of front end electronics readout system.	80
3.22	Gas64 board for the PMD with four chips.	80
3.23	The translator board.	81
3.24	The buffer board.	81
3.25	Pedestal minimum values (in mV) for 5000 chips.	83
3.26	Pedestal minimum vs. pedestal spread for the above chips. Lines are drawn to show the grouping of chips for a uniform chain.	83
3.27	Figures, clockwise from left, (a) Pedestal values versus the channel number, (b) RMS as a function of channel number, (c) Integrated pedestal, and (d) Distribution of RMS values.	84
3.28	Timing diagram for pre-trigger and L0 validation the PMD.	85
4.1	Flow chart for photon reconstruction from the PMD in simulation.	89
4.2	Distribution of charged particle multiplicity obtained with HIJING $Cu + Cu$ events at the center of mass energy of 200 GeV. Vertical lines show the reference multiplicity cuts and the corresponding fraction of the interaction cross-section.	90
4.3	(a) Photons multiplicity and, (b) transverse momentum (p_T) distribution of photons incident on the PMD obtained with HIJING+GEANT $Cu + Cu$ 200 GeV events.	91
4.4	2D hits distribution of the preshower plane after dead cell implementation.	92
4.5	The shaded cell is labeled as isolated if its six neighboring cells (non shaded) have zero signal.	93
4.6	Distribution of energy deposited (E_{dep}) in an isolated cell in simulation.	94
4.7	Hit level characteristics from HIJING+GEANT simulation (a) minimum bias distribution of total hits of the PMD, (b) correlation between the number of hits and the total energy deposited in the PMD, (c) correlation between the reference multiplicity and the total PMD hits, (d) distribution of average energy deposited per hit in the PMD. Units of average energy deposited (E_{dep}) is in KeV.	95
4.8	Cluster level characteristics (a) distribution of the number of clusters without any threshold in the PMD, (b) correlation between the TPC reference multiplicity and the number of clusters in the PMD, (c) distribution of the number of cells in a cluster, (d) distribution of energy (E_{dep}) in a cluster.	96

4.9	Fraction of photon clusters measured per event which deposit energy in one cell only.	97
4.10	Fraction of charged hadron clusters measured per event which deposit energy in one cell only.	98
4.11	Photon counting efficiency (ϵ_γ) and purity of photon samples (f_p) for various E_{dep} cuts on the detected clusters from simulation.	99
4.12	Distributions of the azimuthal angles' difference of the cluster and its incident track (left) and the distribution of difference of their pseudorapidities (right). Top panel is for the PMD alone, whereas, the bottom panel is for the PMD along with all other sub detectors in the STAR experiment. . . .	100
4.13	Photon counting efficiency for 0-10% (most central) and 40-50% (peripheral) centralities.	102
4.14	Purity in photon samples for 0-10% (most central) and 40-50% (peripheral) centralities.	102
4.15	(a) Azimuthal angle distribution of all the clusters in the PMD. (b) Uncorrected pseudo-rapidity distribution of all the clusters in the PMD. Note that the dip near $\eta = -2.8$ is due to SM boundary.	104
4.16	Few events 2D hits display of the PMD with a red boundary at $\eta = -2.8$, showing dead area because of the super-modules boundary.	105
4.17	Acceptance correction factors for various pseudo-rapidity bins in the PMD coverage.	106
4.18	Comparison of raw yield, simulated data (corrected for efficiency, purity, acceptance factors) with incident photons from HIJING only for 0-10% centrality.	107
4.19	Comparison of raw yield, simulated data (corrected for efficiency, purity, acceptance factors) with incident photons from HIJING only for 10-20% centrality.	107
4.20	Comparison of raw yield, simulated data (corrected for efficiency, purity, acceptance factors) with incident photons from HIJING only for 20-30% centrality.	108
5.1	The TPC track multiplicity within $-0.5 < \eta < 0.5$ from data for $Cu + Cu$ collisions at $\sqrt{s_{NN}} = 200$ GeV. Collision centralities or % of cross-section are shown with the arrows in the plot.	111
5.2	Raw channel frequency distribution of chain 23.	113

5.3	ADC distribution of hot channels.	113
5.4	Typical raw chain ADC distribution.	114
5.5	Hit level characteristics of (a) cell, (b) chain, showing abnormal firing of many chains, (c) channel, showing a hot channel, (d) column (e) row, and (f) super-module.	115
5.6	(a) Minimum bias total PMD hits distribution, (b) correlation between total hit ADC and total PMD hits, (c) Average ADC per hit distribution. .	116
5.7	Total PMD hits distribution after cleanup.	117
5.8	Raw channel frequency distribution of chain 32 (before cleanup).	118
5.9	Clean channel frequency distribution of chain 32 (after cleanup).	118
5.10	Global features after cleanup like (a) cell ADC distribution, (b) chain hit frequency, (c) channel hit frequency, (d) column hit frequency, (e) row hit frequency, (f) super-module hit frequency.	119
5.11	Isolated cell ADC distribution of a high gain cell (cell # 124240).	121
5.12	Isolated cell ADC distribution of a low gain cell (cell # 173304).	121
5.13	(a) Distribution of Mean upto 500 ADC of all isolated cells in SM 19 and chain 38, (b) gain distribution of cells in this combination, (c) MPV distribution of all isolated cell in this combination, (d) correlation between MPV and mean values of isolated cells.	122
5.14	Mean value of all isolated cells before calibration in (a) SM 12, (b) SM 13, (c) SM 14, (d) SM 15, (e) SM 16, (f) SM 17.	123
5.15	Mean value of all isolated cells before calibration in (a) SM 18, (b) SM 19, (c) SM 20, (d) SM 21, (e) SM 22, (f) SM 23.	124
5.16	Pseudo-rapidity density distribution, $dN_\gamma/d\eta$, as a function of η for various event centrality classes compared to HIJING model calculations.	127
5.17	Pseudo-rapidity density distribution ($dN_\gamma/d\eta$) per participant pair as a function of η for four centrality classes in $Cu + Cu$ collisions at $\sqrt{s_{NN}} = 200$ GeV.	129
5.18	Variation of N_γ normalized to the number of binary collisions in the PMD coverage, as a function of N_{coll}	130
5.19	$dN_\gamma/d\eta$ normalized to N_{part} as a function of $\eta - y_{beam}$ for various systems and energy.	131

5.20	Minimum bias N_γ distribution in $Cu + Cu$ collisions at the center of mass energy of 200 GeV. The N_γ distribution for top 2% central events is also shown with square symbols.	132
5.21	Gaussian fit parameters, chi-square per degree of freedom (χ^2/ndf) (top panel), sigma (σ) (middle panel) and mean (μ) (bottom panel) of the multiplicity distributions of γ - like clusters for 2% centrality bins. The centrality bins correspond to 0-2%, 2-4%.....40-42% of the minimum bias cross-section.	133
5.22	Variation of μ , σ and fluctuations, $\omega_{N_{part}}$, of the number of participants as a function of centrality.	136
5.23	Relative fluctuations, ω_γ of photon multiplicity distribution compared to calculations from participant model and HIJING. The data presented here is corrected for efficiency, purity and geometrical acceptance factors.	138
6.1	The TPC reference multiplicity within $-0.5 < \eta < 0.5$ from data for $Cu + Cu$ collisions at $\sqrt{s_{NN}} = 62.4$ GeV. Collision centralities or % cross-section are shown with the arrows in the plot.	148
6.2	The TPC reference multiplicity within $-0.5 < \eta < 0.5$ from data for $Cu + Cu$ collisions at $\sqrt{s_{NN}} = 200$ GeV. Collision centralities or % cross-section are shown with the arrows in the plot.	148
6.3	Distribution of z-position of the vertex in $Cu + Cu$ collisions at $\sqrt{s_{NN}} = 200$ GeV.	150
6.4	Uncorrected pseudo-rapidity distribution of all tracks produced within the TPC. Shaded portion shows the selected pseudo-rapidity range for the results presented in Section 4.2.	151
6.5	Uncorrected azimuthal angle distribution of all tracks produced within the TPC. Spikes and bumps structure result from reduced efficiency in the TPC sector boundary gaps.	151
6.6	Transverse momentum distribution of the tracks from the TPC. Shaded portion shows the accepted upper bound of p_T	153
6.7	Zoom-in picture showing the lower bound of the transverse momentum of all tracks. Shaded portion shows the tracks were accepted with $p_T > 0.2$ GeV/c.	153
6.8	Distance of closest approach distribution of the all the tracks from TPC.	154

6.9	Average dip angle as a function of z-vertex position for (a) 0-10% centrality, (b) 10-20% centrality, in $Cu + Cu$ collisions at $\sqrt{s_{NN}} = 200$ GeV.	155
6.10	Average dip angle as a function of z-vertex position for (c) 20-30% centrality, (d) 30-40% centrality, (e) 40-50% centrality, and (e) 50-60% centrality, in $Cu + Cu$ collisions at $\sqrt{s_{NN}} = 200$ GeV.	156
6.11	Mean values of the average dip angle distribution as a function of z-vertex position for (a) 0-10% centrality, (b) 10-20% centrality, (c) 20-30% centrality, (d) 30-40% centrality, (e) 40-50% centrality, and (e) 50-60% centrality, in $Cu + Cu$ collisions at $\sqrt{s_{NN}} = 200$ GeV.	157
6.12	Sigma values of the average dip angle distribution as a function of z-vertex position for (a) 0-10% centrality, (b) 10-20% centrality, (c) 20-30% centrality, (d) 30-40% centrality, (e) 40-50% centrality, and (e) 50-60% centrality, in $Cu + Cu$ collisions at $\sqrt{s_{NN}} = 200$ GeV.	158
6.13	Primary multiplicity within $ \eta < 1$ as a function of reference multiplicity (a) before applying dip angle cut, (b) after applying dip angle cuts for $Cu + Cu$ collisions at $\sqrt{s_{NN}} = 200$ GeV.	159
6.14	Primary multiplicity within $ \eta < 1$ before and after cleanup (a) 0-10% centrality, (b) 10-20% centrality, (c) 20-30% centrality, (d) 30-40% centrality, (e) 40-50% centrality, and (e) 50-60% centrality, in $Cu + Cu$ collisions at $\sqrt{s_{NN}} = 200$ GeV.	161
6.15	Average reference multiplicity as a function of run number for the TPC data in $Cu + Cu$ collisions at center of mass energy of 200 GeV.	162
6.16	Average reference multiplicity distribution showing outlier runs for $Cu + Cu$ collisions at $\sqrt{s_{NN}} = 200$ GeV.	162
6.17	Average reference multiplicity as a function of run number for the TPC data in $Cu + Cu$ collisions at center of mass energy of 62.4 GeV.	164
6.18	Average reference multiplicity distribution showing outlier runs for $Cu + Cu$ collisions at $\sqrt{s_{NN}} = 62.4$ GeV.	164
6.19	Primary multiplicity within $ \eta < 1$ with respect to reference multiplicity in $Cu + Cu$ collisions at center of mass energy of 200 GeV obtained after applying the dip angle cuts, however outlier runs were not removed.	165
6.20	Primary multiplicity within $ \eta < 1$ with respect to reference multiplicity in $Cu + Cu$ collisions at center of mass energy of 200 GeV obtained after applying the dip angle cuts as well as after removing the outlier runs.	165

6.21	Net charge dynamical fluctuations, $\nu_{+-,dyn}$, of particles produced within pseudo-rapidity $ \eta < 0.5$, as a function of the number of participating nucleons.	166
6.22	Comparison of net charge dynamical fluctuation, $\nu_{+-,dyn}$, results from $Cu + Cu$ collisions with $Au + Au$ collisions at various energies, of the particles produced within pseudo-rapidity $ \eta < 0.5$, as a function of the number of participating nucleons.	167
6.23	Individual terms in Eq. 6.7 obtained with unit bin method. With this method adopted the terms show sub-Poissonian behavior. The errors shown are statistical only.	169
6.24	Individual terms in Eq. 6.7 obtained with wide bin method. With this method adopted the terms show super-Poissonian behavior. The errors shown are statistical only.	169
6.25	$\nu_{+-,dyn}$ as a function of vertex position along the beam direction in $Cu + Cu$ collisions at 200 GeV.	170
6.26	Ratio of $\nu_{+-,dyn}$ at a particular z-vertex to the $\nu_{+-,dyn}$ value at z-vertex position of 30 cm, w.r.t. z-vertex position.. . . .	171
6.27	Corrected values of dynamical net charge fluctuations ($\nu_{+-,dyn}^{corr}$) as a function of $\sqrt{s_{NN}}$ (in color online). See text for details.	176
6.28	Net charge dynamical fluctuations, $\nu_{+-,dyn}$, of particles produced with pseudo-rapidity $ \eta < 0.5$ scaled by (a) the produced multiplicity $dN/d\eta$, (b) the number of participants, and (c) the number of binary participants.	179
6.29	Dynamical fluctuations $\nu_{+-,dyn}$, normalized to their value at $\eta = 1$, as function of the integrated pseudorapidity range. (a) Data for $Au + Au$ collisions at $\sqrt{s_{NN}} = 62.4$, 200 GeV (0-10%) along with data for $Cu + Cu$ collisions at $\sqrt{s_{NN}} = 62.4$, 200 GeV (0-10%), are compared to inclusive $p + p$ data at $\sqrt{s_{NN}} = 200$ GeV, and (b) Data for $Au + Au$ collisions at $\sqrt{s_{NN}} = 62.4$, 200 GeV (30-40%) along with data for $Cu + Cu$ collisions at $\sqrt{s_{NN}} = 62.4$, 200 GeV (0-10%), are compared to inclusive $p + p$ data at $\sqrt{s_{NN}} = 200$ GeV [45].	180
6.30	Dynamical fluctuations $\nu_{+-,dyn}$, as a function of the integrated azimuthal range ϕ for selected collision centralities for (a) $Au + Au$ 200 GeV [45], and (b) $Cu + Cu$ 200 GeV.	183

6.31 Dynamical fluctuations $\nu_{+-,dyn}$, as a function of the integrated azimuthal range ϕ for similar number of participating nucleons for $Au + Au$ 200 GeV [45] and $Cu + Cu$ 200 GeV.	184
--	-----

List of Tables

2.1	Accelerators for relativistic heavy-ion collision experiments.	36
2.2	The basic parameters of RHIC.	37
2.3	Basic parameters of the TPC and its associated hardware [8].	45
2.4	The EEMC coverage and performance/parameters [13].	48
2.5	The SMD design parameters [17].	49
2.6	The FTTPC design parameters [6].	51
2.7	The design parameters and performance of the SSD [25].	55
2.8	The design parameters of the CTB.	56
2.9	The design parameters of the ZDC.	56
2.10	The design parameters of the MWC [29].	57
3.1	Basic parameters of the STAR-PMD [1].	60
3.2	Basic parameters of a unit cell [1].	67
3.3	Types of Supermodules.	73
3.4	The PMD Gas System.	77
3.5	Specifications of a gassiplex chip.	79
3.6	Electronic chains.	84
5.1	The percentage of cross-section, number of uncorrected charged particle multiplicity from the TPC within pseudo-rapidity $-0.5 < \eta < 0.5$, number of participating nucleons, N_{part} , and number of binary collisions, N_{coll} , for $Cu + Cu$ collisions at $\sqrt{s_{NN}} = 200$ GeV.	112
6.1	The percentage of cross-section, number of uncorrected charged particle multiplicity from the TPC within pseudo-rapidity $-0.5 < \eta < 0.5$, number of participating nucleons, N_{part} , and the number of binary collisions, N_{coll} , for $Cu + Cu$ collisions at $\sqrt{s_{NN}} = 62.4$ GeV.	149

6.2	The percentage of cross-section, number of uncorrected charged particle multiplicity from the TPC within pseudo-rapidity $-0.5 < \eta < 0.5$, number of participating nucleons, N_{part} , and number of binary collisions, N_{coll} , for $Cu + Cu$ collisions at $\sqrt{s_{NN}} = 200$ GeV.	149
6.3	Systematic error contribution from all sources for different centrality classes in $Cu + Cu$ collisions at the center of mass energy of 200 GeV.	168
6.4	The $\nu_{+-,dyn}$ values for with and without dip angle cuts for $Cu+Cu$ collisions at 62.4 GeV.	173
6.5	The $\nu_{+-,dyn}$ values for with and without dip angle cuts for $Cu+Cu$ collisions at 200 GeV.	173
6.6	Collision centrality, total multiplicity, uncorrected and corrected $\nu_{+-,dyn}$ values for four energies in $Au + Au$ collisions and two energies in $Cu + Cu$ collisions.	175

Chapter 1

Introduction

The matter is made up of molecules which in turn are composed of atoms. These atoms further consist of a nucleus and electrons circling around the nucleus which consists of protons and neutrons. These protons and neutrons are themselves a bound state of quarks and gluons. Our universe originated from a “Big Bang” in a state of almost infinite energy density and temperature. Immediately after the Big Bang, the energy density in our universe was so high that hadrons (which are color singlet bound states of quarks, anti-quarks and gluons), could not be formed. Instead, these quarks and gluons were deconfined and permeated the entire universe in a thermalized state.

The motivation to build large accelerators like Relativistic Heavy Ion Collider (RHIC) came from the quest to understand the strongly interacting matter at energy densities unprecedented in a laboratory environment. Ultra-relativistic heavy ion collisions allow us to study the densest and hottest form of matter that can be created in the laboratory, and to address fundamental questions related to the state of matter at extreme temperatures and densities which may be considered as “extreme” on hadronic scales. The principal aim of relativistic heavy ion physics is to understand Quantum Chromodynamics (QCD) at extreme temperatures and energies over large volumes and to create Quark Gluon Plasma (QGP) [1–3]. Under such extraordinary conditions, it is believed that symmetries of QCD will reveal themselves: color will be deconfined and chiral symmetry will be restored. Besides the issues concerning the state of matter at large densities, there is another fundamental question that needs to be addressed and is playing an increasingly important role in the study of heavy ion reactions: that is the structure of the wavefunction of a nucleus at high energy. The study of dense systems of partons offers exciting challenges as non linear QCD effects can play an important role. The asymptotic form of the wavefunction is directly relevant to the study of heavy ion collisions, as it determines the “initial conditions” for the creation of matter and its

subsequent evolution.

Results from the four RHIC experiments i.e., **S**olenoidal **T**racker At RHIC (STAR), a **P**Hysics Experiment at RHIC (PHENIX), **B**road **R**ange **H**adron **M**agnetic **S**pectrometers (BRAHMS) and PHOBOS (not an acronym, but a name of the first mission to Mars, also a satellite of Mars and a Roman God), already demonstrating that the collider facility has fulfilled its promise to reach such extreme conditions during early stages of nucleus-nucleus collisions. Thus, RHIC is an exciting scientific opportunity to discover the properties of matter under extreme conditions believed to be existing during a critical, though fleeting, stage of the earliest development of the universe following the Big-Bang.

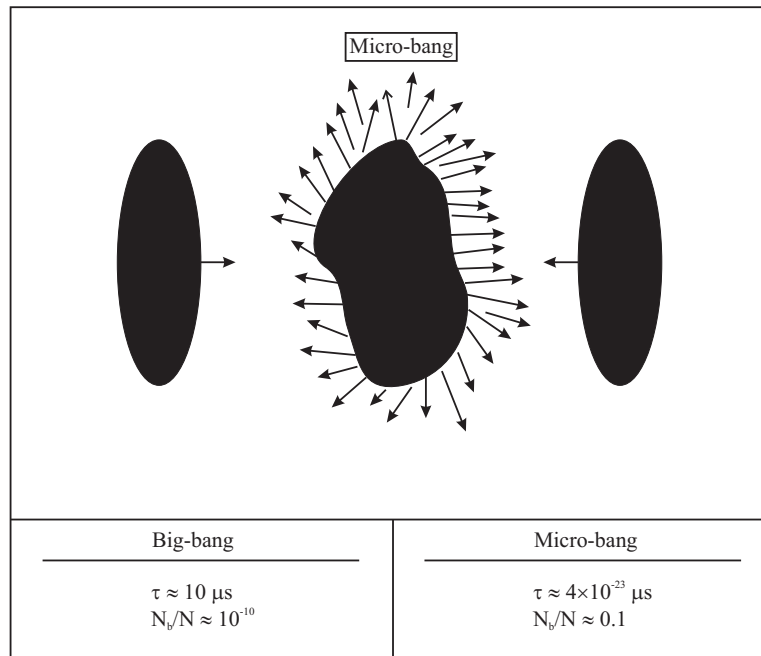


Figure 1.1: Figure depicting a micro-bang taking place in a laboratory.

Fig. 1.1 depicts two Lorentz-contracted nuclei colliding in the center-of-momentum frame and forming a region of dense matter, which finally evolves into a final state of hadrons. The Fig. 1.1 also shows a comparison of two key parameters between the micro-bang and the cosmological big-bang:

- Interplay of the gravitational forces, radiative and Fermi pressure of the hot matter determine the time scale of the expansion of the Universe. Whereas in micro-bang there is no gravitation force acting to slow the expansion, which lasts approximately $10^{-23} \mu\text{sec}$. Such a small time scale of the heavy ion collisions suggests that the size and the (local) properties of the exploding nuclear fireball must change rapidly even

on the scale of hadronic interactions.

- In the laboratory RHIC creates baryon free QGP whereas FAIR (Facility for Antiproton and Ion Research) at low energies (10-40 AGEV) is expected to create baryon rich cold QGP. Thus, unlike in the early Universe, we expect in a laboratory, micro-bang with a finite matter-antimatter asymmetry in particle abundance.

The temporal evolution of the Universe is illustrated in Fig. 1.2, as a function of time. We have little understanding of the earlier period when the nearly symmetric matter-antimatter hadron gas emerged from the quark-gluon phase and evolved into the baryon rich Universe in which we live today. QCD was developed in the 1970's as a

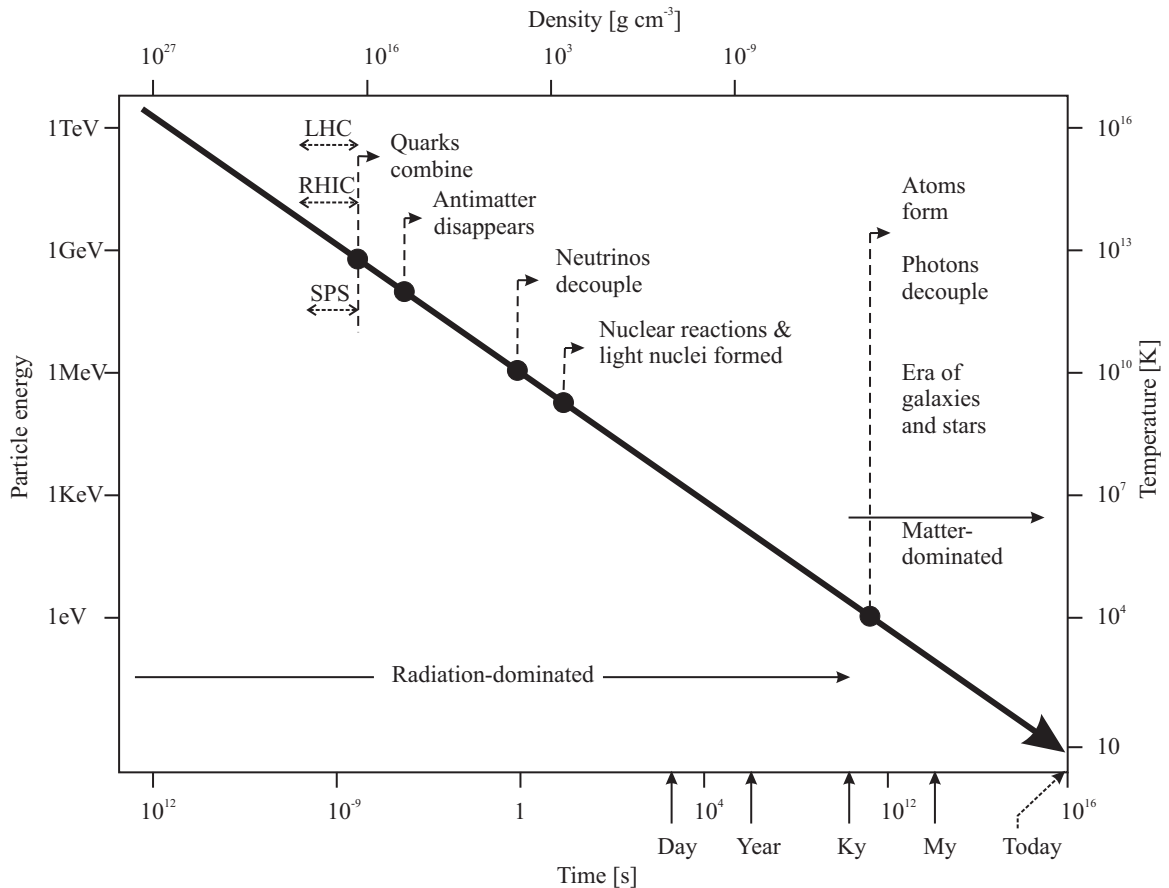


Figure 1.2: Particle energy (temperature) as a function of time in the early Universe. Different evolutionary epochs are shown along with the accessible range of accelerator laboratory experiments.

theory of the strong interaction describing the confinement of quarks in hadrons. An early consequence of this picture was the realization that at sufficiently high temperatures, or energy density, the confining forces were overcome by color screening effects, resulting in a transition from hadronic matter to a Quark-Gluon-Plasma phase, whose bulk dynamical

properties were determined by the quark and gluon degrees of freedom, rather than those of confined hadron. QGP is defined as a thermally equilibrated state of matter in which quarks and gluons are deconfined from hadrons, so that the color degrees of freedom manifest over nuclear, rather than merely nucleonic volumes. A QGP is believed to have existed in the early universe about ten micro-second after the Big-Bang. After that, the coupling between quarks and gluons favoured the formation of color neutral bound states, and the universe transitioned to hadronic matter.

1.1 Heavy Ion Collisions

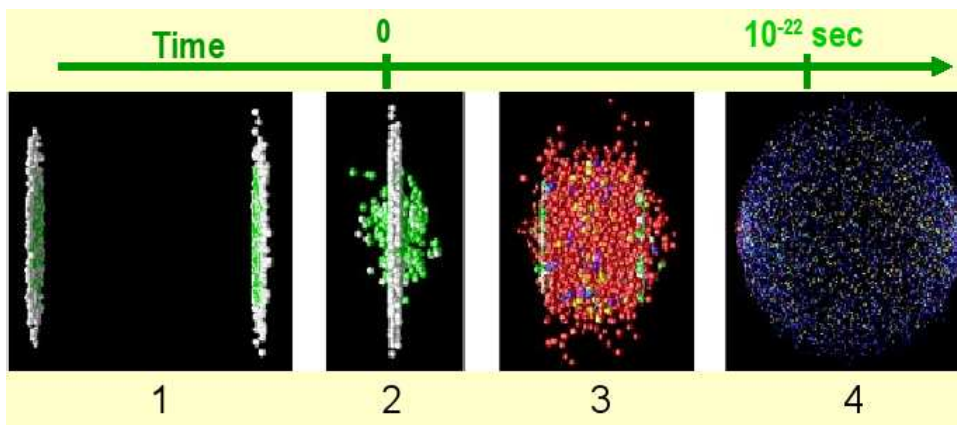


Figure 1.3: Time sequence of a central (head-on) Au-Au collision at RHIC.

Fig. 1.3 shows the time sequence of a central (head-on) Au+Au collision at RHIC. Various stages are explained below: When two nuclei collide at very high energy, they do not see each other as collection of nucleons bound together by nuclear forces. Rather, the relevant degrees of freedom involved in the early stages of a collision at sufficiently high energy are partons, mostly gluons, whose density grows as the energy increases (i.e., when x , their momentum fraction, decreases) - a state known as Color Glass Condensate[4–9]. However, the growth of gluon density should “saturate” when non linear QCD effects start to play a role.

The existence of such a saturation regime has been predicted long ago [10–12]. But it is only during the last decade that equations providing a dynamical description of the saturated regime have been obtained [13–19]. The interaction of these high-density “walls” of gluons describe the initial state of the collision.

The two nuclei collide, heating the local QCD vacuum through the interaction of intense color fields and hence produces a dense, pre-equilibrium state of quarks, anti-

quarks and gluons. Sometimes high energy quarks and gluons are formed, as a consequence of which “jets” of hadrons are produced. Pairs of heavy quarks, charm and beauty, are formed in the initial stage of the collision.

The key difference between the elementary particle collisions and the nuclear collisions is that the quanta created in the primary collisions between the incoming nucleons can't right away escape into the surrounding vacuum, but re-scatter off each other. In this way they create a form of dense, strongly interacting matter which, when thermalizes quickly enough and at sufficiently large energy density, is a Quark-Gluon Plasma. As a result in heavy ion collisions, there is a finite probability to recreate the matter that existed in the very early universe, whereas, with high energy collisions between leptons or single hadrons, it is not.

The hot, dense matter, consisting of quarks, anti-quarks and gluons reaches thermal equilibrium almost instantaneously. It expands and cools through very strong collective interactions behaving like an ideal hydrodynamical fluid - “a perfect liquid” with nearly zero viscosity. High energy quarks and gluons interact with this medium, providing a probe of its density and bulk properties through the measurement of jet phenomena.

As the expanding matter cools below the QCD critical temperature, quarks and anti-quarks coalesce to form hadrons. After hadronization of the fireball, the hadrons keep re-scattering with each other for a while, continuing to build up expansion flow, until the matter becomes so dilute that the average distance between the hadrons exceeds the range of strong interactions. At this point all scattering stops and the hadrons decouple or freeze out. Since the corresponding inelastic cross sections are only a small fraction of the total cross section, inelastic processes stop long before the elastic ones, leading to earlier freeze-out for the hadron abundances than for their momenta. Thus, chemical freeze-out precedes thermal or kinetic freeze-out. At kinetic freeze out all hadrons, including the present unstable resonances, have an approximately exponential transverse momentum spectrum reflecting the temperature of the fireball at that point.

This hadronic final state radiates the particles seen in experimental detectors. The properties of this final state - anisotropies in the spatial distribution of hadrons, and the relative abundance of particles in terms of their quark-constituents - retain a memory of the conditions at the time of freeze-out.

1.1.1 The Space-Time Picture

The dynamics of such heavy ion collisions can be viewed from a different perspective in the space-time diagram with the longitudinal coordinate z and the time coordinate t , as illustrated by Fig. 1.4. The trajectories of the colliding projectile nucleus and target nucleus are shown in the figure. Energy deposited in the collision region around $z \sim 0$ is very high, the quanta which carry this energy can be in the form of quarks, gluons, or hadrons. However, it is still a subject of intense investigation in what form the quanta appear in the first instant after the collision. Soon after the collision of the two nuclei at $(z,t) = (0,0)$, the energy density may be sufficiently high to make it likely that a system of quark-gluon plasma may be formed in the central rapidity region, since the ground state of matter with such an energy density is in the quark-gluon plasma phase and not in the hadron phase. The plasma initially may not be in thermal equilibrium, but subsequent equilibrium may bring it to local equilibrium at the proper time τ_0 , and the plasma may evolve according to the laws of hydrodynamics thereafter. As the plasma expands, its temperature drops down and the hadronization of the plasma will take place at a later proper time. The hadrons will stream out of the collision region when the temperature falls below the freeze-out temperature.

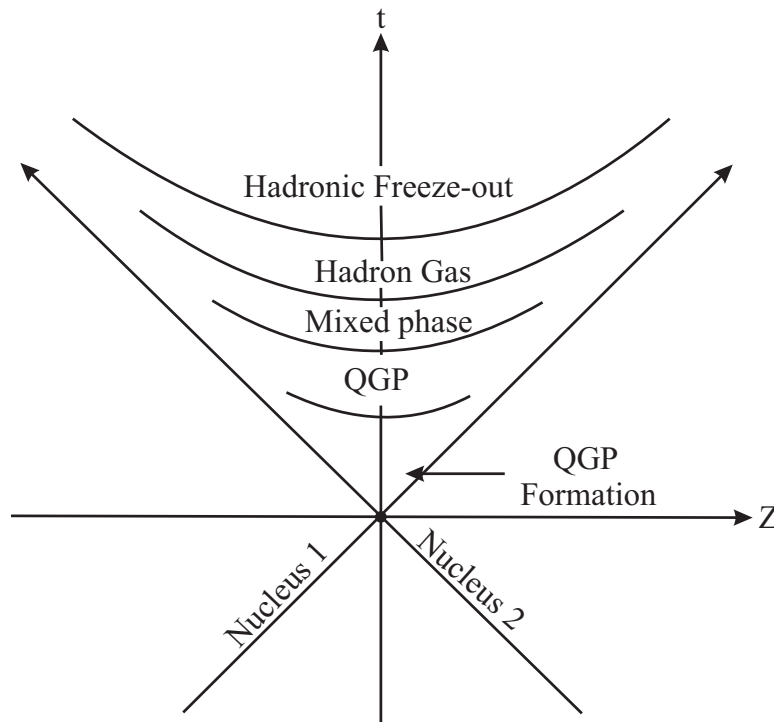


Figure 1.4: The space-time picture of a nucleus-nucleus collision.

1.2 The QCD Phase Diagram

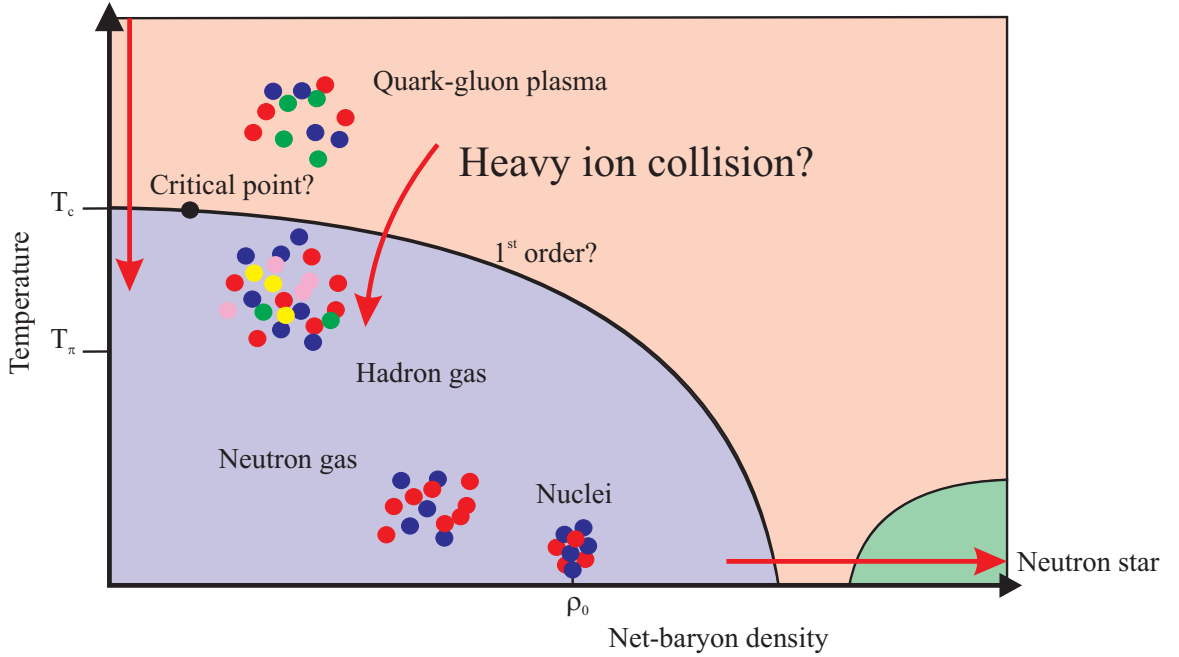


Figure 1.5: The QCD Phase Diagram. See text for details.

Fig. 1.5 shows the phase diagram of strongly interacting matter. At very high temperatures more and more hadron resonances are excited as a result we have a hadron resonance gas. Lattice QCD calculations show that phase transition from a hadron resonance gas to a quark gluon plasma takes place at $T_c \sim 170$ MeV. It also tells that even for realistically small up and down quark masses the transition at $\mu_B = 0$ is most likely not a sharp transition but instead a rapid crossover [20]. For a long time phenomenological models have indicated that at non-zero μ_B the QGP and hadron gas are separated by a critical line which has a roughly constant critical energy density $e_r \sim 1 \text{ GeV}/fm^3$ [21]. Recent QCD models [22] and latest QCD calculations at moderate non-zero baryon chemical potential [23, 24] indicate that transition becomes first order at non-zero μ_B although definite value where such a transition takes place is yet to be determined by performing calculations with more realistic small quark masses. The phase diagram also shows that at low temperatures and asymptotically large baryon densities quarks are again deconfined, however not in Quark-Gluon Plasma state but rather in a state known as Color Superconductor [25]. This color superconducting state is separated from the QGP by the first order transition at a critical temperature estimated of the order of 30-50 MeV [22].

Besides resonance gas, color superconductor and QGP, Fig. 1.5, also indicate a few typical trajectories through the phase diagram which we can follow in relativistic

heavy-ion collisions. The collision starts at the cold nuclear matter point in the phase diagram, it then goes through an early non-equilibrium stage which cannot be mapped onto the phase diagram (hence is indicated by red arrow on the left hand side), and then re-appears in the phase diagram after having thermalized at some high temperature. Unfortunately we cannot use heavy-ion collisions to compress nuclear matter without heating it and hence produce a lot of entropy. Therefore, it is impossible to probe the color superconducting phase of strongly interacting matter. The Compressed Baryonic Matter (CBM) experiment at FAIR, GSI, will investigate nucleus-nucleus collisions from 10-40 AGeV to explore the QCD phase diagram in the region of highest baryonic densities. This facility would be fully functional around 2013.

1.3 Signals of Phase Transition

As previously mentioned, the motivation to build RHIC was to search for the evidence of a QGP formation in heavy ion collisions, and thus to deduce the energies, entropies and temperature of the system formed. Although RHIC has fulfilled its promise of creating a highly dense matter in heavy ion collisions, its observability is a matter of intense debate. There are many proposed possible experimental signatures of QGP. Some of which are mentioned in the subsequent sub-sections.

1.3.1 Strangeness Enhancement

The strangeness content in a QGP is believed to be enhanced from that of normal hadronic matter [26] which acts as a probe to study the QCD phase transition. Hadronic scenarios for strangeness production involves relatively high energy thresholds.

$$\pi + N \rightarrow \Lambda + K \quad E_{threshold} \simeq 530MeV \quad (1.1)$$

A significant enhancement of strangeness production is predicted if a phase transition occurs. Since the temperature at which the QCD transition occurs is very close to the strange quark current mass of 150 MeV, $s\bar{s}$ pairs could be formed copiously through the gluon fusion [1] in a gluon rich QGP state as:

$$g + g \rightarrow s + \bar{s} \quad E_{threshold} \simeq 2m_s \simeq 300MeV \quad (1.2)$$

As a result if we compare the threshold energy for strangeness production in a QGP state via gluon fusion (Eq. 1.2) to the threshold energy in a hadronic scenario (Eq. 1.1), we

would expect more $s\bar{s}$ pairs in QGP state [27, 28]. Indeed, such strangeness enhancement has been observed by the WA97 and NA57 collaborations in $Pb + Pb$ collisions at SPS energies ($\sqrt{s_{NN}} = 17.3$ GeV) [29–31]. The enhancement is defined as the yield per wounded nucleon relative to the yield per wounded nucleon in a light reference system (for example $p + p$ or $p + Be$), for generic collision system AB, the enhancement of a generic particle j is calculated as:

$$E_j = \frac{(Y_j/N_{wound})_{AB}}{(Y_j/N_{wound})_{ref}} \quad (1.3)$$

where Y_j is the yield of the particle in the phase-space window under consideration and N_{wound} is the estimated number of wounded nucleons. Fig. 1.6 shows no enhancement in $p + Pb$ collisions, whereas in $Pb + Pb$ collisions, clear enhancement can be seen. This enhancement is found to increase with centrality and strangeness content, reaching about a factor 20 for the Ω baryons for the most central collisions.

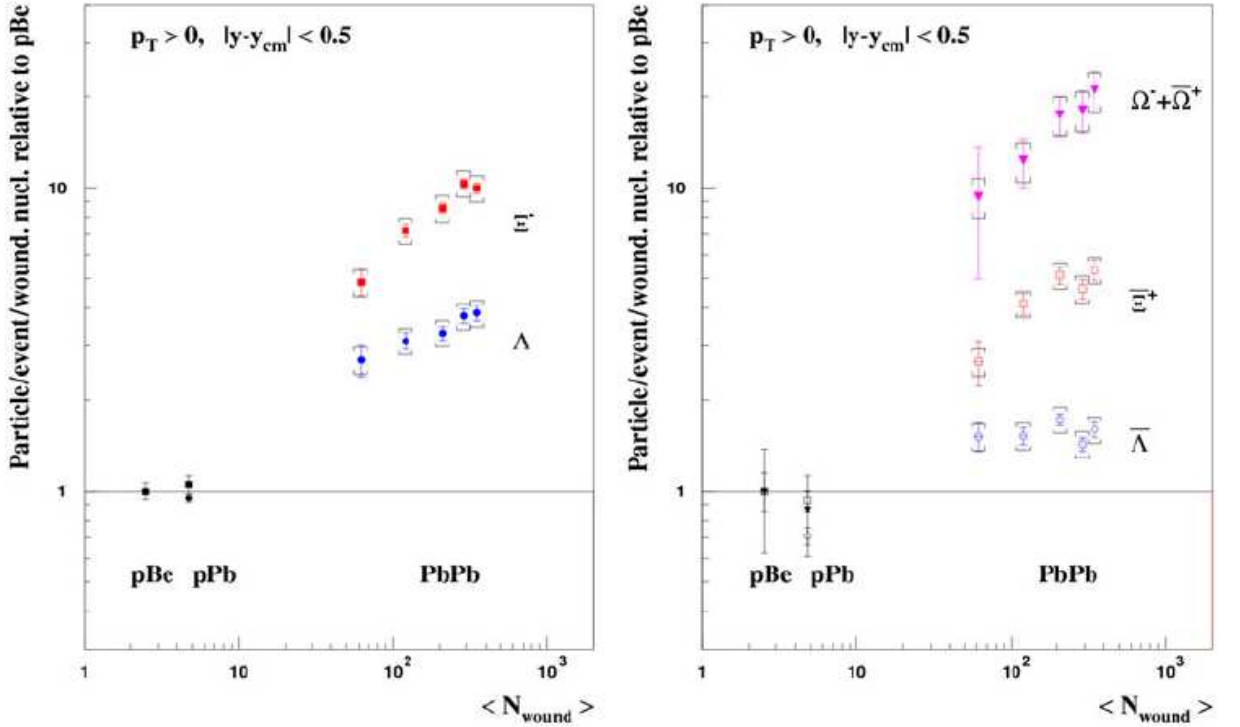


Figure 1.6: Pattern of enhancement of strange and multi-strange baryons at the top SPS energy (NA57).

1.3.2 Collective Flow (v_1, v_2)

Properties of nuclear matter are studied in heavy ion collisions at relativistic energies at high temperature and density. If such a system thermalizes, the thermal pressure

will generate collective transverse expansion [32]. Such collective flow of particles, and especially momentum anisotropy will reflect the time evolution of the pressure gradients of the system. This can reveal important information about the equation of state (EOS) and in particular about the possible formation of the Quark Gluon Plasma [33–67].

In a non central collision the overlap region is asymmetric in the plane transverse to the beam direction. Any interactions in the system created can convert this spatial anisotropy into a momentum space anisotropy. Asymmetric pressure gradient results in larger acceleration of particles along the short axis rather than that along the long axis. The azimuthal anisotropy of the spectra, resulting from asymmetric pressure gradients, can be characterized in terms of second Fourier coefficient, i.e., elliptic flow, which is extensively studied at RHIC. Fourier series expansion of the azimuthal angular distributions of the produced particles with respect to the reaction plane can be written as :

$$\frac{dN}{Tdp_T dy d\phi} = \frac{1}{2\pi} \frac{dN}{p_T dp_T dy} (1 + 2v_1 \cos(\phi) + 2v_2 \cos(2\phi) + \dots) \quad (1.4)$$

where the zeroth, first and the second harmonic in Eq. 1.4 are known as radial flow, directed flow (v_1), and elliptic flow (v_2), respectively. The system formed at RHIC energies also exhibits very strong radial expansion. This is supported by the fact that a variety of identified particle spectra can be fitted with a common temperature if a common radial velocity boost is included. The shape of v_1 in the mid rapidity region is of special interest as it might reveal a signature of a possible Quark-Gluon Plasma (QGP) phase [68–70]. Often, the strength of directed flow is determined from the slope of v_1 at midrapidity. The directed flow (v_1) of the charged particles as a function of pseudorapidity, η , is shown in Fig. 1.7, for centrality 10-70% from $Au + Au$ collisions at $\sqrt{s_{NN}} = 62.4$ GeV. The arrows in the upper panel indicate the direction of flow for spectator neutrons as determined from the ZDC-SMDs (Zero Degree Calorimeter, discussed in chapter 2).

The second harmonic v_2 , elliptic flow for charged particle is presented in Fig. 1.8. The Blast Wave fits are performed assuming that all charged hadrons have the mass of pion. The data are well reproduced by the Blast Wave parameterization when p_T is below 1 GeV/c.

1.3.3 J/ψ Suppression

T. Matsui and H. Satz [73] first predicted J/ψ suppression as one of the clean signals of a Quark Gluon Plasma formation in heavy ion collisions. Their calculation was based on the idea of Debye color screening and its effects on the stability of charmonium bound

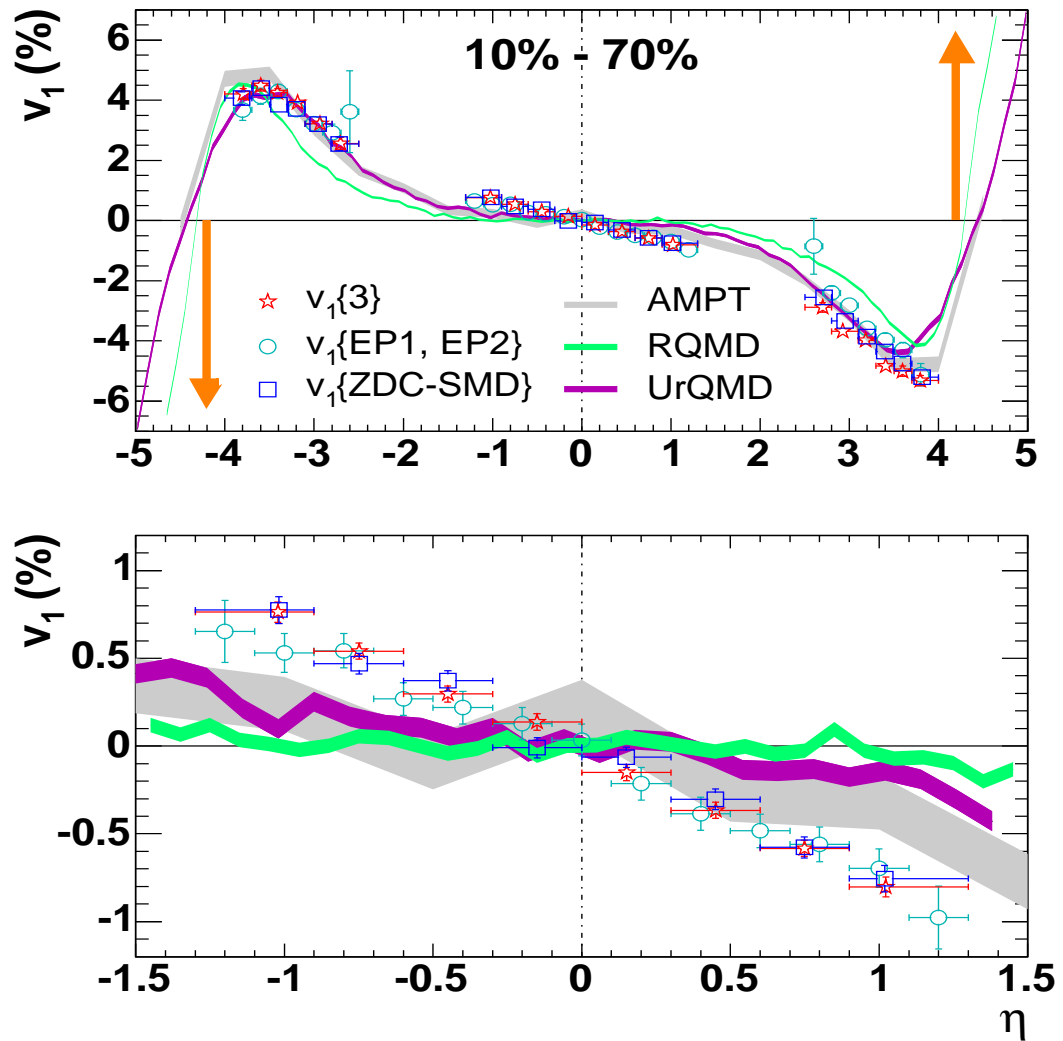


Figure 1.7: Directed flow of charged particles as a function of pseudorapidity, for centrality 10-70%. Lower panel shows the midrapidity region in more detail. Figure is taken from Ref. [71].

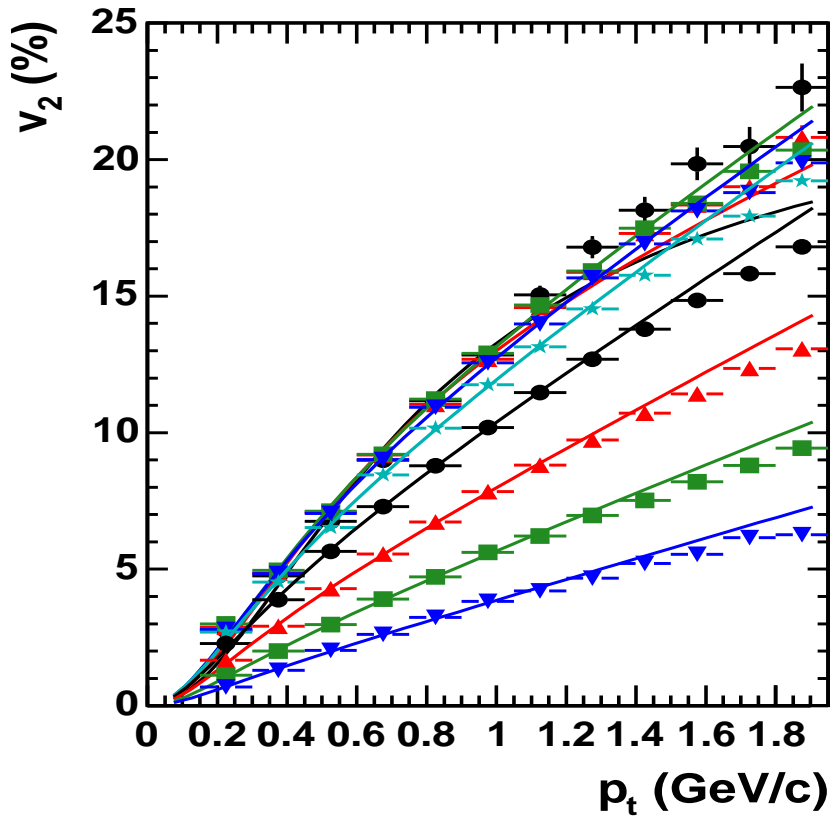


Figure 1.8: (Color online). Charged hadron v_2 vs. p_T for the centrality bins (bottom to top) 5 to 10% and in steps of 10% starting at 10, 20, 30, 40, 50, 60, and 70 up to 80%. Solid lines are Blast Wave fits. Figure is taken from Ref. [72].

states. In general, the primordially produced J/ψ 's will be subsequently dissociated by :

- Nuclear absorption.
- Debye color screening [74].
- Inelastic scattering on “co-moving” hadrons in the final, hadron gas phase of the reaction.

The interaction potential exhibited by the bound states of $c\bar{c}$ system [75] is :

$$V(r) = \sigma r - \frac{\alpha_{eff}}{r} \quad (1.5)$$

where σ is the string tension and α_{eff} is the coulomb interaction coupling. The energy of the bound state including the c-quark kinetic energy and their rest mass can be estimated semi quantitatively by

$$E(r) = 2m + \frac{1}{2mr^2} + V(r) \quad (1.6)$$

Now, with the increasing temperature, $\sigma(T)$ decreases, and at the point of deconfinement $\sigma(T_c) = 0$. However, above deconfinement ($T \geq T_c$, the potential is modified by the color-screened coulomb potential, given by Eq. below [76]

$$V(r) = -\left(\frac{\alpha_{eff}}{r}\right)exp(-r/r_D(T)) \quad (1.7)$$

where $r_D(T)$ is the Debye screening radius. This potential can still allow bound states to be formed. Plugging Eq. 1.7 into Eq. 1.6 and minimizing $E(r)$, one gets :

$$x(x+1)exp(-x) = (m\alpha_{eff}r_D)^{-1} \quad (1.8)$$

with $x \equiv r/r_D$ as the critical condition for a bound state. Matsui and Satz, using the Lattice QCD calculations [77] then calculated $r_{j/\psi}^{max}/r_D = 1.61$ as the universal coulomb J/ψ radius at the last point where such a state is possible. They argued that the existence of $c\bar{c}$ bound state is excluded down to $T/T_c = 1.2$ or less. The formation of a QGP therefore prevents the existence of such a bound state. As a result an observed suppression would imply deconfinement in relativistic heavy ion collisions. However, as previously mentioned, J/ψ 's will also undergo a “normal” suppression, for example, induced by ordinary nuclear effects. Systematic study of J/ψ and ψ' production was carried out by NA38 and NA50 experiments at the CERN-SPS in $p + p$, $p + A$ and $Pb + Pb$ collisions providing intriguing results. The NA50 experiment observed a suppression, known as “anomalous” suppression, of J/ψ production in central $Pb + Pb$ collisions at $\sqrt{s_{NN}} = 17.2$

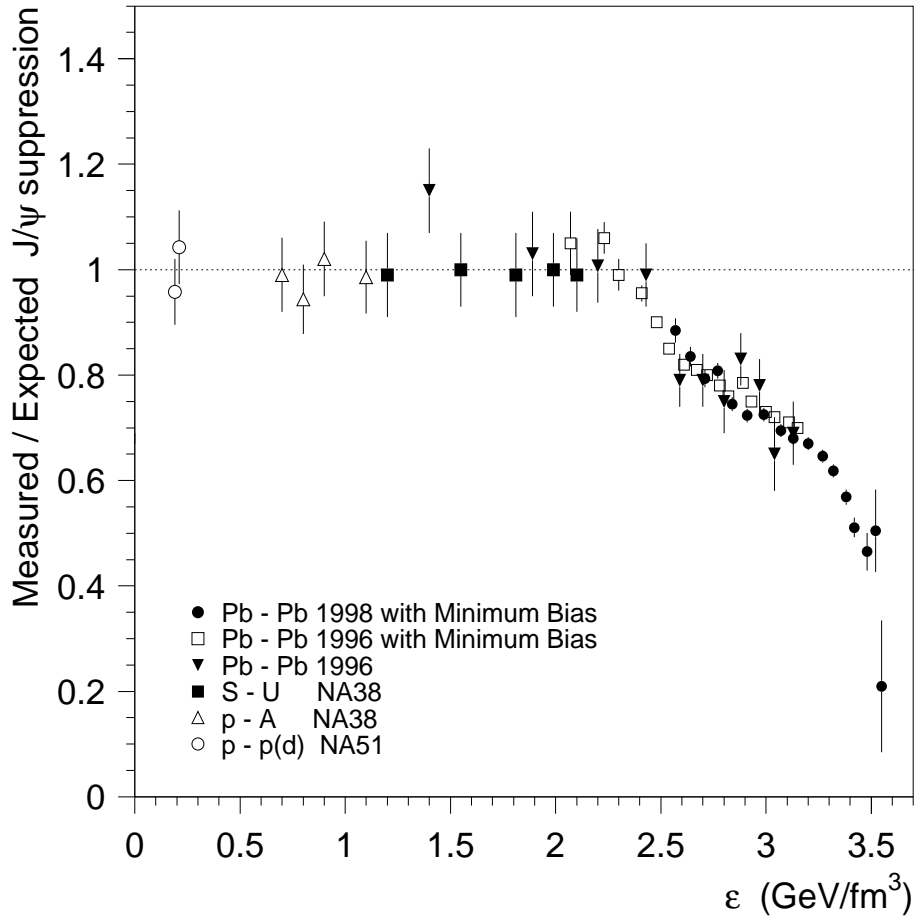


Figure 1.9: Measured J/ψ production yields, normalized to the yields expected assuming that the only source of suppression is ordinary absorption by the nuclear medium. The data is shown as a function of the energy density reached in the several collision system. Figure taken from Ref. [78].

GeV. The suppression, which is of the order of 25% with respect to the normal suppression in nuclear matter, shown in Fig. 1.9, has been interpreted by the NA50 Collaboration as an evidence of deconfinement of quarks and gluons [78]. The strangeness study is also carried out at RHIC energies [20].

1.3.4 High p_T Suppression of Hadrons

Energetic partons propagating through matter lose energy depending strongly on the color charge density [79] through induced gluon radiation. Thus, partonic energy loss is a sensitive probe of the matter created in high energy heavy-ion collisions, in case a QGP is formed if sufficiently high energy density is achieved. The energetic partons originate in the hard scattering of partons from the incoming nuclei. Partonic energy loss can be studied using observables, for example, two-particle azimuthal distributions of high transverse momentum (high p_T) hadrons. In ultra relativistic heavy ion collisions, the measurements of high p_T hadron production revealed strong suppression of not only single-particle inclusive yield [80–83], but also back-to-back pairs in the most central collisions. Jets with large azimuthal separation $\delta\phi$ (away side) were suppressed, whereas, near-side pairs (small $\delta\phi$) exhibit jet-like correlations that are similar to those in $p + p$ collisions [84]. One interpretation of these results could be, energetic partons following hard scattering while traversing the dense medium lose energy, and the observed jets are primarily those created from partons produced near the surface and directed outwards [84]. However, the suppression might also result from initial-state effects prior to the hard scattering, such as saturation of gluon densities in the incoming nuclei [85]. Theoretical expectations of $d + Au$ collisions can be found in references [86–93].

Nuclear effects on hadron production in $d + Au$ and $Au + Au$ collisions are measured through comparison to the $p + p$ spectrum using the ratio.

$$R_{AB}(p_T) = \frac{d^2N/dp_T d\eta}{T_{AB} d^2\sigma^{pp}/dp_T d\eta} \quad (1.9)$$

where $d^2N/dp_T d\eta$ is the differential yield per event in the nuclear collision $A + B$. $T_{AB} = \langle N_{bin} \rangle / \sigma_{inel}^{pp}$ describes the nuclear geometry and $d^2\sigma^{pp}/dp_T d\eta$ is determined from the measured $p + p$ differential cross section, for $p + p$ inelastic collisions [83].

If nuclear effects such as shadowing, Cronin effect or gluon saturation are absent, hard processes are expected to scale with the number of binary collisions, and $R_{AB}(p_T) = 1$. Fig. 1.10 shows $R_{AB}(p_T)$ for minimum bias and central $d + Au$ collisions.

It is observed that $R_{AB}(p_T) > 1$ for $2 < p_T < 7$ GeV/c. Fig. 1.10 also shows $R_{AB}(p_T)$ for central $Au + Au$ collisions [83], showing prominent suppression in hadron production at high p_T . Fig. 1.11(a) shows the two-particle azimuthal distribution $D(\Delta\phi)$, defined as

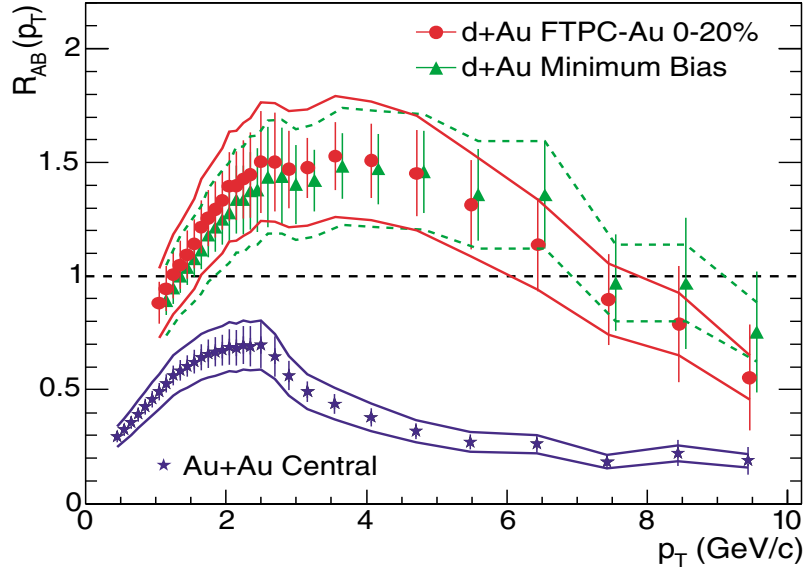


Figure 1.10: $R_{AB}(p_T)$ from Eq. 1.9 for minimum bias and central $d + Au$ collisions, and central $Au + Au$ collisions [83]. The minimum bias $d + Au$ data are displayed 100 MeV/c to the right for clarity. The bands show normalization uncertainties, which are highly correlated point-to-point and between the two $d + Au$ distributions.

$$D(\Delta\phi) \equiv \frac{1}{N_{trigger}} \frac{1}{\epsilon} \frac{dN}{d(\Delta\phi)} \quad (1.10)$$

for minimum bias and central $d + Au$ collisions, and for $p + p$ collisions [84]. $N_{trigger}$ is the number of particles which lie in the p_T range, $4 < p_T^{trig.} < 6$ GeV/c, referred to as trigger particles. The associated particles in the same event lie in the range $2 < p_T < p_T^{trig.}$. ϵ is the tracking efficiency of the associated particles. Fig. 1.11(b) shows the pedestal-subtracted azimuthal distributions for $p + p$ and central $d + Au$ collisions. The azimuthal distributions are also shown for central $Au + Au$ collisions after subtraction of the elliptic flow and pedestal contributions [84]. Observe that the near-side peak is similar in all three systems, while the back-to-back peak in central $Au + Au$ is dramatically suppressed relative to $p + p$ and $d + Au$. The contrast between $d + Au$ and central $Au + Au$ collisions in Fig. 1.10 and 1.11 indicates that the cause of the strong high p_T suppression observed previously is associated with medium produced in $Au + Au$ but not in $d + Au$ collisions. The conclusion reached by all four RHIC experiments is that the suppression is a final state effect and is attributed to the medium induced energy loss. However, by increasing both

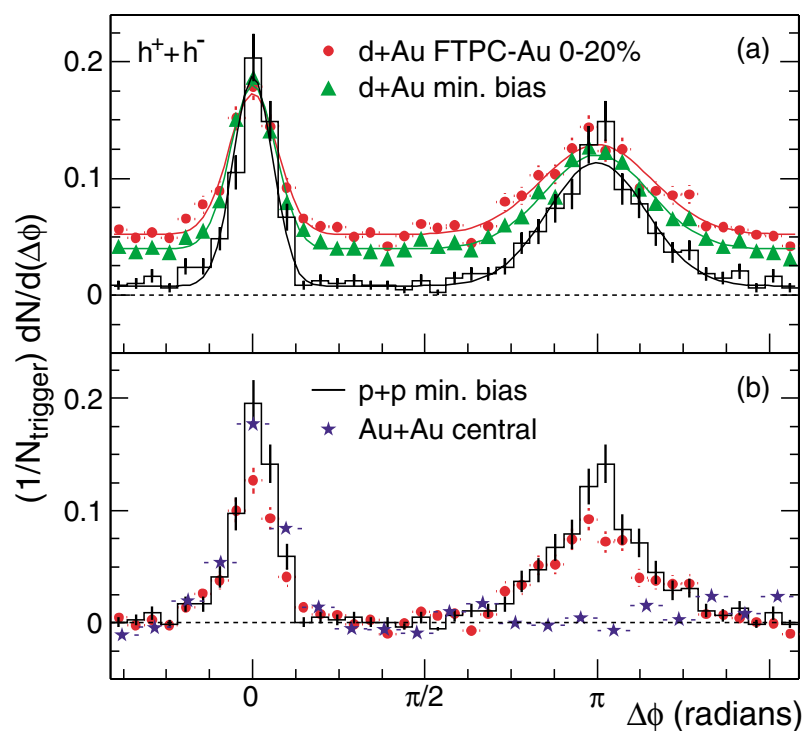


Figure 1.11: (a) Efficiency corrected two-particle azimuthal distributions for minimum bias and central $d + Au$ collisions, and for $p + p$ collisions [84]. (b) Comparison of two-particle azimuthal distributions for central $d + Au$ collisions to those seen in $p + p$ and central $Au + Au$ collisions [84].

the $p_T^{trig.}$ and $p_T^{assoc.}$ thresholds [94], one can recover the away-side partner fragmenting as in vacuum. Fig. 1.12 presents the evolution of the raw azimuthally correlated yield with increasing $p_T^{assoc.}$ for $8.0 < p_T^{trig.} < 15.0$ GeV/c for 20-40% centrality in $d + Au$ system and 0-5% centrality in $Au + Au$ system. As $p_T^{assoc.}$ is increased, the background level decreases and it is negligible in the highest bin, $6.0 < p_T^{assoc.} < p_T^{trig.}$. For most central collisions (0-5%) in $Au + Au$ 200 GeV, a narrow away-side jet peak was observed despite a significant jet quenching at RHIC.

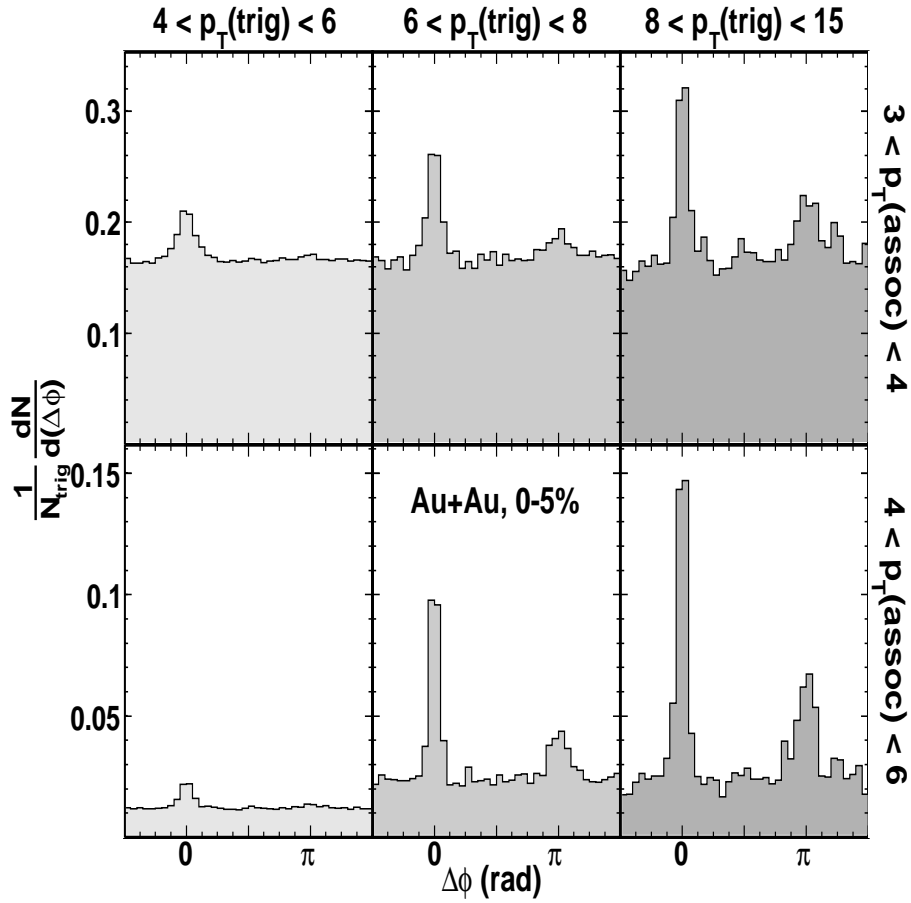


Figure 1.12: Azimuthal correlation histograms of high p_T charged hadron pairs for 0-5% $Au + Au$ events, for various $p_T^{trig.}$ and $p_T^{assoc.}$ ranges. In the lower left panel the yield is suppressed due to the constraint $p_T^{assoc.} < p_T^{trig.}$.

1.3.5 Nonstatistical Event-by-Event Fluctuations and Correlations

A physical system can be characterized by the study and analysis of fluctuations and correlations. In general, fluctuations can be distinguished on the basis of different classes. Quantum fluctuations come at the most fundamental level, which arise if the specific

observable does not commute with the Hamiltonian of the system under consideration. However, quantum fluctuations play a lesser role for the physics of heavy ion collisions. Second, there are “dynamical” fluctuations reflecting the dynamics and responses of the system. They help to characterize the properties of the bulk (semi-classical) description of the system. For instance, density fluctuations are controlled by the compressibility of the system. Finally, there are “trivial” fluctuations induced by the measurement process itself, such as finite number statistics etc. These need to be understood, controlled and subtracted in order to access the dynamical fluctuations which tell about the properties of the system. Fluctuations are related to the variance of a given observable [95] whereas correlations are accessible via the co-variances.

Study of event-by-event (E-by-E) fluctuations is the most efficient way to address fluctuations of a system created in heavy ion collisions, where a given observable is measured on an event-by-event basis and the fluctuations are studied over the ensemble of the events. In many cases (when the fluctuations are Gaussian) the analysis is equivalent to the measurement of two particle correlations over the same region of acceptance [95]. Consequently, fluctuations tell us about the 2-point functions of the system, which in turn determine the response of the system to external perturbations. For example, by measuring fluctuations of the net electric charge in a given rapidity interval, one obtains information on how this (sub)system would respond to applying an external (static) electric field.

The question to what extent the matter created in relativistic heavy ion collisions is equilibrated is central to the interpretation of many observables for the existence of a new phase of matter. A detailed analysis of the inclusive single particle yields of several hadronic species has led many authors [96–99] to believe that chemical equilibrium is achieved rather early. In general, the investigation of the event-by-event fluctuations of particle ratios provides a test bed of the hypothetical chemical equilibration.

In relativistic heavy ion collisions, the multiplicity of an event may differ dramatically from event to event due to the variation of impact parameter, energy deposition, baryon stopping, and other dynamical effects [100–102]. These fluctuations could also be influenced by novel phenomena such as Disoriented Chiral Condensates [103, 104]. There is a finite probability of fluctuation of globally conserved quantities such as net charge, strangeness and baryon number, when measured in a limited rapidity interval. The rapid hadronization of a quark gluon plasma can reduce net-charge fluctuations compared to hadronic expectations [105, 106], whereas phase separation can increase net baryon fluc-

tuations [107]. Study of fluctuations of conserved quantities emerge as one of the best tool to probe the final state of such dynamics as conservation laws limit the degree to which final-state scattering can dissipate them.

Experimentalists studying relativistic heavy ion collisions have followed two approaches to measure event-by-event fluctuations. Many favour following a statistical approach in which fluctuations of particle numbers are characterized by variances, covariances or higher moments [108–111]. These moments can be compared to expectations based on thermal equilibrium or other statistical models; any difference can be attributed to novel dynamics. Whereas, others favor the importance of momentum dependent correlations functions such as mean transverse momentum and balance fluctuations. The correlation-function has emerged as great success in case of identical pion Hanbury Brown-Twiss (HBT) correlations [112, 113].

The results presented in chapter 6 are based on observable, $\nu_{+-,\text{dyn}}$, suggested in [114], which is derived from integrals of the single- and two-particle distribution functions given as:

$$\rho_1(\eta) = \frac{dN}{d\eta} \quad (1.11)$$

$$\rho_2(\eta_1, \eta_2) = \frac{d^2N}{d\eta_1 d\eta_2} \quad (1.12)$$

Eq. 1.11 can be used to extract multiplicity in the rapidity range $\Delta\eta$ as

$$\langle N \rangle = \int_{\Delta\eta} \rho_1(\eta) d\eta \quad (1.13)$$

Where $\langle N \rangle$ represents an average of the observable “N” over an event ensemble. Similarly, by integrating two-particle density one can extract fluctuations of the particle number in this rapidity range.

$$\langle N(N-1) \rangle = \int_{\Delta\eta} \rho_2(\eta_1, \eta_2) d\eta_1 d\eta_2 \quad (1.14)$$

In an event where particle production is completely uncorrelated, then the two-body density factorizes into a product of two one-body densities. In such a situation, we find

$$\langle N(N-1) \rangle_{\text{uncorr}} = \int_{\Delta\eta} \rho_1(\eta_1) \rho_1(\eta_2) d\eta_1 d\eta_2 = \langle N \rangle^2 \quad (1.15)$$

A robust variance [115, 116] is defined as:

$$R_{\alpha\alpha} = \frac{V - \langle N \rangle}{\langle N \rangle^2} \quad (1.16)$$

And the robust covariance for particle species α and β .

$$R_{\alpha\beta} = \frac{V_{\alpha\beta}}{\langle N_\alpha \rangle \langle N_\beta \rangle} \quad (1.17)$$

where the two particle covariance $V_{\alpha\beta}$ is given as:

$$V_{\alpha\beta} = \langle N_\alpha N_\beta \rangle - \langle N_\alpha \rangle \langle N_\beta \rangle \quad (1.18)$$

These quantities have three significant advantages:

- These quantities vanish for $V = \langle N \rangle$ and $V_{\alpha\beta} = 0$. As a result they measure deviation from Poisson-statistical behaviour.
- The ratios, Eqs. 1.16 and 1.17 are robust variables, i.e., they are independent of detector efficiency [114].
- Most important, $R_{\alpha\beta}$ is directly related to the particle correlation as:

$$R_{\alpha\beta} = \frac{\langle N_\alpha N_\beta \rangle - \langle N_\alpha \rangle \langle N_\beta \rangle}{\langle N_\alpha \rangle \langle N_\beta \rangle} \quad (1.19)$$

$$R_{\alpha\beta} = \frac{\langle N_\alpha N_\beta \rangle}{\langle N_\alpha \rangle \langle N_\beta \rangle} - 1 \quad (1.20)$$

Thus Eq. 1.20 can also be written as

$$R_{\alpha\beta} = \frac{\int_{\Delta\eta} \rho_2(\eta_\alpha, \eta_\beta) d\eta_\alpha d\eta_\beta}{\int_{\Delta\eta} \rho_1(\eta_\alpha) d\eta_\alpha \int_{\Delta\eta} \rho_1(\eta_\beta) d\eta_\beta} - 1 \quad (1.21)$$

Rewriting Eq. 1.21 for positive and negative species

$$R_{++} = \frac{\int_{\Delta\eta} \rho_2(\eta_+, \eta_+) d\eta_+ d\eta_+}{\int_{\Delta\eta} \rho_1(\eta_+) d\eta_+ \int_{\Delta\eta} \rho_1(\eta_+) d\eta_+} - 1 \quad (1.22)$$

$$R_{--} = \frac{\int_{\Delta\eta} \rho_2(\eta_-, \eta_-) d\eta_- d\eta_-}{\int_{\Delta\eta} \rho_1(\eta_-) d\eta_- \int_{\Delta\eta} \rho_1(\eta_-) d\eta_-} - 1 \quad (1.23)$$

$$R_{+-} = \frac{\int_{\Delta\eta} \rho_2(\eta_+, \eta_-) d\eta_+ d\eta_-}{\int_{\Delta\eta} \rho_1(\eta_+) d\eta_+ \int_{\Delta\eta} \rho_1(\eta_-) d\eta_-} - 1 \quad (1.24)$$

A dynamic charge observable as a linear combination of R_{++} , R_{--} , R_{+-} is defined as:

$$\nu_{dyn} = R_{++} + R_{--} - 2R_{+-} \quad (1.25)$$

Finally $\nu_{+-,dyn}$ can be written as

$$\nu_{+-,dyn} = \frac{\langle N_+(N_+ - 1) \rangle}{\langle N_+ \rangle^2} + \frac{\langle N_-(N_- - 1) \rangle}{\langle N_- \rangle^2} - 2 \frac{\langle N_+ N_- \rangle}{\langle N_+ \rangle \langle N_- \rangle} \quad (1.26)$$

The term $\nu_{+-,dyn}$ vanishes when the negative and positive hadrons fluctuate simultaneously. An alternative expression [114] of $\nu_{+-,dyn}$ is:

$$\nu_{+-} = \left\langle \left(\frac{N_+}{\langle N_+ \rangle} - \frac{N_-}{\langle N_- \rangle} \right)^2 \right\rangle \quad (1.27)$$

Where N_+ and N_- are the multiplicities of positive and negative hadrons, respectively. However, if particle production is independent, then ν becomes

$$\nu_{stat} = \frac{1}{\langle N_+ \rangle} + \frac{1}{\langle N_- \rangle} \quad (1.28)$$

Thus, the dynamic charge observable is the difference

$$\nu_{+-,dyn} = \nu - \nu_{stat} \quad (1.29)$$

Net-charge fluctuations are observable of interest, as they provide a signature of the existence of a de-confined Quark Gluon Plasma[117–129]. Since the charge fluctuations are proportional to the square of the charge:

$$\langle \delta Q^2 \rangle = q^2 \langle (\delta N)^2 \rangle \quad (1.30)$$

the ratio of charge fluctuation over entropy

$$\frac{\langle \delta Q^2 \rangle}{S} \sim \frac{\langle \delta Q^2 \rangle}{\langle N_{charge} \rangle} \quad (1.31)$$

is sensitive to the fractional charges in a QGP. In Ref. [118], the observable

$$D \equiv 4 \frac{\langle \delta Q^2 \rangle}{\langle N_{charge} \rangle} \quad (1.32)$$

has been proposed and it has been shown that $D = 4$ for an uncorrelated pion gas, $D \simeq 3$ for a resonance gas [130] and $D \simeq 1 - 1.5$ for a Quark Gluon Plasma, respectively. Charge fluctuations have been analyzed by several experiments. PHENIX [131] at RHIC which measures with a small rapidity acceptance, finds charge fluctuations consistent with a resonance gas, if extrapolated to larger acceptance. STAR, which has a large acceptance also finds charge fluctuations consistent with a resonance gas [132]. CERES [133] and NA49 [134], both at SPS energies report preliminary results on charge fluctuations, which are consistent with a pure pion gas. But certainly, none of the measurement is even close to the prediction for the QGP.

Balance function [135, 136] is yet another way to access the non-trivial correlations of the system. The balance function for charged particle, for instance, is defined as:

$$B(\eta|\Delta\eta) = \frac{1}{2} \left[\frac{\langle N_{+-}(\eta|\Delta\eta) \rangle}{\langle N_-(\Delta\eta) \rangle} + \frac{\langle N_{+-}(\eta|\Delta\eta) \rangle}{\langle N_+(\Delta\eta) \rangle} - \frac{\langle N_{++}(\eta|\Delta\eta) \rangle}{\langle N_+(\Delta\eta) \rangle} - \frac{\langle N_{--}(\eta|\Delta\eta) \rangle}{\langle N_-(\Delta\eta) \rangle} \right] \quad (1.33)$$

Where $\langle N_{+-}(\eta|\Delta\eta) \rangle$ is the number of unlike-sign pairs which are η apart from each other within the rapidity window $\Delta\eta$. It essentially measures the average distance in rapidity over which a given charge is neutralized (balanced). The balance function measurement has been reported by the STAR collaboration [137]. Going from peripheral to central collisions, the width of balance function steadily decreases. The trend is what one would expect if more of the system is filled with a QGP as the collision becomes more central. However, since the reduction is only about 20% going from most peripheral to most central, it is not yet clear whether this signals the presence of a QGP, constituent quark clusters [138] or more mundane effect such as strong flow. For example in Ref. [139] the measured balance functions, along with particle ratios and particle spectra, could be explained in an expanding hadron gas model. The relation between balance function and $\nu_{+-,dyn}$ is given as:

$$B(Y|Y) = -\frac{N}{4}\nu_{+-,dyn} \quad (1.34)$$

which is an efficiency dependent observable.

Alternative Measures of Fluctuations

In this section we discuss connection between the variance $\nu_{+-,dyn}$ and other fluctuations measures.

- ϕ measure : Mrowczynski [108] introduced ϕ as a measure of net charge fluctuations. It consists of the difference between the mean of particle production, variances calculated event-by-event and the variance calculated over the entire dataset, Eq. 1.35.

$$\phi = \sqrt{\frac{\langle \Delta X^2 \rangle}{\langle N \rangle}} - \sqrt{\Delta x^2} \quad (1.35)$$

ϕ is related to $\nu_{+-,dyn}$ as :

$$\phi \approx \frac{\langle N \rangle}{8}\nu_{+-,dyn} \quad (1.36)$$

Unlike $\nu_{+-,dyn}$, ϕ is a non robust variable as it explicitly depends on the detection efficiency of positive and negative particles through the factors $\langle N_+ \rangle$ and $\langle N_- \rangle$.

- Particle ratios : Authors of Ref. [106] advocated the approach based on the variance of the ratio of positive and negative particle multiplicities, $R = \langle N_+ \rangle / \langle N_- \rangle$. The advantage of using “R” is that “volume” fluctuation effects cancel out to the first order. The relation between R and charge variance, ν , is

$$\langle \Delta R^2 \rangle = \langle R \rangle^2 \nu \quad (1.37)$$

Observe that neither ν nor $\langle \Delta R^2 \rangle$ are robust.

- Reduced variance : Reduced variance ω_Q is defined as:

$$\omega_Q = \frac{\langle \Delta Q^2 \rangle}{\langle N \rangle} \quad (1.38)$$

where $Q = N_+ - N_-$ and $N = N_+ + N_-$ [106, 125]. The relation between ω_Q and $\nu_{+-,dyn}$ is given as

$$\omega_Q \approx 1 + \frac{\langle N_+ + N_- \rangle}{4} \nu_{+-,dyn} \quad (1.39)$$

Eq. 1.39 indicates that this quantity has the same efficiency dependence as the total number of charged particles.

1.4 Particle Multiplicities

Heavy-ion collisions provide the best opportunity to test the predictions of QCD for matter under conditions close to the expected QCD phase-transition or resembling the conditions in the early universe. However, the system created in a heavy-ion collision is different from that simulated in lattice calculations or the early universe in several important aspects. The small size of the available nuclei set the scale of the temporal and spatial extent of the high density system created in the collision.

One can obtain important information about the collision dynamics by studying dependencies of the particle multiplicity and pseudorapidity distributions on collision centrality, energy, system size etc. Multiplicity distributions have been used to understand the particle production mechanism based on participant scaling, binary scaling, two component model [140] and recently by invoking the Color Glass Condensate (CGC) [4–9] model. Pseudorapidity distributions coupled with the measurement of average transverse energy provide information about the energy density achieved in the collision using the Bjorken formula [141] and on the nature of the system produced using hydrodynamics with CGC [4–9] as the initial condition.

The first physics results from RHIC were the measurements of pseudo-rapidity density of charged hadrons, $dN_{ch}/d\eta$, near mid-rapidity in central Au+Au collisions at collision energies of $\sqrt{s_{NN}} = 130$ and 200 GeV [142]. These first results surprisingly proved much smaller increase in multiplicities than those from lower energies against expectation in the vast majority of theoretical approaches. Further, RHIC with its measurements at top energy of 200 GeV reported logarithmic rise in the mid-rapidity particle density from the AGS [143]. A summary of these measurements for central Au+Au (Pb+Pb) collisions as a function of collision energy is shown in Fig. 1.13 (right panel), while Fig. 1.13 (left panel) shows a compilation of predictions in comparison to data at 200 GeV [144, 145]. It has been suggested that the relatively low multiplicity seen at RHIC is a

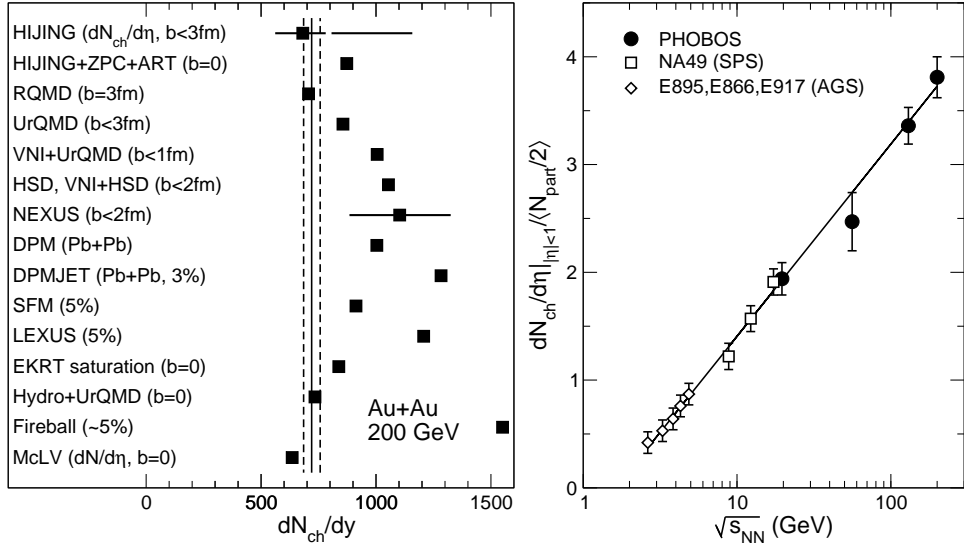


Figure 1.13: (Left panel) Results of PHOBOS measurement of charged particle density near mid-rapidity in central $Au + Au$ collisions at $\sqrt{s_{NN}} = 200$ GeV (shown by vertical line with the dashed lines denoting the systematic uncertainty) compared to theoretical prediction. (Right panel) Charged particle multiplicity density per participant near mid-rapidity for central nucleus-nucleus collisions as a function of $\sqrt{s_{NN}}$.

consequence of parton saturation, based on the idea that at high energies the density of low- x gluons in the transverse plane of the colliding nuclei will no longer allow them to interact independently. Rather, they will form a Color Glass Condensate [4–9], with the resultant coherent interaction of the constituents of the nuclei limiting the growth of particle multiplicity as a function of the collision energy. Model calculations based on the idea of parton saturation, in combination with local parton-hadron duality, have had impressive success in describing the energy, centrality and rapidity dependence of charged hadron production in nucleus-nucleus collisions.

Longitudinal Scaling of Charged Particle Pseudorapidity Density

The BRAHMS collaboration first pointed out one of the very interesting observations [146] that pseudo-rapidity distributions for inclusive charged hadrons is independent of collision energy, when viewed in the rest frame of one of the colliding nuclei. It is termed as “longitudinal scaling” [147]. This hypothesis states that the produced particles, in the rest frame of one of the colliding hadrons, will approach a limiting distribution. These universal distributions describe the momentum distributions of the fragments of the other hadron. It was assumed that the total hadronic cross section would become constant at large center-of-mass energy. If this occurred, the excitation and break-up of a hadron would be independent of the center-of-mass energy and distributions in the fragmentation region would approach a limiting curve.

Longitudinal scaling (also known as limiting fragmentation) was earlier observed in elementary collisions also. This concept led to the prediction of two types of scaling laws for the distribution of final state particles in the regions of the longitudinal momentum space which are either near to or far from the colliding partners. Fig. 1.14 shows $dN/d\eta$ for $p(\bar{p})+p$ collisions [148, 149] and $dN/d(y_T)$ for $e^+ + e^-$ collisions [150]. In both cases, the collisions exhibit longitudinal scaling (energy independence) when viewed in the “target” rest frame.

Such an observation was also confirmed by PHOBOS [151] and recently by STAR [152]. Very small amount of work is available for photons produced in terms of longitudinal

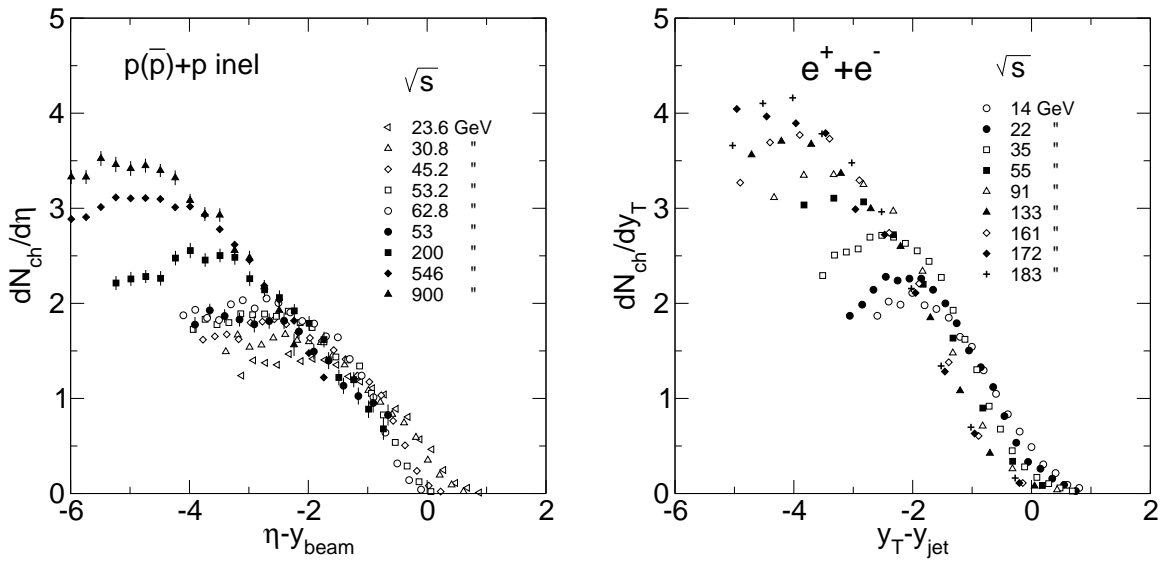


Figure 1.14: (Left panel) Pseudorapidity density distributions of charged particles in $p(\bar{p}) + p$ collisions at a range of energies versus the $\eta - y_{beam}$. (Right panel) Similar data for particles emitted along the jet axis in an $e^+ + e^-$ collision versus $y_T - y_{jet}$.

scaling in heavy ion collisions. Only preshower detectors at the Super Proton Synchrotron (SPS) and the STAR at RHIC have explored forward pseudorapidity regions [152–155].

1.5 Organization of the Thesis

The results presented in this thesis are based on $Cu + Cu$ collisions at $\sqrt{s_{NN}} = 62.4$ and 200 GeV. Chapter 4 presents simulation studies for the Photon Multiplicity Detector for $Cu + Cu$ system at $\sqrt{s_{NN}} = 200$ GeV and chapter 5 presents the pseudorapidity distribution of photons and relative fluctuation in photon multiplicity studies from data. Chapter 6 presents results on dynamical net charge fluctuations from $Cu + Cu$ collisions at the center of mass energies of 62.4 and 200 GeV. Finally, conclusions are given in chapter 7.

Bibliography

- [1] S.A. Bass, M. Gyulassy, H. Stöcker and W. Greiner, (1998), [arXiv:hep-ph/9810281].
- [2] F. Wilczek, *Physics Today*, **53** (2000) 22.
- [3] F. Wilczek, (2000), [arXiv:hep-ph/0003183].
- [4] J.J. Marian, *J. Phys. G*, **30** (2004) S751-S758.
- [5] E. Iancu and R. Venugopalan, (2003), [arXiv:hep-ph/0303204].
- [6] D. Kharzeev, E. Levin and M. Nardi, (2001), [arXiv:hep-ph/0111315].
- [7] D. Kharzeev, E. Levin and M. Nardi, *Nucl. Phys. A* **730** (2004) 448.
- [8] J.J. Marian, (2002), [arXiv:nucl-th/0212018].
- [9] T. Hirano and Y. Nara, (2004), [arXiv:nucl-th/0403029].
- [10] L.V. Gribov, E.M. Levin, and M.G. Ryskin, *Phys. Rept.* **100** (1983) 1-150.
- [11] A.H. Mueller and J.W. Qiu, *Nucl. Phys. B* **268** (1986) 847.
- [12] J.P. Blaizot and A.H. Mueller, *Nucl. Phys. B* **289** (1987) 847.
- [13] I. Balitsky, *Nucl. Phys. B* **463** (1996) 99-160.
- [14] Y.V. Kovchegov, *Phys. Rev. D* **61** (2000) 074018.
- [15] J.J. Marian, A. Kovner, A. Leonidov, and H. Weigert, *Nucl. Phys. B* **504** (1997) 415-431;
Phys. Rev. D **59** (1999) 014014.
- [16] Y.V. Kovchegov, *Phys. Rev. D* **54** (1996) 5463-5469.
- [17] E. Iancu, A. Leonidov, and L.D. McLerran, *Nucl. Phys. A* **692** (2001) 583-645;
Phys. Lett. B **510** (2001) 133-144.
- [18] H. Weigert, *Nucl. Phys. A* **703** (2002) 823-860.

- [19] E. Ferreira, E. Iancu, A. Leonidov, and L. McLerran, Nucl. Phys. A **703** (2002) 489-538.
- [20] F. Karsch, E. Laermann, R.C. Hwa and X.N. Wang (Eds.) World Scientific, Singapore, (2004), [arXiv:hep-lat/0305025].
- [21] U. Heinz, P.R. Subramanian, H. Stöcker and W. Greiner, J. Phys. G **12** (1986) 1237.
- [22] K. Rajagopal, Nucl. Part. Phys. A **2** (2002) 120, [arXiv:hep-ph/0009058].
- [23] Z. Fodor and S.D. Katz, JHEP **03** (2002) 014.
- [24] K.K. Szabo and A.I. Toth, JHEP **03** (2002) 008.
- [25] F. Karsch, E. Laermann and A. Peikert, Phys. Lett. B **478** (2000) 447.
- [26] J. Rafelski and B. Muller, Phys. Rev. Lett. **48** (1982) 1066.
- [27] J. Rafelski, Phys. Rep. **88** (1982) 331.
- [28] J. Rafelski and B. Müller, Phys. Rev. Lett. **48** (1982) 1066.
- [29] E. Anderson *et al.*, (WA97 Collaboration), Phys. Lett. **433** (1998) 209.
- [30] F. Antinori *et al.*, (NA57 Collaboration), Nucl. Phys. A **698** (2002) 118c.
- [31] G. Bruno *et al.*, (NA57 Collaboration), J. Phys. G: Nucl. Part. Phys. **30** (2004) S717-24.
- [32] M. Hofmann *et al.*, Nucl. Phys. **A** 566 (1994) 15c.
- [33] W. Cassing and U. Mosel, Prog. Part. Nucl. Phys. **25** (1990) 235.
- [34] H. Stöcker and W. Greiner, Phys. Rep. **137** (1996) 277.
- [35] H.H. Gutbrod, A.M. Poskanzer and H.G. Ritter, Rep. Prog. Phys. **52** (1989) 1267.
- [36] C. Gale, G.M. Welke, M. Prakash, S.J. Lee, and S.D. Gupta, Phys. Rev. C **41** (1990) 1545.
- [37] J. Zhang, S.D. Gupta, C. Gale, Phys. Rev. C **50** (1994) 1617.
- [38] V.N. Russkikh and Y.B. Ivanov, Nucl. Phys. A **591** (1995) 699.
- [39] M.D. Partlan *et al.*, (EOS Collaboration), Phys. Rev. Lett. **75** (1995) 2100.
- [40] N. Herrmann *et al.*, (FOPI Collaboration), Nucl. Phys. A **610** (1996) 49c.

- [41] J. Chance *et al.*, (EOS Collaboration), Phys. Rev. Lett. **78** (1997) 2535.
- [42] P. Danielewicz *et al.*, Phys. Rev. Lett. **81** (1998) 2438.
- [43] J.Y. Ollitrault, Phys. Rev. D **46** (1992) 229.
- [44] W. Reisdorf and H.G. Ritter, Ann. Rev. Nucl. Part. Sci. **47** (1997) 1.
- [45] P. Braun-Munzinger and J. Stachel. Nucl. Phys. A **638** (1998) 3c.
- [46] Q. Pan and P. Danielewicz, Phys. Rev. Lett. **70** (1993) 2062.
- [47] T. Maruyama, W. Cassing, U. Mosel, S. Ties and K. Weber, Nucl. Phys. A **573** (1994) 653.
- [48] D. Rischke, Nucl. Phys. A **610** (1996) 88c.
- [49] S.A. Bass *et al.*, Prog. Part. Nucl. Phys. **41** (1998) 225; J. Phys. G **25** (1999) R1.
- [50] S.K. Ghosh, S.C. Phatak and P.K. Sahu, Z. Phys. A **352** (1996) 457.
- [51] B.A. Li, C.M. Ko, A.T. Sustich, and B. Zhang, Phys. Rev. C **60** (1999) 011901(R).
- [52] J. Brachmann, S. Soff, A. Dumitru, H. Stöcker, J.A. Maruhn, W. Greiner, L.V. Bravina, and D.H. Rischke, Phys. Rev. C **61** (2000) 024909.
- [53] A. Hombach, W. Cassing, S. Teis, and U. Mosel, Eur. Phys. J. A **5** (1999) 157.
- [54] Y. Nara, N. Otuka, A. Ohnishi, and T. Maruyama, Prog. Theor. Phys. Suppl. **129** (1997) 33.
- [55] M. Belkacem, M. Brandstetter, S.A. Bass *et al.*, Phys. Rev. C **58** (1998) 1727; L.V. Bravina *et al.*, J. Phys. G **25** (1991) 351.
- [56] L.V. Bravina, A. Faessler, C. Fuchs, and E.E. Zabrodin, Phys. Rev. C **61** (2000) 064902.
- [57] P.K. Sahu, A. Hombach, W. Cassing, M. Effenberger and U. Mosel, Nucl. Phys. A **640** (1998) 493.
- [58] A.B. Larionov, W. Cassing, C. Greiner, and U. Mosel, Phys. Rev. C **62** (2000) 064611.
- [59] Y.B. Ivanov, E.G. Nikonov, W. Norenberg, V.D. Toneev, and A.A. Shandenko, Heavy Ion Phys. **15** (2002) 117.
- [60] P.K. Sahu, W. Cassing, Nucl. Phys. A **712** (2002) 357.

- [61] P. Danielewicz, R. Lacey, and W.G. Lynch, *Science* **298** (2002) 1592.
- [62] M. Isse, A. Ohnishi, N. Otuka, P.K. Sahu, and Y. Nara, *Phys. Rev. C* **72** (2005) 064908.
- [63] T. Hirano, *Phys. Rev. Lett.* **86** (2001) 2754.
- [64] H. Liu, S. Panitkin, and N. Xu, *Phys. Rev. C* **59** (1999) 348.
- [65] L.P. Csernai and D. Roehrich, *Phys. Lett. B* **458** (1999) 454.
- [66] E.E. Zabrodin, C. Fuchs, L.V. Bravina, and A. Faessler, *Phys. Rev. C* **63** (2001) 034902.
- [67] H. Stöcker, E.L. Bratkovskaya, M. Bleisher, S. Soff, and Z. Zhu, *J. Phys. G* **31** (2005) S929.
- [68] J. Brachmann *et al.*, *Phys. Rev. C* **61** (2000) 024909.
- [69] L.P. Csernai and D. Rohrich, *Phys. Lett. B* **458** (1999) 454.
- [70] H. Stöcker, *Nucl. Phys. A* **750** (2005) 121.
- [71] J. Adams *et al.*, (STAR Collaboration), *Phys. Rev. C* **73** (2006) 034903.
- [72] J. Adams *et al.*, (STAR Collaboration), *Phys. Rev. C* **72** (2005) 014904.
- [73] T. Matsui and H. Satz, *Phys. Lett. B* **178** (1986) 416.
- [74] E.V. Shuryak, *Phys. Lett. B* **78** (1978) 150.
- [75] C. Quigg and J.L. Rosner, *Phys. Rep.* **56** (1979) 167.
- [76] K. Kanaya and H. Satz, *Phys. Rev. D* **34** (1986) 3193.
- [77] N.S. Craigie, *Phys. Rep.* **47** (1978) 1.
- [78] M.C. Abreu, *Phys. Lett. B* **477** (2000) 28-36.
- [79] R. Baier, D. Schiff and B.G. Zakharov, *Ann. Rev. Nucl. Part. Sci.* **50** (2000) 37.
- [80] C. Adler *et al.*, (STAR Collaboration), *Phys. Rev. Lett.* **89** (2002) 202301.
- [81] K. Adkox *et al.*, (PHENIX Collaboration), *Phys. Rev. Lett.* **88** (2002) 022301.
- [82] B.B. Back *et al.*, (PHOBOS Collaboration), [arXiv:nucl-ex/0302015].
- [83] J. Adams *et al.*, (STAR Collaboration), [arXiv:nucl-ex/0305015].

- [84] C. Adler *et al.*, (STAR Collaboration), Phys. Rev. Lett. **90** (2003) 082302.
- [85] D. Kharzeev, E. Levin, and L. McLerran, Phys. Lett. **561** (2003) 93.
- [86] X.N. Wang, Phys. Rev. C **61** (2000) 064910.
- [87] Y. Zhang *et al.*, Phys. Rev. C **65** (2002) 034903.
- [88] B.Z. Kopeliovich *et al.*, Phys. Rev. Lett. **88** (2002) 232303.
- [89] A. Accardi, [arXiv:hep-ph/0212148].
- [90] I. Vitev, Phys. Lett. B **562** (2003) 36.
- [91] K.J. Eskola and H. Honkanen, Nucl. Phys. A **713** (2003) 167.
- [92] S.R. Klein and R. Vogt, [arXiv:nucl-th/0305046].
- [93] R. Baier, A. Kovner and U. Wiedemann, [arXiv:hep-ph/0305265].
- [94] J. Adams *et al.*, (STAR Collaboration), Phys. Rev. Lett. **97** (2006) 162301.
- [95] A. Bialas and V. Koch, Phys. Lett. B **456** (1999) 1, [arXiv:nucl-th/9902063].
- [96] M. Becattini, M. Gazdzicki, and J. Sollfrank, Eur. Phys. J. C **5** (1998) 143.
- [97] P. Braun-Muzinger, I. Heppe, and J. Stachel, [nucl-th/9903010].
- [98] J. Cleymans and K. Redlich, Phys. Rev. C **60** (1999) 054908.
- [99] U. Heinz, J. Phys. G **25** (1999) 263.
- [100] G. Baym, G. Friedman, and I. Sarcevic, Phys. Lett. B **219** (1989) 205.
- [101] M. Gazdzicki and S. Mrowczynski, J. Phys. C **54** (1992) 127.
- [102] H. Heiselberg, Phy. Rep. **351** (2001) 161.
- [103] K. Rajagopal and F. Wilczek, Nucl. Phys. B **399** (1993) 395.
- [104] S. Gavin, Nucl. Phys. A **590** (1995) 163c.
- [105] S. Jeon and V. Koch, Phys. Rev. Lett. **85** (2000) 2076.
- [106] V. Koch, M. Bleicher, and S. Jeon, Nucl. Phys. A **698** (2002) 261.
- [107] D. Bower and S. Gavin, Phys. Rev. C **64** (2001) 051902(R).
- [108] S. Mrowczynski, [arXiv:nucl-th/0112007].

- [109] H. Heiselberg and A.D. Jackson, Phys. Rev. C **63** (2001) 064904.
- [110] STAR, T.A. Trainor in *Proceedings of the 17th Winter Workshop Nuclear Dynamics, 2001*, edited by G.D. Westfall and W. Bauer (Ep Systems, Debrecen, 2001), p.1.
- [111] J. Zaranek, [arXiv:hep-ph/0111228].
- [112] G.A. Miller and J.G. Cramer, Nucl. Phys. A **782** (2007) 251-258.
- [113] W.N. Zhang, Y.Y. Ren and C.Y. Wong, Phys. Rev. C. **74** (2006) 024908.
- [114] C. Pruneau, S. Gavin and S. Voloshin, Phys. Rev. C **66** (2002) 044904.
- [115] J. Whitemore, Phys. Rep. **27** (1976) 187.
- [116] L. Foa, Phys. Rep. **22** (1975) 1.
- [117] M. Asakawa, U.W. Heinz, and B. Muller, Phys. Rev. Lett **85** (2000) 2072, [arXiv:hep-ph/0003169].
- [118] S. Jeon and V. Koch, Phys. Rev. Lett **85** (2000) 2076, [arXiv:hep-ph/0003168].
- [119] J.W. Harris and B. Muller, Ann. Rev. Nucl. Part. Sci. **46** (1996) 71.
- [120] M. Stephanov, K. Rajagopal and E. Shuryak, Phys. Rev. Lett. **81** (1998) 4816.
- [121] M. Stephanov, K. Rajagopal and E. Shuryak, Phys. Rev. D **60** (1999) 114028.
- [122] S.A. Voloshin, V. Koch and H.G. Ritter, Phys. Rev. C **60** (1999) 024901.
- [123] S.A. Bass, M. Gyulassy, H. Stöcker and W. Greiner, J. Phys. G: Nucl. Part. Phys. **25** (1999) R1.
- [124] M. Asakawa, U. Heinz and B. Muller, Phys. Rev. Lett. **85** (2000) 2076.
- [125] Zi-wei Lin and C.M. Ko, Phys. Rev. C **64** (2001) 041901.
- [126] H. Heiselberg and A.D. Jackson, Phys. Rev. C **63** (2001) 064904.
- [127] M. Stephanov, Phys. Rev. D **65** (2002) 096008.
- [128] Q. Liu and T.A. Trainor, Phys. Lett. B **567** (2003) 184.
- [129] S. Gavin (2003), [arXiv:nucl-th/0308067].
- [130] S. Jeon and V. Koch, Phys. Rev. Lett. **83** (1999) 5435, [arXiv:nucl-th/9906074].

- [131] K. Adcox *et al.*, (PHENIX Collaboration), Phys. Rev. Lett. **89** (2002) 082301, [arXiv:nucl-ex/0203014].
- [132] J. Adams *et al.*, (STAR Collaboration), Phys. Rev. C. **68** (2003) 044905.
- [133] H. Appelshauser *et al.*, (CERES Collaboration), Nucl. Phys. A **752** (2005) 394, [arXiv:nucl-ex/0409022].
- [134] C. Blume *et al.*, (2002), [arXiv:nucl-ex/0208020].
- [135] S.A. Bass, P. Danielewicz, and S. Pratt, Phys. Rev. Lett. **85** (2000) 2689, [arXiv:nucl-th/0005044].
- [136] S. Jeon and S. Pratt, Phys. Rev. C **65** (2002) 044902, [arXiv:hep-ph/0110043].
- [137] J. Adams *et al.*, (STAR Collaboration), Phys. Rev. Lett. **90** (2003) 172301, [arXiv:nucl-ex/0301014].
- [138] A. Bialas, (2003), [arXiv:hep-ph/0308245].
- [139] P. Bozek, W. Broniowski, and W. Florkowski, (2003), [arXiv:nucl-th/0310062].
- [140] M. Biyajima *et al.*, Phys. Rev. Lett. B **515** (2001) 470-476.
- [141] J.D. Bjorken, Phys. Rev. D **27** (1983) 140.
- [142] B.B. Back *et al.*, (PHOBOS Collaboration), Phys. Rev. C **65** (2002) 061901R.
- [143] B.B. Back *et al.*, (PHOBOS Collaboration), Phys. Rev. Lett. **88** (2002) 022302.
- [144] K.J. Eskola, Nucl. Phys. A **698** (2002), [arXiv:hep-ph/0104058].
- [145] B.B. Back *et al.*, (PHOBOS Collaboration), [arXiv:nucl-ex/0410022].
- [146] I.G. Bearden *et al.*, (BRAHMS Collaboration), Phys. Rev. Lett. **88** (2002) 202301.
- [147] J. Benecke, T.T. Chou, C.N. Yang and E. Yen, Phys. Rev. **188** (1969) 2159.
- [148] G.J. Alner *et al.*, (UA5 Collaboration), Phys. Rep. **154** (1987) 247.
- [149] W. Thome *et al.*, Nucl. Phys. B **129** (1977) 365.
- [150] P. Abreu *et al.*, (DELPHI Collaboration), Phys. Lett. B **459** (1999) 397.
- [151] B.B. Back *et al.*, (PHOBOS Collaboration), Phys. Rev. Lett. **91** (2003) 052303.
- [152] J. Adams *et al.*, (STAR Collaboration), Phys. Rev. Lett. **95** (2005) 062301.

- [153] J. Adams *et al.*, (STAR Collaboration), Phys. Rev. C **73** (2006) 034906.
- [154] M.M. Aggarwal *et al.*, (WA98 Collaboration), Phys. Rev. C **65** (2002) 054912.
- [155] M.M. Aggarwal *et al.*, (WA98 Collaboration), Phys. Rev. C **64** (2001) 011901,
Phys. Rev. Lett. B **403** (1997) 390-396,
Phys. Rev. Lett. B **404** (1997) 207-212.

Chapter 2

Experimental Facility

2.1 Relativistic Heavy Ion Collider (RHIC)

The Relativistic Heavy Ion Collider located at Brookhaven National Laboratory in Upton, New York [1], focuses on the study of primordial form of matter that existed in the universe shortly after the Big Bang [2] and also the structure of protons. At present, RHIC is the most powerful heavy-ion collider in the world. It is also the only collider in the world which can collide spin-polarized protons. Past, present and future heavy-ion accelerators and their achieved (planned) energies are listed in Table 2.1.

Table 2.1: Accelerators for relativistic heavy-ion collision experiments.

Accelerator	Ion species	$\sqrt{s_{NN}}$ (GeV)	Starting year
AGS, BNL	O, Si	5.4	1986
	Au	4.9	1992
SPS, CERN	O, S	19.4	1986
	Pb	17.3	1994
RHIC, BNL	Au	130	2000
	Au	200	2001
RHIC, BNL	Cu	200	2005
LHC, CERN	Pb	5500	2009

2.1.1 The Accelerator

RHIC is an intersecting storage ring (ISR) particle accelerator. Two independent rings which are arbitrarily denoted as “blue” and “yellow” rings allow a virtually free choice of colliding projectiles. The hexagonally shaped double storage rings of RHIC are shown in Fig. 2.1. RHIC has a circumference of 3,834 m and curved edges deflect the stored

particles with the help of 1740 super-conducting niobium titanium magnets kept at a temperature of < 4.6 K. There are 6 interaction points, where the two rings cross, allowing the particles to collide. The interaction points are enumerated by clock positions, with the injection point at “6 o’clock” position. 2 out of 6 interaction points are unused and left for further expansion of RHIC. Fig. 2.2 shows the position of four experiments around the RHIC ring. The basic parameters of RHIC are listed in Table 2.2.

Among the two larger detectors, STAR is aimed in the detection of hadrons with the largest Time Projection Chamber (TPC) so far, covering a large solid angle. While PHENIX is further specialized in detecting rare and electromagnetic particles, using a partial coverage detector system in a super-conductively generated axial magnetic field. Other smaller detector like PHOBOS has the largest pseudo-rapidity coverage and is tailored for bulk particle multiplicity and angular measurements, while BRAHMS is designed for momentum spectroscopy in order to study the so called “small-x” and saturation Physics. A particle before reaching the RHIC storage ring passes through

Table 2.2: The basic parameters of RHIC.

Parameters	
No. of bunches/ring	57
No. of ions/bunch	1×10^9
Bunch separation (ns)	213
No. of crossing points	6
Average luminosity ($cm^{-2}sec^{-1}$)	$\sim 2 \times 10^{26}$
lifetime of beam (hour)	5 ~ 10

several stages of boosters as discussed below:

- **Tandem Van de Graaff:** The tandem uses static electricity to accelerate atoms by removing some of their electrons, which are in a cloud around the nucleus. What is left behind is a charged atom known as an ion. A partial lack of electrons gives each ion a strong positive charge. The tandem gives billions of these ions a boost of energy, sending them on their way towards the booster.
- **Tandem-to-Booster (TTB) line:** From the tandem, the bunches of ions enter the tandem-to-booster beamline, which carries them through the vacuum via magnetic field to the booster. At this point they attain velocity about 5% of the speed of light.
- **Linear accelerator (linac):** In addition to heavy ions, some experiments at RHIC

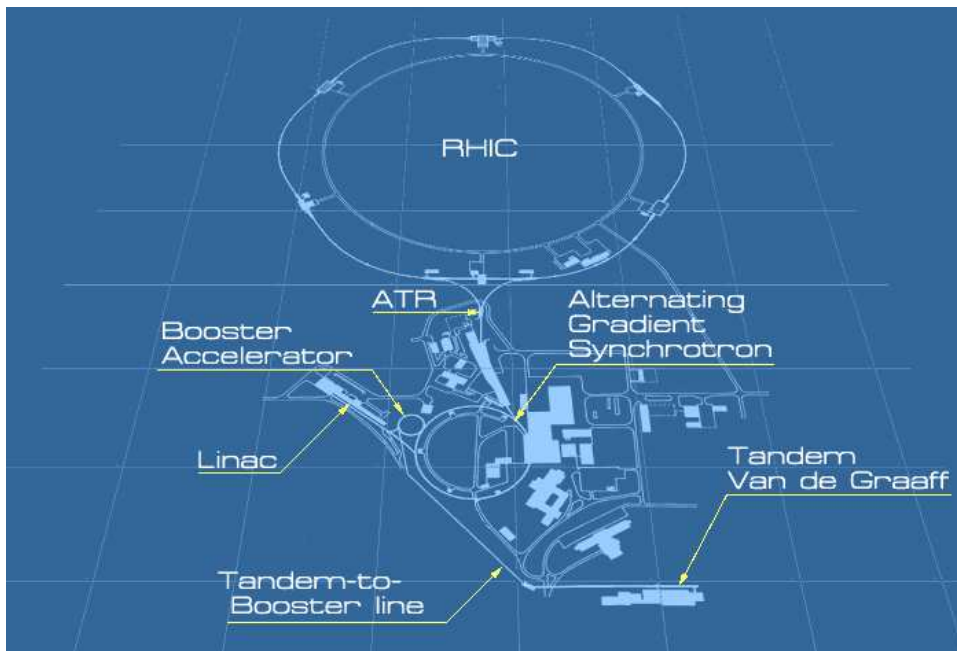


Figure 2.1: Schematic view of the RHIC complex. The figure highlights various stages in the acceleration of heavy ions or pp collisions.

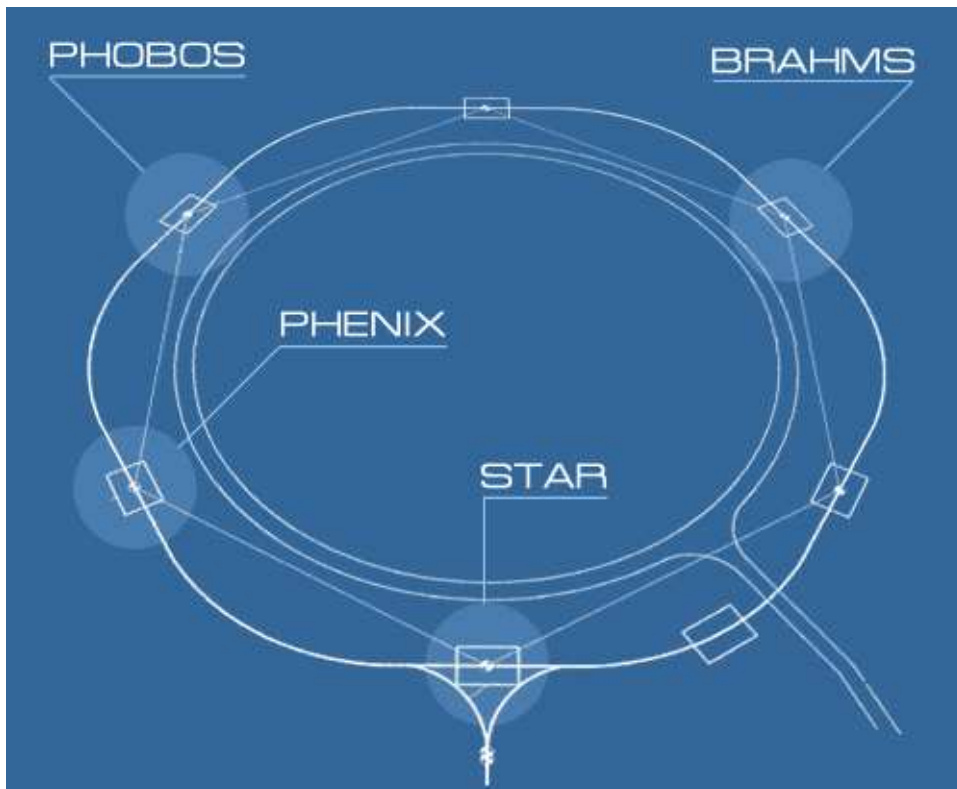


Figure 2.2: Position of four experiments around the RHIC ring. The STAR experiment is at 6 o'clock position and other experiments, PHENIX, PHOBOS and BRAHMS are located at 8 o'clock, 10 o'clock and 2 o'clock positions, respectively.

use colliding beams of protons. For these experiments, energetic protons are supplied by the 200 MeV linac. Protons from the linac are transferred to the booster.

- **The Booster synchrotron:** The booster synchrotron is a powerful and compact circular accelerator that provides more energy to the ions, by having them “surf ride” on the downhill slope of radio frequency electromagnetic waves. The ions are propelled forward at higher and higher speeds, getting closer and closer to the speed of light. The booster feeds the beam into the Alternating Gradient Synchrotron (AGS).
- **Alternating Gradient Synchrotron:** When ions enter the AGS from the Booster, they are traveling at about 37% of the speed of light. As they whirl around the AGS and are accelerated as in the Booster, ions get even more energy until they are traveling at 99.7% of the speed of light.
- **ATR:** When the ion beam is traveling at top speed in the AGS, it is taken down another beam line called the AGS-To-RHIC (ATR) transfer line. At the end of this line, there is a “fork in the road”, where the switching magnets sends the ion bunches down one of two beam lines. Bunches are directed either left to clockwise RHIC ring or right to travel counter-clockwise in the second RHIC ring. From here on the beam in the rings are made to collide into one another at four interaction point.

As an example for the stages described above, gold nuclei leaving Tandem Van de Graaff have an energy of about 1 MeV per nucleon and have an electric charge $Q = +32$ (32 electrons stripped from the gold atom). The particles are then accelerated by the booster Synchrotron to 95 MeV per nucleon, which injects the projectile now with $Q = +77$ into the Alternating Gradient Synchrotron (AGS), before they finally reach 8.86 GeV per nucleon and are injected in a $Q = +79$ state (no electrons left) into the RHIC storage ring over the AGS-To-RHIC Transfer Line (ATR), sitting at the 6 o’clock position.

The main types of particle combination used at RHIC are p+p, d+Au, Cu+Cu and Au+Au. These projectiles typically travel at a speed of 99.995% of the speed of light. For Au+Au collisions, the center-of-mass energy is typically 200 GeV (or 100 GeV per nucleon). A center-of-mass energy of 400 GeV was briefly achieved during Run-5 in p+p collisions.

The RHIC has a unique capability of producing polarized protons and it holds the record of producing the highest energy polarized protons. These polarized protons are injected into RHIC and preserving this state throughout the energy ramp is a difficult

task that can only be accomplished with the aid of siberian snakes (a chain of solenoids and quadrupoles for aligning particles [3]) and AC dipoles.

2.2 The STAR Experiment in Year 2006

The main devices of the STAR experiment are a large-cylinder Time Projection Chamber (TPC) and a solenoidal magnet. The STAR detector [4] uses the TPC as its primary tracking device [5–9]. The TPC covers the interaction point at 6 o'clock collision point of the RHIC ring over the length of 4 m in the beam direction and it is 4 m in diameter. The solenoidal magnet surrounding TPC is capable of maximum magnetic field strength of 0.5 T. In addition to the sub detectors used in event reconstruction, two Zero-Degree Calorimeters (ZDCs) and a Central Trigger Barrel (CTB) are used for event triggering. A layout of the STAR sub detectors is shown in Fig. 2.3.

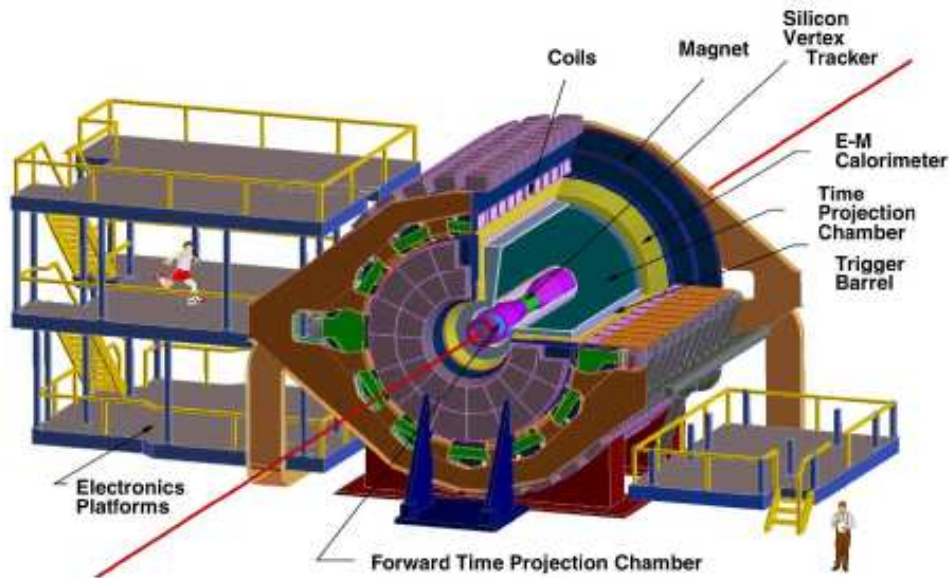


Figure 2.3: Experimental setup of the STAR detector.

2.2.1 The Magnet

The magnet system was designed by R.D. Schlueter of Lawrence Berkeley Laboratory [10]. The present design of the magnet produces a near uniform field over the operating range $0.25 < |B_z| < 0.5$ T parallel to the beam direction (z -direction) over the entire TPC volume. Magnetic-field mapping was performed before the TPC installation. The radial component of the magnetic field (B_r) is measured at both ends of the TPC ($Z = \pm 2.1$ m) and the obtained value is approximately ± 25 Gauss for the half-field ($|B_z| = 0.25$ T) operation. The azimuthal component (B_ϕ) is less than ± 1.5 Gauss over the TPC volume.

The magnet is roughly cylindrical in geometry and consists of 30 flux return bars (backlegs), four end rings and two poletips. The 6.85 m long flux return bars are trapezoidal in cross section and weighing 18 tons each. They form the outer wall of the cylinder which encloses the main and space trim coils and are attached to an inner and outer ring pair at each end of the magnet. The inner end rings have an inner diameter of 5.27 m with 30 chord surfaces on the 6.28 m outer diameter to fix the azimuth location of each flux return bar. The outer rings are the structural connection between the ends of the flux return bars and have the same inner diameter as the inner rings with a 7.32 m outer diameter and 203 mm axial thickness, weighing 35 tons each. More details of the magnet can be seen in [11].

2.2.2 The Time Projection Chamber

The TPC is designed to record low-multiplicity to high multiplicity collision events in which more than 2000 charged particles per event could be produced over its large acceptance. It stores sufficient information to reconstruct 3-dimensional images of charged particles' trajectories. It records tracks of the particles, measures their momenta and identifies the particles by measuring their ionization loss (dE/dx). The TPC acceptance covers ± 1.8 units of pseudo-rapidity through the full azimuthal angle. Particles are identified over the momentum range from 100 MeV/c to greater than 1 GeV/c. The TPC (shown

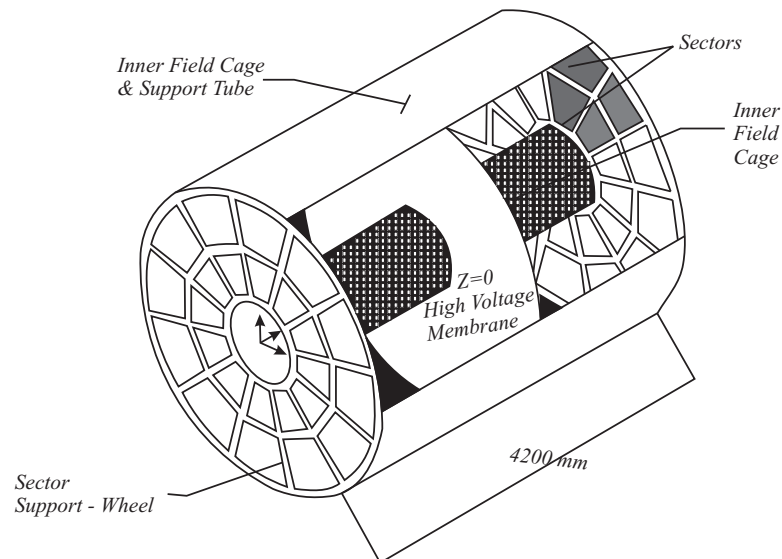


Figure 2.4: Schematic view of the Time projection chamber.

schematically in Fig. 2.4) is 4.2 m long and 4 m in diameter. It is an empty volume filled with P10 gas (10% methane, 90% argon) [12]. This gas mixture is chosen to minimize the attenuation of the drifting electrons and to provide a drift velocity ~ 5.4 cm/ μ s. Air which consists of water and oxygen can influence the drift velocity of the electrons. To

minimize this effect the TPC is regulated at 2 mbar above atmospheric pressure. The primary attribute of this gas is a fast drift velocity which peaks at a low electric field. The high-voltage Central Membrane (CM) is at the center of the TPC ($z = 0$ cm) and Multi-Wire Proportional Chambers (MWPC) are at both end-caps ($z = \pm 210$ cm). The electronic read out of the TPC consist of 12 pairs of inner and outer sectors of pads on each end. Each sector is divided into inner and outer subsectors. The TPC volume is divided at its center along the beam direction by a high voltage cathode membrane. Detailed view of the TPC end cap can be seen in Fig. 2.5. The outer field cage consist of wide concentric cylinders which provide a series of equipotential rings to divide the voltage evenly. The grounded end caps (operated at 0 V), the central membrane (operated at 28 kV), and equipotential rings of the outer field cage provide the necessary uniform electric field. Fig. 2.6 shows the inner sector of the TPC which consists of 13 pad rows

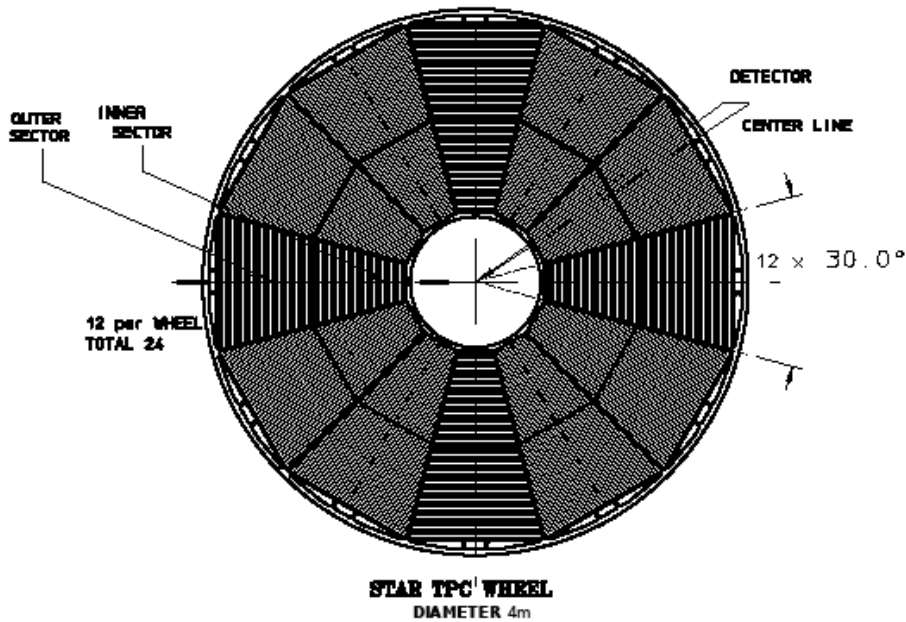


Figure 2.5: End view of the STAR TPC. 12 sectors on each end cover the full azimuth range. Inner and outer sectors can be seen in the figure.

with a total of 1750 small pads ($2.85 \text{ mm} \times 11.5 \text{ mm}$). The outer sector has 32 pad rows with 3940 smaller pads ($6.20 \text{ mm} \times 19.5 \text{ mm}$). The small pads in the inner sector are arranged in widely spaced rows to extend the position measurements along the track to small radii in a high track density environment. Whereas the outer sector has densely packed (i.e, very less space between pad rows) larger pads to minimize the dE/dx resolution. Full track ionization signal is collected and more ionized electrons improve statistics on the dE/dx resolution with larger pads in the outer sector. The readout MWPC (Multi Wire Proportional Counter) have 3 wire planes: a gating grid, ground plane, and anode

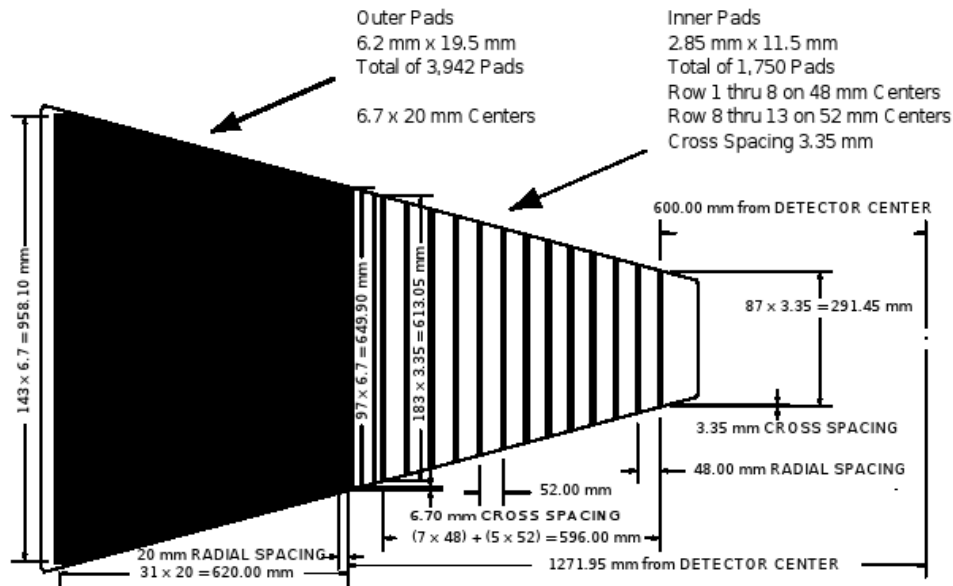


Figure 2.6: Detailed view of a single sector of the TPC showing inner and outer sub-sector. The inner sub-sector is on the right side and has small pads arranged in widely spaced rows. The outer sector which is seen on the left has densely packed pads.

wires are presented in Fig. 2.7. The drifting electrons are amplified by a grid of wires on each end of the TPC. The signals are measured with small pads behind the anode wires. The gating grid is the outermost wire plane on the sector structure. The gating grid is normally closed in order to minimize the buildup of positively charged ions in the drift volume. Its operating voltage alternates between ± 75 V from the nominal value. The gating grid opens when a trigger is received. The TPC pad plane together with the anode wires and ground plane (shield grid) forms STAR's multi-wire proportional chamber. Electrons initiate avalanches when they pass the gating grid and drift to the anode wires (which are operated at 1170 V for the inner sector and 1390 V for the outer sector). The readout pads directly below the anode wires detect the signal induced by the ions created by the avalanche. The track of a primary particle passing through the TPC is reconstructed by finding ionization clusters along the track for x,y and z-space separately. The x and y coordinates of a cluster are determined by the charge measured on adjacent pads in a single row. The z coordinate of a point inside the TPC is determined by measuring the drift time of a cluster of ionized electrons from the point of origin to the anodes on the endcap and dividing by the average velocity. A charged particles passing through the gas mixture produces ion pairs which are accelerated towards the endcap by the electric field applied parallel to the beam axis. Drifting electron clusters are amplified by high electric field near the anode wires on the readout board which induces image charges on the pad plane. The 3-D coordinates and sizes of the image charges are stored as raw data of time sequence of ADC values from each pad. For reduction of the data volume, the

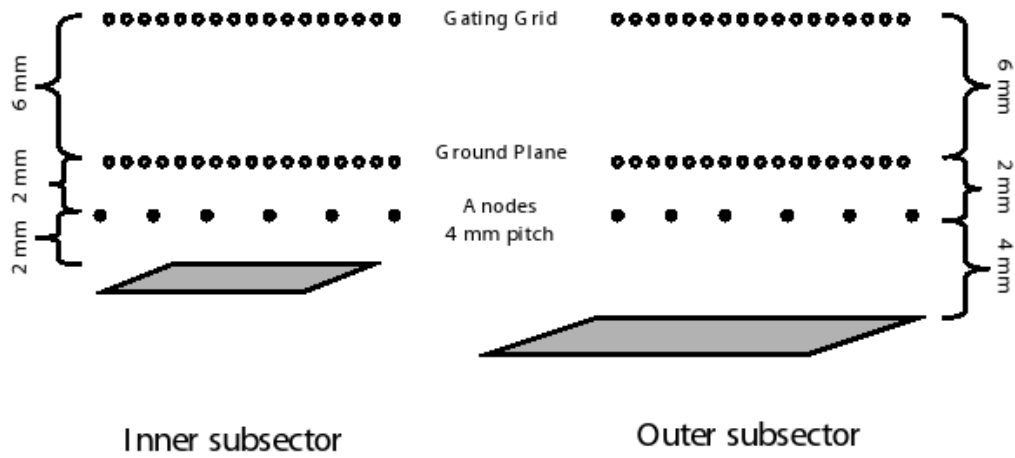


Figure 2.7: The readout chamber region of the STAR TPC. The gating grid and ground plane wires are on a 1 mm pitch, while the anode wires are spaced every 4 mm.

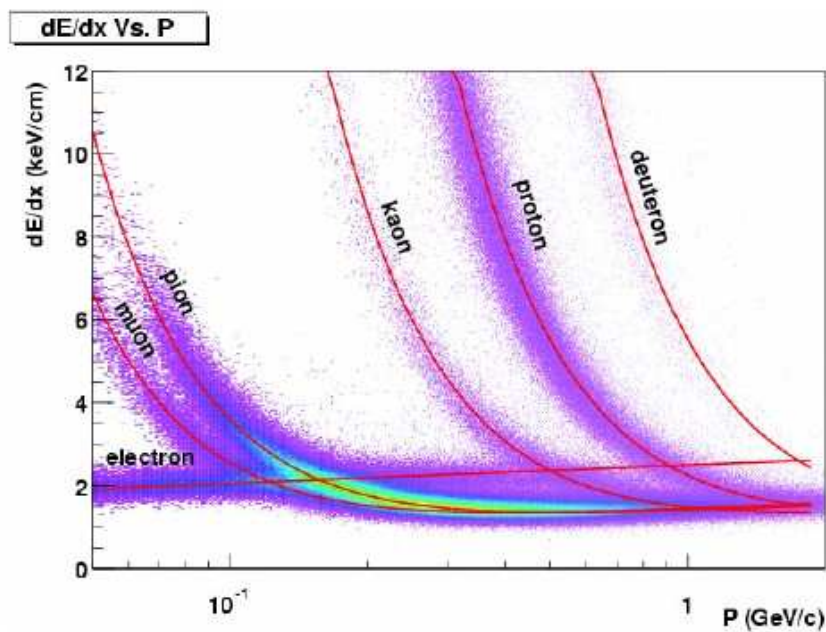


Figure 2.8: The energy loss distribution for the primary and secondary particles in the STAR TPC as a function of p_T . The magnetic field was set at 0.25 T.

background noise is calculated as data average with beam on and this noise is subtracted from the data event-by-event before it is stored. More details about the TPC are given in Table 2.3.

Fig. 2.8 presents the energy loss for both primary and secondary particles in the TPC as a function of the particle momentum. The data shown in Fig. 2.8 was corrected for signal and gain variations. The resolution of the detector is 8% for the tracks that cross 40 pad-rows. The prominent proton, deuteron, and muon bands come from secondary interactions in the beam pipe, and from pion and kaon decays. Pions and protons can be separated from each other up to 1 GeV/c.

Table 2.3: Basic parameters of the TPC and its associated hardware [8].

Item	Dimension	Comment
Length of the TPC	420 cm	Two halves, 210 cm long
Outer Diameter of the Drift Volume	400 cm	200 cm radius
Inner Diameter of the Drift Volume	100 cm	50 cm radius
Distance: Cathode to Ground Plane	209.3 cm	Each side
Cathode	400 cm diameter	At the center of the TPC
Cathode Potential	28 kV	Typical
Drift Gas	P10	10% methane, 90% argon
Pressure	Atmospheric + 2 mbar	Regulated at 2 mbar
Drift Velocity	5.45 cm/ μ s	Typical
Transverse Diffusion (σ)	230 μ m/ \sqrt{cm}	140 V/cm & 0.5 T
Longitudinal Diffusion (σ)	360 μ m/ \sqrt{cm}	140 V/cm
Number of Anode sectors	24	12 per end
Signal to Noise Ratio	20:1	
Electronics Shaping Time	180 ns	FWHM
Signal Dynamic Range	10 bits	
Sampling Rate	9.4 MHz	
Sampling Depth	512 time buckets	380 time buckets Typical
Magnetic Field	0, ± 0.25 T, ± 0.5 T	Solenoidal

2.2.3 The Endcap Electromagnetic Calorimeter

The EEMC [13] provides coverage for pseudorapidity values $1 \leq \eta \leq 2$, over the full azimuthal range, supplementing the Barrel EMC (BEMC) described in the subsequent subsection. The EEMC enhances STAR's capability to detect photons and electromagnetically decaying mesons (π^0 , η). It identifies electrons and positrons and can be used to trigger on high-energy e^+/e^- particles. The EEMC includes a shower-maximum detector optimized to discriminate between photons and π^0 or η mesons over 10-40 GeV energy region. It also includes preshower and postshower layers intended for electrons vs. hadron discrimination. The major demand for such forward calorimetry arose from the program of experiments to be carried out with colliding polarized proton beams at RHIC [14–16].

The EEMC is a traditional Pb/plastic scintillator sampling calorimeter. The full annulus is divided into two halves, with one shown in Fig. 2.9. The figure shows the subdivision into half of the total 720 towers. The towers are projective, with edges aligned with the center of the beam interaction region, 2.7 m distant along the z-axis from the EEMC front face. Towers span $\delta\phi = 0.1$ in azimuthal angle, and varying size in pseudorapidity ($\delta\eta = 0.057$ to 0.099). On the right of the Fig. 2.9, cross sectional view at constant ϕ is shown, with depth (z-) profile of the calorimeter and the structural tie-rods used at 30° intervals in ϕ . Indicated in the figure are preshower, postshower and shower-maximum detector layers, and the stainless steel mounting ring that will be inserted into a pole tip recess to partially support the weight of the lower half the EEMC. Table 2.4 lists some details and performance of the EEMC.

2.2.4 The Barrel Electromagnetic Calorimeter (BEMC)

The STAR experiment utilizes the BEMC [17] to trigger on rare, high p_T processes (e.g., jets, leading hadrons, direct hadrons, heavy quarks). The BEMC provides large acceptance for photons, electrons, π^0 and η mesons in systems spanning polarized pp through $Au + Au$ collisions. To accomplish various physics goals including the detection of 60 GeV electromagnetic showers, the calorimeter has a total depth of approximately twenty radiation length ($20X_0$) at $\eta = 0$. The STAR Physics program require the calorimeter to reconstruct the π^0 's and isolated (direct) photons at relatively high $p_T \sim 25$ -30 GeV/c and identify single electrons and pairs in intense backgrounds from heavy vector mesons i.e., W and Z decays. All these measurements require precise electromagnetic shower reconstruction with high spatial resolution. Therefore, shower maximum detectors which is essentially two layers of gas wire pad chambers, within the BEMC lead/scintillator stack provide high spatial resolution measurements of shower distributions in two mutually orthogonal transverse dimensions.

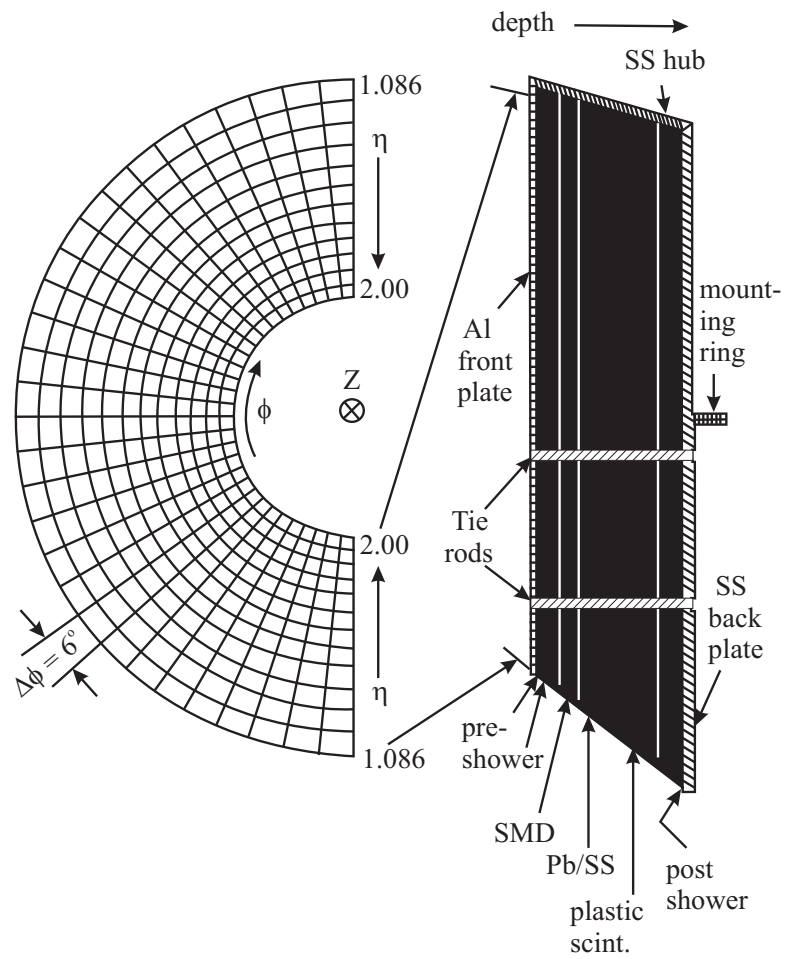


Figure 2.9: Schematic diagram of the EEMC tower structure. See text for details.

Table 2.4: The EEMC coverage and performance/parameters [13].

Features	Requirements	Driving Physics Goals
Geom. Acceptance	$1 \leq \eta \leq 2$; full ϕ	γ +jet sensitivity to $0.01 \leq x_g \leq 0.3$
E_{min} in One Tower	~ 0.2 GeV	MIP's for calibration; γ 's from asymmetric π^0 decay; $\sim 2\%$ shower leakage from $p_T = 10$ GeV/c γ 's.
E_{max} in One Tower	150 GeV	e^\pm from W^\pm decay at $\eta = 2$
Linearity	$< 10\%$ integral non-linearity, $\sim 1 - 150$ GeV	Correct to give W^\pm daughter p_T to ± 1 GeV/c from lower-E calibrations.
Depth	$> 20X_0$, $<$ hadron interaction length	$< 10\%$ shower leakage for 150 GeV e^\pm ; minimize hadron sensitivity to fit within existing space.
Energy Resolution	$(\frac{\sigma E}{E}) < (\frac{16\%}{\sqrt{E}}) + (2\%)$	x_g uncertainty $< \pm 0.01$ for W^\pm reconstruction at $p_T \leq 30$ GeV/c.
$\frac{\gamma}{\pi^0}$ Discrimination	$\frac{\gamma}{\pi^0}$ suppress factor > 3 for $p_T \sim 10-20$ GeV/c \Rightarrow SMD	keep background subtraction from enlarging $\Delta G(x)$ errors by more than a factor of 2.
Timing Response	< 1 RHIC beam period (110 ns)	aid TPC pileup reject; no occupancy from neighbouring beam crossings.
$\frac{e^\pm}{h^\pm}$ Discrimination	suppress h^\pm/e^\pm by > 10 for $p_T > 5$ GeV/c \Rightarrow pre/post-shower	reach $> 3:1$ W signal/hadronic bkgrd. ratio for $p_T > 20$ GeV/c; enhance Drell-Yan signal/bkgrd.

The design for the BEMC includes a total of 120 calorimeter modules, each subtending 6° in $\delta\phi$ (~ 0.1 radian) and 1 unit in $\delta\eta$. Sixty modules are mounted in ϕ and two in η . Each module is roughly 26 cm wide and 293 cm long with an active depth of 23.5 cm plus about 6.6 cm is structural plates (of which ~ 1.9 cm lies in front of the detector). The modules are segmented into 40 towers, 2 in ϕ and 20 in η , with each tower subtending 0.05 radians in $\delta\phi$ and 0.05 in $\delta\eta$. The full Barrel Calorimeter is thus physically segmented into a total of 4800 towers, each of which is projective, pointing back to the center of the interaction diamond. The calorimeter is a sampling calorimeter, and the core of each module consists of a lead-scintillator stack and shower maximum detectors situated approximately 5 radiation lengths from the front of the stack.

A shower maximum detector (SMD) is used to provide fine spatial resolution in a calorimeter which has segmented (towers) significantly larger than an electromagnetic size. Each of 4800 towers of the BEMC span $\delta\eta \times \delta\phi = 0.05 \times 0.05$ which at the radius of the inner face of the detector correspond to the tower sizes $\sim 10 \times 10 \text{ cm}^2$ at $\eta = 0$ increasing towards $\eta = 1$. While the BEMC towers provide precise energy measurements for isolated electromagnetic showers, the high spatial resolution provided by the SMD is essential for π^0 reconstruction, direct γ identification and electron identification. Table 2.5 describes the SMD design parameters.

Table 2.5: The SMD design parameters [17].

Chamber depth inside EMC	$\sim 5X_0$ at $\eta = 0$
Rapidity Coverage (Single Module)	$\delta\eta = 1.0$
Azimuthal coverage (Single Module)	$\delta\phi = 0.105$ Radians (6 degrees)
Occupancy (p+p)	$\sim 1\%$
Occupancy (Au+Au)	> 5 to $\sim 25\%$ (depends on threshold cut)
Chamber Depth (Cathode to Cathode)	20.6 mm
Anode Wire Diameter	50 μm
Gas Mixture	90% - Ar/10%-CO ₂
Gas Amplification	~ 3000
Signal Length	110 ns
Strip Width (Pitch) in η for $ \eta < 0.5$	1.46 (1.54) cm
Strip Width (Pitch) in η for $ \eta > 0.5$	1.88 (1.96) cm
Strip Width (Pitch) in ϕ	1.33 (1.49) cm
Number of Strips per Modules	300
Total Number of Modules	120
Total Number of Readout Channels	36000

2.2.5 The Forward Time Projection Chamber (FTPC)

The Forward Time Projection Chambers were installed to enhance the acceptance of the STAR experiment [6]. They cover the pseudorapidity range $2.5 < |\eta| < 4.0$ on both sides of the STAR experiment and measure momenta and production rates of positively and negatively charged particles as well as neutral strange particles. The FTPC can be

used to study physics like, event-by-event observables for instance $\langle p_T \rangle$ fluctuations, fluctuations of charged particle multiplicity and collective flow. The FTPC not only enables the study of asymmetric systems like p+A collisions but also improves event characterization in STAR.

The FTPC design was determined mainly by two considerations: firstly by the high particle density with tracks under small angles with respect to the beam direction and secondly by the restricted available space inside the TPC [18]. The FTPC has a cylindrical structure, 74 cm in diameter and 120 cm in length. It has radial drift field and readout chambers are located in 5 rings on the outer cylinder surface. The radial drift configuration was chosen to improve the two-track separation in the region close to the beam pipe where the particle density is highest. The present design of the FTPC has some unusual and new features of the TPC:

- The electrons drift in a radial electrical field perpendicular to the solenoidal magnetic field.
- Curved readout chambers are used to keep the radial field as ideal as possible.
- A two-track separation of 1-2 mm is expected, which is an order of magnitude better than in all previously built TPCs with pad readout.

Due to short drift length of only 23 cm, a cool gas mixture with CO_2 is used in the FTPC. It has low diffusion coefficient for electrons and a small Lorentz angle [19]. Ar and CO_2 in a ratio of 50::50 was meticulously selected as it is non-flammable and shows no or little ageing effect in comparison to hydrocarbons. The design of the front end electronics closely follows that of the TPC [20]. Table 2.6 lists the basic design parameters of the FTPC.

2.2.6 The Silicon Vertex Tracker (SVT)

The Silicon Vertex Tracker [21] was added to the STAR experiment to enhance physics capabilities of the main STAR sub detector, the STAR Time Projection Chamber (TPC). Besides improving the primary vertexing, the two track separation resolution and the energy-loss measurement for particle identification, the SVT also enables the reconstruction of very short-lived particles (primary strange and multi-strange baryons and potentially D-mesons). It also expands the kinematical acceptance for primary particles to very low momentum by using independent tracking in the SVT alone for charged particles that do not reach the active volume of the TPC due to the applied magnetic field.

The SVT is based on silicon drift technology in order to handle the expected high charge multiplicities and to minimize the number of readout channels [22, 23]. The detector consists of two half-detectors separated by the dividing central cathode that receives

Table 2.6: The FTPC design parameters [6].

Configuration	
Number of TPC	2
Rows per TPC	10
Sectors per pad row	6
pads per sector	2×160
Sensitive Volume	
Inner radius	8.0 cm
Outer radius	30.5 cm
Chamber length	120.0 cm ($150 < z < 270$ cm)
Acceptance	$2.5 < \eta < 4.0$ ($2.0^0 < \theta < 9.3^0$)
Field Cage	
Drift Cathode voltage	10-15 kV
Drift Electrical Field	240-1400 V/cm (radial)
Solenoid Magnetic Field	0.5 T
Gas	
Gas Mixture	Ar(50%)-CO ₂ (50%)
Drift Velocity	0.3 - 2.0 cm/ μ s
Trans. diffusion (D_T)	100-130 μ m/ \sqrt{cm}
Long. diffusion (D_L)	100-130 μ m/ \sqrt{cm}
Lorentz Angle	4 deg. (at 0.5 T)
Gas gain	$\sim 1-2 \times 10^3$
Readout	
Number of Pads	19200
Time bins per pad	256
Pad pitch	1.9 mm
pad length	20 mm
Anode wire-pad gap	1.5 mm
ADC dynamic range	10 bits

the maximum voltage bias. Electrons in the half-detectors drift in opposite directions from one another. The main justification for the half-detector design is the need to limit the maximum drift voltage by limiting the maximum drift distance.

2.2.7 The Silicon Strip Detector (SSD)

The Silicon Strip Detector (SSD) [24, 25] constitutes the fourth layer of the inner tracking system. Installed between the Silicon Vertex Tracker (SVT) and the Time Projection Chamber (TPC), the SSD enhances the tracking capabilities of the STAR experiment by measuring accurately the two dimensional hit position and energy loss of the charged particles.

The SSD is placed at a distance of 230 mm from the beam axis, covering a pseudorapidity range of $|\eta| < 1.2$ which leads to a total silicon surface close to 1 m^2 . The design of SSD is based on two clamshells, each containing 10 carbon fiber ladders. Each ladder supports 16 wafers using double-sided silicon strip technology (768 strips per side) and connected to the front-end electronics (6 ALICE 128 C chips per side) by means of the Tape Automated Bonded (TAB) technology [26]. The ladders are tilted with respect to their long axis, allowing the overlap of the detectors in the transverse plane for better hermiticity and alignment performance. A bus cables transports the analog signals along the ladder to two 10 bits ADC boards installed at both ends. After digitization, the signals are sent to Readout Boards which are linked to the DAQ system through Gigalink optical fibers. The cooling system is based on an air-flow through the ladder which is embedded in a mylar sheet. The total radiation length has been estimated to be around 1%. Performance and summary of the SSD is listed in Table 2.7.

2.2.8 The STAR Trigger

The STAR Trigger [27] is a pipelined system in which digitized signals from the fast trigger detectors are examined at the RHIC crossing rate ($\sim \text{MHz}$). This information is used to determine whether to begin the amplification-digitization-acquisition (ADA) cycle for slower, more finely grained detector or not. Data flow through the trigger (TRG) is shown in Fig. 2.10. The trigger detectors consist of the following detectors :

- The Central Trigger Barrel (CTB).
- Two Zero Degree Calorimeters (ZDC East and ZDC West).
- The Barrel Electromagnetic Calorimeter.
- The Multi-Wire Counter.
- The Beam Beam Counter.

- The Forward Pion Detector.
- The Endcap Electromagnet Calorimeter (EEMC).

Each detector channel is digitized for every RHIC crossing and fed into a Data Storage and Manipulation (DSM) board where it is analyzed and combined with the other signals in a multi-layer pipeline that forms a fast decision tree. Output from the DSM tree is then fed to the Trigger Control Unit (TCU) where it is combined with detectors status bits to act as an 18 bit address to a lookup table (LUT) which holds the trigger word that goes with each bit combination. The trigger word then acts as an address into the Action Word LUT which holds the information on which detectors are to be involved and what action is to be taken for this trigger. This DSM-based decision tree constitutes Level 0 of the trigger and is constrained to issue a decision within $1.5 \mu\text{s}$ from the time of the interaction. When an interaction is selected at Level 0, each STAR detector designated to participate in this type of event is notified using a 4-bit Trigger Command and told to identify this event with a 12-bit token [28].

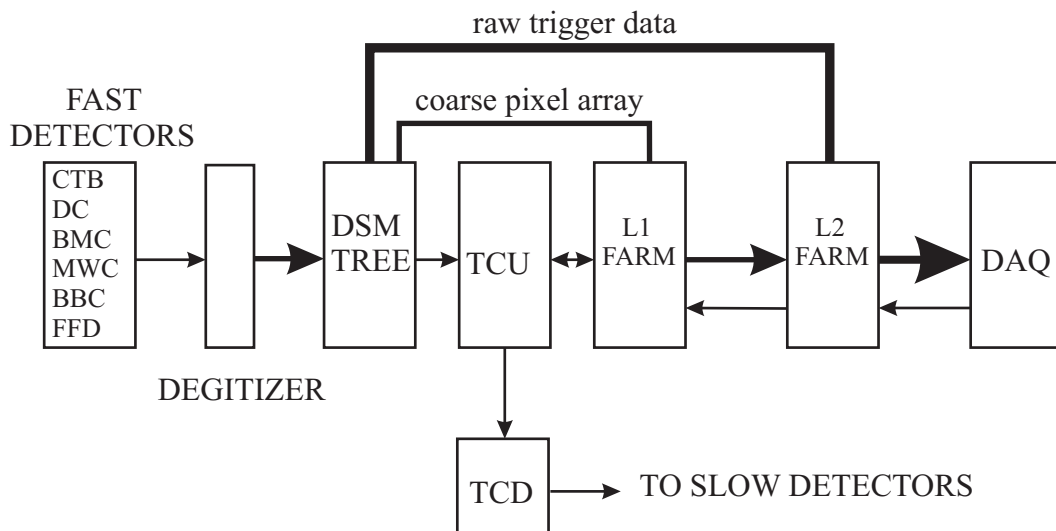


Figure 2.10: Data flow through the trigger.

2.2.9 The Central Trigger Barrel (CTB)

The CTB consists of 240 scintillator slats arranged in 4 cylindrical bands each covering $1/2$ unit of pseudorapidity. The CTB slats cover the outer shell of the 4m diameter TPC. Details of the CTB are mentioned in Table 2.8. Each slat consists of a radiator, light guide and mesh dynode photomultiplier tube. The PMTs are attached to the radiators using ultraviolet-transmitting acrylic plastic light guides. Each PMT is powered by a channel of LeCroy 1440 high voltage and has an independent light-emitting diode (LED) attached to the far end of the slat for calibration purposes.

2.2.10 The Zero Degree Calorimeter (ZDC)

All the four experiments at RHIC use a pair of Zero Degree Calorimeter as a common tool for monitoring interactions at each interaction point. They are placed at nearly identical positions along the beam lines on either side of the interaction regions. Each ZDC consists of three modules, where each module consists of a series of tungsten plates alternating with layers of wavelength shifting fibres that route cherenkov light to a PMT. The ZDCs are used for monitoring, triggering and locating interaction vertices. More details of the ZDC are listed in Table 2.9.

2.2.11 The Multi Wire Counter (MWC)

The MWC is not a separate detector, but simply uses the TPC anode wires as a fast detector. More details of the MWC are listed in Table 2.10. The primary function of the TPC anode wires is to provide (avalanche) gas gain for the clouds of electrons that drift through the gas volume and are admitted through the gating grid. The images of these avalanches form the pad signals used for tracking in the TPC.

The STAR MWC Front-End Electronics (FEE) uses a variant of the STAR shaper Amplifier (SAS) with resistive feedback to provide an always-alive preamplifier (not gated) [29].

Table 2.7: The design parameters and performance of the SSD [25].

General Layout	
Radius	230 mm
Ladder length	1060 mm
Acceptance	$ \eta < 1.2$
Number of ladders	20
Number of wafers per ladder	16
Total number of wafers	320
Silicon wafer characteristics	
Number of slides per wafer	2
Number of strips per side	768
Total readout channels	491520
Silicon wafer sensitive area	73×40 mm
Total silicon surface	0.98 m^2
Wafer pitch	$95 \text{ }\mu\text{m}$
$r\phi$ resolution	$20 \text{ }\mu\text{m}$
z resolution	$740 \text{ }\mu\text{m}$
Operating voltage	20 - 50 V
Leakage current for one wafer	1 - 2 μA
Readout Front-End Electronics	
Number of input channels per circuit	128
Total number of circuits	3840
Dynamical Range	± 13 MIPS
Shaping time	1.2 - 2 μs
Signal/Noise	30-50
SSD total readout time	<5 ms
Expected Performance	
Dead channels level	$\sim 2\%$
Hit reconstruction efficiency	$\sim 95\%$
Hit reconstruction purity	$\sim 98\%$

Table 2.8: The design parameters of the CTB.

Paramter	Description
Purpose	Measures charged particle multiplicity in $-1 < \eta < 1$
Coverage by single slat	$\pi/30$ in ϕ ; 0.5 in η
Average occupancy	10/slat for central Au+Au interactions
Multiplicity (M) measurement accuracy	$< 3\%$ at $M > 1000$; single hits at low M
Channel (slats)	240
Radiator	BC408 : 1 cm \times 21 cm \times 112.5 or 130 cm^5
Light detectors	Hamamatsu R5946 PMTs

Table 2.9: The design parameters of the ZDC.

Paramter	Description
Purpose	Verify centrality in A+A collisions, provide hadronic minimum bias signal and interaction signal for RHIC operation
Average occupancy	~ 25 neutrons for central Au+Au collisions
Channels (modules)	6
ADC (PMT amplitude)	8 bits, 2.4 pC per count
Radiator	PMMA fibres with W plates
Light detector	Hamamatsu 2490-05 PMT

Table 2.10: The design parameters of the MWC [29].

Paramter	Description
Purpose	Measures charged particle multiplicity in $-2 < \eta < 1$ and $-1 < \eta < -2$.
Cell coverage	Variable in η and ϕ
Average occupancy	0.1 - 0.2 per cell in central Au+Au
Multiplicity (M) measurement accuarcy	$< 3\%$ at $M > 1000$; single hits at low M
Channels	96 from 24 sectors each having 4 subsectors of 8 wires. The 7200 wires are fed in groups of 20 to front end boards, summed to 5 bits each and then sent to receiver boards where they are grouped by sub sectors forming 96 sums sent to Level 0.

Bibliography

- [1] M. Harrison, T. Ludlam & S. Ozaki, Nucl. Instr. & Meth. Phys. Res. A **499** (2003) 235.
- [2] M. Riordan and W.A. Zajc, Scientific American **34** (2006) 294.
- [3] <http://www.cerncourier.com/main/article/42/3/2>.
- [4] <http://www.star.bnl.gov>.
- [5] H. Wieman *et al.*, IEEE Trans. Nuc. Sci. **44** (1997) 671.
- [6] K.H. Ackermann *et al.*, Nucl. Instr. & Meth. Phys. Res. A **499** (2003) 713.
- [7] J. Thomas *et al.*, Nucl. Instr. & Meth. Phys. Res. A **478** (2002) 166.
- [8] M. Anderson *et al.*, Nucl. Instr. & Meth. Phys. Res. A **499** (2003) 659.
- [9] M. Anderson *et al.*, Nucl. Instr. & Meth. Phys. Res. A **499** (2003) 679.
- [10] F. Bergsma *et al.*, Nucl. Instr. & Meth. Phys. Res. A **499** (2003) 633.
- [11] R.L. Brown *et al.*, Proc. of the IEEE 1997 Particle Accelerator Conference (1998) 3230.
- [12] L. Kotchenda *et al.*, Nucl. Instr. & Meth. Phys. Res. A **499** (2003) 703.
- [13] C.E. Allgower *et al.*, Nucl. Instr. & Meth. Phys. Res. A **499** (2003) 740.
- [14] G. Bunce, N. Saito, J. Soffer and W. Vogelsang, Annu. Rev. Nucl. Part. Sci. **50**, (2000) 525.
- [15] L.C. Bland, (2000), [arXiv:hep-ex/0002061].
- [16] L.C. Bland *et al.*, STAR Note 401 (1999).
- [17] M. Beddo *et al.*, Nucl. Instr. & Meth. Phys. Res. A **499** (2002) 725.
- [18] H. Wieman *et al.*, IEEE Trans. Nuc. Sci. **44** (1997) 671.

- [19] X. Bittl *et al.*, Nucl. Instr. & Meth. Phys. Res. A **398** (1997) 249.
- [20] S. Klein *et al.*, Front-End Electronics for the STAR TPC, IEEE Trans. Nucl. Sci. **43** (1996) 1768.
- [21] R. Bellweid *et al.*, Nucl. Instr. & Meth. Phys. Res. A **499** (2003) 640.
- [22] E. Gatti and P. Rehak, Nucl. Instr. & Meth. Phys. Res. A **225** (1984) 608.
- [23] W. Chen *et al.*, IEEE Trans. Nucl. Sci. **41** (1994) 941.
- [24] STAR, "Proposal for a silicon strip detector for STAR", STAR note SN-0400.
- [25] L. Arnold *et al.*, Nucl. Instr. & Meth. Phys. Res. A **499** (2003) 652.
- [26] S. Bouvier, Proceedings of the 4th workshop on electronics for LHC experiments, Rome, Sept. 1998.
- [27] F.S. Beiser *et al.*, Nucl. Instr. & Meth. Phys. Res. A **499** (2003) 766.
- [28] H.J. Crawford and V. Lindenstruth, US patent 5, 918, 055 (1999).
- [29] E. Beuville *et al.*, IEEE Trans. Nucl. Sci. **43** (1996) 1619.

Chapter 3

The Photon Multiplicity Detector (PMD)

The Photon Multiplicity Detector (PMD) in the STAR experiment is capable of studying photon multiplicity and collective flow in nucleus-nucleus collisions at RHIC energies in the forward region where high particle density precludes the use of a calorimeter [1–4]. The PMD enhances the phase space coverage of the STAR experiment by covering a pseudorapidity region of $-2.3 \leq \eta \leq -3.8$ with full azimuthal acceptance. This region has been selected to minimize the effect of upstream materials and to maximize the overlap with the coverage of the FTPC [5]. The detector is mounted on the east side of the Wide Angle Hall (WAH), as shown in Fig. 3.1. Basic parameters of the STAR-PMD (Charged Particle Veto (CPV) and pre-shower plane) are listed in Table 3.1. Z-distance of the PMD is 542 cm from the center of the TPC (the nominal collision point). Design and working of the PMD will be presented in detail in this chapter.

Table 3.1: Basic parameters of the STAR-PMD [1].

Parameter	Value
Distance from Vertex	542 cm
η -coverage	-2.3 - -3.8
Configuration	veto and pre-shower
Area of the detector	4.2 m^2
Cell size (area)	1 cm^2
Total numbers of channels	82,944
Weight of the detector	900 Kg

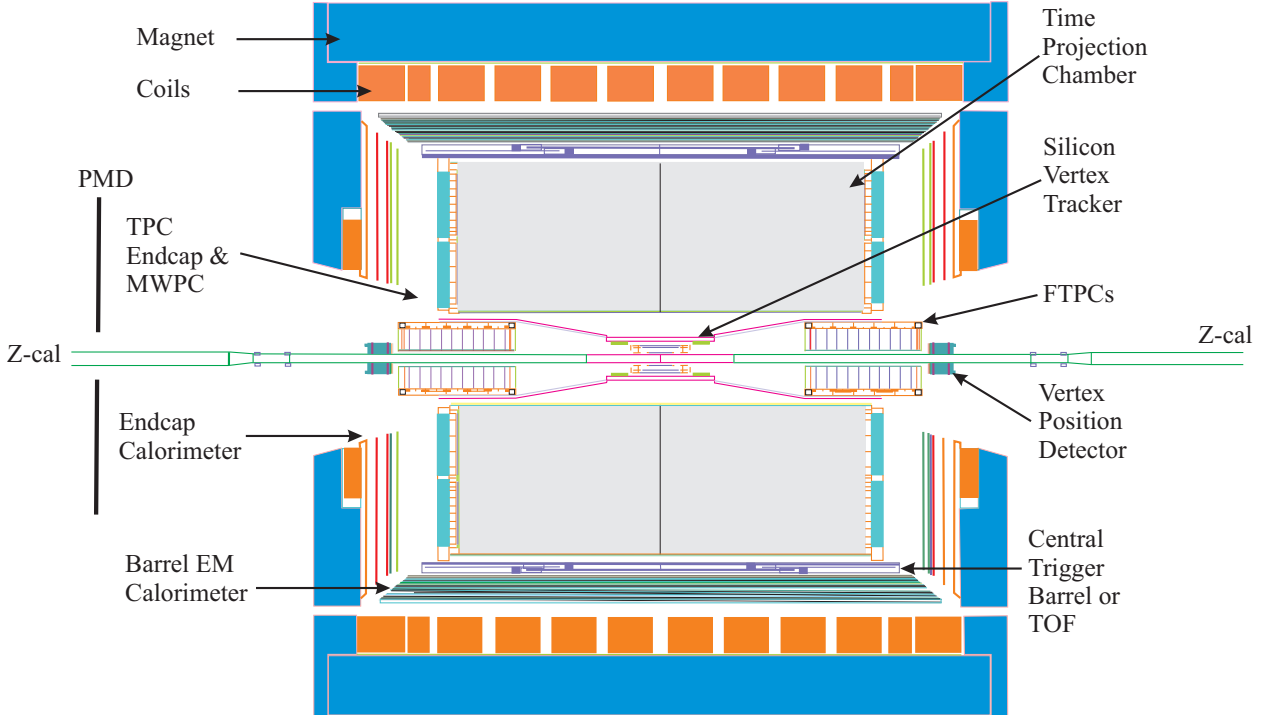


Figure 3.1: Cross-sectional view of the STAR experiment. The PMD is shown with thick black lines on the East side.

3.1 History and Future of the PMD

A pre-shower PMD having an array of plastic scintillator pads behind a 3 radiation length ($3X_0$) thick Pb converter plate was used in WA93 and WA98 experiments at the CERN SPS to study sulphur and lead induced reactions [6, 7]. After successful completion of data taking by the PMD in WA93 and WA98 experiments, the PMD was installed in the STAR experiment at RHIC, BNL in 2003. The PMD is being installed in the ALICE experiment [8] at the LHC (Large Hadron Collider), CERN (European Organization for Nuclear Research) and is expected to start taking data in 2008.

3.2 Physics Goals of the PMD

The preshower Photon Multiplicity Detector (PMD) allows event-by-event measurement of photon and their spatial distribution. In combination with information from other detectors, the PMD is capable of addressing the following broad topics of physics:

- Signals of chiral symmetry restoration (e.g. Disoriented Chiral Condensates (DCC) [9–15]) through the measurement of charged-particle multiplicity (N_{ch}) in a common part of phase space and study of the observables N_γ and N_γ/N_{ch} with full azimuthal coverage. The primary signature of DCC is a large event-by-event fluctuation in photon to charged-particle multiplicity. This requires careful measurement

of photons and charged particles in common coverage. The challenge is to design sophisticated analysis tools on an event-by-event basis to identify DCC amidst the large background due to conventionally produced particles [16–19]. Such studies have already been performed by using a pre-shower PMD and a set of charged particle multiplicity detectors in WA98 experiment at the SPS [20].

- Determination of reaction plane and the probes of thermalization via studies of azimuthal anisotropy and flow.
- Critical phenomena near the phase boundary leading to fluctuations in global observables like multiplicity and pseudorapidity distributions. Density fluctuations such as droplet formation and hot spots can be studied by the power spectrum method [21–23].

3.3 Principle of a Pre-shower Detector

The PMD consists of a highly segmented detector placed behind a lead converter plate of 3 radiation lengths ($3X_0$). A veto detector in front of the converter is used to reject the charged particles. A photon while traversing through the lead plate produces an electromagnetic shower as shown in Fig. 3.2. These shower particles produce signals in several cells of the sensitive volume of the detector. Charged hadrons usually affect only one cell and produce a signal resembling those of Minimum Ionizing Particles (MIPs).

Thickness of the lead plate is meticulously chosen to be $3X_0$ as it serves dual purpose:

- The conversion probability of photons is high.
- Transverse shower spread is small which minimize shower overlap in a high multiplicity environment.

The detector consists of a large number of honeycomb chambers, also known as cells, where each cell acts as an independent proportional counter. They are filled with Ar and CO_2 gas in 70:30 ratio as this gas mixture is insensitive to neutrons. In order to cope up with the high particle density environment in the forward region, the detector technology has been chosen keeping the following considerations in mind:

- Multihit probability should be less.
- MIPs should be contained in one cell.
- Low energy delta electrons should be prevented from traveling to nearby cells such that the cross-talk among the adjacent cells can be prevented.

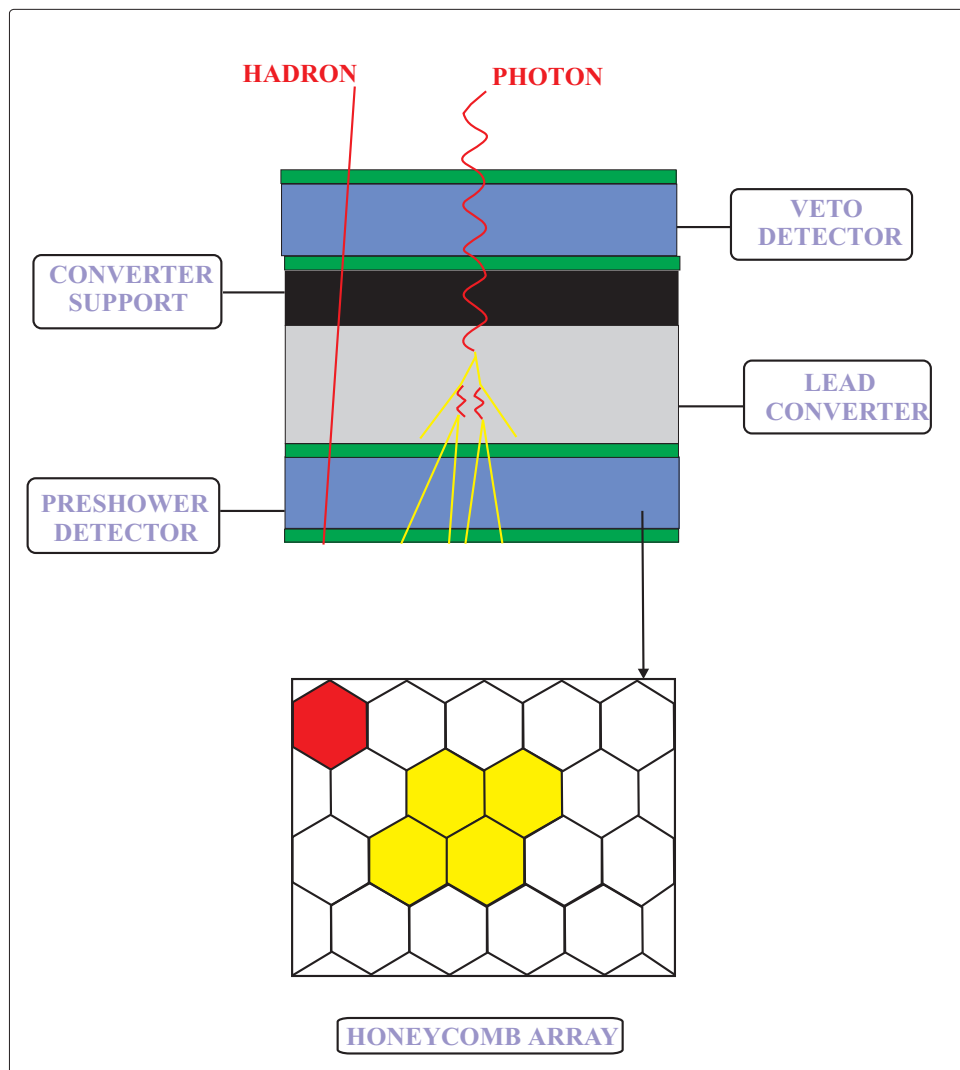


Figure 3.2: Principle of a preshower detector. Single cell hit is due to a MIP, whereas signal deposited in continuous cells is due to a photon.

- The detector technology should be amenable to modular design with minimum dead space at the boundaries.
- The detector should be placed in contact with the converter without large airgaps. Also the active volume of the detector should be thin and very close to the converter so that the transverse spread of the shower is minimized.
- The detector material (gas mixture) should be insensitive to neutrons. In a homogeneous medium, neutrons tend to produce large signals due to recoil protons, which can mimic a photon signal.

Fig. 3.3 is the schematic diagram, showing the veto plane, lead converter and the preshower plane. Stainless Steel (SS) is the support plate on which lead plates and the chambers are mounted.

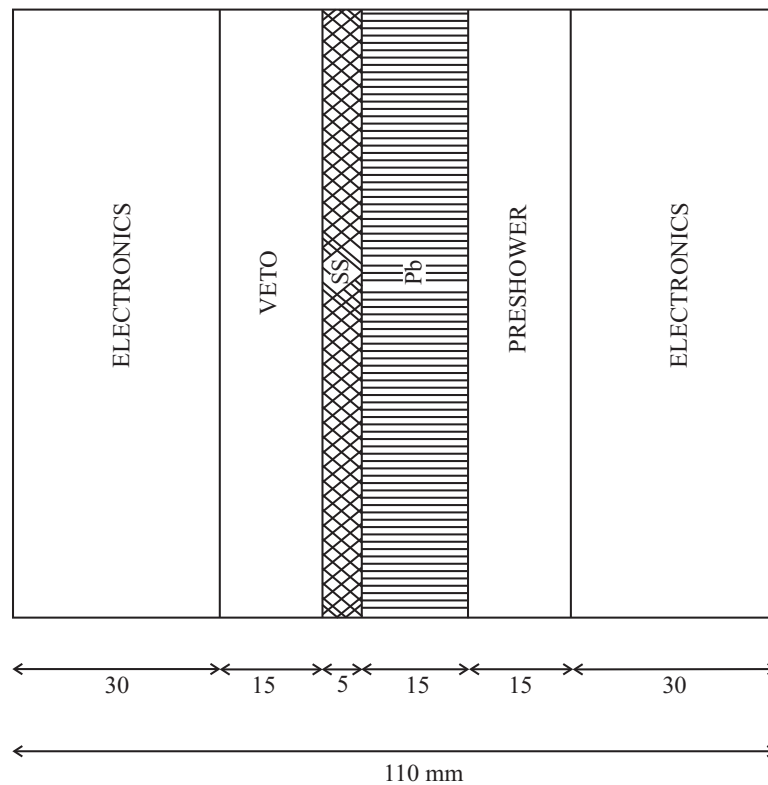


Figure 3.3: Cross-sectional view of the PMD.

3.4 Design of the PMD

The honeycomb structure with wire readout was selected for the STAR-PMD because of its closeness to a circular approximation which provides close packing of large arrays. Fig. 3.4 and Fig. 3.5 schematically show the wire readout and cross-sectional view of the

extended cathode cell, respectively. Each honeycomb cell is physically isolated from each other by thin metallic walls in order to contain δ -rays.

The honeycomb body forms a common cathode and is kept at a large negative voltage. It supports printed circuit boards (PCBs). The individual anode wires in each cells are grounded through the input channels of the readout electronics. The choice of the material and thickness of the honeycomb cells are dictated by the following:

- The material should help to reduce the transverse size of the preshower by containing low energy electrons moving at large angles.
- The thickness should be kept low to avoid large amount of materials.

Honeycomb chambers are made of copper as it is non-magnetic in nature and can be easily shaped. It is also very good for soldering the joints. In Au+Au collisions, the average energy of photons with PMD acceptance is ~ 2 GeV. 0.4 mm wall thickness was chosen for cell fabrication.

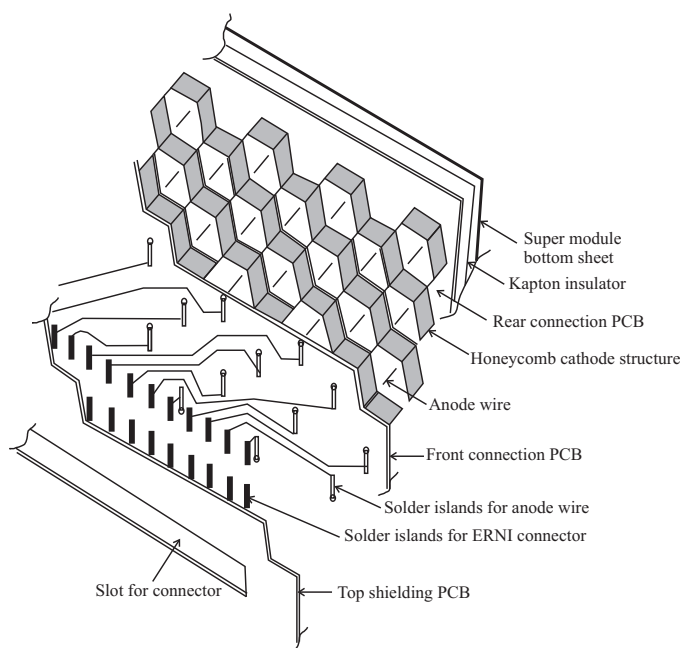


Figure 3.4: Schematic design of the honeycomb chamber and wire readout.

3.5 Characteristics of Charged Particle Detection

The operating voltage of -1400 V and gas mixture of Ar and CO_2 in the ratio of 70:30 were optimized after a detailed study of the variation of the charged particle detection efficiency as a function of voltage and gas mixture. A typical ADC spectrum of an isolated cell in Cu+Cu collision for Charge Particle Veto (CPV) plane is shown in Fig. 3.6. The

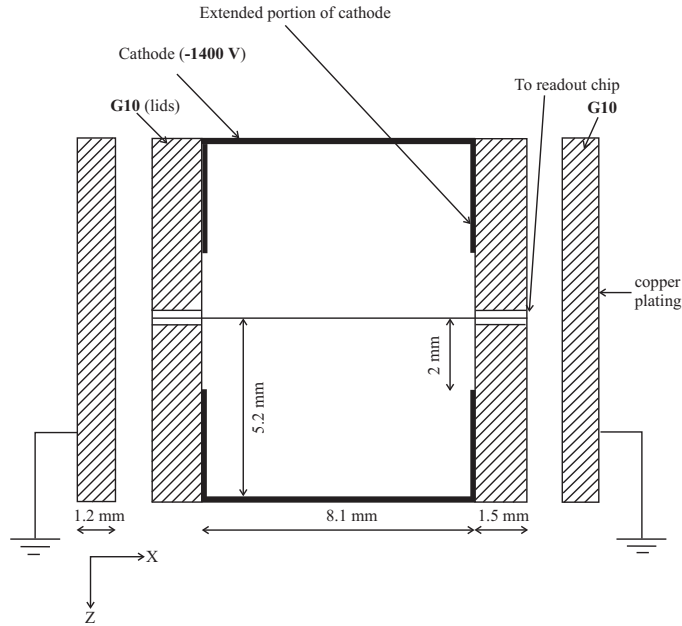


Figure 3.5: Cross-sectional view of an extended cathode cell.

mean value of the fitted distribution is taken as a measure of average energy deposition by a charged particle. We see that Landau tail of this isolated cell distribution extends at the most upto 500 ADC, as a result we truncate isolated cell distribution to 500 ADC in the pre-shower plane to calculate mean ADC value deposited by charged particle in that cell.

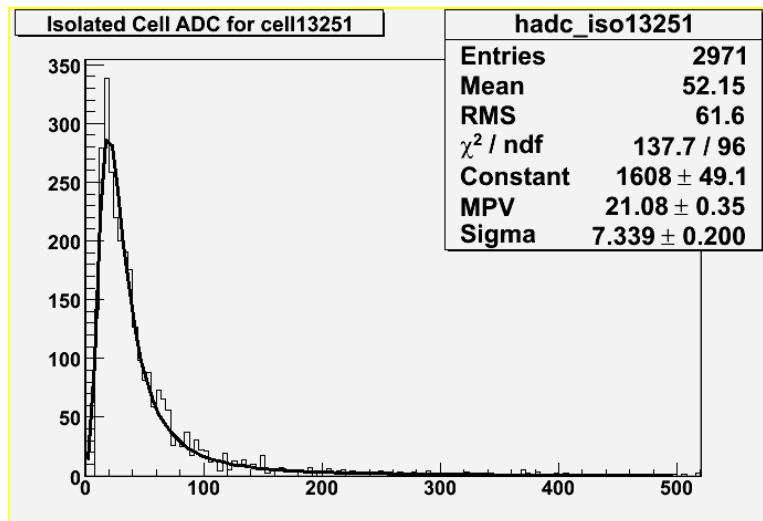


Figure 3.6: ADC distribution of an isolated cell in the CPV plane.

3.6 Description of the PMD

3.6.1 Mechanical Design and Construction

The PMD consists of the following mechanical parts :

- Modular honeycomb chambers (identical for pre-shower and the charged particle veto).
- Lead converter plates.
- Support assembly: The two halves of the STAR-PMD can be independently assembled and installed. They have independent movements of opening on either sides of the beam pipe.

3.6.2 Fabrication of Honeycomb Array

The honeycomb is fabricated using 0.2 mm thick copper sheets. These cells are arranged in a matrix of 24×24 in a high precision jig and spot-soldered to form a honeycomb. A unit honeycomb module has stiff 1 mm diameter copper studs which are attached by reflow soldering. These studs are situated at eight different locations, four at the corners of the rhombus and four at the centers of each edge as shown in Fig. 3.7. They are used to bring out the high voltage connections of the cathode onto the PCBs. They also act as guides for attaching the PCBs on both sides of the honeycomb array, which ensure proper alignment. Small notches are provided at the corners of each cells so that gas flows from one cell to another smoothly.

The copper honeycomb obtained from the manufacturer is first washed in a soap solution and water in ultrasonic cleaners and then dried in warm air. The honeycomb cathode structure is then dip-coated with high conductivity graphite paint. The basic parameters of a unit cell are listed in Table 3.2.

Table 3.2: Basic parameters of a unit cell [1].

Parameter	Value
Shape	Hexagonal
Total number of cells (CPV + Preshower)	82,944
Cell cross-section	1.0 cm^2
Cell depth	0.8 cm

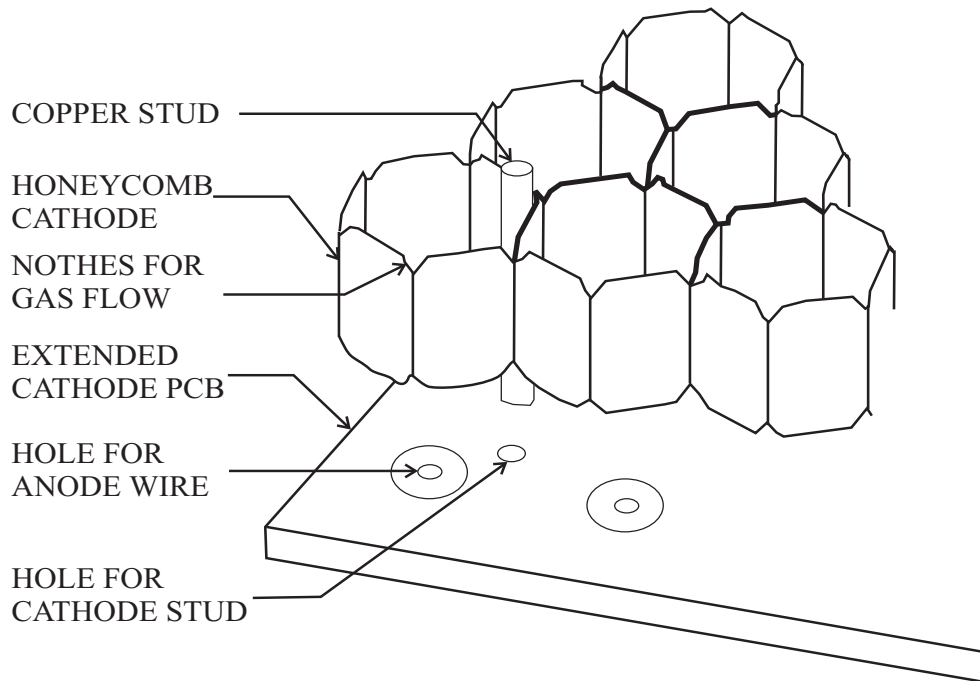


Figure 3.7: A close-up view of a small region of the cells in a unit module showing studs and notches in detail.

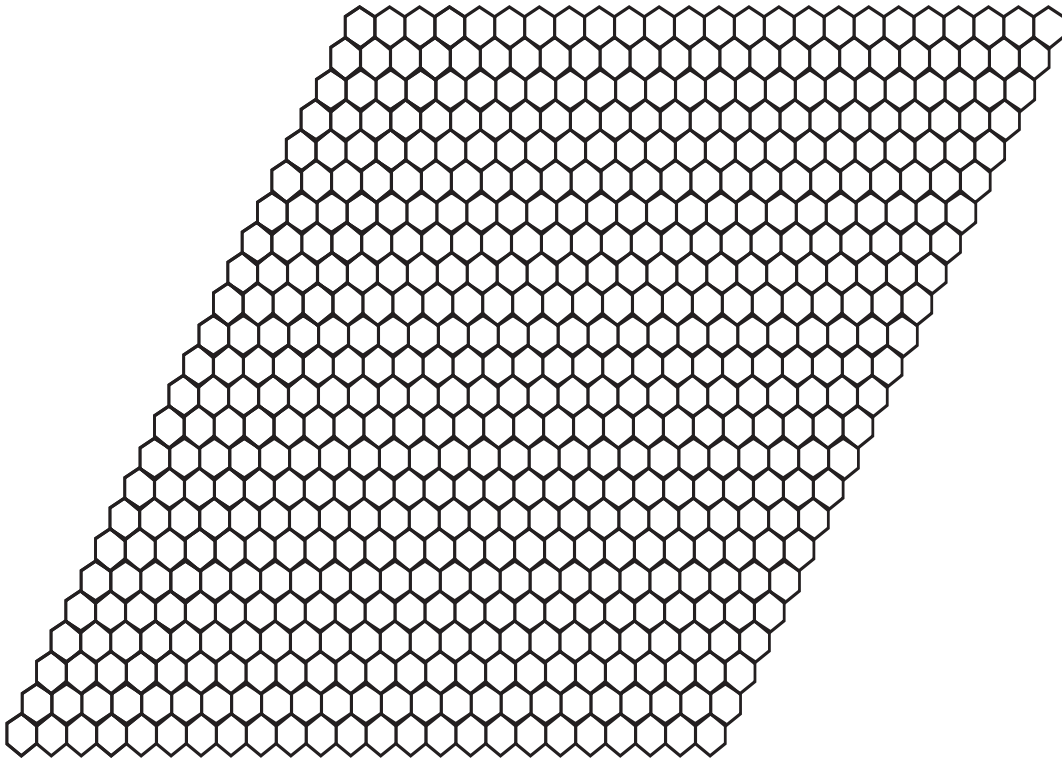


Figure 3.8: Rhombus shaped unit module containing an array of 24×24 hexagonal cells.

3.6.3 Honeycomb Chambers

For convenience, honeycomb chambers are first fabricated in the form of unit modules. A unit module consists of a rhombus of side approx. 260 mm containing a matrix of 24×24 cells as shown in Fig. 3.8. This shape has identical boundaries on all four sides. The wall thickness at the boundaries is half that of the inner walls. When such arrays are joined together to form a supermodule, the half thick boundary walls merge to form a seamless array of hexagonal cells as shown in Fig. 3.9. In order to keep the numbers of these independent proportional counters reasonably small and to reduce the dead area due to the boundaries, nine unit modules arranged in a 3×3 matrix are enclosed within a gas tight enclosure known as a supermodule. This design helps in reducing the splitting of clusters at the boundaries, which affects photon counting efficiency.

3.6.4 Assembly of a Unit Module

Fig. 3.10 shows the various components of a unit module. The major steps involved in the assembly of a unit module is described briefly in the subsequent subsections.

Mounting the PCBs

The top PCB, containing the electronic boards, has solder-islands at the centre of each cell with a 0.4 mm gold-plated through-hole. Signal tracks from 64 cells are brought out to a 70 pin connector as shown in Fig. 3.11. The PCBs on the bottom side have only soldering islands without signal tracks, which serve as anchor points. The two PCBs are attached on both sides of the honeycomb, aligned with copper studs.

Wire Insertion

Gold-plated tungsten wires (20 μm dia.) are first cleaned and wound onto smaller spools. This wire is then stretched through the holes on the PCB, using a simple jig shown in Fig 3.12. The basic aim of this jig is to provide tension (30% of the elastic limit) to the wire before soldering onto the island on the PCB. Other end of the hole, from where the wire emerges, are then closed with a tiny amount of fast-setting epoxy to make them gas tight. This scheme prevents solder flux creeping into the cell and makes soldering easier. At the end of the assembly, all the soldered joints are tested for dry solder using a milli-ohmmeter.

3.6.5 Assembly of a Supermodule

A supermodule consists of a 3×3 array of unit modules bonded in a gas-tight enclosure made up of 3 mm thick FR4 grade glass epoxy sheet with a 6 mm thick and 30 mm

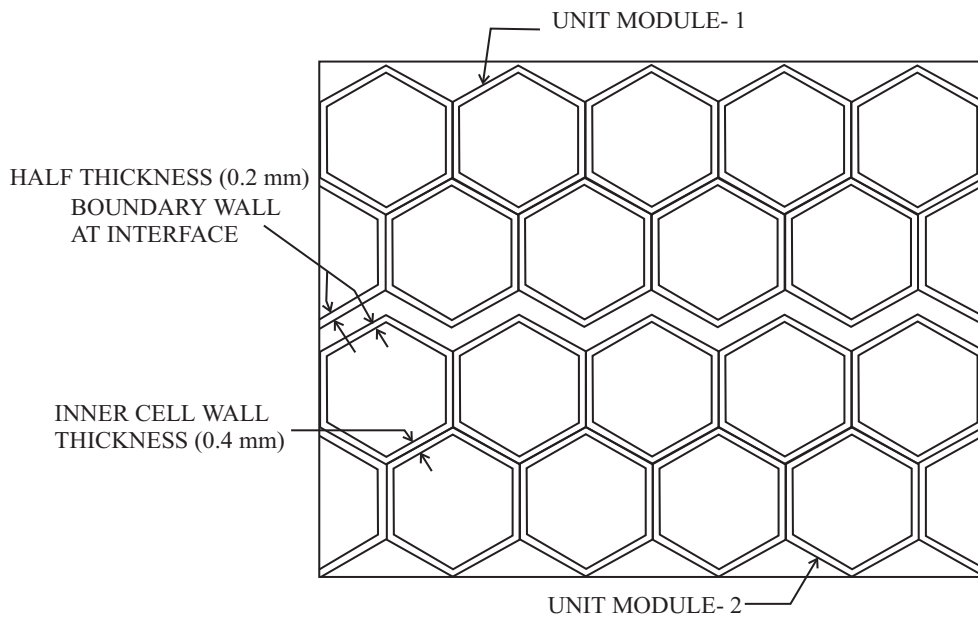


Figure 3.9: Schematic view showing the junction of two unit modules. The cell walls at the boundaries are half as thick as those inside and make a seamless joint with cells from adjoining unit module.

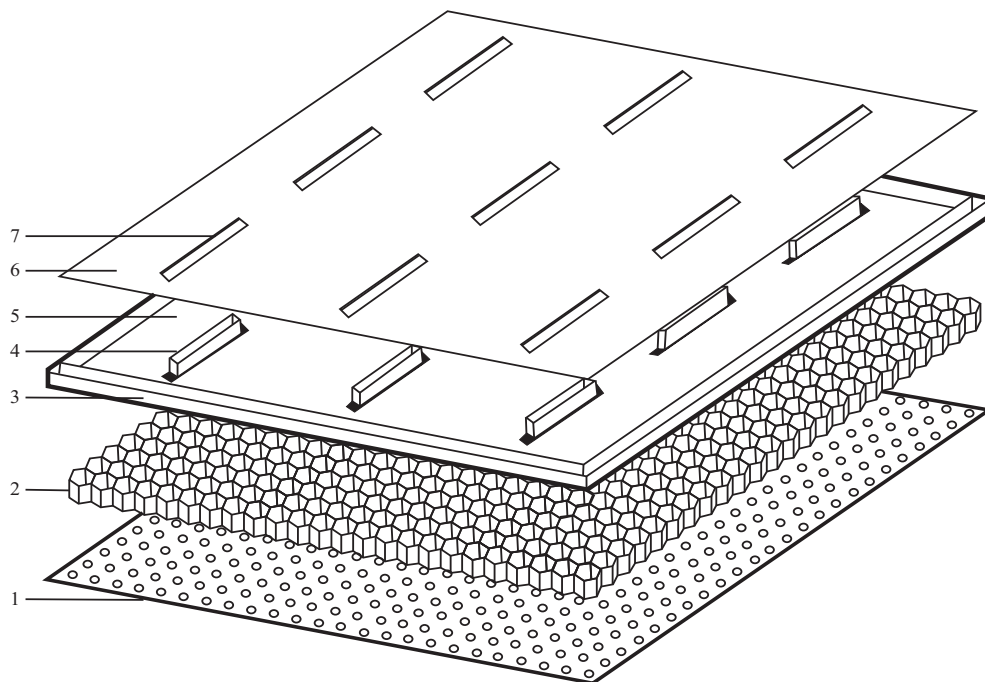


Figure 3.10: Components of the unit module : (1) bottom PCB, (2) honeycomb cathode, (3) moulded frame, (4) SAMTEC connectors, (5) top PCB, (6) shielding PCB, and (7) slot for connector.

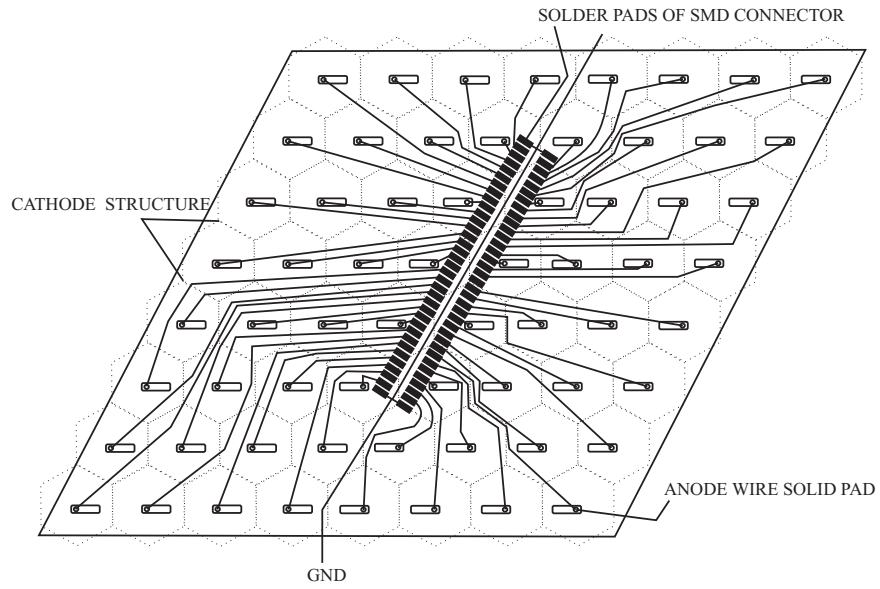


Figure 3.11: Wire scheme for an array of 64 cells to 70 pin connector.

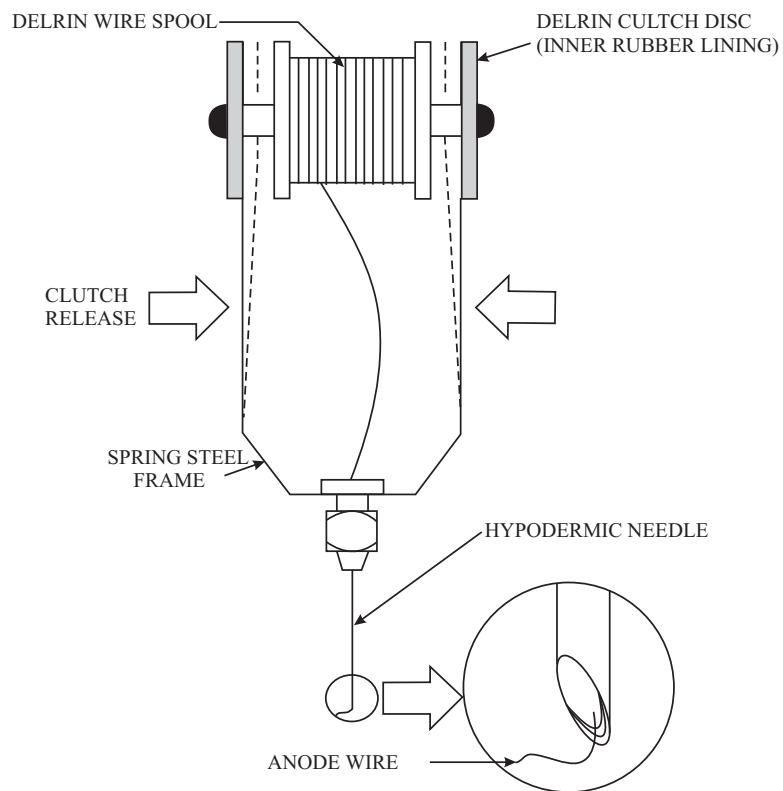


Figure 3.12: Jig used for wire insertion during assembly of the unit module.

high aluminium boundary wall. One cell each at the four corners of the supermodule is retained without anode wire, to allow screws to pass through a glued gas-tight SS tube for fixing the supermodules onto the support plate.

Assembly Procedure

The basic steps in the supermodule assembly are described below :

- A base frame made of 50 mm × 25 mm aluminium channels is fixed to the bottom to retain planarity of the bottom sheet during further operation. A schematic of a section of the supermodule showing different components such as gas inlet, high voltage feeder, support channels and sealing for gas tightness is shown in Fig. 3.13.
- Nine assembled unit modules are placed to fill the inner area of the supermodule enclosure, leaving 1 mm gap on all the sides to accommodate general assembly tolerance and to provide insulation between the honeycomb cathode and the boundary (Fig. 3.14). Several polyimide spacers are inserted into this gap all along the boundary to prevent movement of the unit modules and also to insulate the honeycomb cathode from the walls.

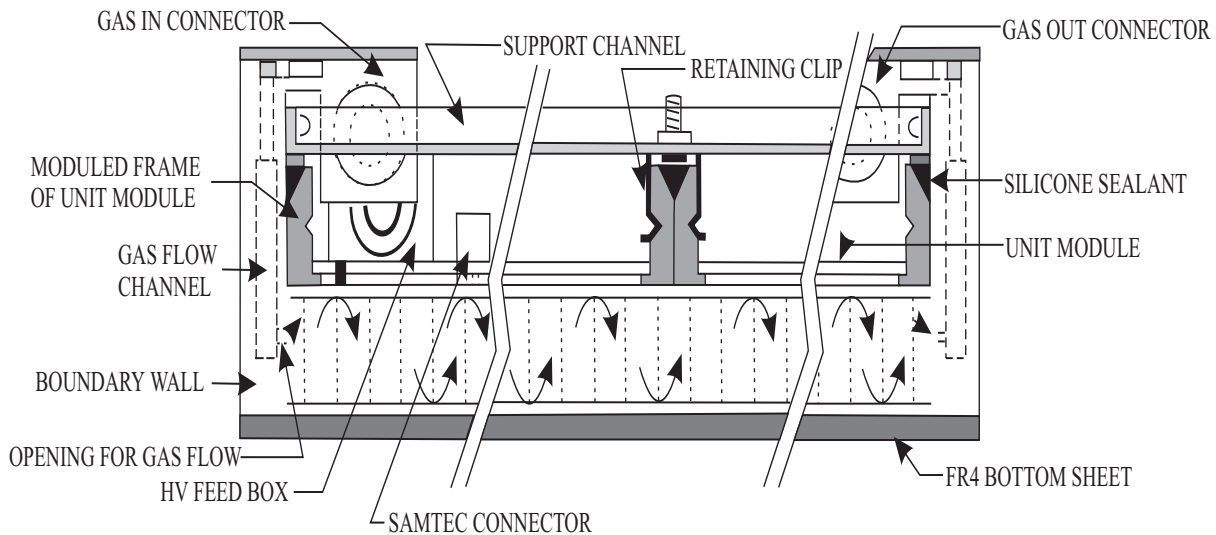


Figure 3.13: Schematic of a section of the supermodule showing different components.

Five different types of supermodules which make the PMD, are listed in table 3.3: Further supermodules are divided into two categories i.e., (a) Mirror type, (b) Normal type.

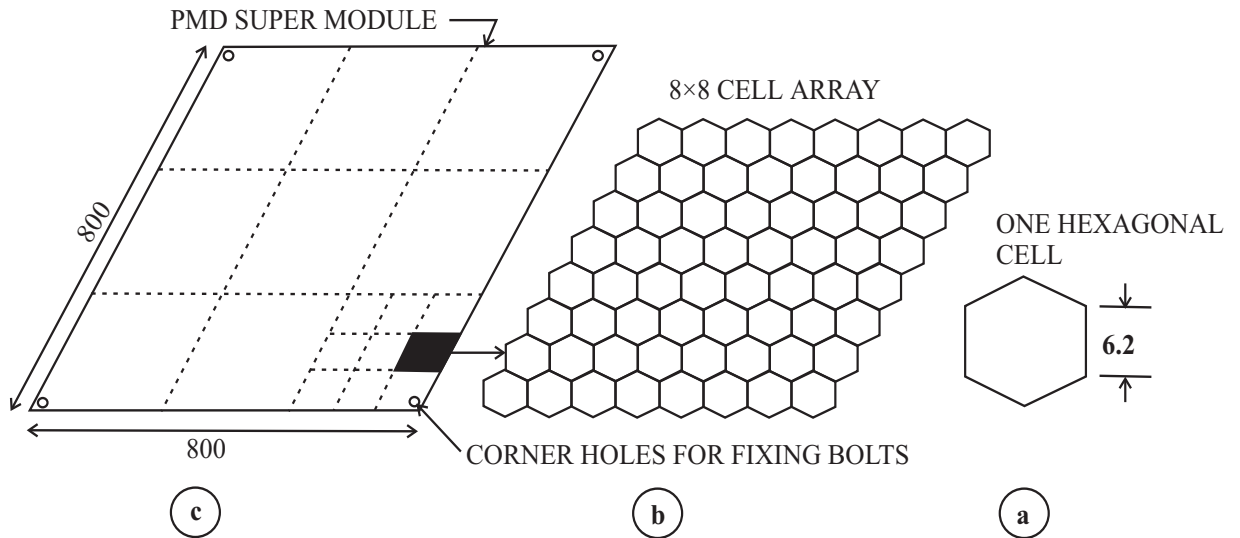


Figure 3.14: Unit modules assembled in a supermodule.

Table 3.3: Types of Supermodules.

Type	Total number
SM4 (with 4 UM)	6
SM5 (with 5 UM)	2
SM6 (with 6 UM)	10
SM8 (with 8 UM)	4
SM9 (with 9 UM)	2

3.6.6 Gas Flow within a Supermodule

Fig. 3.15 depicts gas feed channels on the boundary walls of the supermodule enclosure. Each supermodule has 24 openings for gas flow into the chamber. The gas flow impedance for the entire chamber is kept low by incorporating the following scheme:

- Small notches are provided at the corners of each cells as shown in Fig. 3.7 so that gas flows from one cell to another smoothly.
- Gas is fed through the connector at the end of the long gas feed channel. It enters through all the entry points in the channel simultaneously, at a depth of 4 mm from the bottom of the chamber. It then flows through the notches and exits at the other edge of the supermodule through 24 openings of the output channel.

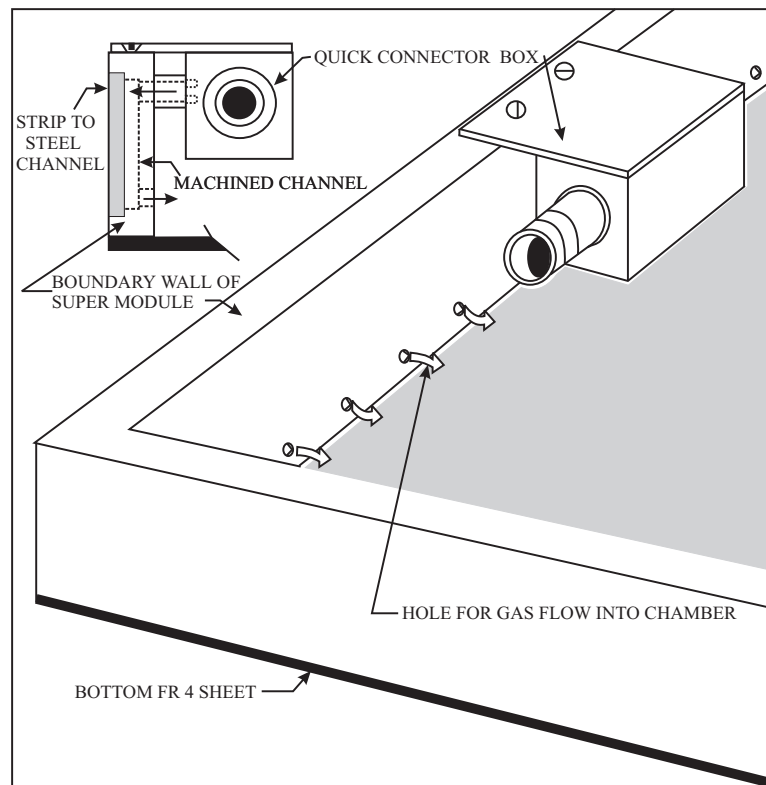


Figure 3.15: Gas feed sub-assembly placed at the top of the supermodule.

3.6.7 The CPV and the PMD Numbering Scheme

As mentioned earlier, the CPV and the pre-shower plane consist of 12 supermodules each with 4, 5, 6, 8 or 9 unitmodules. As a result it becomes important to adopt a standard numbering scheme to assign every channel in each supermodule a particular address. This address plays an important role for hardware to software mapping of the

detector. The CPV and the PMD numbering scheme are shown in Fig. 3.16 and Fig. 3.17, respectively. Supermodules are numbered from 1 to 12 in the CPV plane, where as, in the PMD planes, they are numbered from 13 to 24. Arrows associated with “i” and “j” in the figure correspond to the direction of row and column for every supermodule. One corner of the supermodule chamber is marked to denote the origin of the rhombus array. The x-axis increases towards the right and the y-axis increases upwards (Figs. 3.16 & 3.17). The origin mark is used to orient the supermodule during installation so that one-to-one correspondence is established between the physical coordinates of the cells and the coordinates implemented in simulation.

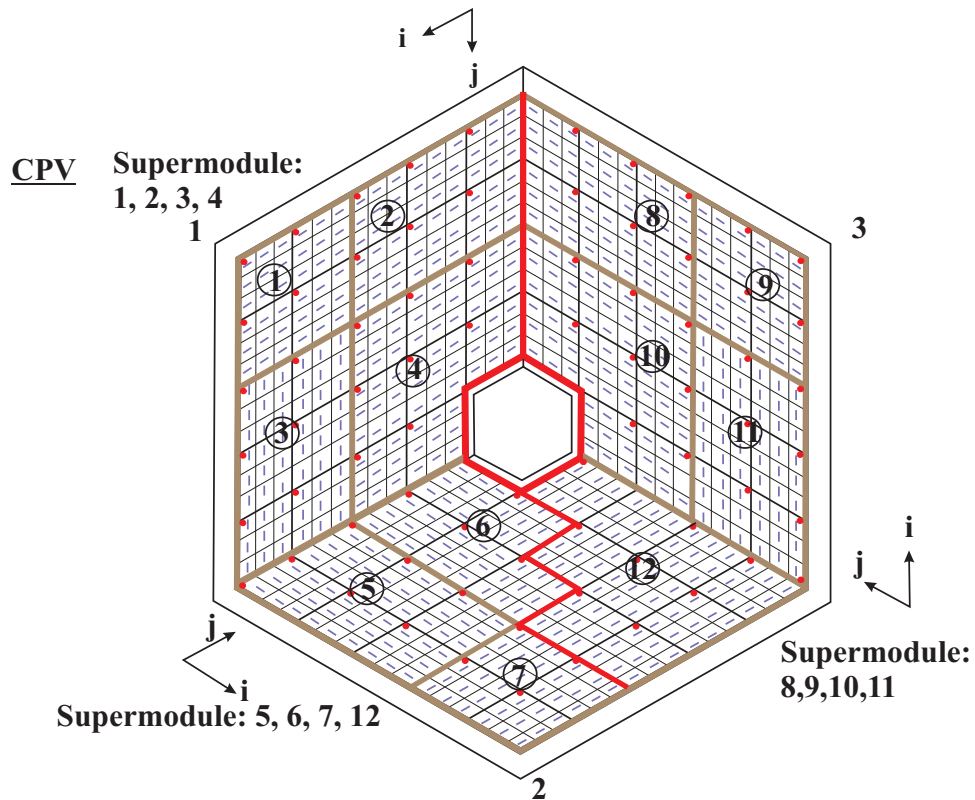


Figure 3.16: The CPV SM numbering scheme and row, column scheme. “i” and “j” represent the direction of row and column for every supermodule.

3.6.8 Converter Plates

Rhombus shaped lead converter plates of side 265 mm are machined and sandwiched between the CPV and the pre-shower plane. This size has been chosen as it serves the following purpose:

- An integral number (nine) of the lead plates fill the area of a supermodule.
- Each piece weighs around 10 kg which is convenient to handle during installation.

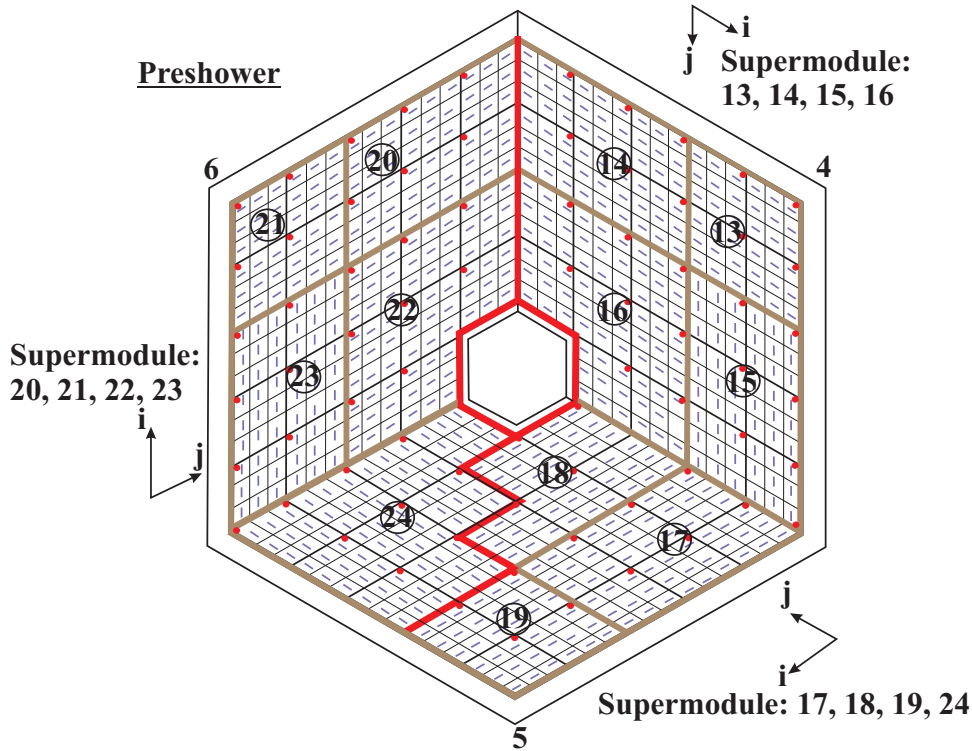


Figure 3.17: The PMD SM numbering scheme and row, column scheme. “i” and “j” represent the direction of row and column for every supermodule.

3.6.9 Support Assembly

The support assembly consists of two parts:

- The support plates: A 5 mm thick flat stainless steel plate is used to support the lead converter plates and the supermodules in each half of the PMD. It has tapped holes for screws corresponding to hole positions in the lead plate and in the supermodule.
- The suspension mechanism for the PMD is shown in Fig. 3.18. The weight of the detector is 2500 kg. The two halves of the detector are supported on the cross beams and hang freely in a vertical position. Each half of the detector can be separated with the help of independent x- and z- movements on the cross beam. When the detector is fully opened, the two halves provide sufficient clearance for the pole tip support for the STAR magnet to move in.

3.7 Gas System for the PMD

Various aspects of PMD gas system are listed in the Table 3.4. Rear and front pictures of the gas system are shown in Fig. 3.19 and Fig. 3.20, respectively.

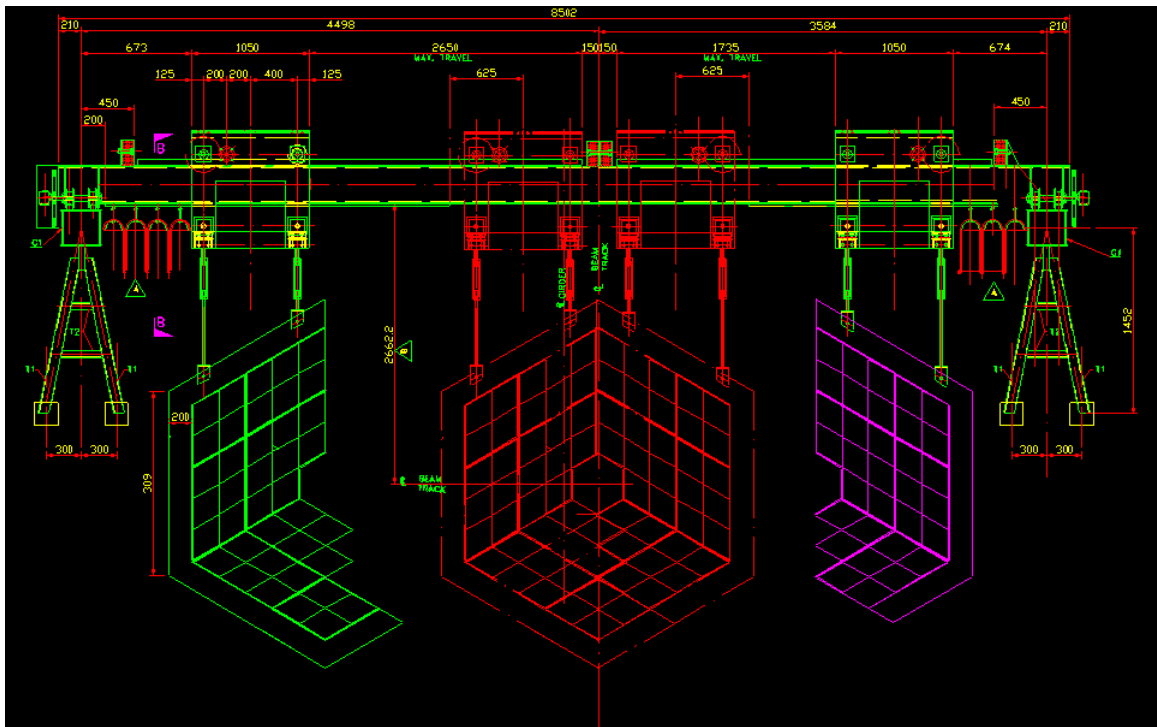


Figure 3.18: Suspension mechanism of the PMD showing movement along the x-direction. The two halves of the PMD are shown separated.

Table 3.4: The PMD Gas System.

Components	Features	Safety aspects
Two component gas system	Ar(70%) + CO ₂ (30%)	Non inflammable
Valve	Manual Control	Operating pressure is 1 mbar above atmospheric pressure.
Flow meters	Manual monitoring Ar : 50 litres/hr CO ₂ : 30 litres/hr	Total flow rate 45 litres/hr.

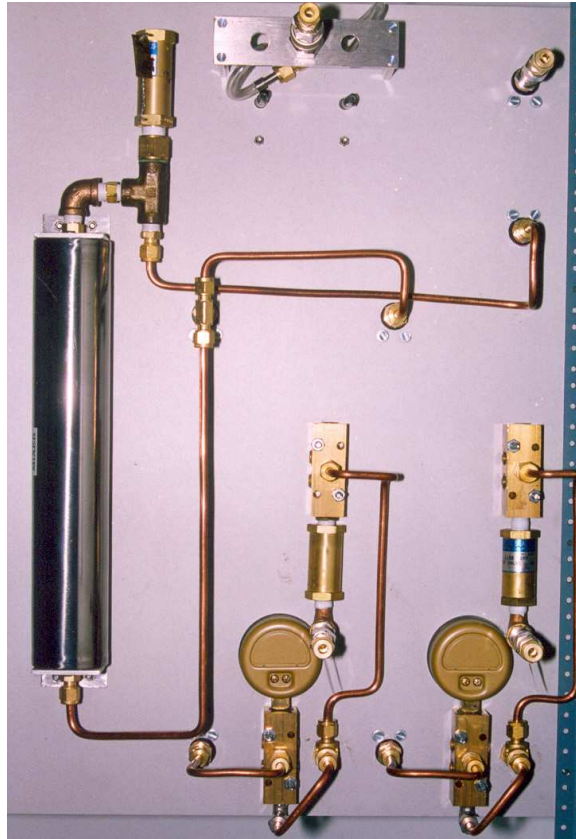


Figure 3.19: Rear view of the PMD gas system.



Figure 3.20: Front view of the PMD gas system.

3.8 Front End Electronics

The front end electronics for processing the PMD signals is based on the use of low noise 16-channel ASIC (Application Specific Integrated Chip) i.e., gassiplex chips [3] developed at CERN. Each of the 16 channels consists of a charge sensitive amplifier (CSA), deconvolution/switchable filter, a shaping amplifier and a Track and Hold (T/H) to store charges in a capacitor [24]. The low noise amplifier is characterized by an integration time of about 800 ns duration. Detailed specifications of the gassiplex chip are listed in the Table 3.5 below.

Table 3.5: Specifications of a gassiplex chip.

Parameter	Value
Linear dynamic range	-250 fC - -300 fC
Conversion gain	4.9 mV/fC
Range peaking time	400-1000 ns
Base line recovery	$\leq 0.5\%$ after 3 μ sec
Noise at peaking time	485 e^- RMS at 0 pF
Noise slope at peaking time	15.8 e^- RMS/pF
Power dissipation	6 mW/ch
Analog readout speed	10 MHz max.

3.8.1 Use of Gassiplex Chips in the PMD

The Front End Electronics readout system of the PMD (Fig. 3.21) consists of three types of boards i.e., (a) Gas64, (b) translator board, and (c) buffer board, which are described below:

- **Gas64:** The Gas64 board comprises of four Gassiplex chips, shown in Fig. 3.22. A zone of 64 channels/cells of the detector are connected to one Gas64 board. Nine Gas64 cover one unit module as one unit module has nine 9 such zones. Rhombus shaped boards match the layout of 8×8 cell block (zone) on the chamber PCB. A board has two sets of 10 pin FRC connectors on each sides for the daisy chaining of the control signals and analog output. Three pin power connector on the board enables daisy chaining of the low voltage bias for the chips.
- **Translator:** Translator board (Fig. 3.23) shifts the level of the control signal from fast NIM to the logic level of the chip.

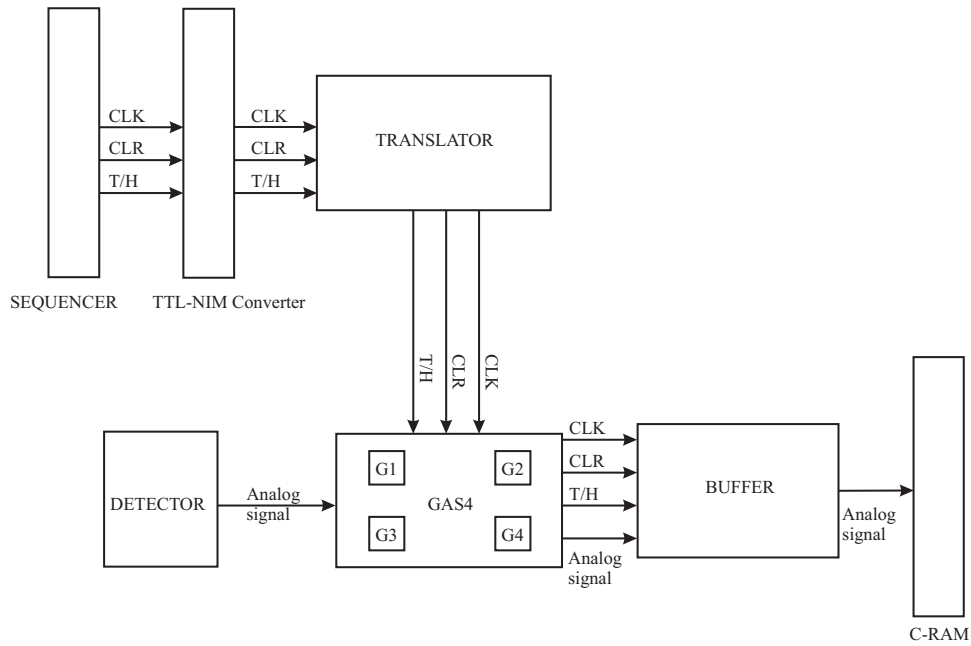


Figure 3.21: Block diagram of front end electronics readout system.

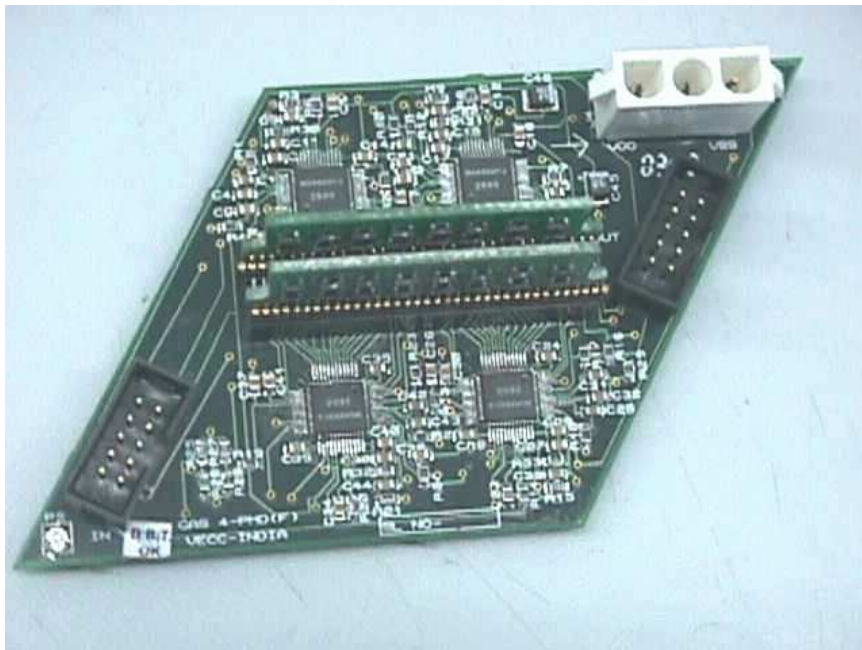


Figure 3.22: Gas64 board for the PMD with four chips.

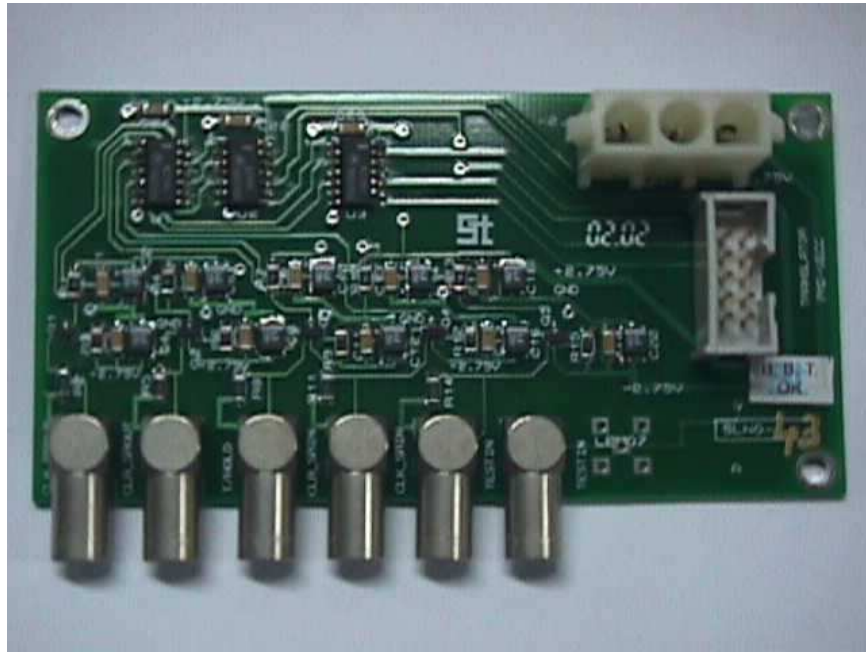


Figure 3.23: The translator board.

- Buffer board: The analog output from the chain of Gas64 boards passes through the buffer board which is needed for the impedance matching of the signal, (Fig. 3.24).

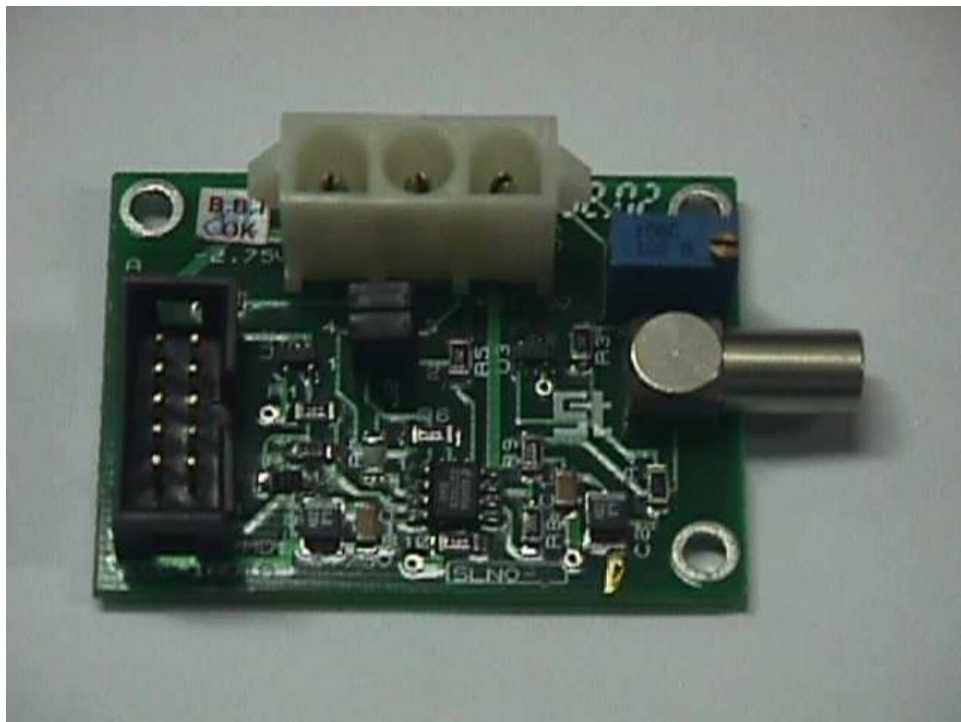


Figure 3.24: The buffer board.

3.8.2 Electronic Noise/Pedestal

Pedestal is defined as the minimum noise level of the electronics itself. It is important to know the pedestal level of gassiplex boards as the data rides over the noise level. Pedestal values are set by the use of a variable potentiometer that is common to all channels of a given GAS64. All pedestals must lie in the negative range of values as it is an input polarity required for the ADC. All gassiplex chips are first grouped into four pedestal classes. Fig. 3.25 shows the distribution of pedestal minima and Fig. 3.26 shows the scatter plot of pedestal minima vs. pedestal spread for 5000 chips. Only chips from the same group are mounted on the same GAS64 board, (Fig. 3.22). The GAS64 boards are then adopted in order to obtain a maximal homogeneity in the pedestal values. The four pedestal classes based on pedestal minima are as follows :

- from 0 to 20 mV
- from 20 to 50 mV
- from 50 to 110 mV
- above 110 mV

3.8.3 Experimental Results

A number of GAS64 circuits were tested in the laboratory. The electronic noise and pedestal value of each channel was measured before connecting to the detector. The results for a daisy chain (27 GAS64 boards) are shown in Fig. 3.27. Top panel of the Fig. 3.27 shows pedestal value mean (left) and sigma (right) of each channel in one chain. It is seen that channels > 1200 have a large constant mean pedestal value (top left). This shows that a few boards in this chain were not working. Right plot on the top panel shows the sigma of each channel in this chain. The distribution of sigma for all the channels can be seen in the bottom right panel. Similarly the distribution of the mean pedestal value of all channels is given in bottom left panel.

3.8.4 Electronic Chains

One electronic chain of the detector consists of one translator board, 27 Front End Electronic boards and a buffer board. More detailed specifications of the electronic chains are listed in the Table 3.6.

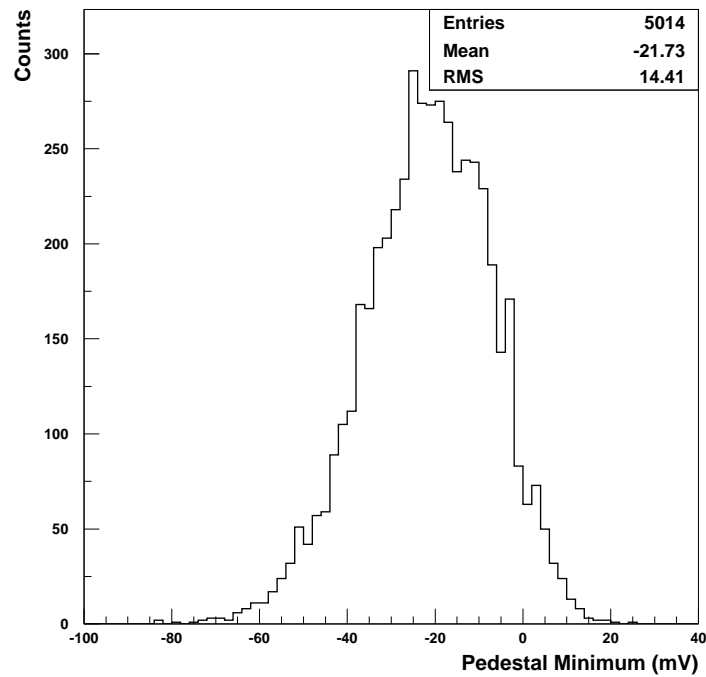


Figure 3.25: Pedestal minimum values (in mV) for 5000 chips.

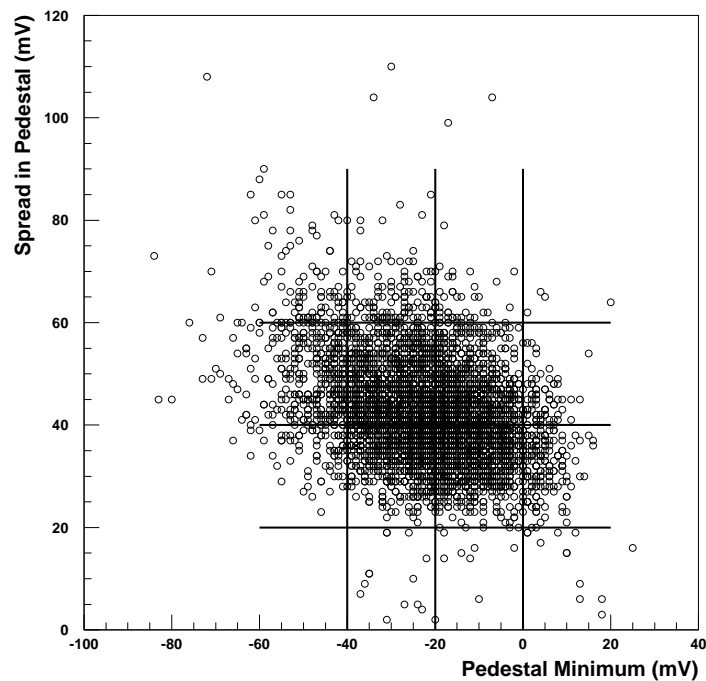


Figure 3.26: Pedestal minimum vs. pedestal spread for the above chips. Lines are drawn to show the grouping of chips for a uniform chain.

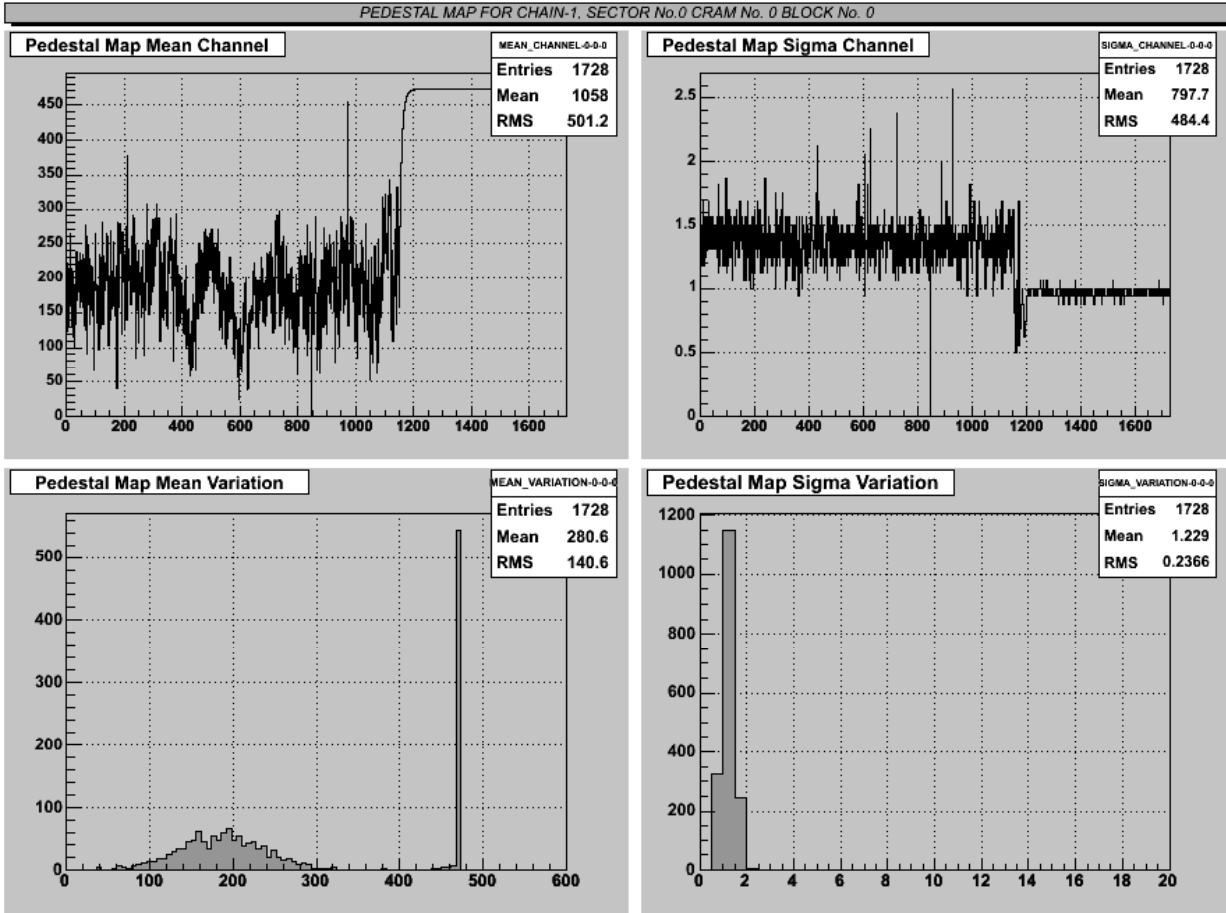


Figure 3.27: Figures, clockwise from left, (a) Pedestal values versus the channel number, (b) RMS as a function of channel number, (c) Integrated pedestal, and (d) Distribution of RMS values.

Table 3.6: Electronic chains.

Parameter	Value
No. of chains per plane	24
Total no. of chains (preshower+CPV)	48
No. of UM in one daisy chain	3
No. of channels in a chain	1728
No. of Gas64 boards per chain	27
No. of translator boards	1
No. of buffer board	1

3.9 Trigger Logic for the PMD

After the RHIC collision, the level 0 trigger arrives in about $1.1 \mu\text{s}$. However, the peaking time of the gassiplex is only about $1 \mu\text{sec}$. This necessitates the use of a pre-trigger which is generated earlier and sent to gassiplex to strobe the track/hold. The STAR trigger scheme provides for such a pre-trigger signal [4].

The signals on the T/H stage of the gassiplex are held until the arrival of the validation of L0 to continue with digitization and data transfer. If L0 is not validated within the specified time, as shown in Fig. 3.28, a clear signal is generated which resets the gassiplex and makes it available for taking fresh interaction after about $10 \mu\text{s}$.

However, when L0 arrives within its pre-defined time, T/H and busy signals are sent. And if for this L0, the corresponding pre-trigger exists, then a trigger is sent to sequencer which in turn generates the clock, T/H, clear, busy etc. Clock, T/H clear etc. sent to several FEEs are all FAN IN/OUT.

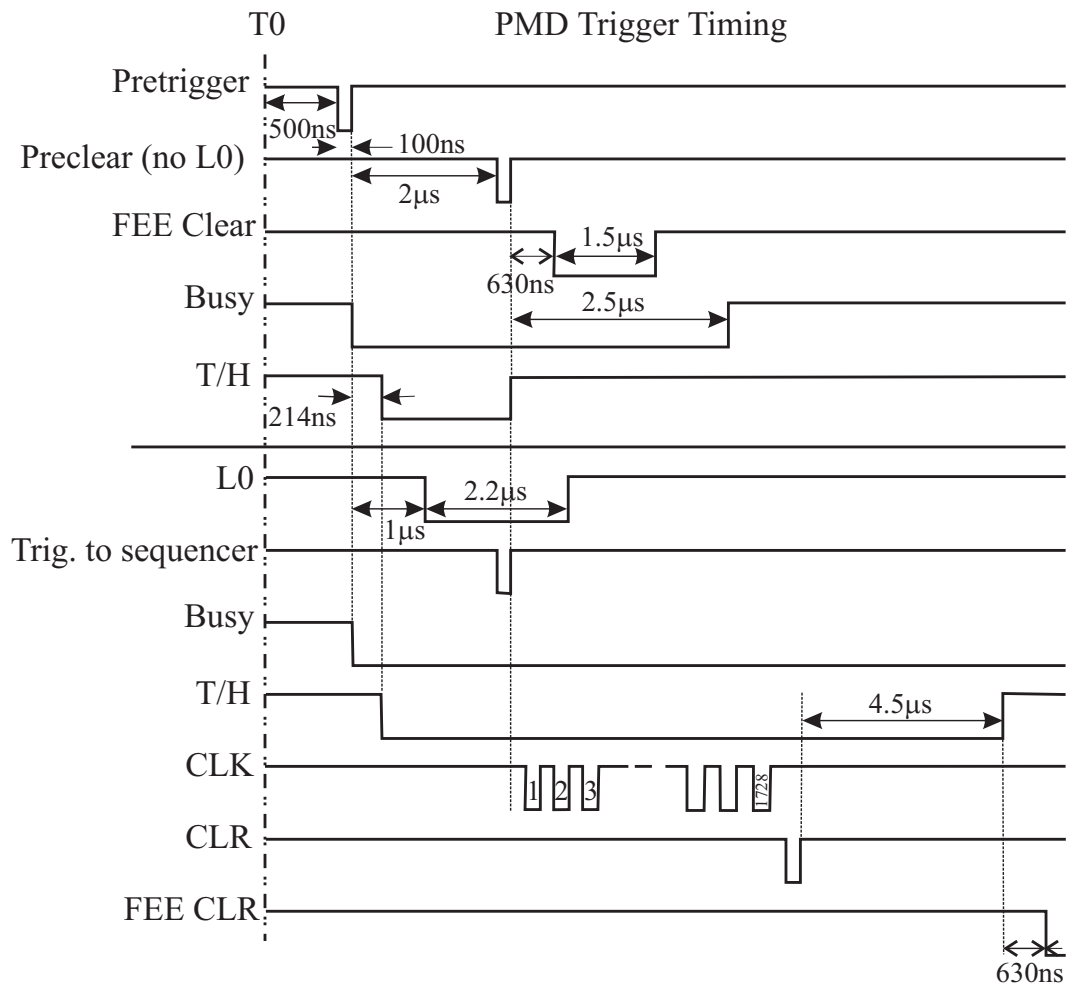


Figure 3.28: Timing diagram for pre-trigger and L0 validation the PMD.

Bibliography

- [1] M.M. Aggarwal *et al.* Nucl. Instr. & Meth. in Phys. Res. A **499** (2003) 751.
- [2] Photon Multiplicity Detector for STAR:technical proposal, VECC Internal report VECC/EQC/00-04, May 2000 (revised:January 2001).
- [3] ALICE HMPID Technical Design Report, CERN/LHCC 98-19 (1998); J.C. Santiard *et al.*, ALICE Collaboration.
- [4] STAR RICH Proposal, YRHI-98-22 (1998); G.J. Kunde *et al.*, STAR Note SN0349 (1998).
- [5] STAR FTPC Proposal, MPI-PhE/98-3 (1998).
- [6] M.M. Aggarwal *et al.*, (WA98 Collaboration), Nucl. Instr. & Meth. in Phys. Res. A **372** (1996) 143.
- [7] M.M. Aggarwal *et al.*, (WA98 Collaboration), Nucl. Instr. & Meth. in Phys. Res. A **421** (1999) 558.
- [8] ALICE Photon Multiplicity Detector Technical Design Report CERN/LHCC-32 (1999).
- [9] B. Mohanty and B. Serreuu, Phys. Rept. **414** (2005) 263.
- [10] T.C. Brooks *et al.*, (Minimax Collaboration), Phys. Rev. D **55** (1997) 390.
- [11] M.M. Aggarwal *et al.*, (WA98 Collaboration), Phys. Lett. B **420** (1998) 169.
- [12] T.K. Nayak *et al.*, (WA98 Collaboration), PANIC '99 proceedings, Nucl. Phys. A **663** (2000) 745c.
- [13] T.K. Nayak *et al.*, (WA98 Collaboration), Quark Matter '97 proceedings, Nucl. Phys. A **638** (1998) 249c.
- [14] B.K. Nandi *et al.*, Phys. Lett. B **461** (1999) 142.

- [15] B.K. Nandi, Ph.D. Thesis, Utkal Univ. (1999);
D.S. Mukhopadhyay, Ph.D. Thesis, Univ. of Calcutta (1999);
Z. Ahammed, Ph.D. Thesis, Jadavpur Univ. (1999).
- [16] B.K. Nandi, T.K. Nayak, B. Mohanty, D.P. Mahapatra, and Y.P. Viyogi, Phys. Lett. B **461** (1999) 142.
- [17] B. Mohanty, D.P. Mahapatra, and T.K. Nayak, Phys. Rev. C **66** (2002) 044901.
- [18] B. Mohanty, Int. J. Mod. Phys. A **18** (2003) 1067.
- [19] M.M. Aggarwal, G. Sood, Y.P. Viyogi, Phys. Lett. B **638** (2006) 39.
- [20] M.M. Aggarwal *et al.*, (WA98 Collaboration), Phys. Lett. B **458**, (1999) 422.
M.M. Aggarwal *et al.*, (WA98 Collaboration), Phys. Rev. C **64** (2001) 011901(R).
M.M. Aggarwal *et al.*, (WA98 Collaboration), Pramana **60** (2003) 987.
- [21] F. Takagi, Phys. Rev. Lett. **53** (1984) 427.
- [22] A.C. Das and Y.P. Viyogi, Phys. Lett. B **380** (1996) 437.
- [23] M.M. Aggarwal, V.S. Bhatia, A.C. Das and Y.P. Viyogi, Phys. Lett. B **438** (1998) 357.
- [24] ALICE Dimuon Forward Spectrometer Technical Design Report, CERN/LHCC 99-22.

Chapter 4

Simulation of the PMD

This chapter of the thesis presents results of simulations based on HIJING (Heavy Ion Jet Interaction Generator) and GEANT (GEometry ANd Tracking) used to study the response of the PMD. Response of the charged particle in an isolated cell is studied in detail in simulations. Hit and cluster level characteristics are presented in this chapter. Important parameters like the photon counting efficiency and purity of the photon samples are obtained from simulations. These parameters along with the acceptance correction factors are used to correct the raw photon yield obtained in the data.

As already explained in chapter 3, the PMD consists of a highly segmented detector based on the principle of proportional counters placed behind a lead converter plate of three radiation lengths ($3X_0$). A high energy photon traversing through the converter plate produces an electromagnetic shower whereas most of the hadrons pass through the converter plate without any interactions. Indeed, test beam and simulation studies have revealed that incident photons deposit signal in more than one cell whereas charged hadron signal is typically confined to a single cell. Thus, a clustering algorithm is adopted to reconstruct photon clusters on an event-by-event basis. In order to discriminate between charged hadrons and photon signals, a suitable discriminating threshold is applied to the reconstructed photon clusters. For the PMD to count photons on an event-by-event basis and measure their spatial distribution (x,y) or (η,ϕ) , it is necessary to know the following parameters :

- Photon counting efficiency & purity of the photon samples.
- Accuracy of the spatial distribution of the detected photons relative to the incident photons. Specifically one needs to calculate the resolution i.e., $(\eta_{track} - \eta_{clus})$, where η_{track} is the original value of the track resulting a cluster at a position denoted by $\eta_{cluster}$.
- Acceptance factors.

4.1 Simulation Framework

In order to calculate the photon counting efficiency and purity in the photon samples, we use minimum bias $Cu + Cu$ collisions at $\sqrt{s_{NN}} = 200$ GeV data generated using HIJING (0-10 fm). Option of decaying resonances and π^0 were switched “on” for this study to simulate the production of photons from π^0 decays in heavy ion collisions. The particles were processed through GEANT and the STAR analysis framework i.e., GSTAR. The reconstruction procedure of photons from simulation is shown in Fig. 4.1. The clusters are assigned identification (ID’s), such as hadrons/photons on the basis of their Monte-Carlo tracks and energy deposited in the detector. A discriminating threshold is applied to get γ -like clusters. Finally, the efficiency and purity are calculated for each centrality. γ – like clusters are corrected for efficiency, purity and geometrical acceptance factors to obtain reconstructed photons from the simulated data.

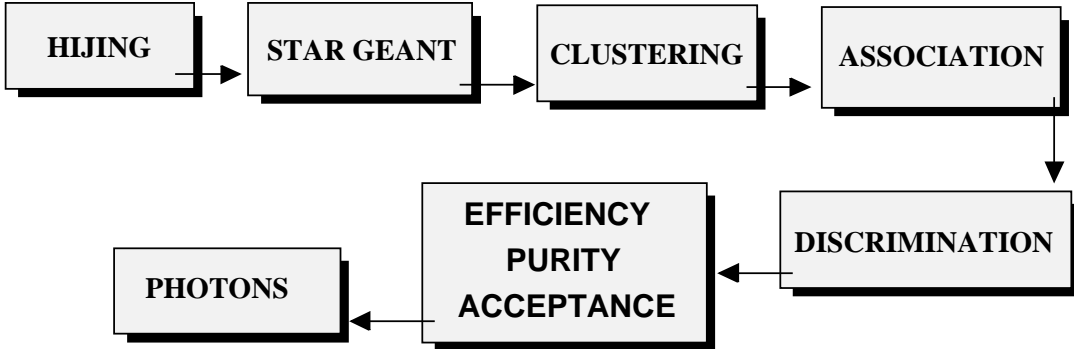


Figure 4.1: Flow chart for photon reconstruction from the PMD in simulation.

4.2 Data Selection in Simulation

- **Z-vertex selection** : HIJING events were embedded in the STAR simulation with a vertex distribution mimicking that observed in the experiment. Simulated events were been selected with a collision vertex position within 50 cm from the center of the TPC along the longitudinal direction. A nominal cut of ± 50 cm was applied in order to accept more events in simulation.

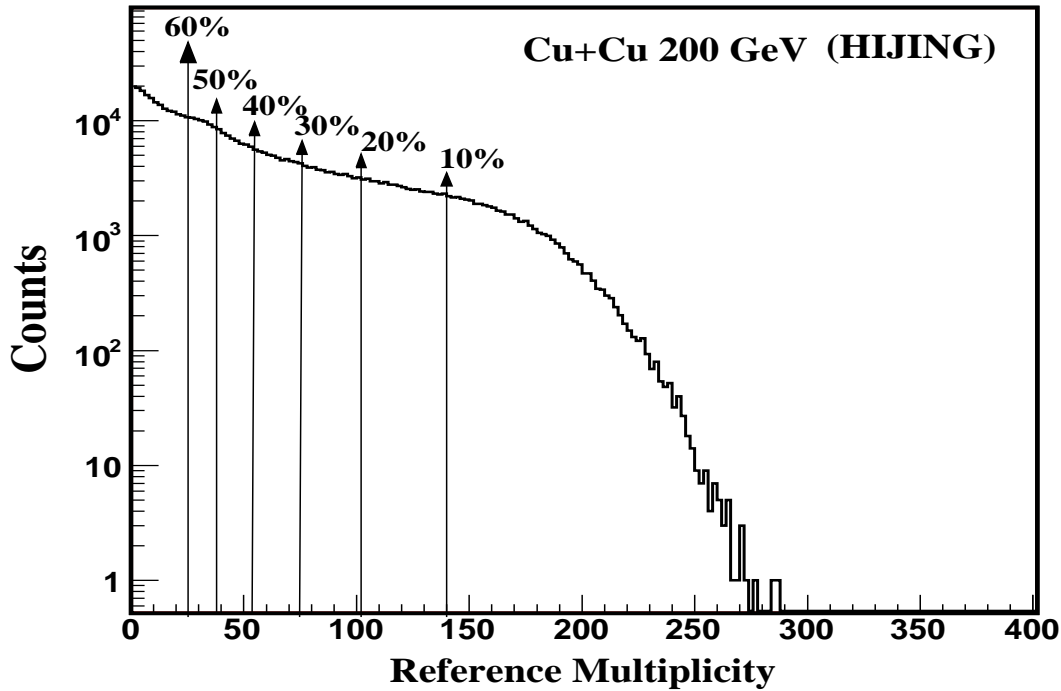


Figure 4.2: Distribution of charged particle multiplicity obtained with HIJING $Cu + Cu$ events at the center of mass energy of 200 GeV. Vertical lines show the reference multiplicity cuts and the corresponding fraction of the interaction cross-section.

- **Centrality selection :** The collision centrality is estimated following the procedure used in the experimental data (will be discussed in the subsequent chapter), on the basis of uncorrected charged particle multiplicity measured within the TPC in the pseudo-rapidity range $-0.5 < \eta < 0.5$, as used in the data, shown in Fig. 4.2.

4.3 Photons Distribution in the PMD Acceptance

The information of incident photons, for instance, transverse momentum (p_T) distribution and their exact number on an event-by-event in the PMD coverage is required in order to count photon multiplicity and evaluate their spatial distribution in the forward rapidity regions. However, photons with $p_T < 20 MeV$ are absorbed within the lead converter plate of the PMD. As a result, a minimum threshold of $p_T > 20 MeV$ was applied in the present simulation study. Fig. 4.3(a) and Fig. 4.3(b) show the minimum bias incident photon multiplicity and transverse momentum (p_T) distributions of photons incident on the PMD, respectively. We observe that in $Cu + Cu$ collisions at $\sqrt{s_{NN}} = 200 GeV$, maximum number of photons incident on the PMD is 200 with maximum transverse momentum, $p_T \sim 3.5 GeV/c$.

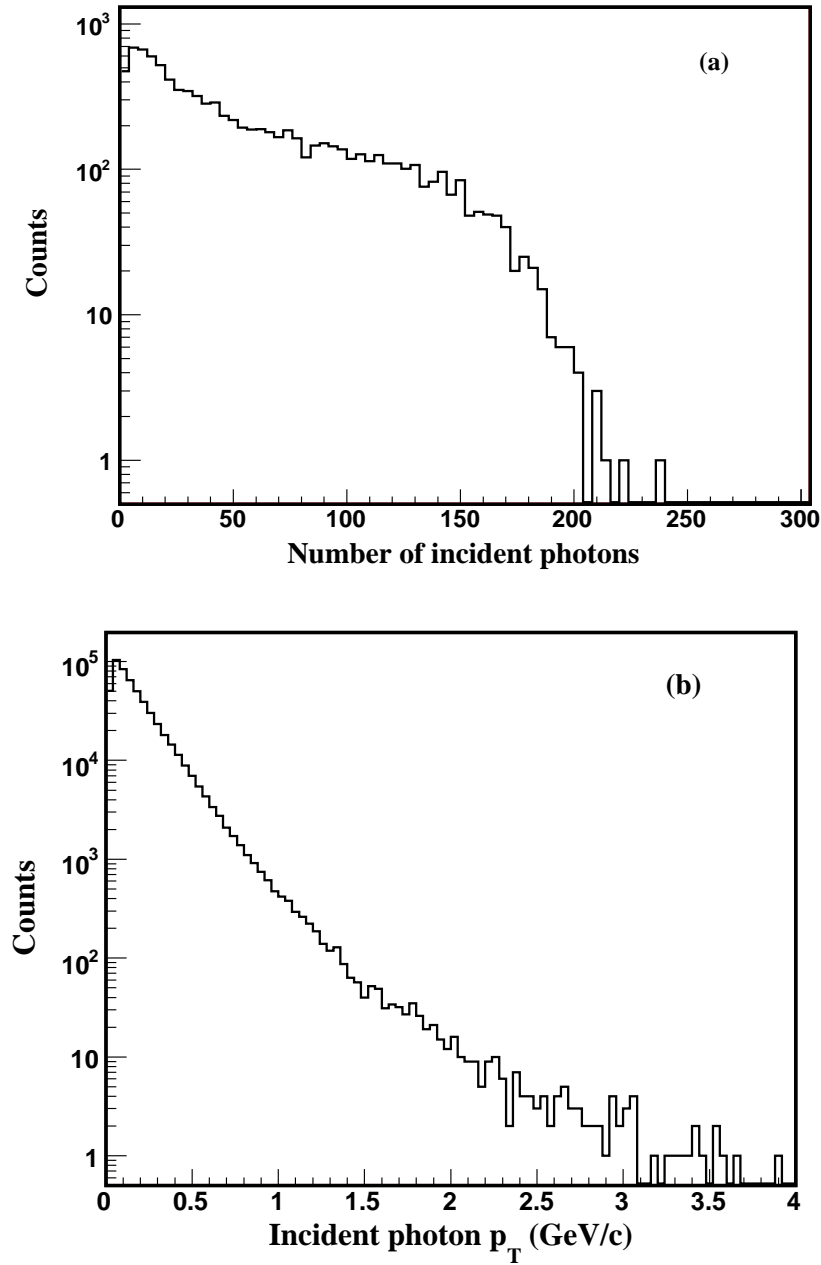


Figure 4.3: (a) Photons multiplicity and, (b) transverse momentum (p_T) distribution of photons incident on the PMD obtained with HIJING+GEANT $Cu + Cu$ 200 GeV events.

4.4 Implementation of Dead Cells

The PMD (CPV + preshower planes) nominally consists of 82,944 cells in totality, with 41472 cells in each plane. During the experiment, all cells were not working. We label cells with very low gain as dead cells. Therefore, in order to make simulation look like data, it is imperative to implement dead cells in simulations. The total number of live cells in the preshower plane is 28789. Fig. 4.4 shows the spatial distribution of the preshower plane with dead cells implementation.

The thickness of the honeycomb cell walls correspond to a dead area of 7% for normal incidence of charged particles. When particles are incident at larger angles, the contribution of the cell walls to the dead area is considerably reduced. The walls of the super-module contribute only 2.5% to the dead area. In the preshower plane, there are shower particles traveling at different angles and several cells are affected. Hence, there is effectively no dead area within a preshower super-module.

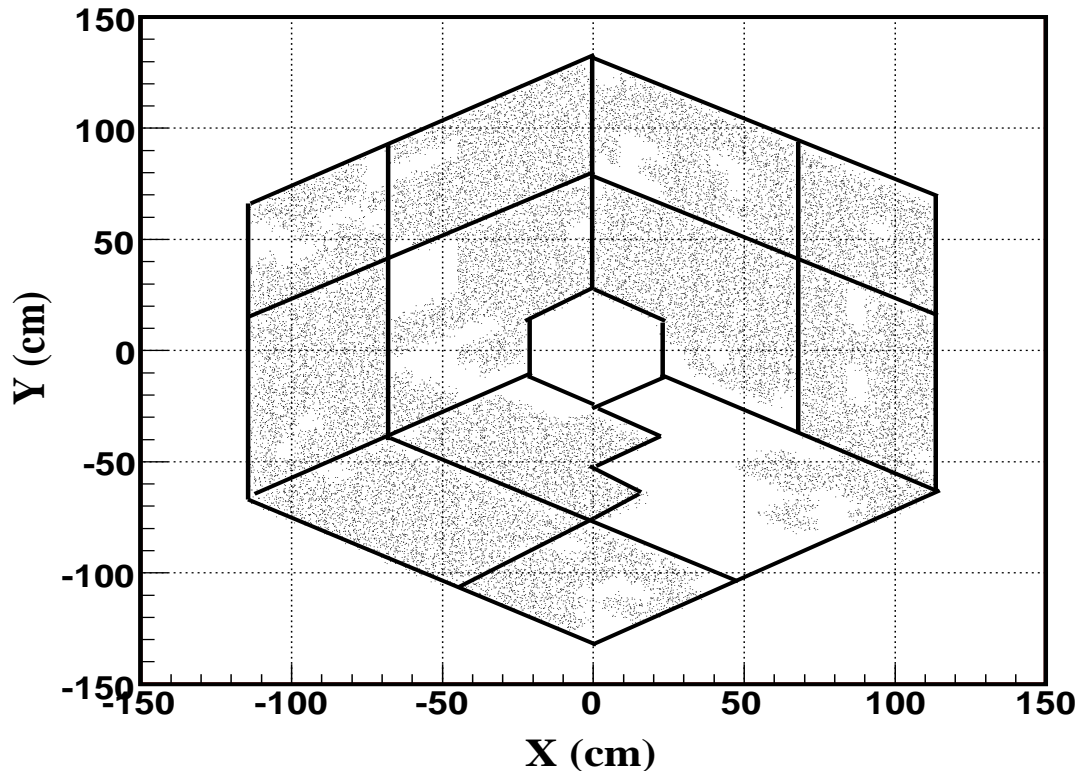


Figure 4.4: 2D hits distribution of the preshower plane after dead cell implementation.

4.5 Simulation of the Expected Signal in a Cell

The response of the detector towards minimum ionizing particles (MIP) [3] is studied in order to determine the average energy deposited by these particles in the preshower plane. The PMD is designed in such a way that energy deposition by charged particles is essentially confined to a single cell. Therefore, isolated cell in an event enable us to determine the gain of each cell. However, the gain of each cell may vary overtime due to variations of temperature and humidity. Cell-to-cell gain differences are also possible due to edges and notches caused during the cell manufacturing. The signal of these particles recorded by the detector is in terms of ADC in data and in KeV in simulation. A cell with signal, surrounded by cells with no signal, is considered as an isolated cell, as shown in Fig. 4.5. The shaded cell represents an isolated cell. The mean of the Landau distribution of such an isolated cell reflects its gain. Fig. 4.6 shows energy deposited distribution of minimum ionizing particles from HIJING+GEANT simulation. One finds the average energy deposited by a charged particle is ~ 2.6 KeV.

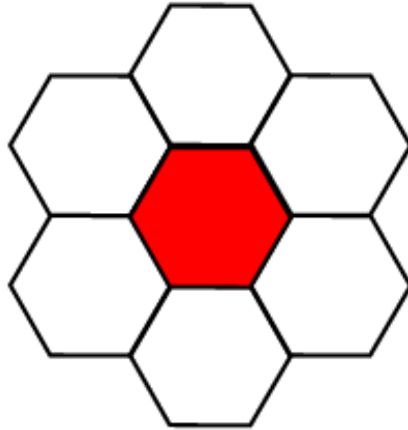


Figure 4.5: The shaded cell is labeled as isolated if its six neighboring cells (non shaded) have zero signal.

4.6 Hit Level Characteristics

Signal deposition in the sensitive volume of the detector is known as a hit. Fig. 4.7(a) shows total number of hits distribution of the preshower plane obtained with the HIJING $Cu + Cu$ collisions at $\sqrt{s_{NN}} = 200$ GeV using GSTAR. Fig. 4.7(b) displays a linear relationship between number of hits and total energy deposited (E_{dep}) in the preshower plane. Similarly, Fig. 4.7(c) shows a linear relationship between reference multiplicity (uncorrected charged particle multiplicity within $-0.5 < \eta < 0.5$) and number of hits on

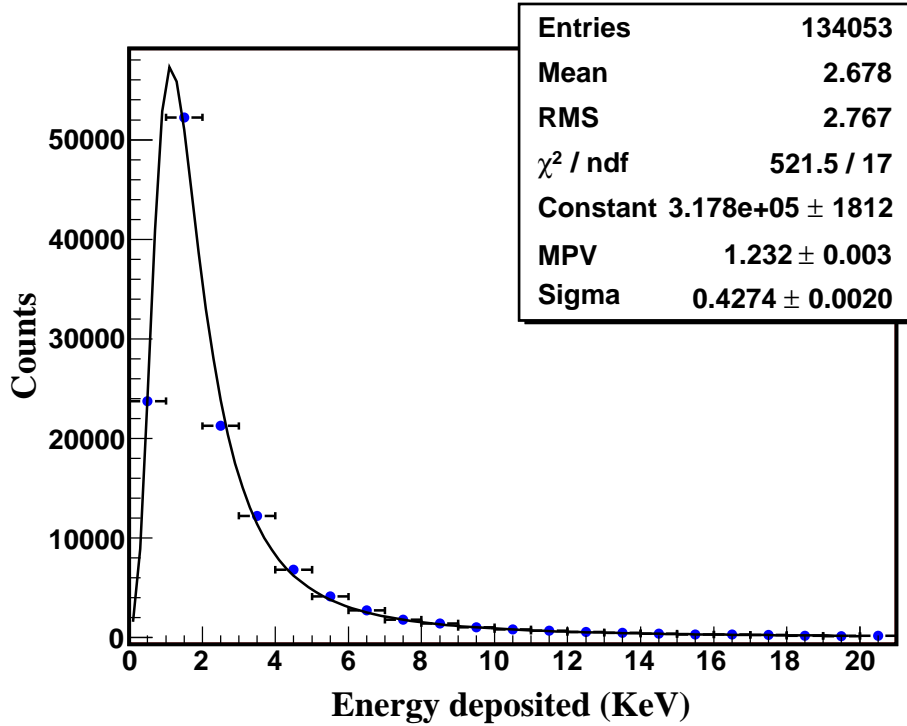
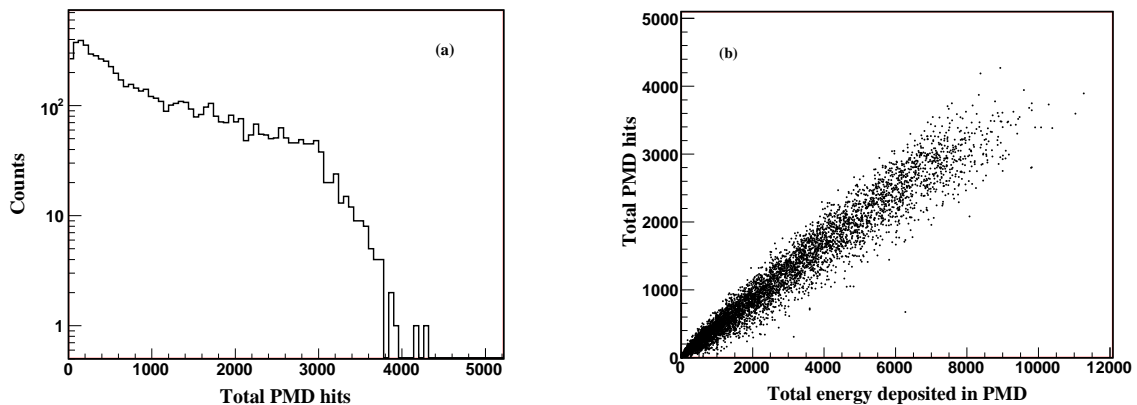


Figure 4.6: Distribution of energy deposited (E_{dep}) in an isolated cell in simulation.

the PMD. Another important parameter at the hit level is the average energy deposited per hit (E_{dep}/hit), which is shown in Fig. 4.7(d). The mean value of this distribution should be close to the average energy deposited by a charged particle. The value of E_{dep}/hit is ~ 2.4 KeV.



4.7 Results from Clustering

The basic principle of the clustering algorithm adopted in the present analysis is as follows :

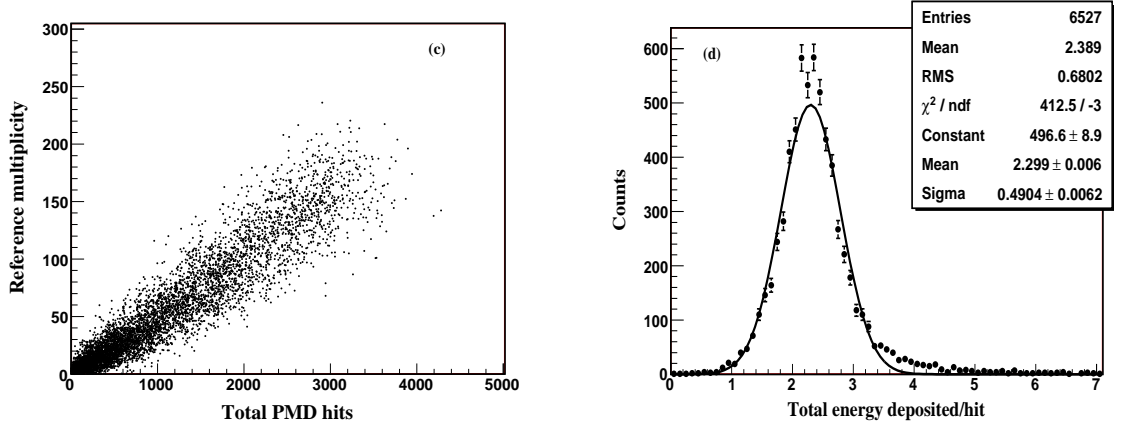


Figure 4.7: Hit level characteristics from HIJING+GEANT simulation (a) minimum bias distribution of total hits of the PMD, (b) correlation between the number of hits and the total energy deposited in the PMD, (c) correlation between the reference multiplicity and the total PMD hits, (d) distribution of average energy deposited per hit in the PMD. Units of average energy deposited (E_{dep}) is in KeV.

- A super-cluster is first formed connecting all the cells having non-zero ADC or E_{dep} values.
- Cells are ordered in the descending order of their ADC value (data) or energy deposited (E_{dep}) (simulation) values.
- Super-clusters are broken into refined clusters.
- The final cluster output is written in terms of (a) cluster ADC or E_{dep} , (b) cluster X, Y positions, (c) cluster η and ϕ values, (d) number of cells in a cluster.

Fig. 4.8 shows typical features of the clusters from the PMD, for example (a) shows the distribution of the number of clusters without any threshold in the PMD. It is seen that the number of clusters are much less as compared to the number of hits (Fig. 4.7(a)). The correlation between the TPC reference multiplicity (charged particle multiplicity within $|\eta| < 0.5$) and the number of clusters in the PMD is displayed in Fig. 4.8(b). Distribution of the number of cells in a cluster is plotted in Fig. 4.8(c) and the distribution of energy in a cluster i.e., E_{dep} , is shown in Fig. 4.8(d). The physics performance of the preshower plane of the PMD depends on the two quantities :

- Photon counting efficiency (ϵ_γ), and
- Purity (f_p) of the photon samples.

These two quantities are discussed in Section 4.9 and 4.10, respectively.

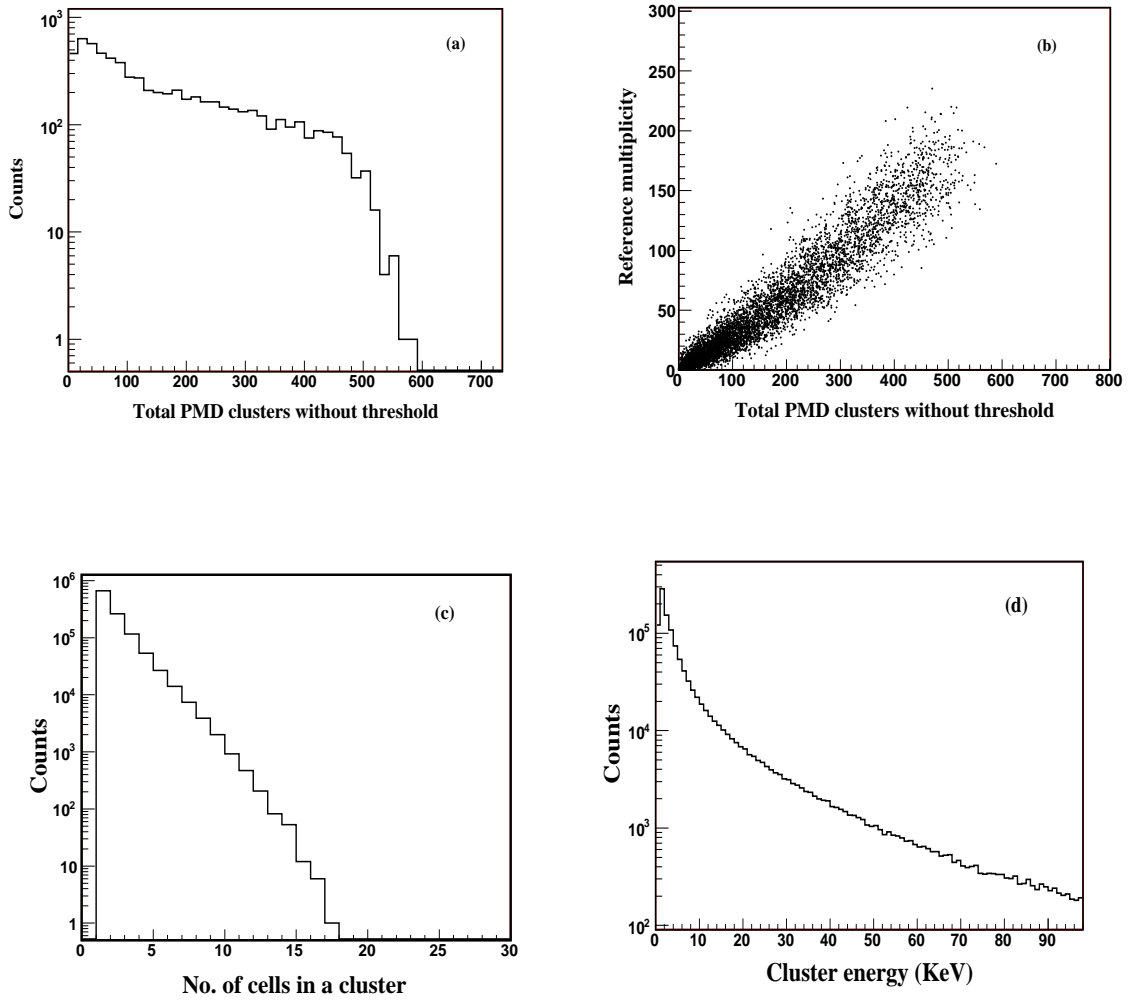


Figure 4.8: Cluster level characteristics (a) distribution of the number of clusters without any threshold in the PMD, (b) correlation between the TPC reference multiplicity and the number of clusters in the PMD, (c) distribution of the number of cells in a cluster, (d) distribution of energy (E_{dep}) in a cluster.

4.7.1 Photon Hadron Discrimination

We classify clusters as photons or charged hadrons on the basis of the following features :

- On an average photons will deposit more energy in the sensitive medium of the detector than a charged hadron.
- A photon cluster will have a larger number of cells hit in the preshower plane and a charged hadron will be typically confined to a single cell.

The classification process is complicated by the fact that there is a finite probability that the clustering algorithm may assign a cluster as a photon cluster with number of

cells (N_{cell}) equal to 1. As a result an attempt was made to estimate the fraction of photons which exist with $N_{cell}=1$ (i.e., what fraction of photons deposit energy in one cell). Fig. 4.9 shows that 13% photon clusters have a probability of having $N_{cell}=1$. Additionally, there is a finite probability that an energetic charged particle may interact with the converter material (for $3X_0$ radiation length, the probability is $\sim 13\%$) and may hit a large number of cells, thus, depositing energy in more than one cell i.e., a charged hadron may mimic a photon signal. This study shows that hadrons can mimic photon signal and hence an appropriate discrimination threshold is imperative to limit the misidentification/contamination. Fig. 4.9 shows that 13% of the photon clusters would be lost if we apply a discriminating threshold of $N_{cell} > 1$. Also, Fig. 4.10 clearly shows that $\sim 14\%$ of the charged hadron clusters may mimic photon signal. As a result, a threshold cut on N_{cell} only will have contamination due to charged particles in the detected photon samples. We may increase the threshold of N_{cell} to reduce the impurity in the photon samples, but this leads to reduction in the photon counting efficiency. The N_{cell} cut is not sufficient to identify a photon cluster. We also need to have a discriminating threshold on the basis of energy of the clusters.

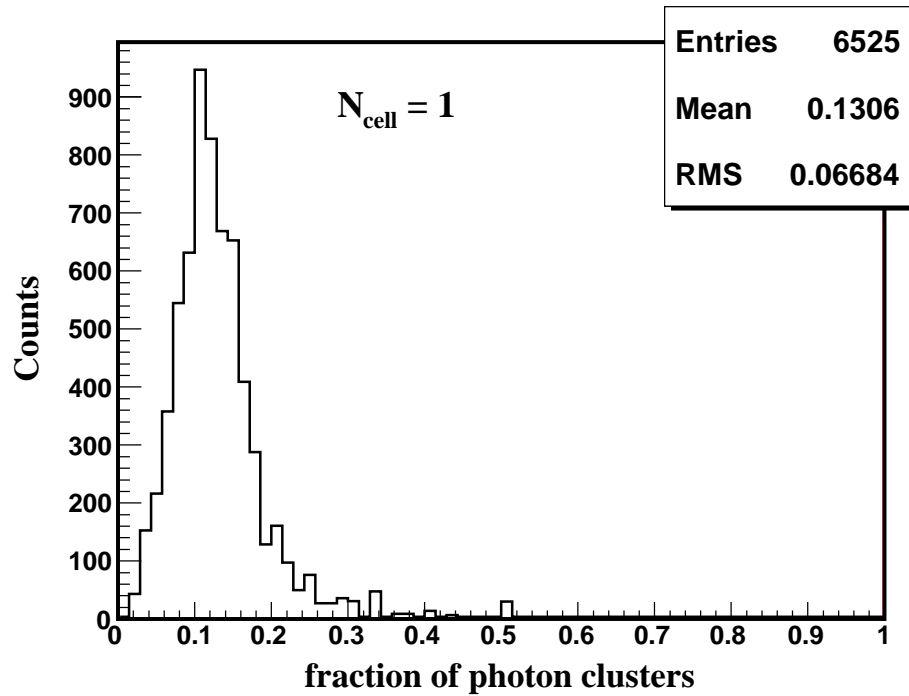


Figure 4.9: Fraction of photon clusters measured per event which deposit energy in one cell only.

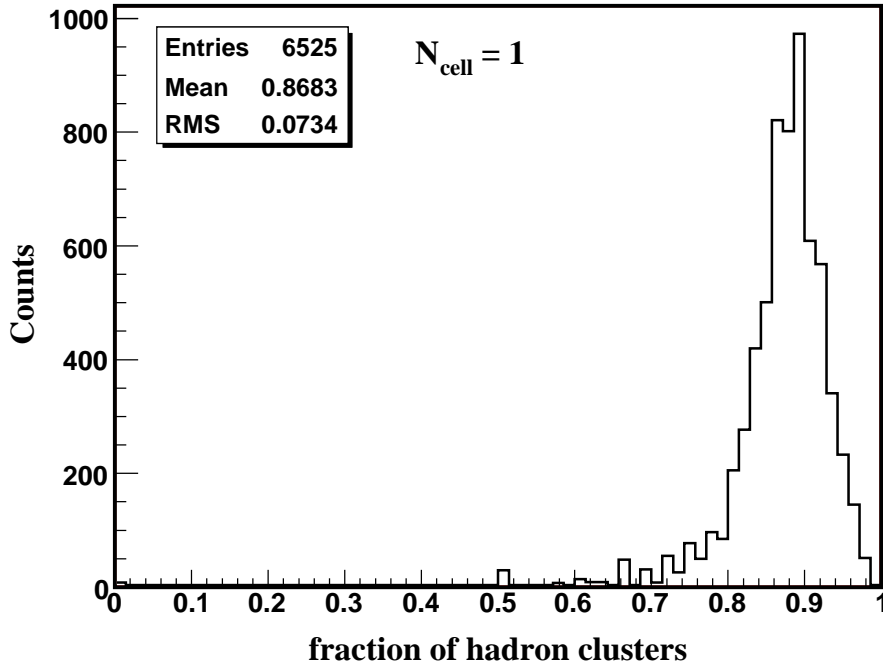


Figure 4.10: Fraction of charged hadron clusters measured per event which deposit energy in one cell only.

4.7.2 Optimization of Discrimination Threshold

The optimization of photon/hadron discriminating threshold is achieved by varying E_{dep} cuts. As mentioned in the preceding section, the average energy deposited by a charged hadron is ~ 2.6 KeV, and this energy is typically confined within one cell. Therefore, we keep N_{cell} cut constant at $N_{cell} > 1$ and vary the E_{dep} cut. Fig. 4.11 shows that by increasing the E_{dep} cut from $0 \times E_{dep}$ to $6 \times E_{dep}$, the efficiency, defined as: the ratio of the number of true photon clusters detected above the hadron discrimination threshold to the number of incident photons, decreases from a maximum of 60% to 35%, whereas, the purity, defined as: the ratio of the number of true photon clusters detected to the number of γ -like clusters, increases from a minimum of 35% to 58%. We select an appropriate E_{dep} cut where both efficiency and purity of the detector are equal. Fig. 4.11 shows the cross over between efficiency and purity occurs at $3 \times MIP$ i.e, 3 times the average energy deposited by a minimum ionizing particle, while the number of cells cut is kept constant at $N_{cell} > 1$. Hence, for the rest of the analysis discussed in the present and the subsequent chapter, the clusters with $N_{cell} > 1$ and energy deposition $> 3 \times MIP$ are termed as γ -like clusters.

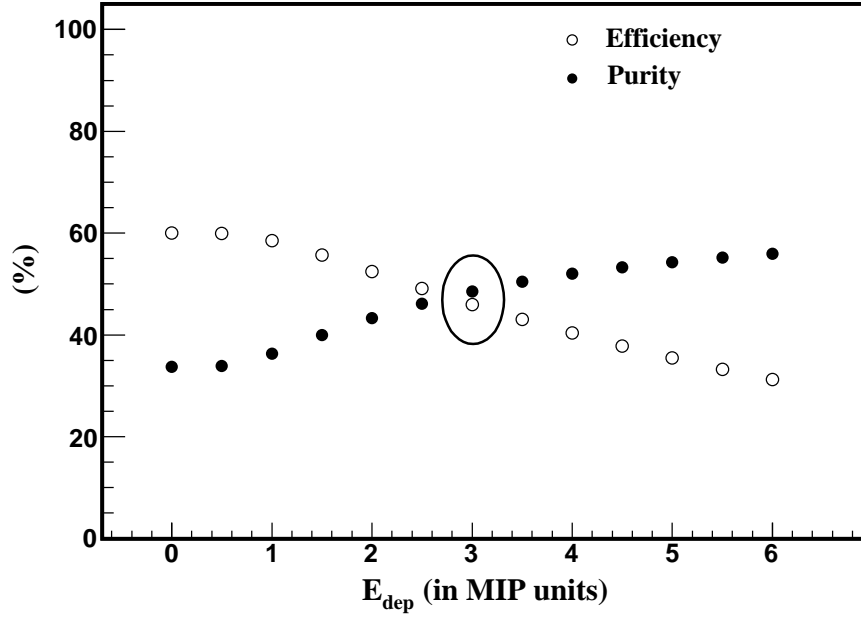


Figure 4.11: Photon counting efficiency (ϵ_γ) and purity of photon samples (f_p) for various E_{dep} cuts on the detected clusters from simulation.

4.8 Effect of Upstream Material

The effect of upstream material is described in terms of deviation of incoming photons from their original tracks. The most important effect of upstream material is on the conversion and scattering of photons because of which they hit the detector with a large deflection. This also affects the efficiency and purity. Ideally, a cluster should have the same η and ϕ position or X or Y position as of its parent track. As a result, the difference between η or ϕ of a cluster from its corresponding parent track's η or ϕ should be zero. Besides this, there could be other reasons, for example, limitations in the clustering algorithm and finite position resolution of the detector. In order to have an estimate of the effect of the upstream material, we carried out studies (a) for the PMD present alone in the cave, and (b) the PMD with all other detectors in the STAR experiment. Fig. 4.12 displays the distribution of $\delta\eta (= \eta_{cluster} - \eta_{track})$ and $\delta\phi (= \phi_{cluster} - \phi_{track})$ for the PMD alone and for the PMD in presence of all upstream material. Here η_{track} and ϕ_{track} stand for the original value of the track resulting in a cluster at a position denoted by $\eta_{cluster}$ and $\phi_{cluster}$ on the detector plane. For the case of full STAR simulation, a large number of photons appear on the PMD after scattering from various upstream materials.

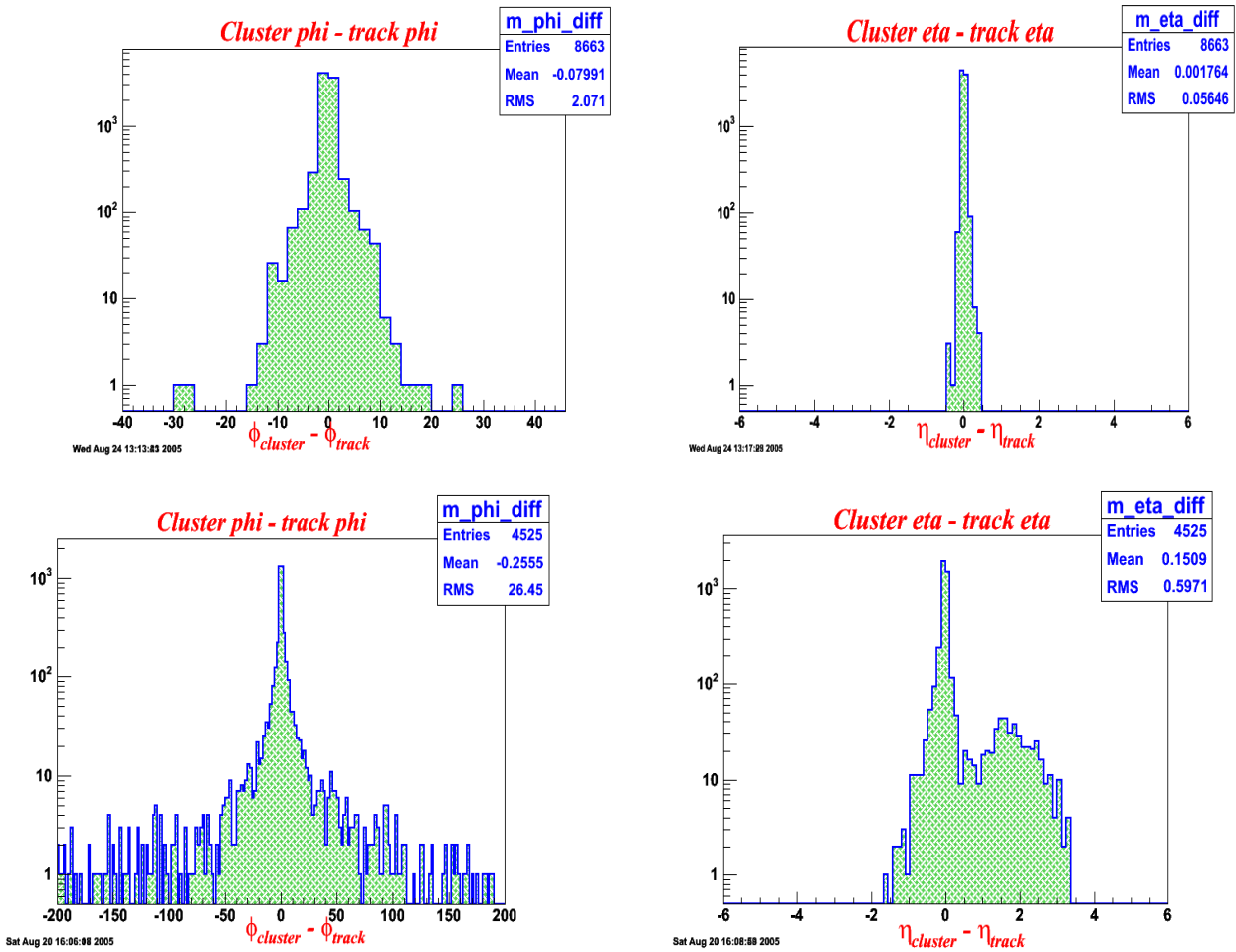


Figure 4.12: Distributions of the azimuthal angles' difference of the cluster and its incident track (left) and the distribution of difference of their pseudorapidities (right). Top panel is for the PMD alone, whereas, the bottom panel is for the PMD along with all other sub detectors in the STAR experiment.

4.9 Photon Counting Efficiency

The clusters which remain above the hadron rejection threshold are termed as γ - like clusters. A majority of these clusters correspond to photons with some fraction of hadrons present as contaminants:

- They originate from an incident particle other than photon.
- There is more than one cluster of photon track because of upstream material or splitting of cluster at the boundary of a supermodule. In such a case, the cluster with higher signal is treated as a photon cluster and the other one is treated as a contaminant.
- Clusters which have $\delta\eta > 0.1$ or $\delta\phi > 20^\circ$. Such a condition takes care of large scattering angles.

The photon counting efficiency, (ϵ_γ), is defined as:

$$\epsilon_\gamma = \frac{N_{cls}^{\gamma,th}}{N_{inc}^\gamma} \quad (4.1)$$

Where :

- N_{inc}^γ : Number of incident photons from the event generator.
- $N_{cls}^{\gamma,th}$: Number of photon clusters above the hadron rejection threshold.

However, the efficiency and purity depend on various other parameters, such as, the conversion probability and the hadron rejection criteria applied. These, in turn, depend on centrality and pseudo-rapidity because of change in particle multiplicity and energy. Fig. 4.13 shows the photon counting efficiency for two centralities, 0-10% (most central) and 40-50% (most peripheral). Statistical errors are of the order of 1%. The efficiency varies from 35% for $\eta = -2.4$ to 55% for $\eta = -3.6$. We also observe that the efficiency remains constant with respect to the collision centrality.

4.10 Purity of Photon Samples

The purity of the photon samples is defined as:

$$f_p = \frac{N_{cls}^{\gamma,th}}{N_{\gamma-like}} \quad (4.2)$$

Where :

- $N_{cls}^{\gamma,th}$: Number of incident photons from the event generator.

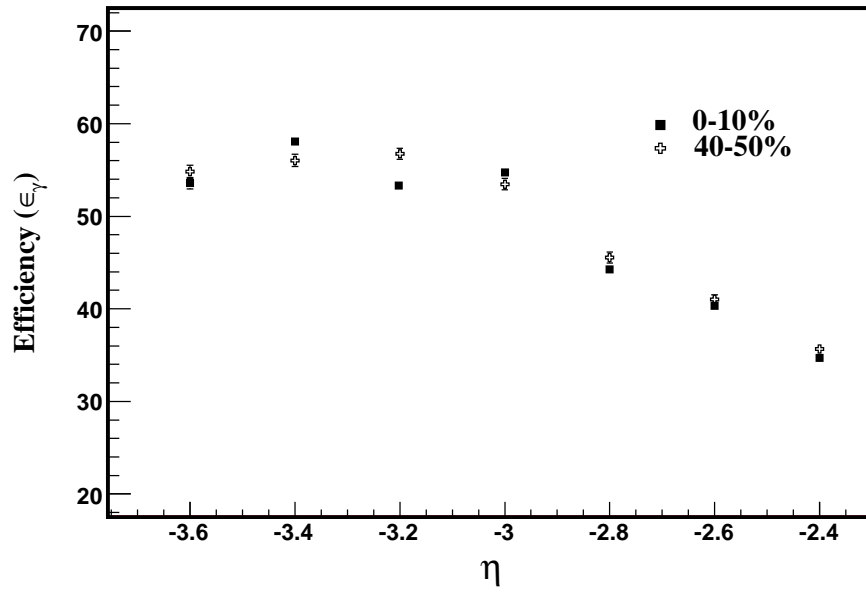


Figure 4.13: Photon counting efficiency for 0-10% (most central) and 40-50% (peripheral) centralities.

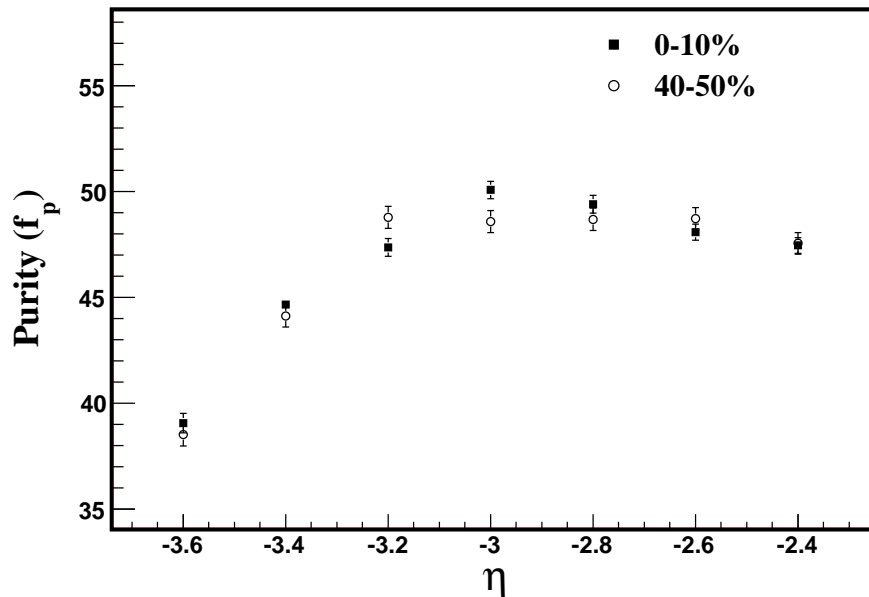


Figure 4.14: Purity in photon samples for 0-10% (most central) and 40-50% (peripheral) centralities.

- $N_{\gamma\text{-like}}$: Total number of clusters above the hadron rejection threshold.

The purity in the photon samples varies from 38% at $\eta = -3.6$ to 47% for $\eta = -2.4$ as shown in Fig. 4.14. We observe that purity does not vary appreciably with collision centrality. The efficiency and purity thus obtained are used to evaluate the number of photons produced (N_{γ}^{est}) as:

$$N_{\gamma}^{est} = \frac{N_{\gamma\text{-like}} \times f_p \times \text{Acceptance factor}}{\epsilon_{\gamma}} \quad (4.3)$$

4.11 PMD Acceptance Factors

Fig. 4.15(a) shows the azimuthal angle distribution of all clusters (without any threshold) in the PMD. In principle, the azimuthal angle distribution of these clusters is expected to be flat since the PMD has a full azimuthal coverage at forward rapidity. However, there are valleys present in the distribution. These valleys are caused by dead cells and defective super-modules. The large valley at -1 radians in the azimuthal angle distribution appears because SM 23 is not included in the analysis. Infact, only those super-modules which were operated at the same voltage during Run V are included in the present analysis. SM 23 which consists of 9 unit modules was operated at -1300 V during the data taking. The test beam analysis have revealed that the gain of each cell is optimum at ~ -1400 V. As a result SM 23 has low gain. Besides SM 23, we also removed five other super-modules during the analysis of this data as they had very low gain. The super-modules used in the present analysis were SM # 12, 14, 16, 18, 20 and 21. The super-module numbering scheme used here is 0-23, i.e., 0-11 super-modules belong to the CPV plane and 12-23 belong to the PMD plane. Thus, acceptance factors are calculated to correct for any dead area in the detector.

Fig 4.15(b) shows the uncorrected pseudo-rapidity distribution of the clusters. The valley seen at $\eta = -2.8$ in the distribution exists because of the super-module boundary at that rapidity. In order to clearly show the super-module boundary, 2D hits display of the PMD is again shown with a boundary drawn in red color. At this pseudo-rapidity two super-modules combine together make a considerable amount of dead space in the PMD.

The large dip structures present in the azimuthal and uncorrected pseudo-rapidity distributions, as seen previously, make acceptance factors calculation important for this analysis. We define acceptance factors as :

$$\begin{aligned} \text{Acceptance factor} &= \frac{\text{Total number of cells within a pseudorapidity bin}}{\text{Total number of active cells}} \\ &= \frac{N^{TOT}(\eta)}{N^{LIVE}(\eta)} \end{aligned} \quad (4.4)$$

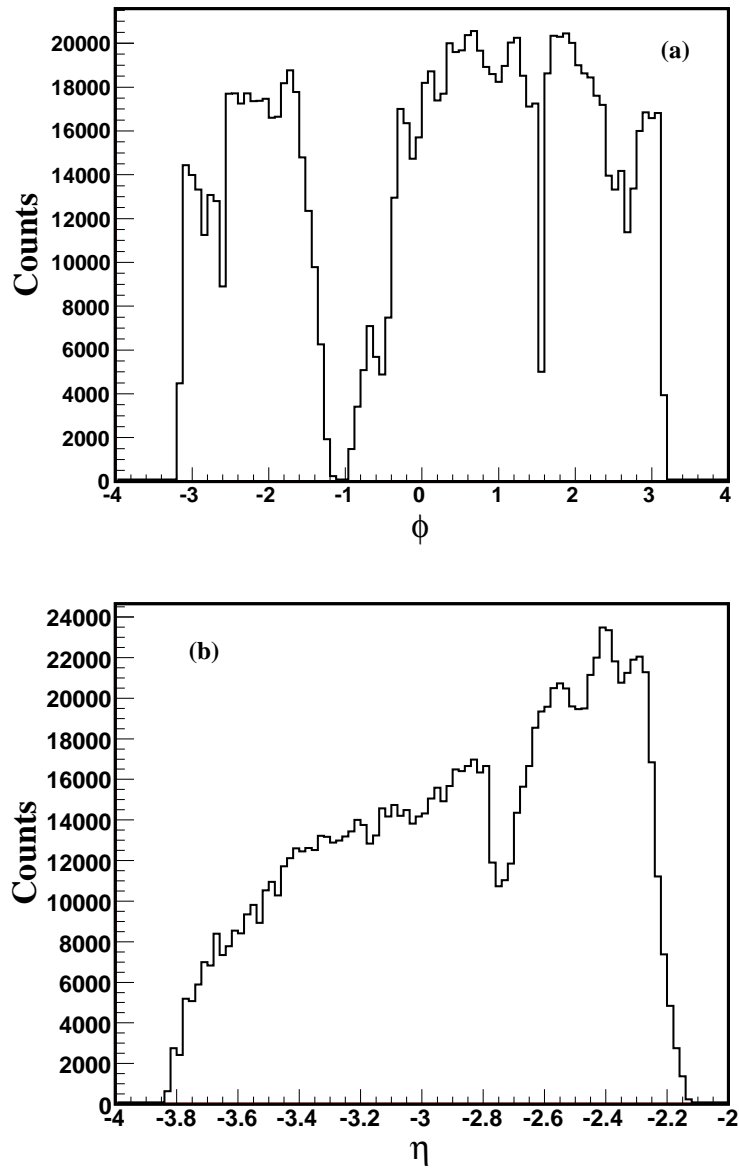


Figure 4.15: (a) Azimuthal angle distribution of all the clusters in the PMD. (b) Uncorrected pseudo-rapidity distribution of all the clusters in the PMD. Note that the dip near $\eta = -2.8$ is due to SM boundary.

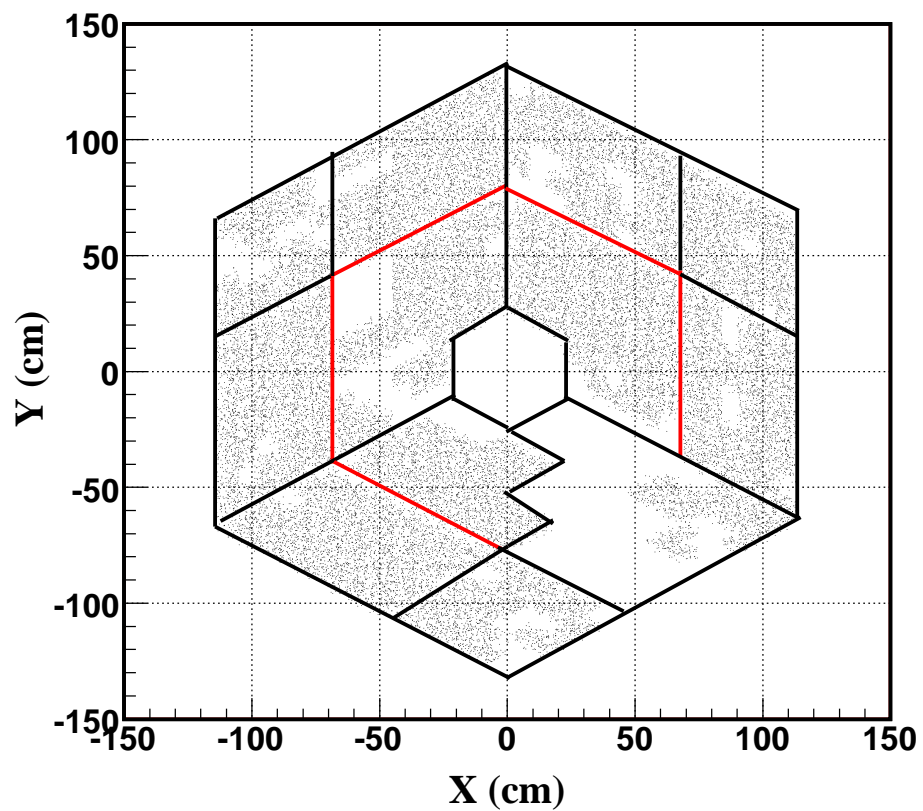


Figure 4.16: Few events 2D hits display of the PMD with a red boundary at $\eta = -2.8$, showing dead area because of the super-modules boundary.

Fig. 4.17 shows the acceptance correction factors obtained for the seven pseudo-rapidity

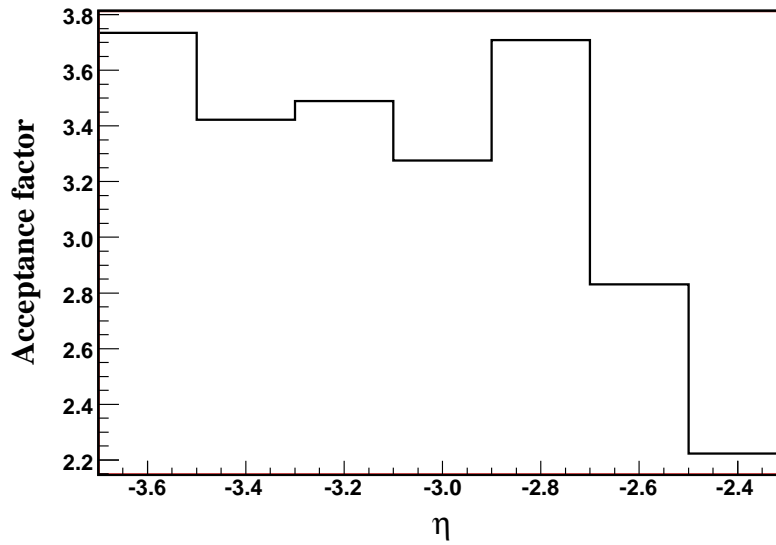


Figure 4.17: Acceptance correction factors for various pseudo-rapidity bins in the PMD coverage.

bins used in the analysis.

4.11.1 Consistency Checks

Once the efficiency and purity factors are obtained, it is imperative to do a sanity check, i.e, to verify if we get back the actual number of incident photons in the pseudo-rapidity range studied from HIJING in the stand alone mode. This is done in the following way :

- We get the pseudo-rapidity distribution of photons from HIJING within the PMD coverage for three centrality classes, 0-10%, 10-20% and 20-30%.
- Efficiency, purity and acceptance factors are applied to the $\gamma - like$ photon clusters obtained from HIJING+GEANT simulation. Figs. 4.18, 4.19, 4.20 show raw $\gamma - like$ photon yield, incident photons from HIJING only and HIJING+GEANT simulated data corrected for efficiency, purity and acceptance factors for three different centrality classes.

We observe that, within statistical uncertainty, the HIJING photon spectrum for photons in the stand alone mode agrees well with the $\gamma - like$ clusters corrected for efficiency, purity and acceptance factors obtained from HIJING+GEANT simulation.

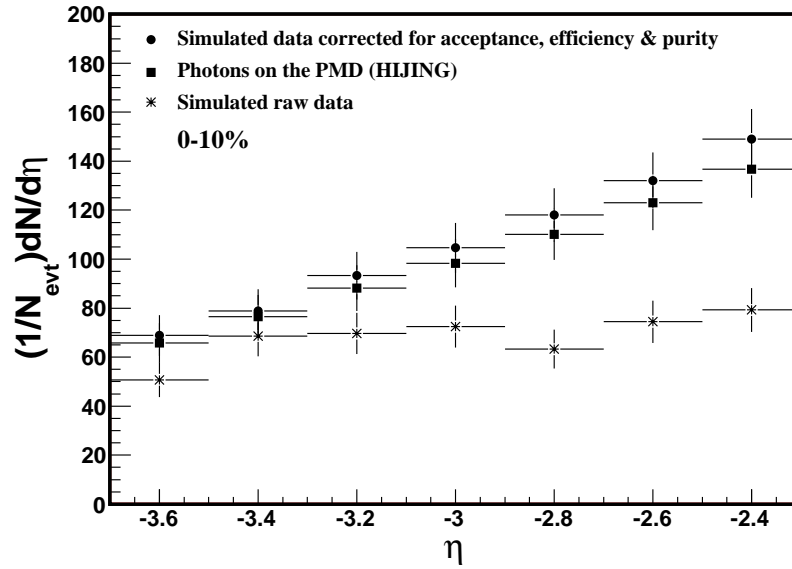


Figure 4.18: Comparison of raw yield, simulated data (corrected for efficiency, purity, acceptance factors) with incident photons from HIJING only for 0-10% centrality.

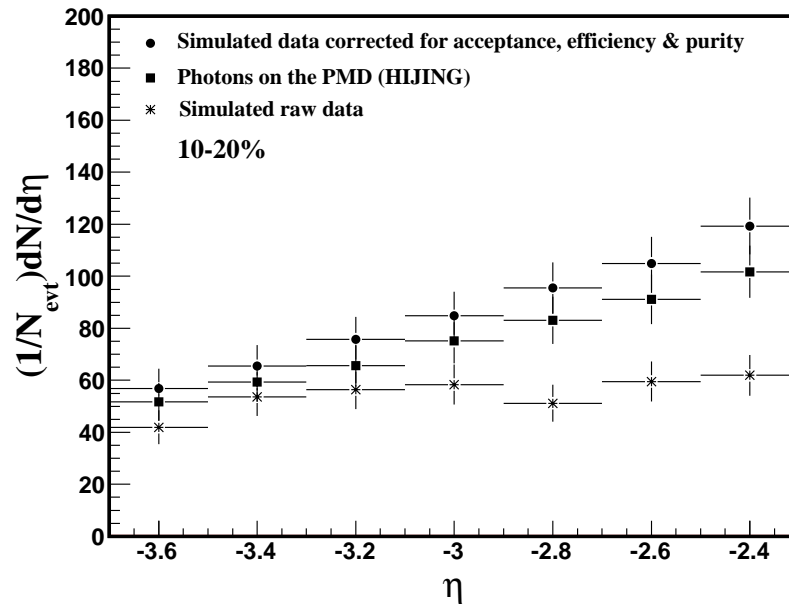


Figure 4.19: Comparison of raw yield, simulated data (corrected for efficiency, purity, acceptance factors) with incident photons from HIJING only for 10-20% centrality.

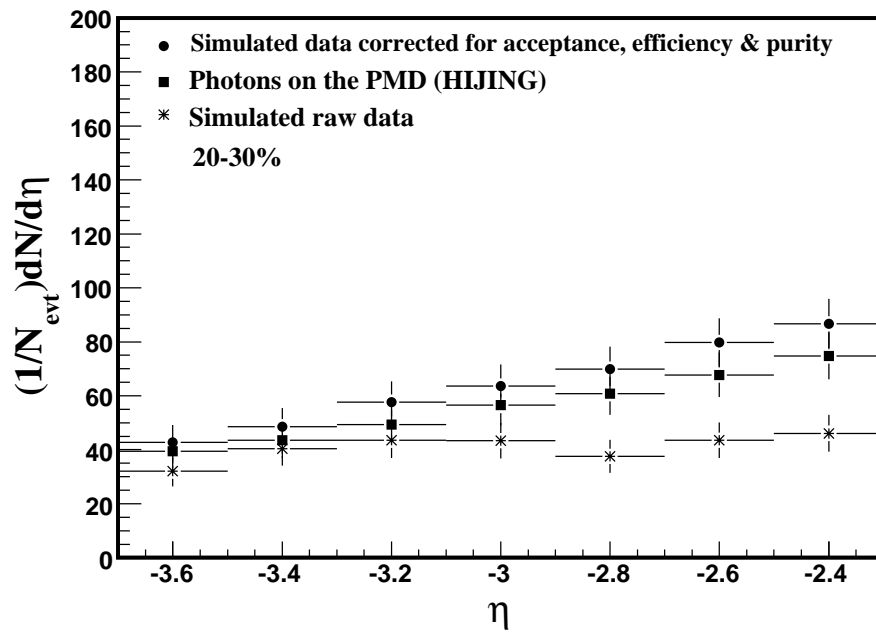


Figure 4.20: Comparison of raw yield, simulated data (corrected for efficiency, purity, acceptance factors) with incident photons from HIJING only for 20-30% centrality.

Bibliography

- [1] X.N. Wang and M. Gyulassy, Phys. Rev. D **44** (1991) 3501.
- [2] V. Fine and P. Nevski, in proceedings of CHEP-2000, Padova, Italy.
- [3] Particle Data Group, C. Caso *et al.*, Eur. J. Phys. C **3** (1998) 1.

Chapter 5

Data Analysis of the PMD

This chapter presents the measurements of photon multiplicity and rapidity distribution in Cu+Cu collisions at 200 GeV center of mass energy. The measurements were carried out with the STAR Photon Multiplicity Detector (PMD) during Run-V, 2005. The PMD data were analyzed from “P05id” STAR production.

5.1 Data Selection

The data were selected through the following steps :

1. **Trigger selection** : The data were acquired with minimum bias triggers accomplished by requiring a coincidence signal from two Zero Degree Calorimeters (ZDCs) located at 18 m from the center of the interaction region on either sides of the STAR detector and using the charged particle hits from an array of scintillator slats arranged in a barrel, called the Central Trigger Barrel, surrounding the TPC. Trigger was selected with a minimum of at least 17 hits on the CTB. Details of trigger in STAR experiment are described in chapter 2.
2. **Centrality selection** : This analysis uses the standard collision centrality as defined by STAR on the basis of the uncorrected multiplicity of charged particle tracks measured within the TPC in the pseudo-rapidity range $-0.5 < \eta < 0.5$ [1]. The pseudo-rapidity range $-0.5 < \eta < 0.5$ was used rather than the full range $-1.0 < \eta < 1.0$, in principle measurable with the TPC, to minimize the effects of detector acceptance and efficiency on the collision centrality determination. The centrality bins were calculated as a fraction of this multiplicity distribution starting at the highest multiplicities. The ranges used in $Cu + Cu$ collisions at $\sqrt{s_{NN}} = 200$ GeV were 0-10% (most central collisions), 10-20%, 20-30%, 30-40%, 40-50% and 50-60% (most peripheral collisions studied). More peripheral collisions yield low multiplicity and centrality selection is not reliable for 60-100%. We, therefore, have studied only six centralities in $Cu + Cu$ collisions at the center of mass

energy of 200 GeV. Fig. 5.1 shows the centrality selection from minimum bias uncorrected charged particle distribution in $Cu + Cu$ collisions at $\sqrt{s_{NN}} = 200$ GeV. With the narrow cut $-0.5 < \eta < 0.5$, the detection efficiency is rather insensitive to the position of the collision vertex along the beam direction.

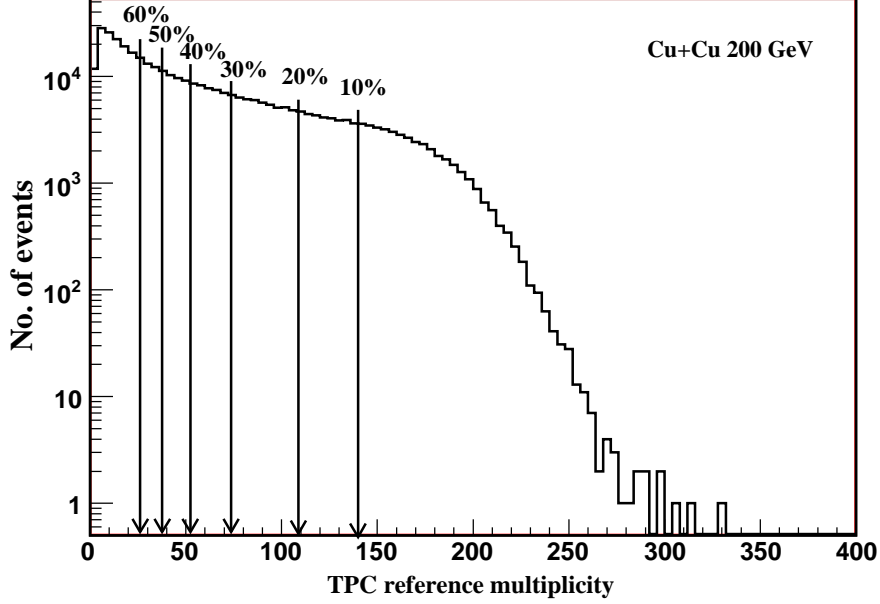


Figure 5.1: The TPC track multiplicity within $-0.5 < \eta < 0.5$ from data for $Cu + Cu$ collisions at $\sqrt{s_{NN}} = 200$ GeV. Collision centralities or % of cross-section are shown with the arrows in the plot.

Each centrality bin is associated with the average number of participating nucleons, N_{part} , and number of binary collisions, N_{coll} , obtained from Glauber Monte Carlo calculations using Woods-Saxon distribution for the nucleons inside the Cu nucleus. The systematic uncertainties on N_{part} and N_{coll} are determined by varying the Woods-Saxon parameters. Table 5.1 lists the percentage of cross-section, the corresponding uncorrected charged particle multiplicity (N_{ch}) in the pseudo-rapidity region $-0.5 < \eta < 0.5$, the number of participating nucleons (N_{part}), and the number of binary collisions (N_{coll}) for $Cu + Cu$ collisions at $\sqrt{s_{NN}} = 200$ GeV, used in the STAR-PMD analysis.

3. **PMD Data selection :** The analysis of only the preshower plane is presented in this chapter. The PMD data were sorted into three categories based on the number of chains working during the data acquisition. More details about the chains are listed in chapter 3. The categories were :

- (a) **Category I :** All chains working on the preshower plane.

Table 5.1: The percentage of cross-section, number of uncorrected charged particle multiplicity from the TPC within pseudo-rapidity $-0.5 < \eta < 0.5$, number of participating nucleons, N_{part} , and number of binary collisions, N_{coll} , for $Cu + Cu$ collisions at $\sqrt{s_{NN}} = 200$ GeV.

% Cross-section	N_{ch}	$\langle N_{part} \rangle$	$\langle N_{coll} \rangle$
0-10%	>140	$98.34_{-1.1}^{+1.1}$	$185.64_{-6.1}^{+5.6}$
10-20%	103-140	$74.47_{-2.1}^{+2.4}$	$125.92_{-6.8}^{+6.6}$
20-30%	74-103	$54.0_{-2.5}^{+2.8}$	$80.95_{-5.8}^{+6.9}$
30-40%	53-74	$38.56_{-2.4}^{+2.7}$	$51.07_{-4.7}^{+5.6}$
40-50%	37-53	$26.29_{-2.3}^{+3.0}$	$30.61_{-3.8}^{+3.9}$
50-60%	25-37	$17.61_{-2.6}^{+3.1}$	$18.16_{-3.5}^{+3.4}$

(b) **Category II** : One chain not working on the preshower plane.

(c) **Category III** : More than one chain not working on the preshower plane.

The results discussed in this chapter are from category I data-set.

5.2 Data Cleanup

The PMD Data needs to be filtered or cleaned up to eliminate hot and noisy channels. The channels which have abnormally high frequency of firing, i.e., more than 10 times the average frequency of firing during the data taking are termed as hot channels. Whereas, channels which have random low ADC hit are termed as noisy channels.

The following steps were involved in the identification and removal of hot channels.

- Find the frequency of channels hit for each chain for a large number of events.
- Calculate the mean and RMS for this channel frequency distribution and remove the channel if the hit frequency deviates by more than five standard deviations from the mean. Fig. 5.2 shows channel frequency distribution before data cleanup. The red circle points out hot channels in a chain which have extremely low ADC values shown in Fig. 5.3.
- Besides removing hot channels, a 10 ADC cut is also applied in order to remove noise which is present because of the pedestal width of the signal as shown in Fig. 5.4.

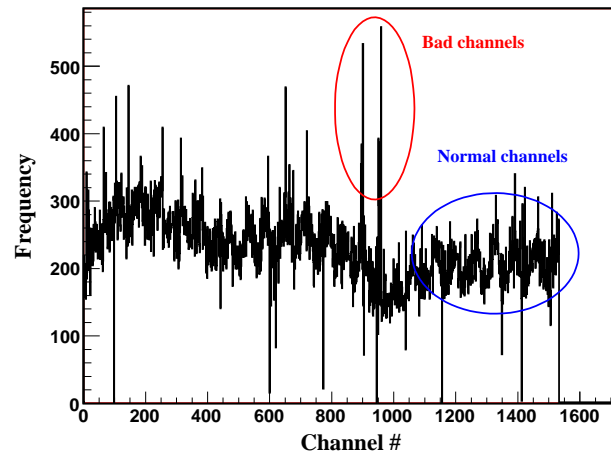


Figure 5.2: Raw channel frequency distribution of chain 23.

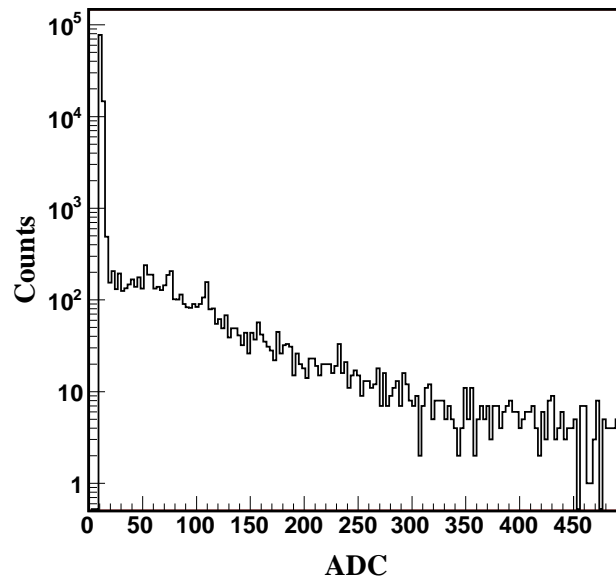


Figure 5.3: ADC distribution of hot channels.

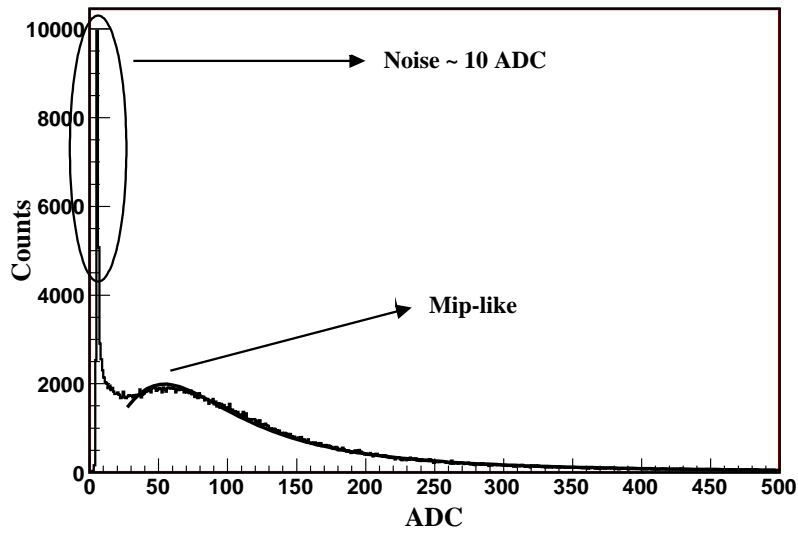


Figure 5.4: Typical raw chain ADC distribution.

5.3 Hit Level Information

In order to have data quality assessment, we studied the behavior of super-modules (SM), row, column, chain, channels and cells at the hit level. Figs. 5.5(a) - (f) show hit level characteristics of cell, chain, channel, column, row, and SM, respectively. Fig. 5.5(a) displays cell ADC distribution which shows saturation beyond 3000 ADC value. Fig. 5.5(b) shows chain frequency distribution of chains used in the pre-shower plane. Chains 31, 33, 45 and 47 show a large number of channels firing abnormally high as compared to other channels. Fig. 5.5(c) displays channel frequency distribution. One hot channel is pointed out with a circle in the figure. Fig. 5.5(d) displays column frequency distribution. Fig. 5.5(e) and (f) show row and SM frequency distribution, respectively. The presence of hot channels in the data leads to an odd shaped minimum bias hits distribution on the PMD as shown in Fig. 5.6(a). Fig. 5.6(b) shows correlation between total hit ADC and total number of hits on the PMD. This plot clearly shows more than one correlation band, suggesting that the PMD data needs to be cleaned first before one attempts to extract physics. Fig. 5.6(c) shows average ADC per hit distribution which is a Gaussian distribution, as expected. However, there is a shoulder in the figure on the left side. Thus, after adopting the data cleanup procedure explained previously in this chapter we next show global features of cleaned data to ensure the data are ready for further analysis.

5.4 Data After Cleanup

Fig. 5.7 shows total hits distribution of preshower plane after data cleanup. Channel frequency distribution of chain 32 before and after cleanup are shown in Figs. 5.8 and

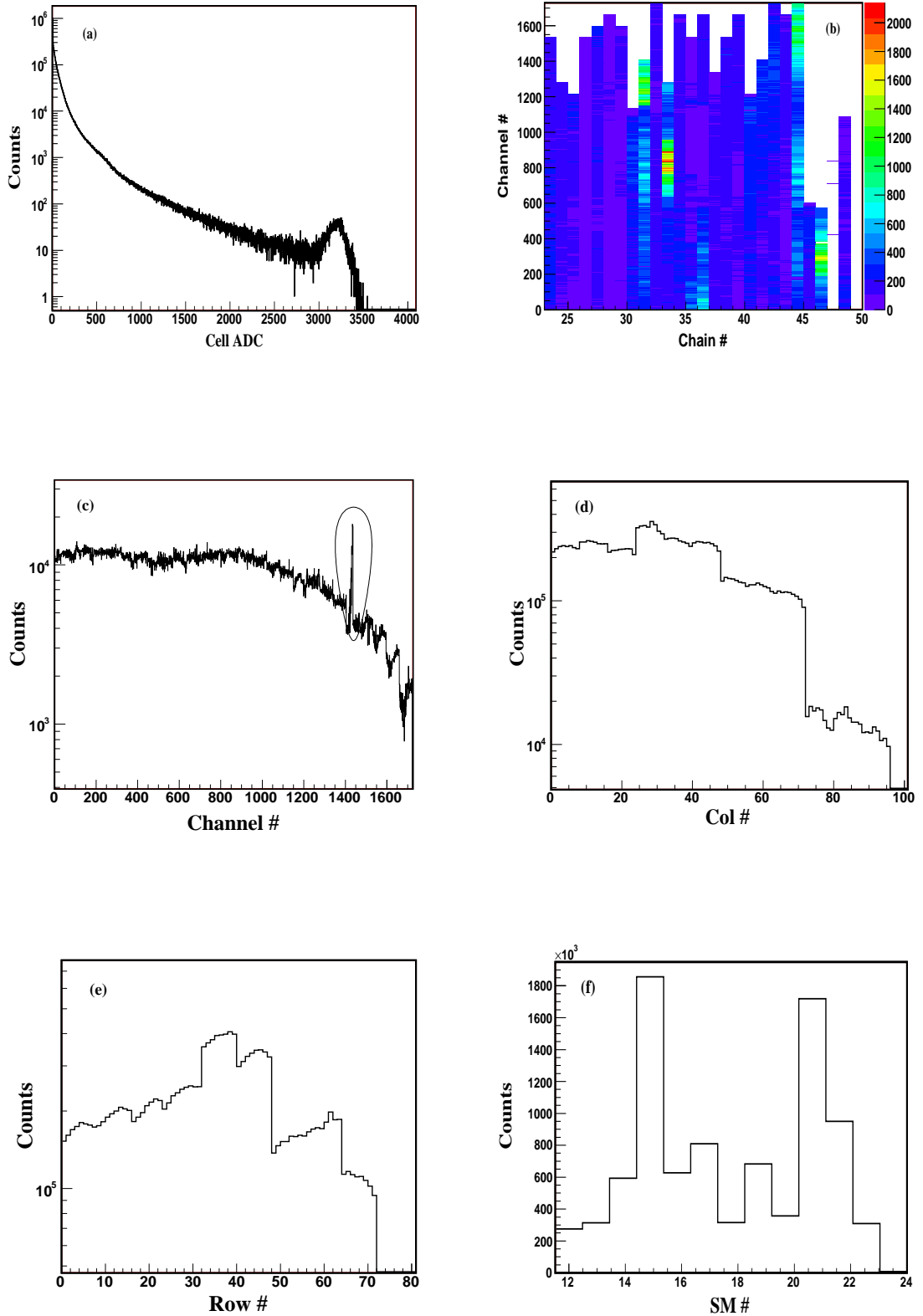


Figure 5.5: Hit level characteristics of (a) cell, (b) chain, showing abnormal firing of many chains, (c) channel, showing a hot channel, (d) column (e) row, and (f) super-module.

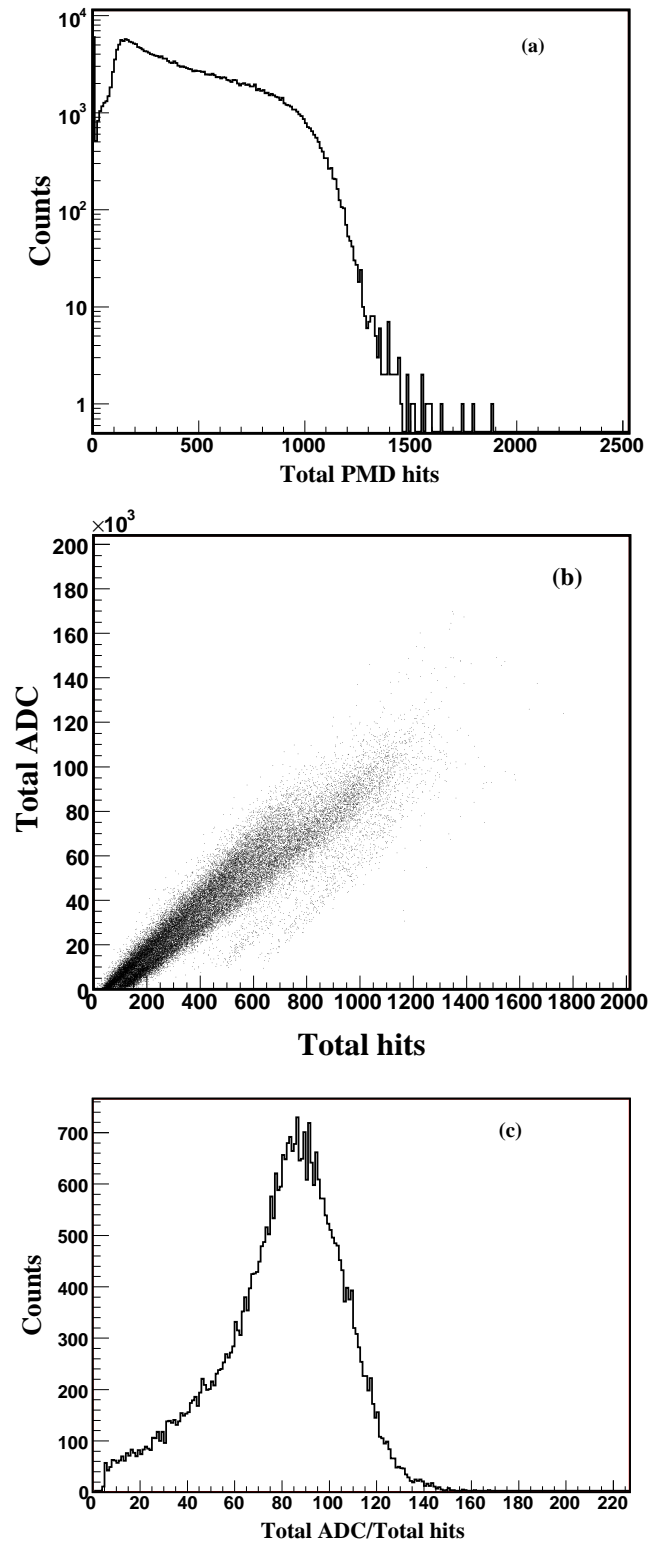


Figure 5.6: (a) Minimum bias total PMD hits distribution, (b) correlation between total hit ADC and total PMD hits, (c) Average ADC per hit distribution.

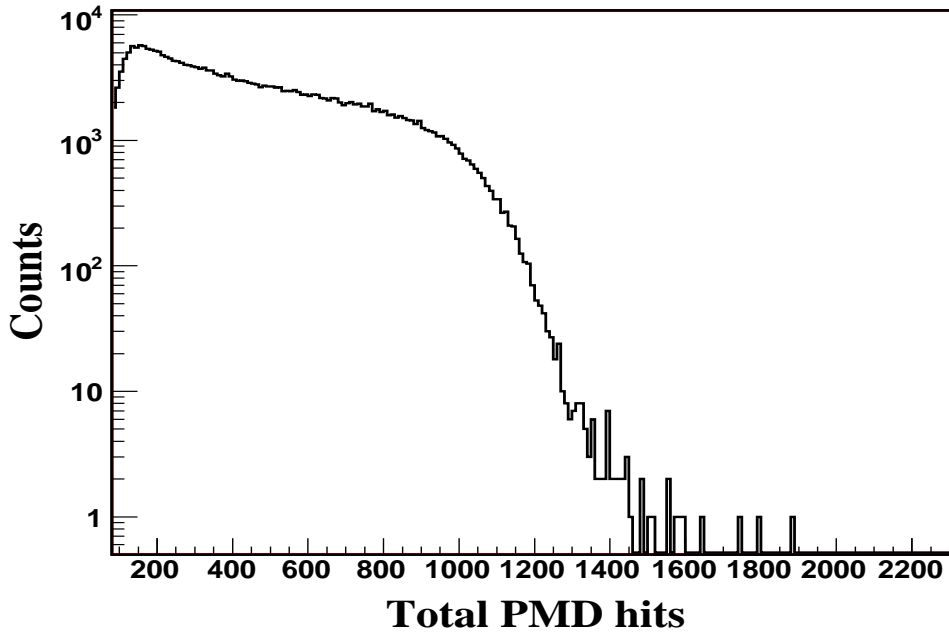


Figure 5.7: Total PMD hits distribution after cleanup.

5.9, respectively. It clearly shows that channels with frequency larger than $5 \times \text{RMS}$ from the mean of the distribution are removed. Figs. 5.10(a) - (f) display global features for cell, chain, channels, column, row and SM, respectively, after data cleanup. Fig. 5.10(a) shows cell ADC distribution after cleanup. The saturation beyond ADC value of 3000 is still seen. This is because the data acquisition system (DAQ) of the PMD uses 12 bit ADC. Fig. 5.10(b) displays hit frequency of chains 24 - 48. Fig. 5.10(c) shows channel hit frequency. One hot channel seen previously before cleanup is now removed. Fig. 5.10(d) displays column hit frequency. Row and SM hit frequency after cleanup can be seen from Figs. 5.10(e) and (f), respectively.

5.5 Single Cell Response

It is essential to understand the response of each cell because of the following two reasons :

- Response of each cell reflects the gain of a cell.
- To ensure uniformity of response over the entire detector it is important that response of these cells do not vary much in η and ϕ . However, in real life scenario, it is impossible to have a uniform response of the cells over the entire detector. As a result data has to be calibrated first.
- The results of test beam in the previous years have indicated that the charged hadrons deposit signal in a single cell. The energy deposited by charged particles is

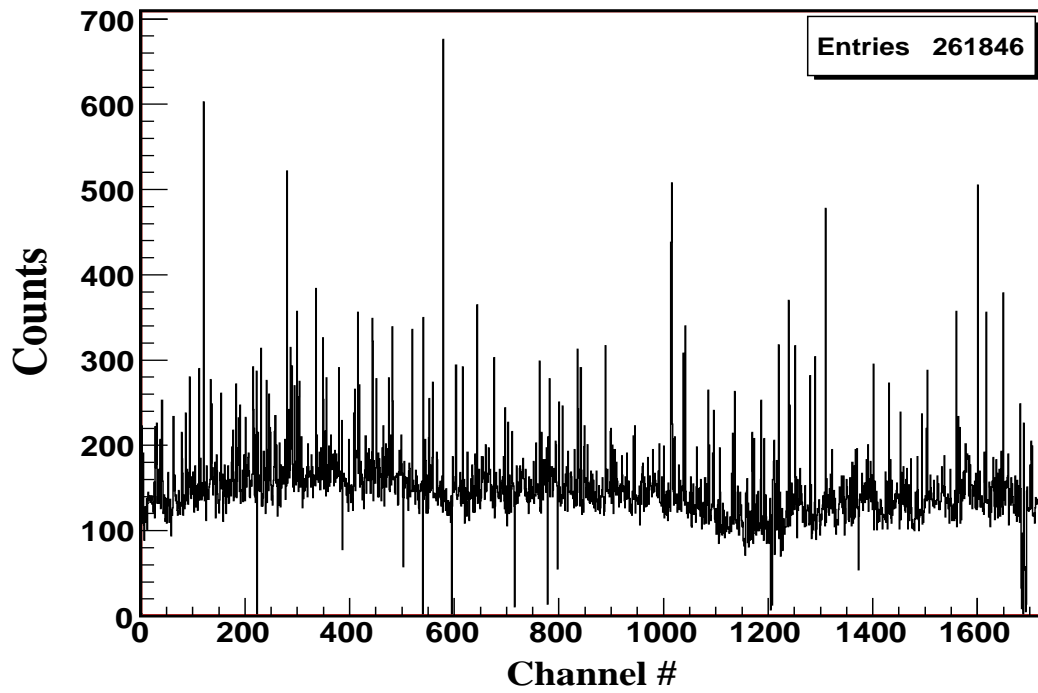


Figure 5.8: Raw channel frequency distribution of chain 32 (before cleanup).

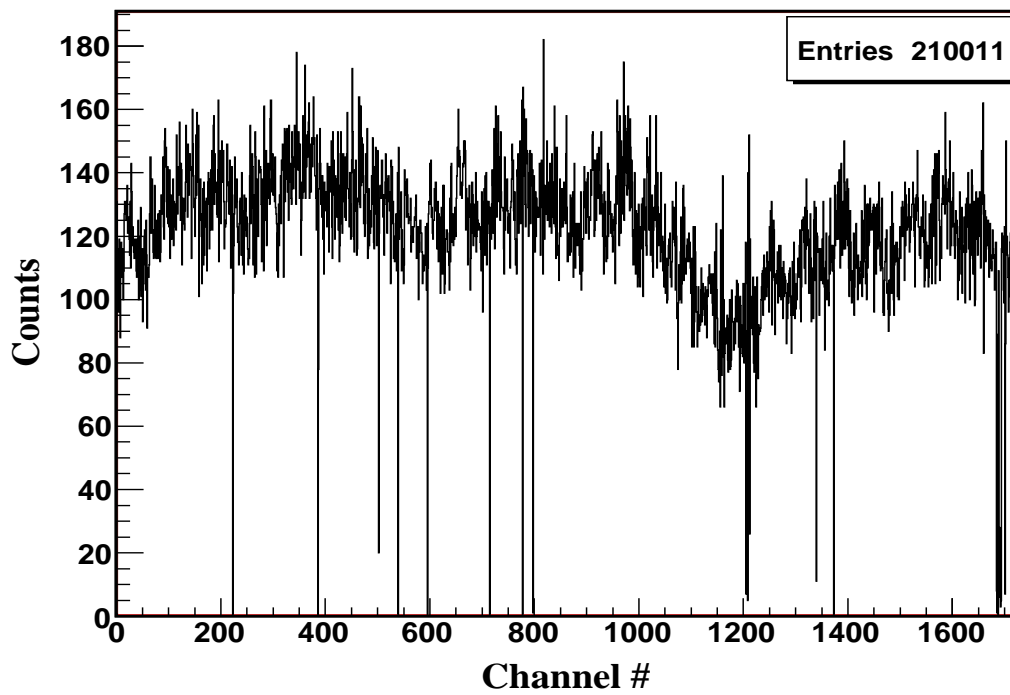


Figure 5.9: Clean channel frequency distribution of chain 32 (after cleanup).

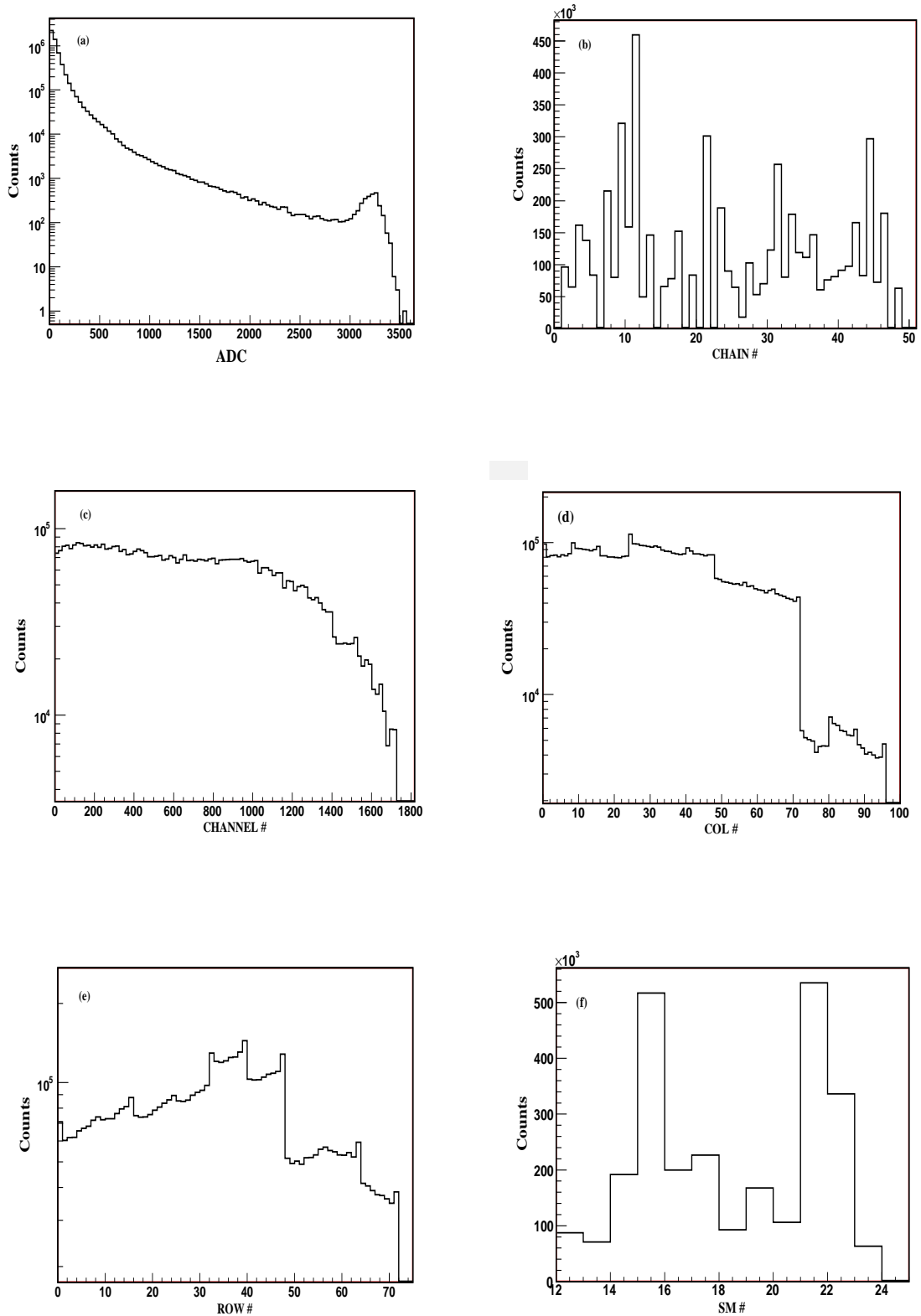


Figure 5.10: Global features after cleanup like (a) cell ADC distribution, (b) chain hit frequency, (c) channel hit frequency, (d) column hit frequency, (e) row hit frequency, (f) super-module hit frequency.

then used to discriminate photons from hadrons and carry out the gain calibration.

Figs. 5.11 and 5.12 show isolated cell spectra of cell numbers 124240 and 173304, respectively. Cell numbers are assigned to a cell based on SM, row and column numbers in every SM. The first two digits represent super-module number, to which a cell belongs, middle two and last two digits represent the row and column number, respectively. The tail seen in Fig. 5.11 is known as Landau tail. Two isolated cell spectra are presented here to show typical examples of a high gain cell and a low gain cell. Typically, a high gain cell will have a well developed Landau with its tail extending up to an ADC value of 500. However, as seen in Fig. 5.12, cell 173304 is a low gain cell with not a fully developed Landau and its tail extending only up to 300 ADC. It is also observed that mean ADC and MPV (most probable value) are linearly related (discussed in the next section). Hence, mean of such cells was used in calibration.

5.6 Calibration of Data

The PMD is comprised of 12 super-modules and overall 41,472 cells. Data from these cells are processed along 24 chains. The cells and chains while in principle designed to have nearly the same gain and response, turns out, in practice exhibit a finite range of gain and response. The data, must therefore, be normalized. As each super-module is a separate gas tight and high voltage entity, calibration, in principle, should be carried out SM wise. However, one SM may contain one or more chains which may behave differently. We thus calibrated the PMD data on the basis of SM and CHAIN combination.

We first find the mean of all isolated cell ADC distribution in a SM and CHAIN combination. We define this mean as global mean. The ratio of the mean of each isolated cell ADC distribution to the global mean is known as the calibration gain factor. All the cells are calibrated by this factor to have uniform response throughout each SM and CHAIN combination. The global means are later used as photon discriminating threshold. Fig. 5.13 shows various features of a SM and CHAIN combination. For instance Fig. 5.13(a) shows Gaussian distribution of mean value of all isolated cells in SM 19 and Chain 38. Fig. 5.13(b) shows the gain distribution of all cells in SM 19, Chain 38. Similarly, Fig. 5.13(c) shows the most probable value of all isolated cells in this SM and CHAIN combination, which is again a Gaussian distribution. Linear correlation between the mean value and most probable value (MPV) is shown in Fig. 5.13 (d). Global means, later on used as the threshold for photon identification for each SM, are shown in Figs. 5.14 and 5.15. Global mean distribution for SM 15 & SM 16 and SM 21, shown in Fig. 5.14(d), Fig. 5.14(e) and Fig. 5.15(d), respectively, exhibit pronounced shoulder beside the main peak. A large number of cells in these SM have very high gain which results in a very large mean value. We do not remove such cells in our analysis as it would affect the

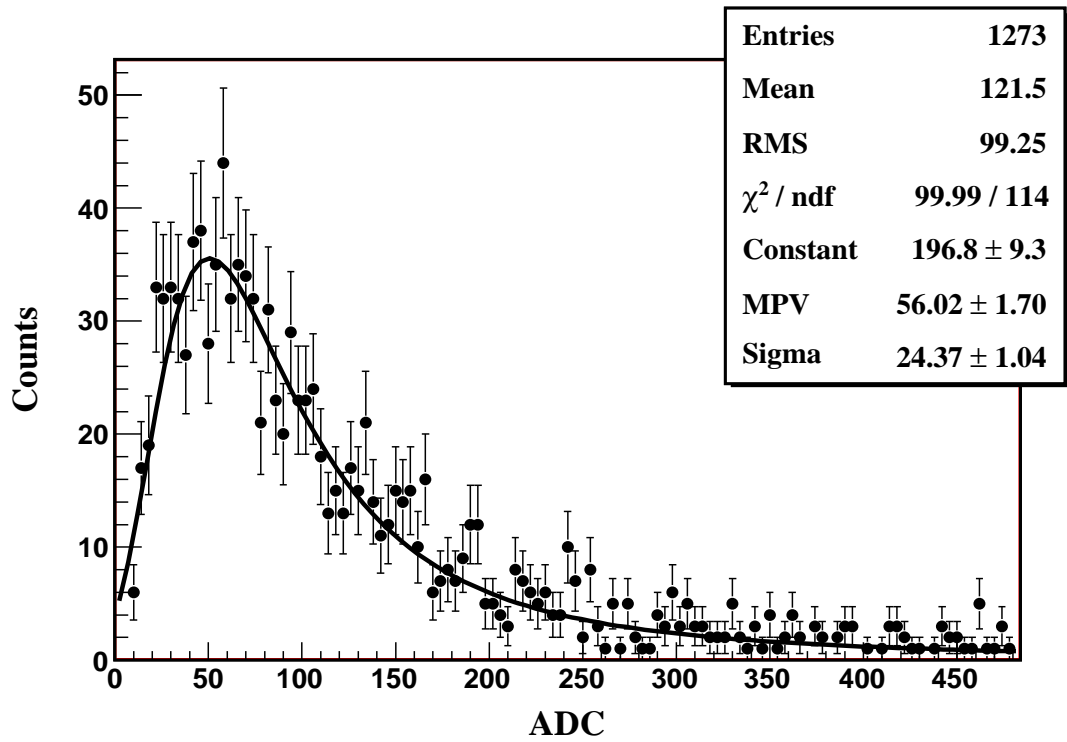


Figure 5.11: Isolated cell ADC distribution of a high gain cell (cell # 124240).

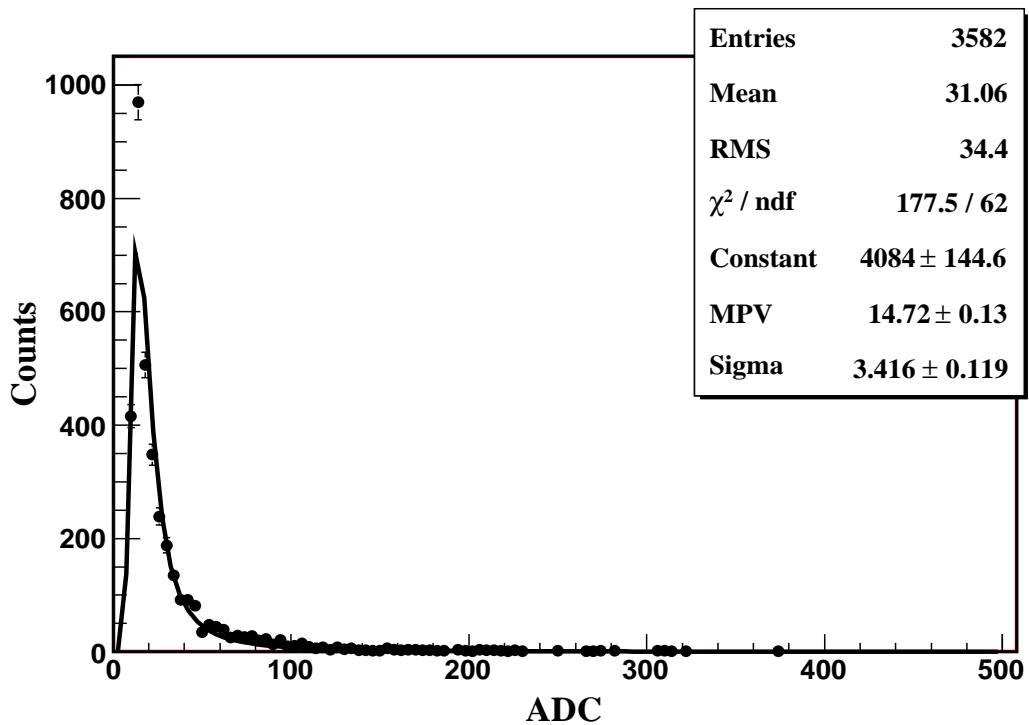


Figure 5.12: Isolated cell ADC distribution of a low gain cell (cell # 173304).

detector acceptance. Also, since large variation of gain is seen from one SM to another, we also changed the E_{dep} in simulation based on the factors obtained in the data while taking SM 12 as a reference. This was done to ensure that simulation has similar gain variation as seen in data.

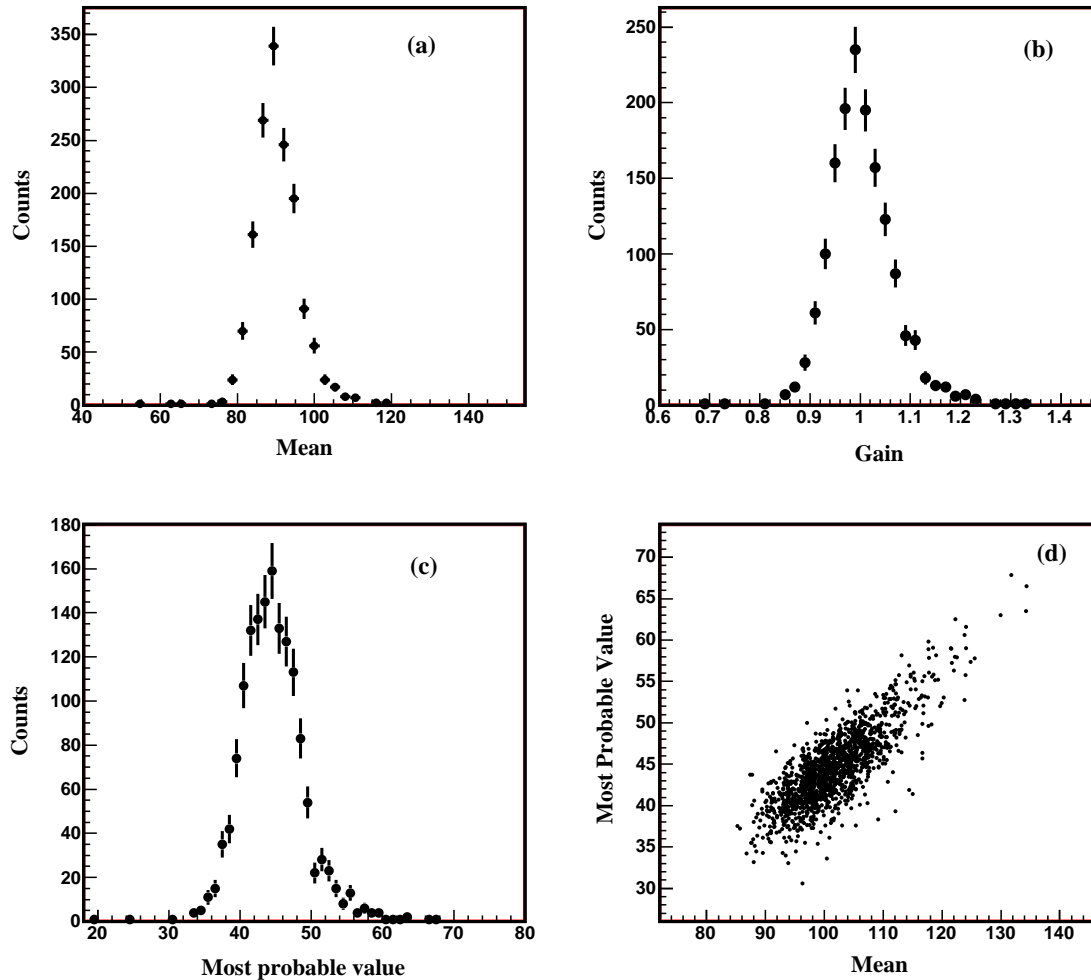


Figure 5.13: (a) Distribution of Mean upto 500 ADC of all isolated cells in SM 19 and chain 38, (b) gain distribution of cells in this combination, (c) MPV distribution of all isolated cell in this combination, (d) correlation between MPV and mean values of isolated cells.

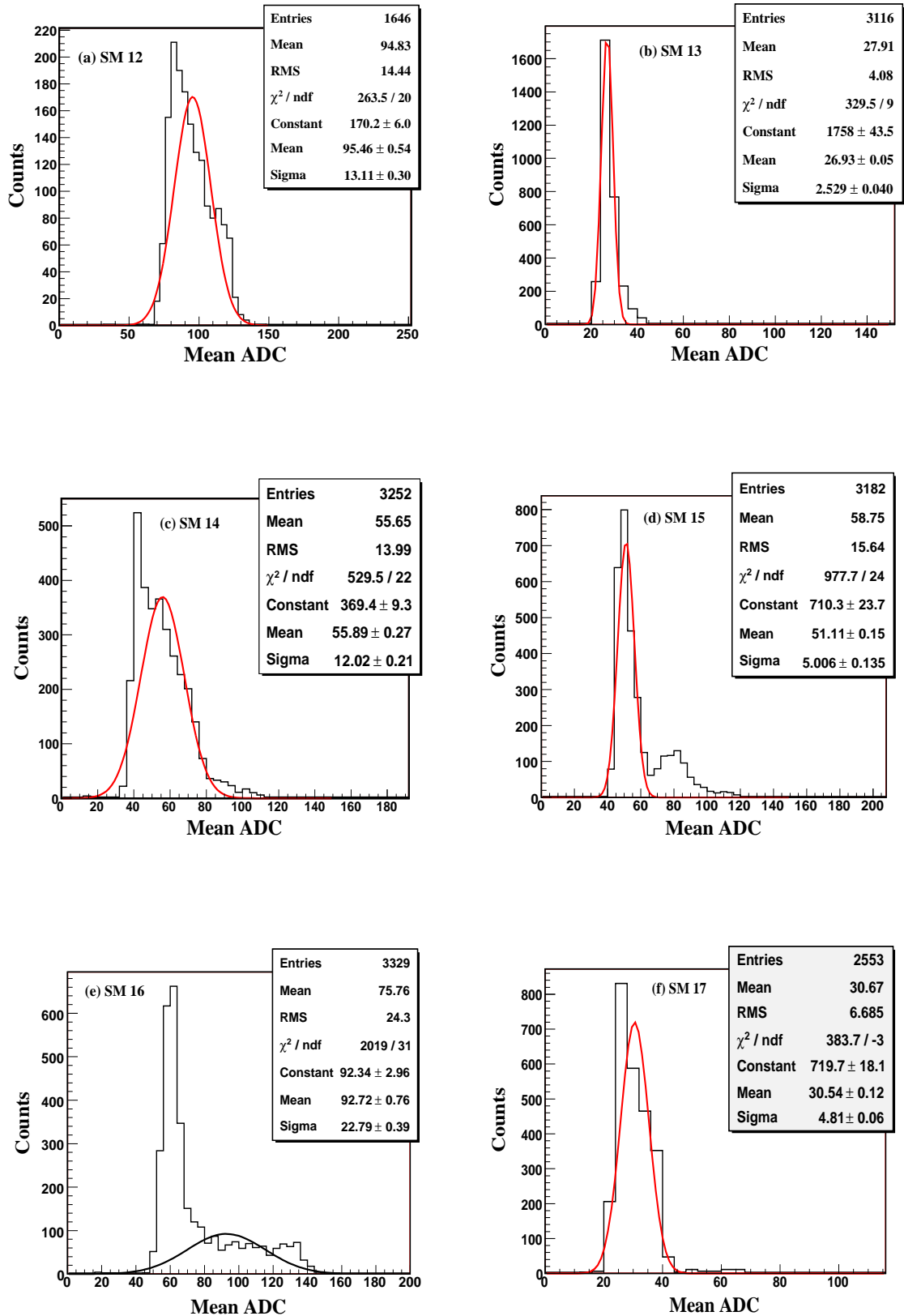


Figure 5.14: Mean value of all isolated cells before calibration in (a) SM 12, (b) SM 13, (c) SM 14, (d) SM 15, (e) SM 16, (f) SM 17.

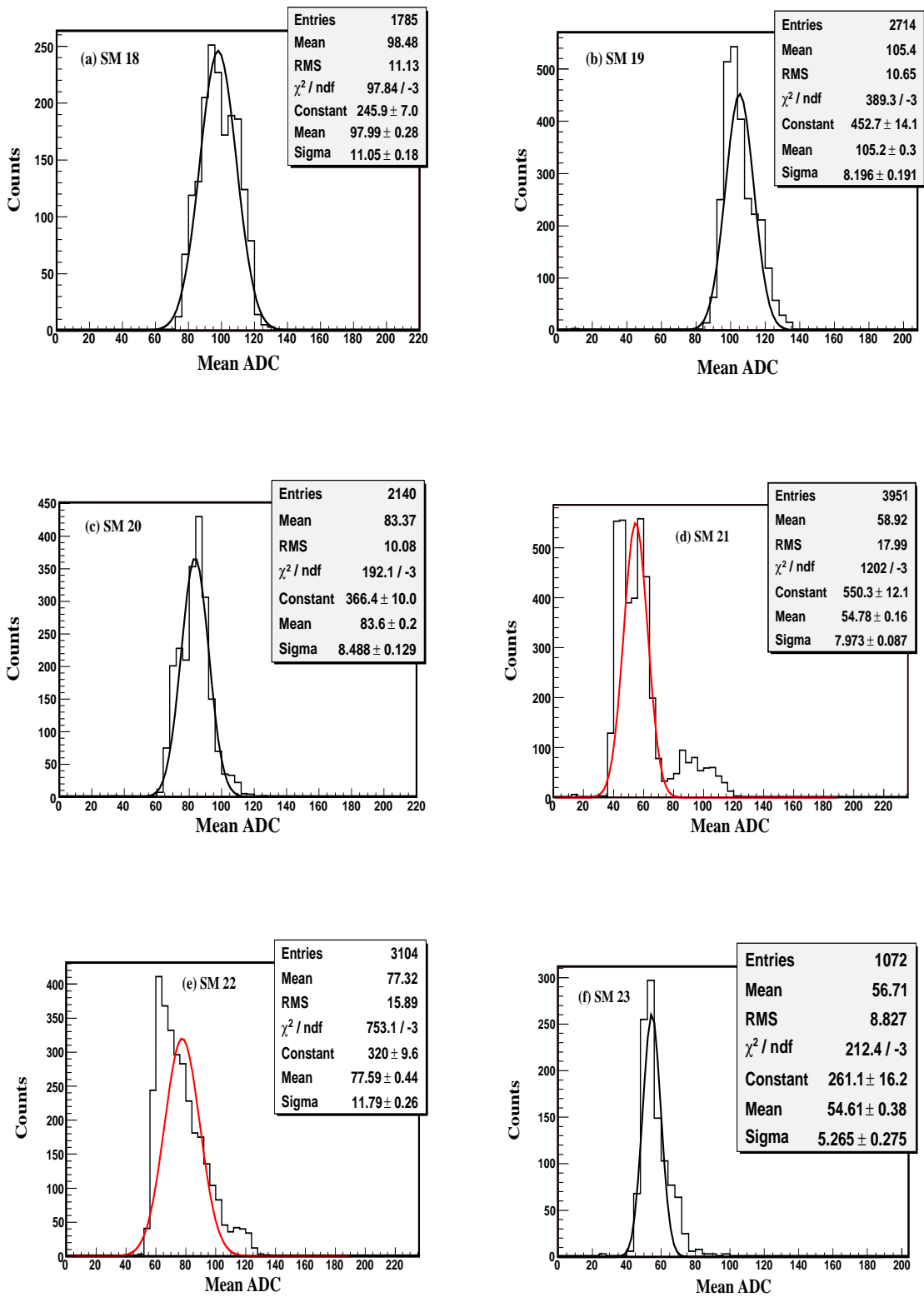


Figure 5.15: Mean value of all isolated cells before calibration in (a) SM 18, (b) SM 19, (c) SM 20, (d) SM 21, (e) SM 22, (f) SM 23.

5.7 Event Generator: (HIJING)

In order to understand heavy ion collisions it is important to compare their results with different models. Unlike heavy ion collisions at AGS(BNL) and SPS(CERN) energies, most of the physical processes occurring at very early times in the violent collisions of heavy nuclei at RHIC(BNL) and the upcoming CERN(LHC) energies involve hard or semihard parton scattering [2]. This will result in enormous amount of jet production and can be described in terms of perturbative QCD (pQCD). Jets are defined as hadronic clusters whose transverse energy (E_T) is reconstructed from calorimeters [3, 4]. However, with decreasing transverse energy of a jet, $E_T < 5$ GeV, it becomes increasingly difficult to identify it from the underlying background [5]. Such jets are referred as minijets whose transverse energy is too low to be resolved experimentally. In heavy collisions, minijets have been estimated to produce 50% (80%) of the transverse energy in central collisions at RHIC (LHC) energies [2]. These minijets could lead to a wide variety of correlations among observables such as multiplicity, strangeness, transverse momentum etc., that compete with the expected signatures of a QGP.

Thus, Monte Carlo model, HIJING (Heavy Ion Jet INteraction Generator) [6] was developed to provide a theoretical laboratory for studying jets in high-energy nuclear interactions. HIJING combines a QCD inspired model for jet production with the Lund model [7] for jet fragmentation. HIJING is designed mainly to explore the range of possible initial conditions that may occur in relativistic heavy ion collisions. To study the nuclear effects, nuclear shadowing [8] of parton structure functions and a schematic model of final state interaction of high p_T jets in terms of effective energy loss parameter, dE/dx [9, 10] was also included. This model has been tested extensively against data on $p + p(\bar{p})$ over a wide energy range, $\sqrt{s_{NN}} = 50 - 1800$ GeV and $A + A$ collisions at $\sqrt{s_{NN}} = 20 - 200$ GeV. However, HIJING model does not include re-scattering of the produced particles.

5.8 Photon Pseudo-rapidity Distribution Results from the PMD

Photon production is an important tool to identify the quark gluon plasma (QGP) in ultra relativistic heavy ions collisions at RHIC and LHC energies [11–14]. The multiplicity of charged/neutral particles is a central observable in relativistic heavy ion collisions, which provides information on the properties of the hot and dense fireball formed in such collisions. For example, measurement of particle density in pseudo-rapidity provides information on energy density, initial temperature and velocity of sound in the medium formed in such heavy ion collisions [15]. More detailed information is embedded in identified particle spectra. However, it is practically not possible to get such spectra over the

full pseudo-rapidity range. Hence, such an information is obtained from non-identified charged/neutral particle measurements, which provide unique opportunity to study the bulk properties of the colliding system [16]. Cu+Cu run at RHIC was chosen to study systematics of global observables as a function of beam energy and system size which may shed light on the onset of the formation of a new state of deconfinement. The particle density in pseudo-rapidity also provides a testing ground for various particle production models, such as parton saturation model [17] and semi-classical QCD, also known as Color Glass Condensate (CGC) [18]. Besides this, study of variation of particle density in pseudo-rapidity with respect to centrality, expressed in terms of the number of participating nucleons (N_{part}) and/or the number of binary collisions (N_{coll}), may shed light on soft and hard processes in particle production.

Recently PHOBOS experiment reported Color Glass Condensate scenario of charged particle production at $\sqrt{s_{NN}} = 200$ GeV [19]. Energy dependence of limiting fragmentation phenomena has also been explained within the framework of CGC [20]. It is expected that the fragmentation region in a high energy heavy ion collision is similar to high energy proton nucleus collision. This is because a QGP is expected to be formed only in the mid-rapidity region. Particle production mechanism remains un-affected in the forward rapidity region. Thus, target nucleus can be treated as a dilute system of quarks and gluons while the projectile nucleus must be treated as a Color Glass Condensate due to large number of gluons, in the forward rapidities. This is essentially same as a proton nucleus system getting scattered from quarks and gluons coming from the proton on the dense nucleus.

Photons are produced at all stages of the system created in heavy-ion collisions. Being chargeless particles they do not interact with the system and hence carry information about the entire history of the collision. About 93-96% of the inclusive photons come from the decay of π^0 , as a result the measurements of multiplicity of photons is complementary to charged particle measurements. Forward rapidity region precludes the use of a calorimeter due to high level of overlap of fully developed showers. Previous measurements of photon multiplicities in the forward region are reported from preshower detector [21] at the Super Proton Synchrotron (SPS) [22].

As previously mentioned in chapter 1 that fluctuations in physical observables have been a topic of interest for recent years because they might provide important signals about a QGP formation in heavy ion collisions. In this chapter too, we study fluctuations in the photons produced at forward rapidities in $Cu + Cu$ collisions at $\sqrt{s_{NN}} = 200$ GeV in the STAR experiment.

5.8.1 Photon Pseudo-rapidity Distribution

Fig. 5.16 presents the pseudo-rapidity distribution of photons within $-2.8 < \eta < -3.6$ for five centrality classes in $Cu + Cu$ collisions at the center of mass energy of 200 GeV. We observe at forward rapidities the pseudo-rapidity distributions are roughly linear. Photon yield and also the overall cross-section increases with the collision centrality. However, there is a finite increase in the slope with the increase in centrality. We also present a comparison of the data with HIJING theoretical model. This model is based on perturbative QCD processes which leads to multiple jet production and jet interaction with the medium as discussed in Section 5.7. The statistical errors of the data are within the symbol size. Based on the figure, we observe that there is a qualitative but not quantitative agreement with the HIJING model which shows similar features as that of the data. Besides this, there is an anomaly observed at $\eta = -3.2$. We observe the yield at $\eta = -3.2$ is larger for 0-10% and 10-20% centralities than expected from linear interpolation of the cross-section at $\eta \leq -3.4$ and $\eta \geq -3.0$. This could partly be attributed to the large systematic errors which are of the order of 17% here [23] and partly due to the apparent difference in the efficiency and purity shown in Figs. 4.13 and 4.14, respectively, in the preceding Chapter.

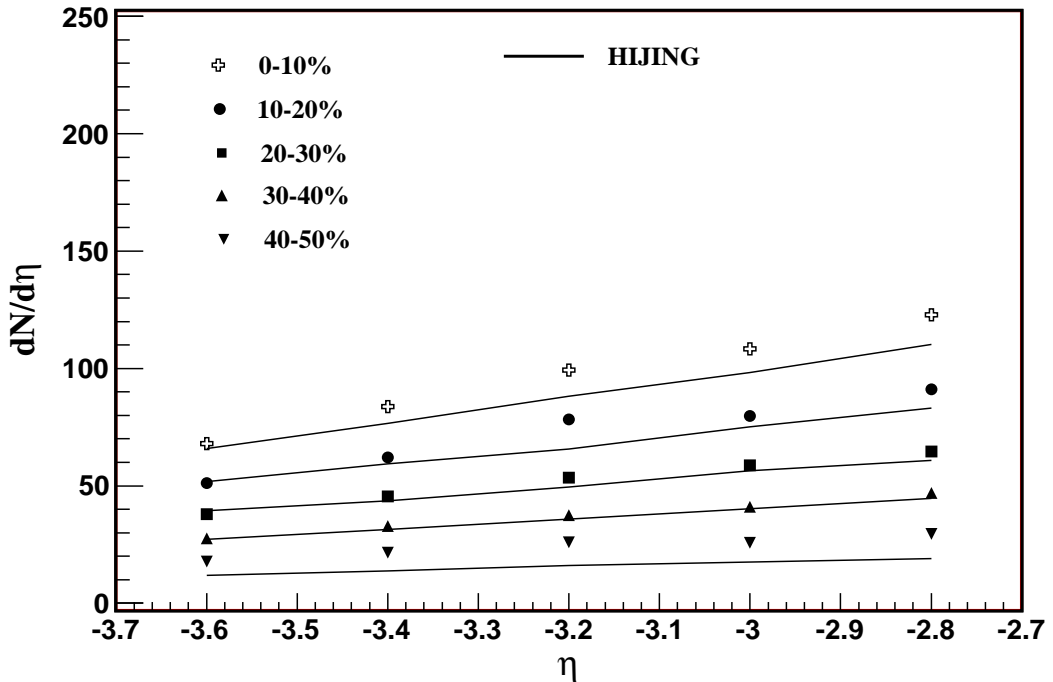


Figure 5.16: Pseudo-rapidity density distribution, $dN_\gamma/d\eta$, as a function of η for various event centrality classes compared to HIJING model calculations.

5.8.2 Centrality Dependence of Photon Production

As previously mentioned, collision centrality can also be expressed in terms of the number of participating nucleons (N_{part}) or the number of binary collisions (N_{bin}). N_{part} and N_{bin} scaling shed light on the particle production mechanism by providing information on the contribution of hard (pQCD jets) and soft processes. Scaling of particle production with N_{part} shall indicate the dominance of soft processes while scaling with N_{bin} would indicate the onset of hard processes.

Various studies at SPS energies have reported scaling of particle production with N_{part} :

$$\frac{dN}{d\eta} \propto N_{part}^{\alpha} \quad (5.1)$$

where the value of α for photons and charged particles were found to be 1.12 ± 0.03 and 1.07 ± 0.05 , respectively [24, 25]. Note that the value of α within the quoted systematic errors is approximately same for both the photons and the charged particles. The value of α indicates a deviation from the picture of a naive Wounded Nucleon Model ($\alpha = 1$).

However, at RHIC energies, hard processes play an important role in particle production mechanism [26]. Therefore, the centrality dependence of charged particle pseudo-rapidity density ($dN_{ch}/d\eta$) is expressed as follows :

$$\frac{dN_{ch}}{d\eta} = \alpha N_{part} + \beta N_{col} \quad (5.2)$$

Where α stands for the relative fraction of particles produced in soft collisions, and β stands for the relative fraction of particles produced in hard collisions.

Fig. 5.17 presents the centrality dependence of photon production at forward rapidities for all measured centralities. The pseudo-rapidity distribution normalized to the number of participating nucleons are plotted as a function of pseudo-rapidity, η . We observe that the forward pseudo-rapidity distribution of photons per participant pair is independent of collision centrality. The fact that $dN_{\gamma}/d\eta$ scales with the number of participating nucleons indicates contribution from soft processes only in the photon production at forward rapidities. We understand that contribution from only the soft processes result in the longitudinal scaling of the particles in the forward rapidities, which does not happen at mid rapidity where both hard and soft processes play a major role in particle production mechanism.

5.8.3 Scaling of Photon Production with N_{coll}

Fig. 5.18 shows the variation of the total number of photons normalized to the number of binary collisions at forward rapidities, i.e., in the PMD coverage ($-2.8 \leq \eta \leq -3.6$),

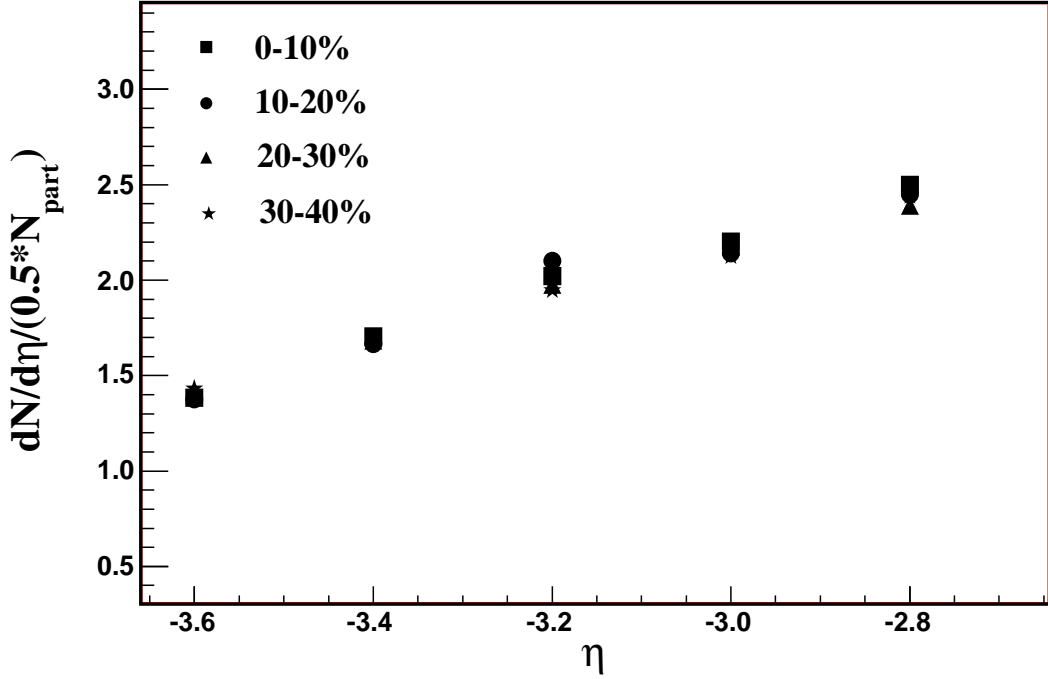


Figure 5.17: Pseudo-rapidity density distribution ($dN_\gamma/d\eta$) per participant pair as a function of η for four centrality classes in $Cu + Cu$ collisions at $\sqrt{s_{NN}} = 200$ GeV.

as function of the number of binary collisions. Higher N_{coll} values correspond to more central collisions, or collisions with smaller impact parameter. We observe that photon production at forward rapidities at RHIC do not scale with the number of binary collisions. The data value decreases from peripheral to most central collisions in $Cu + Cu$ collisions at $\sqrt{s_{NN}} = 200$ GeV, clearly indicating that the contribution of hard processes to particle production at forward rapidity is small. The statistical errors in the figure are within the symbol size.

5.8.4 Centrality and System Size Dependence of Longitudinal Scaling of Photon Production

Longitudinal scaling (previously known as limiting fragmentation) at forward rapidities has been of great interest in heavy ion collisions. This has been reported for the past two decades in $p + p$ and $A + A$ collisions, however, mostly for charged particles. This section of the thesis presents results on longitudinal scaling behavior of inclusive photons at forward rapidities.

Fig. 5.19 shows system size and centrality dependence of longitudinal scaling of photon production at forward rapidities. We compare results of pseudo-rapidity distribution per participant pair as a function of $\eta - y_{beam}$ (where, y_{beam} refers to the beam

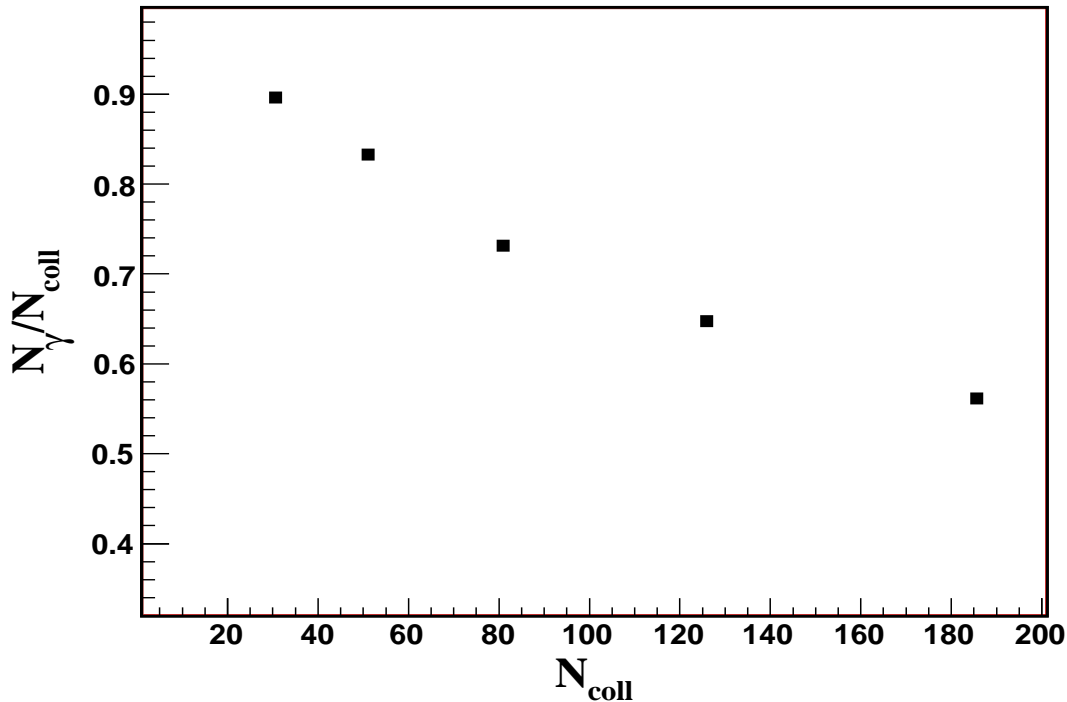


Figure 5.18: Variation of N_{γ} normalized to the number of binary collisions in the PMD coverage, as a function of N_{coll} .

rapidity) for $Cu + Cu$ collisions at the center of mass energy of 200 GeV with $Au + Au$ collisions at $\sqrt{s_{NN}} = 62.4$ GeV for 0-5% (most central) and 40-50% (peripheral) collisions [23], $Cu + Cu$ collisions at $\sqrt{s_{NN}} = 62.4$ GeV for 0-10% (most central) collisions [27]. The WA98 [24] data at $\sqrt{s_{NN}} = 17.3$ GeV and UA5 [28] data for $p\bar{p}$ at $\sqrt{s_{NN}} = 540$ GeV are also displayed. It is interesting to note that the cross-section for different system sizes and energies remain constant at a particular pseudo-rapidity, however, the cross-section for $p\bar{p}$ data is prominently different. One of the reason for this difference could be the annihilation process in $p\bar{p}$ collisions which does not take place in heavy ion collisions. Instead, in heavy ion collisions a finite number of protons always sit at the beam rapidity. We thus conclude that inclusive photon production per participant pair follow universal limiting pseudo-rapidity distribution away from mid rapidity which is independent of energy, centrality and system size.

5.9 Photon Multiplicity Fluctuations

From $N_{\gamma\text{-like}}$ samples, actual incident N_{γ} is determined by using the efficiency, purity and geometrical acceptance factors obtained from simulation and data, on an event-by-event basis. Calculation of efficiency, purity and acceptance factors are discussed in detail in chapter 4 (Simulation of the PMD). The Minimum bias distribution of N_{γ} clusters is

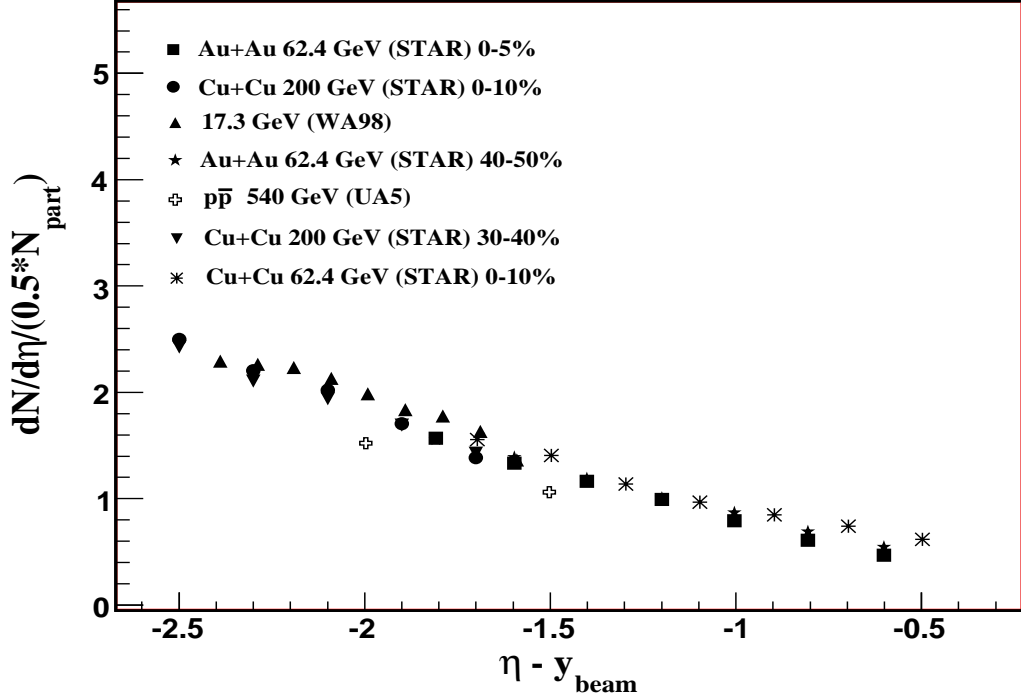


Figure 5.19: $dN_\gamma/d\eta$ normalized to N_{part} as a function of $\eta - y_{beam}$ for various systems and energy.

presented in Fig. 5.20. Fig. 5.20 also shows top 2% central N_γ distribution (square symbol) which seems to be Gaussian.

Enormous theoretical interest has been directed towards the subject of event-by-event fluctuations, motivated by the near perfect Gaussian distributions in particle multiplicities. The variance or the width of such Gaussian distributions are expected to contain information about the reaction mechanism as well as the nuclear geometry [29–32].

The relative fluctuations (ω_X) in an observable X can be expressed as:

$$\omega_X = \frac{\sigma_X^2}{\langle X \rangle} \quad (5.3)$$

where σ_X^2 is the variance of the distribution and $\langle X \rangle$ is the mean value. The value of ω_X which can be extracted from experimental data has contributions from both the trivial statistical effects and the dynamical effects. Thus, one has to understand the contributions from statistics and other sources of fluctuations in order to extract the dynamical part associated with any new physics from these observed fluctuations. Examples of known sources of fluctuations contributing to the observed experimental value of ω_X include finite particle multiplicity, effect of limited acceptance of the detectors, impact parameter fluctuations, fluctuations in the number of primary collisions, effect of re-scattering of secondaries, resonance decays, and Bose-Einstein correlations. More detailed study of

these sources of fluctuations, along with the estimates of the ω_X contributions have been carried out by Stephanov *et al.* [32] and by Heiselberg *et al.* [29]. They show that the resonance decay increase fluctuations, while the role of re-scattering is still uncertain. Further, in this chapter, we present fluctuations in the multiplicities of photons over a large range of centralities as measured in the STAR experiment. We have also compared the fluctuations observed in the experimental data for varying centrality conditions to those obtained from Wounded Nucleon Model.

In order to study fluctuations in the produced photons, we chose various 2% centrality bins. The reason of choosing very small bins in centrality was to minimize the impact parameter fluctuations. We studied Gaussian fit parameters, such as, mean (μ), sigma (σ) and chi-square per degree of freedom (χ^2/ndf) for 0-2%, 2-4%..... 40-42% centrality bins in $Cu + Cu$ collisions at the center of mass energy of 200 GeV. Fig.

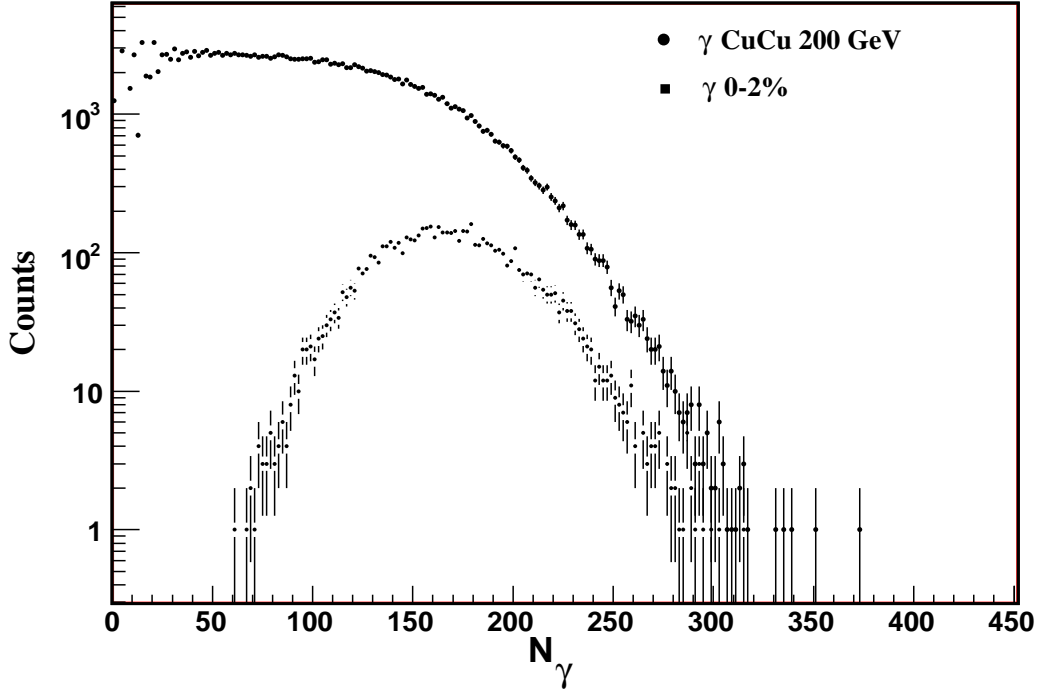


Figure 5.20: Minimum bias N_γ distribution in $Cu + Cu$ collisions at the center of mass energy of 200 GeV. The N_γ distribution for top 2% central events is also shown with square symbols.

5.21 shows chi-square per degree of freedom (χ^2/ndf) (top panel), the standard deviation (σ) (middle panel) and the variation of the mean (μ) (bottom panel) of photons for 2% centrality bins. We observe that χ^2/ndf values remain between 1.0 and 1.5 for 0-34% centrality (in 2% centrality bins (CS)), whereas, for further peripheral collisions the value rises abruptly to 2.5. The mean (μ) and sigma (σ) values decrease from 0-2% centrality to 40-42% centrality.

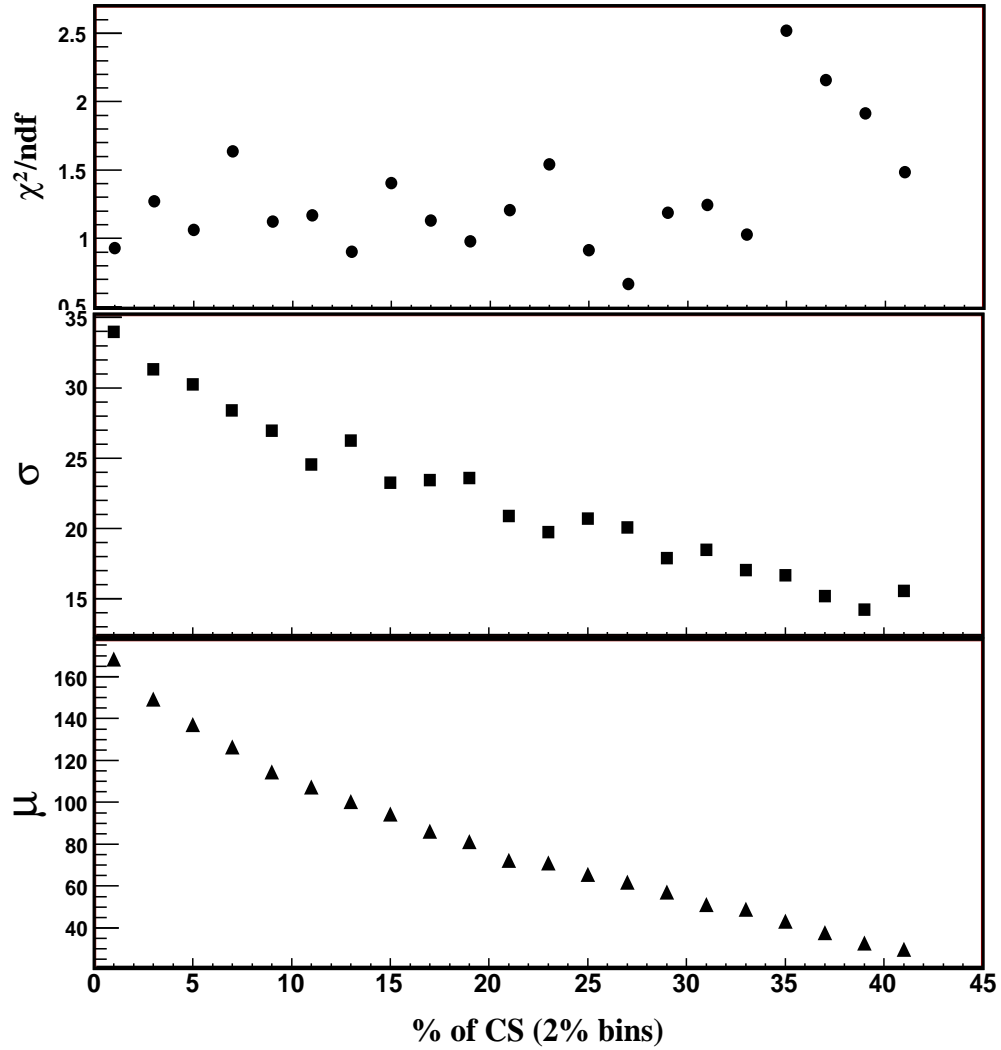


Figure 5.21: Gaussian fit parameters, chi-square per degree of freedom (χ^2/ndf) (top panel), sigma (σ) (middle panel) and mean (μ) (bottom panel) of the multiplicity distributions of γ -like clusters for 2% centrality bins. The centrality bins correspond to 0-2%, 2-4%.....40-42% of the minimum bias cross-section.

5.9.1 Estimation of Fluctuation in a Participant Model

In a situation, where nucleus-nucleus collision is considered as the sum of contributions from many sources created in the early stage of the interaction, the variance of the distribution of any observable can have contributions from:

- Fluctuations due to different impact parameters. Even if impact parameter window is narrowed, density fluctuations within the nucleus will make this contribution non-zero.
- Fluctuations due to any dynamical process or critical behavior in the evolution of the system.

The contribution from the first source mentioned leads to fluctuations in the number of participating nucleons which may be related to the initial size of the interacting system before it gets thermalized. Resonance decays have also been shown to increase the multiplicity fluctuations by a large factor [29, 32]. Following a simple participant model [33–35], the particle multiplicity (of the produced photons), N , may be expressed as:

$$N = \sum_{i=1}^{N_{part}} n_i \quad (5.4)$$

where n_i is the number of particles produced in the detector acceptance by the i^{th} participant and N_{part} is the number of participants. On an average, the mean value of n_i is the ratio of the average multiplicity in the detector coverage to the average number of participants, i.e.,

$$\langle n \rangle = \frac{\langle N \rangle}{\langle N_{part} \rangle} \quad (5.5)$$

As a result, fluctuations in N will have contributions due to fluctuations in N_{part} ($\omega_{N_{part}}$) and also due to fluctuations in the number of particles produced per participant (ω_n). In the absence of correlations between the n_i 's, the multiplicity fluctuations, ω_N can be expressed as:

$$\omega_N = \omega_n + \langle n \rangle \omega_{N_{part}} \quad (5.6)$$

A comparison of data with the results of such model will reveal the extent to which the principle of superposition of nucleon-nucleon interactions is valid in case of heavy ion collisions. In the subsequent sections we discuss the calculations of $\omega_{N_{part}}$ and ω_n used in the Eq. 5.6.

Calculation of $\omega_{N_{part}}$

The impact parameter fluctuations are reflected in the fluctuations of the number of participants. We estimated this contribution using the HIJING event generator with default setting. A set of 600K minimum bias $Cu + Cu$ collisions at the center of mass energy of 200 GeV was generated for the calculation of the fluctuations in the number of participants.

The distributions of N_{part} for the same narrow (2%) bins of centrality, as discussed previously for the data, are well described by Gaussian distributions. Fig. 5.22 (upper panel), (middle) and (lower panel) show the variation of mean (μ), sigma (σ) and relative fluctuations $\omega_{N_{part}}$, respectively, calculated from the fit parameters with the 2% centrality bins. We observe that the relative fluctuations in the number of participants, $\omega_{N_{part}}$, increases from a minimum in most central collisions to a maximum in mid peripheral collisions.

Calculation of ω_n

To study Wounded Nucleon Model (WNM), we note that the mean number of photons produced in nucleon-nucleon collisions as a function of center of mass energies (\sqrt{s} from 2 GeV to 500 GeV) is given by Eq. 5.7 :

$$\langle N_\gamma \rangle^{NN} = -9.9(\pm 2.1) + 8.5(\pm 1.9)s^{0.113(\pm 0.015)} \quad (5.7)$$

For $Cu + Cu$ at the center of mass energy of 200 GeV, this parameterized equation gives the average number of photons to be 18.24. Thus, average photon multiplicity per participant is 9.12. Eq. 5.7 has been confirmed by various experiments, such as, bubble chamber, UA5, ISR, FNAL, E735 [36–39]. In addition, σ for photon multiplicity in nucleon-nucleon collisions shows a linear dependence with the average charged particle multiplicity as $0.576(\langle N_{ch}^{NN} \rangle - 1)$ [40]. We use this to calculate ω_m , which is given as:

$$\omega_m = 0.33 \frac{(\langle N_{ch} \rangle - 1)^2}{\langle N_{ch} \rangle} \quad (5.8)$$

We used the same parameterization for photons. For photons at RHIC energies, this gives a value of $\omega_m = 2.385$. Since limited acceptance is a major source of fluctuations per participant, we define a quantity, f , as the ratio of the number of particles accepted to the total number of particles produced, i.e.,

$$f = \frac{\langle n \rangle}{\langle \nu \rangle} \quad (5.9)$$

Relation between ω_m , ω_n , and f is given as follows:

$$\omega_n = (1 - f) + f \times \omega_m \quad (5.10)$$

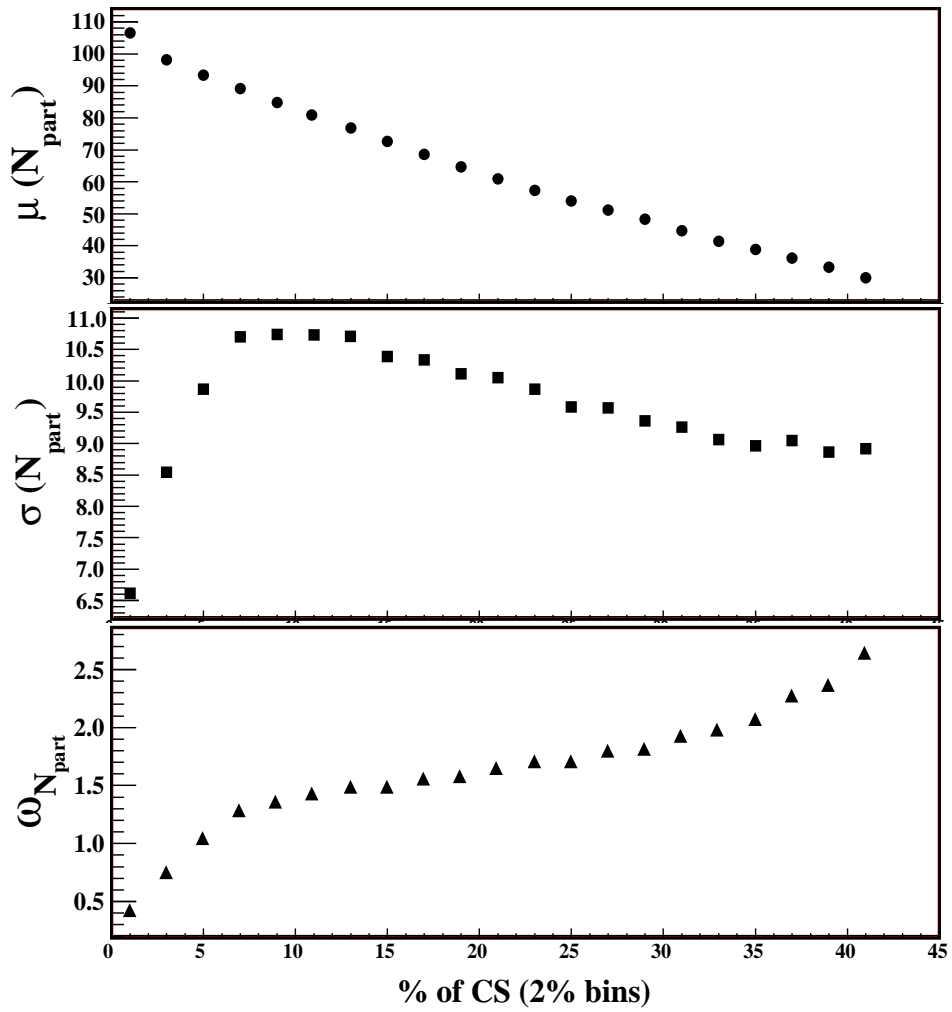


Figure 5.22: Variation of μ , σ and fluctuations, $\omega_{N_{part}}$, of the number of participants as a function of centrality.

For better clarity we show calculations of some of the terms for $Cu+Cu$ collisions at $\sqrt{s_{NN}} = 200$ GeV, for 0-2% centrality.

$$\begin{aligned} \langle n \rangle &= \frac{\langle N \rangle}{\langle N_{part} \rangle} \\ &= \frac{168.3}{106.5} \\ &= 1.58 \end{aligned} \tag{5.11}$$

$$\begin{aligned} f &= \frac{\langle n \rangle}{\langle \nu \rangle} \\ &= \frac{1.58}{9.12} \\ &= 0.173 \end{aligned} \tag{5.12}$$

$$\begin{aligned} \omega_n &= (1 - f) + f \times \omega_m = (1 - 0.173) + 0.173 \times 2.385 \\ &= 1.23 \end{aligned}$$

From the values of $\langle n \rangle$, ω_n and $\omega_{N_{part}}$, the value of ω_N can be calculated.

5.9.2 Comparison of Data with Results from Model Calculations

We compare experimental results of photon multiplicity fluctuations with HIJING and participant model. The results are calculated with very fine centrality bins, i.e., 2% centrality bins. Fig. 5.23 clearly shows that relative photon multiplicity fluctuations, ω_γ in data are more or less constant within the statistical error bars, with a value of ~ 7 . Whereas, HIJING model calculations show slightly large relative photon multiplicity fluctuations with a value of ~ 8 . A comparison of data and HIJING values is also made with participant model in this figure. Relative fluctuations in this model gradually rise from a value of ~ 2 and remain constant for the rest of the centrality, with a value of ~ 3 . Fig. 5.23 also shows that the participant model clearly fails to explain the observed photon multiplicity fluctuations in $Cu + Cu$ collisions. The error bars shown here are statistical only.

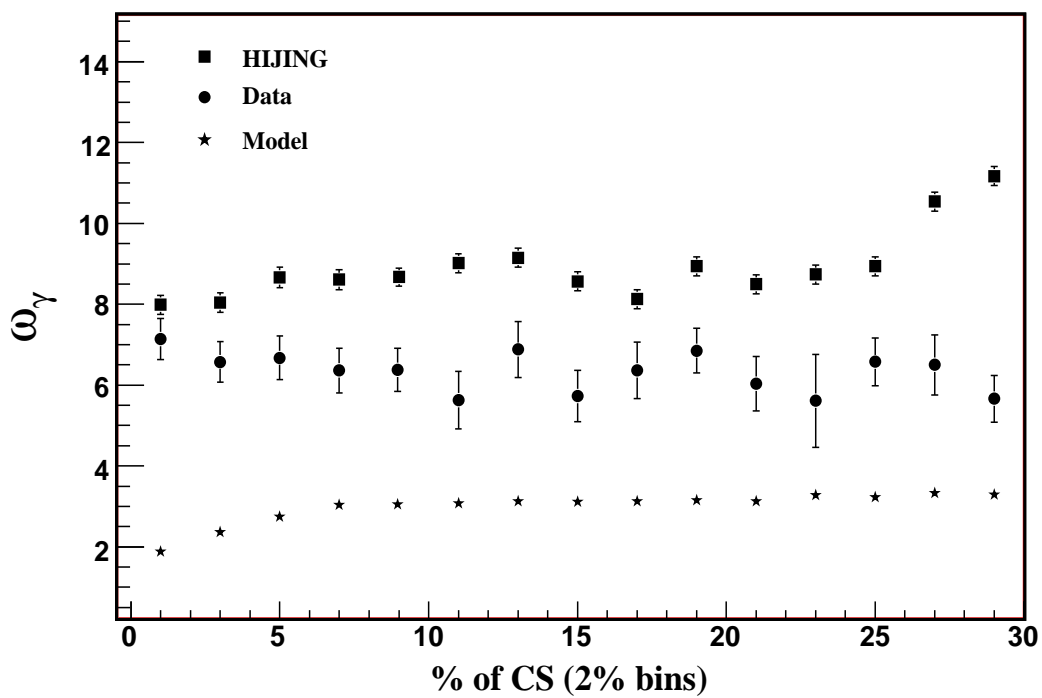


Figure 5.23: Relative fluctuations, ω_γ of photon multiplicity distribution compared to calculations from participant model and HIJING. The data presented here is corrected for efficiency, purity and geometrical acceptance factors.

Bibliography

- [1] J. Adams *et al.*, (STAR Collaboration), (2003), [arXiv:nucl-ex/0311017].
- [2] K. Kajantie, P.V. Landshoff and J. Lindfors, Phys. Rev. Lett. **59** (1987) 2517;
K.J. Eskola, K. Kajantie and J. Lindfors, Nucl. Phys. B **323** (1989) 37; G. Calucci
and D. Treleani, Phys. Rev. D **41** (1990) 3367.
- [3] M. Manner *et al.*, Phys. Lett. B **118** (1982) 203.
- [4] C. Albajar *et al.*, Nucl. Phys. B **335** (1990) 261.
- [5] C. Albajar *et al.*, Nucl. Phys. B **309** (1998) 405.
- [6] X.N. Wang and M. Gyulassy, Phys. Rev. D **44** (1991) 3501.
- [7] B. Andersson, G. Gustafson, G. Ingelman and T. Sjöstrand, Phys. Rep. **97** (1983)
31.
- [8] J. Ashman, *et al.*, (EM Collaboration), Phys. Lett. B **202** (1988) 603.
- [9] X.N. Wang and M. Gyulassy, Phys. Rev. D **68** (1992) 148.
- [10] M. Gyulassy, *et al.*, Nucl. Phys. A **538** (1992) 37c. [arXiv:nucl-th/9907017].
- [11] T. Peitzman and M. H. Thoma, (2001), [arXiv:hep-ph/0111114].
- [12] J. Alam, S. Raha and B. Sinha, Physics Reports **273** (1996) 243.
- [13] D.K. Srivastava *et al.*, Eur. Phys. J. **12** (2000) 109.
- [14] D.K. Srivastava and B. Sinha, Phys. Rev. C **64** (2001) 034902.
- [15] J.D. Bjorken, Phys. Rev. D **27** (1983) 140; L.D. Landau, Izv. Akad. Nauk. Ser. Fiz.
17 (1953) 51;
S. Belenkij and L.D. Landau, Usp. Fiz. Nauk. **56** (1955) 309; Nuovo Cim Suppl. S
10 (1956) 15;
R.C. Hwa and K. Kajantie. Phys. Rev. D **32** (1985) 1190;
J. Alam *et al.*, Annals of Phys. **286** (2000) 159;
B. Mohanty and J. Alam, Phys. Rev. C **68** (2003) 064903.

- [16] B.B. Back, Phys. Rev. C **72** (2005) 064906.
- [17] L.V. Gribov, E.M. Levin and M.G. Ryskin, Phys. Rep. **100** (1983) 1; J.P. Blaizot and A.H. Mueller, Nucl. Phys. B **289** (1987) 847.
- [18] L. McLerran and R. Venugopalan, Phys. Rev. D **49** (1994) 2233; L. McLerran and R. Venugopalan, Phys. Rev. D **50** (1994) 2225; Y.V. Kovchegov, Phys. Rev. D **54** (1996) 5463; E. Iancu and L. McLerran, Phys. Lett. B **510** (2001) 145; A. Krasnitz and R. Venugopalan, Phys. Rev. Lett. **84**, (2000) 4309.
- [19] B.B. Back *et al.*, (PHOBOS Collaboration), Phys. Rev. Lett. **87** (2001) 102303.
- [20] J. Jalilian-Marian, Phys. Rev. C **70** (2004) 027902.
- [21] M.M. Aggarwal *et al.*, Nucl. Instrum. Methods Phys. Res., Sect. A **424** (1999) 395.
- [22] M.M. Aggarwal *et al.*, (WA93 Collaboration), Phys. Rev. C **58** (1998) 1146; M.M. Aggarwal *et al.*, (WA93 Collaboration), Phys. Lett. B **403** (1999) 390.
- [23] J. Adams *et al.*, (STAR Collaboration), Phys. Rev. Lett. **95** (2005) 062301.
- [24] M.M. Aggarwal *et al.*, (WA98 Collaboration), Phys. Lett. B **458** (1999) 422.
- [25] M.M. Aggarwal *et al.*, (WA98 Collaboration), Eur. Phys. J. C **18** (2001) 052301.
- [26] D. Kharzeev and M. Nardi, Phys. Lett. B **507** (2001) 121; D. Kharzeev and E. levin, Phys. Lett. B **523** (2001) 79.
- [27] N. Gupta, University of Jammu, Jammu, India, [Private Communications].
- [28] K. Alpgard *et al.*, (UA5 Collaboration), Phys. Lett. B **115** (1982) 72.
- [29] G. Baym, G. Friedman and I. Sarcevic, Phys. Lett. B **219** (1989) 205.
- [30] F. Corriveau *et al.*, (NA34 Collaboration), Z. Phys. C **38** (1988) 15; J. Schukraft *et al.*, (NA34 Collaboration), Z. Phys. C **38** (1988) 59.
- [31] R. Albrecht *et al.*, Z. Phys. C **45** (1989) 31.
- [32] M. Stephanov, K. Rajagopal and E. Shuryak, Phys. Rev. Lett. **81** (1998) 4816; Phys. Rev. D **61** (1999) 114028.
- [33] G. Baym and H. Heiselberg, Phys. Lett. B **469** (1999) 7.
- [34] R.C. Hwa, Phys. Lett. B **201** (1988) 165.

- [35] A. Giovannini and L. Van. Hove, *Z. Phys. C* **30** (1986) 391.
- [36] J. Whitmore, (Bubble Chamber), *Phys. Rep.* **27** (1976) 187.
- [37] H. Boggild *et al.*, (ISR Collaboration), *Ann. Rev. Nucl. Sci* **451** (1974).
- [38] G.J. Alner *et al.*, (UA5 Collaboration), *Z. Phys. C* **33** (1986) 1; *Phys. Rep.* **154** (1987) 247.
- [39] C.S. Lidsey *et al.*, (E735 Collaboration), *Nucl. Phy. A* **544** (1992) 343c.
- [40] J. Whitmore, *Phys. Rep.* **10** (1974) 274.

Chapter 6

Dynamical Net Charge Fluctuations

The study of fluctuations (variation about a mean) can provide evidence for the production of a quark gluon plasma (QGP) in the relativistic heavy ion collisions [1–16]. Anomalous transverse momentum (temperature fluctuations) and net charge event-by-event fluctuations are proposed as some of the observables of the formation of a quark gluon plasma (QGP) in high-energy heavy ion collisions. The focus of several experiments (SPS [17–19] and RHIC [20–24]) have been on the study of fluctuations in relativistic heavy ion collisions. The most efficient way to address the problem of “or” the physics of fluctuations of a system created in a heavy ion collisions is via the study of event-by-event (E-by-E) fluctuations, where a given observable is measured on an event-by-event basis and the fluctuations are studied over an ensemble of events. Fluctuations, in principle, may be used to measure the susceptibilities of the system. These susceptibilities also determine the response of the system to external forces.

One can explore various regions of temperature and baryon density by changing the beam energy and varying the system size. The RHIC, which collides heavy ions at $\sqrt{s_{NN}} = 200$ GeV (top energy) creates system with a very small net baryon density, whereas it is expected that the creation of highest possible baryon densities occur at more moderate beam energies ($\sqrt{s_{NN}} = 10$ GeV). FAIR (Facility for Antiproton and Ion Research) accelerator at GSI, Darmstadt, Germany, may provide such beams in near future. In this chapter we shall focus on the net charge fluctuation analysis.

Many authors [6, 7, 11] have argued that entropy conserving hadronization of a plasma of quarks and gluons should produce a final state characterized by a dramatic reduction of the net charge fluctuations relative to that of a hadron gas. Their prediction is based on the notion that quark quark correlation can be neglected, and hadronization of gluons which produces pairs of positive and negative particles do not contribute to the net charge fluctuations. The variance of the ratio of positive and negative particles scaled by the total charged particle multiplicity, a quantity called D, should be approximately four times smaller than that of a gas of hadrons. However, quark-quark correlations may not

be negligible; Koch *et al.* [6] extended their original estimates to include susceptibilities calculated on the lattice. They found the observable D is quantitatively different from their initial estimate but nonetheless still dramatically smaller than the values expected for a hadron gas. Observable of net charge fluctuations is defined as (according to Koch *et al.* [6])

$$D(Q) = 4 \frac{\delta Q^2}{\langle n_{ch} \rangle} \quad (6.1)$$

where,

$$\delta Q^2 = \langle Q^2 \rangle - \langle Q \rangle^2, \text{ where } Q = n^+ - n^- \quad (6.2)$$

n^+ and n^- are, respectively, the numbers of positive and negative particles observed in the acceptance of interest. The average is calculated over all events in the sample.

In case particle production is completely uncorrelated (Poissonian distribution), then $\delta Q^2 = \langle n_{ch} \rangle$, i.e., $D(Q) = 4$ for an independent emission. Further predictions made by the authors of Ref. [6] are listed in the equation below:

$$\tilde{D} = \begin{cases} 1 & \text{for quark gluon gas} \\ 3 & \text{for resonance gas} \\ 4 & \text{for uncorrelated pion gas} \end{cases} \quad (6.3)$$

Various issues complicate the measurement and interpretation of net charge fluctuations. First, one must acknowledge that particle final state systems produced in heavy ion collisions although large, are nonetheless finite and therefore subject to charge conservation effects. Second, one may question whether the dynamical net charge fluctuations produced within the QGP phase may survive the hadronization process. Shuryak and Stephanov [12] have argued based on solutions of the diffusion equation within the context of a model involving Bjorken boost invariance, that diffusion in rapidity space considerably increases the net charge fluctuations. They further argued that the reduced fluctuations predicted for a QGP might be observable only if fluctuations are measured over a very large rapidity range (e.g. of order of 4 units of rapidity). Unfortunately, charge conservation effects increase with the rapidity range considered at a given beam energy and might become dominant for rapidity ranges of four units or more. Gavin *et al.* [25] however argued that the classical diffusion equation yields non-physical solutions in the context of relativistic heavy ion collisions. They proposed a causal diffusion equation as a substitute of the classical diffusion equation for studies of net charge fluctuation dissipation. They found that causality substantially limits the extent to which diffusion can dissipate these fluctuations.

Thirdly, there exists the possibility that the treatment by Koch *et al.* [6] of quark and gluons behaving as independent particles carrying full entropy may be inappropriate. Consider for instance that recent measurements of elliptical anisotropy of particle emission in $Au+Au$ collisions show that mesons and baryon elliptical flow, v_2 , scale in proportion to the number of constituent quarks for transverse momenta in the range 1-4 GeV/c thereby suggesting hadrons are produced relatively early in the collisions through “coalescence” or combination of constituent quarks [26]. In a constituent quark scenario, the role of gluons in particle production is reduced. Bialas [27] conducted a simple estimate of such a scenario, and reported net charge fluctuations D may be of order 3.3. Interestingly, this estimate suggests fluctuations might be even larger than that expected for a resonance gas, and as such should also be identifiable experimentally.

Theoretical estimates of the effect of hadronization on net charge fluctuation have restricted mostly to the studies of the role of resonances, diffusion [12, 28, 29], and thermalization [29, 30]. One must, however, confront the notion that collective motion of the produced particles is clearly demonstrated in relativistic heavy ion collisions. Voloshin pointed out in Ref. [31] that induced radial flow of particles produced in parton-parton collisions at finite radii in nucleus-nucleus collisions generate momentum-position correlations not present in elementary proton-proton collisions. Specifically, the effect of radial flow is to induce azimuthal correlations and to modify particle correlation strengths in the longitudinal direction. Voloshin showed that the two-particle momentum correlations $\langle \Delta p_t, \Delta p_t \rangle$ are in fact sensitive to the radial velocity profile as well as the average flow velocity. While one may not intuitively expect net charge fluctuations to exhibit a dramatic dependence on radial flow, simulations based on a simple multinomial particle production model including resonances such as the $\rho(770)$, indicate that net charge correlations are in fact also sensitive to the radial flow through azimuthal net charge correlations [32]. They may as such be used to complement the estimates of radial velocity obtained from fits of single particle spectra with blast-wave parameterization or with similar phenomenologies.

Measurements of charged particle fluctuations have also been proposed as tool to discriminate between predictions of various microscopic models of nuclear collisions. Zhang *et al.* [33] find that the measurements of dynamical fluctuations with the observable D should exhibit sensitivity to rescattering effects based on calculations w/o rescattering with models VNIb and RQMD. They also found that models VNIb, HIJING, HIJING/BB and RQMD predict qualitatively different dependences on collision centrality. Similar conclusions are obtained by Abdel Aziz [34].

Bopp and Ranft [35] compared the predictions of the net charge fluctuations (at central rapidities) by the dual parton model and the statistical (thermal) models, and found significant differences in the dispersion of the charges predicted by these mod-

els. They argued that the charged particle fluctuations should provide a clear signal of the dynamics of heavy ion processes, and enable a direct measurement of the degree of thermalization reached in heavy ion collisions. Gavin [29, 30] similarly argued, based on the data from PHENIX [36, 37] and STAR [38–40] experiments that measured transverse momentum and net charge fluctuations, indeed present evidence for thermalization at RHIC.

In this work, rather than measuring the event by event fluctuations of a ratio of positive and negative particle multiplicities (in a given acceptance), one considers the second moment of the difference between the relative multiplicity $N_+ / \langle N_+ \rangle$ and $N_- / \langle N_- \rangle$ as follows

$$\nu_{+-} = \left\langle \left(\frac{N_+}{\langle N_+ \rangle} - \frac{N_-}{\langle N_- \rangle} \right)^2 \right\rangle \quad (6.4)$$

The Poisson limit, $\nu_{+-,stat}$ of this quantity is equal to:

$$\nu_{+-,stat} = \frac{1}{\langle N_+ \rangle} + \frac{1}{\langle N_- \rangle} \quad (6.5)$$

The “non-statistical” or “dynamical” fluctuations can thus be expressed as the difference between the above two quantities:

$$\begin{aligned} \nu_{+-,dyn} &= \nu_{+-} - \nu_{+-,stat} & (6.6) \\ &= \frac{\langle N_+(N_+ - 1) \rangle}{\langle N_+ \rangle^2} + \frac{\langle N_-(N_- - 1) \rangle}{\langle N_- \rangle^2} \end{aligned}$$

$$- 2 \frac{\langle N_+ N_- \rangle}{\langle N_- \rangle \langle N_+ \rangle} \quad (6.7)$$

From a theoretical standpoint, $\nu_{+-,dyn}$ can be expressed in terms of two-particle integral correlation functions as $\nu_{+-,dyn} = R_{++} + R_{--} - 2R_{+-}$, where the terms R_{ab} are ratios of integrals of two and single particle densities defined as follows :

$$R_{\alpha\beta} = \frac{\int d\eta_\alpha d\eta_\beta \frac{dN}{d\eta_\alpha d\eta_\beta}}{\int d\eta_\alpha \frac{dN}{d\eta_\alpha} \int d\eta_\beta \frac{dN}{d\eta_\beta}} - 1 \quad (6.8)$$

The net charge dynamical fluctuations variable $\nu_{+-,dyn}$ is thus basically a measure of the relative correlation strength of $++$, $--$, and $+-$ particles pairs. Note that by construction, these correlations are identically zero for Poissonian, or independent particle production. As in practice, produced particles are partly correlated, either through the production of resonances, string fragmentation, jet fragmentation, or other mechanisms, the relative and absolute strengths of R_{++} , R_{--} , and R_{+-} may vary with colliding systems, and beam energy. Note additionally that by virtue of charge conservation, the

production of a pair of positive and negative particles implies that $+-$ are more strongly correlated than $++$ or $--$ pairs. For this reason, it is reasonable to expect $2R_{+-}$ to be larger than R_{++} or R_{--} . One in fact finds experimentally that $2R_{+-}$ is actually larger than the sum $R_{++} + R_{--}$ in $p + p$ and $p + \bar{p}$ collisions measured at the ISR and FNAL [41, 42]. Measurements of $\nu_{+-,dyn}$ are thus expected and have indeed been found to yield negative values in nuclei-nuclei collisions also [39].

Another approach [43] focuses on the variance of the ratio of positive and negative particle multiplicities, $R = \langle N_+ \rangle / \langle N_- \rangle$. For small fluctuations, the variance of the ratio can be related to the charge variance ν (Eq. 6.4). A small fluctuation of $R = \langle N_+ \rangle / \langle N_- \rangle$ satisfies:

$$\frac{\Delta R}{R} = \frac{\Delta N_+}{N_+} - \frac{\Delta N_-}{N_-} \quad (6.9)$$

so that

$$\frac{\langle \Delta R^2 \rangle}{\langle R \rangle^2} = \frac{\langle \Delta N_+^2 \rangle}{\langle N_+ \rangle^2} + \frac{\langle \Delta N_-^2 \rangle}{\langle N_- \rangle^2} - 2 \frac{\langle \Delta N_+ \Delta N_- \rangle}{\langle N_+ \rangle \langle N_- \rangle} \quad (6.10)$$

Expanding the square in Eq. 6.4, we see that

$$\langle \Delta R^2 \rangle = \langle R \rangle^2 \nu_{+,-} \quad (6.11)$$

According to the measure D , used by Koch, Bleicher and Jeon [43]

$$\begin{aligned} D \equiv \langle N \rangle \langle \Delta R^2 \rangle &= \langle N \rangle \langle R \rangle^2 \nu_{+,-} \\ &= \langle N \rangle \langle \frac{N_+}{N_-} \rangle^2 (\nu_{+-,dyn} + \nu_{stat}) \end{aligned} \quad (6.12)$$

For $\langle N_+ \rangle \sim \langle N_- \rangle$, $\langle N_+ \rangle \sim \langle N_- \rangle \sim \langle N \rangle / 2$, we have

$$\begin{aligned} D &= \langle N \rangle \nu_{+-,dyn} + \langle N \rangle \left(\frac{1}{\langle N_+ \rangle} + \frac{1}{\langle N_- \rangle} \right) \\ &= 4 + \langle N \rangle \nu_{+-,dyn} \end{aligned} \quad (6.13)$$

6.1 Data Selection

The data presented in this chapter are from minimum-bias trigger samples for $Cu + Cu$ collisions at $\sqrt{s_{NN}} = 62.4$ and 200 GeV. We present the first analysis of beam energy and system size dependence of net charge fluctuations. Data were selected through the following steps :

1. **Trigger selection** : The data were acquired with minimum bias triggers accomplished by requiring a coincidence signal from two Zero Degree Calorimeters (ZDCs)

located at 18 m from the center of the interaction region on either sides of the STAR detector and using the charged particle hits from an array of scintillator slats arranged in a barrel, called the Central Trigger Barrel, surrounding the TPC. A cut of >17 on the CTB multiplicity is applied to accomplish the trigger selection. Details of trigger in STAR experiment are described in Chapter 2.

2. **Centrality selection** : This analysis uses the standard collision centrality as defined by STAR on the basis of estimates of the collision centrality on the uncorrected multiplicity of charged particle tracks measured within the TPC in the pseudo-rapidity range $-0.5 < \eta < 0.5$ [44]. The pseudo-rapidity range $-0.5 < \eta < 0.5$ used for collision centrality estimated rather than the full range $-1.0 < \eta < 1.0$ in principle measurable with the TPC, to minimize the effects of detector acceptance and efficiency on the collision centrality determination. With the narrow cut $-0.5 < \eta < 0.5$, the detection efficiency is rather insensitive to the position of the collision vertex along the beam direction. The centrality bins were calculated as a fraction of this multiplicity distribution starting at the highest multiplicities. The ranges used in $Cu + Cu$ collisions at $\sqrt{s_{NN}} = 62.4$ and 200 GeV were 0-10% (most central collisions), 10-20%, 20-30%, 30-40%, 40-50% and 50-60% (most peripheral collisions). Figs. 6.1 and 6.2 show the centrality selection from minimum bias uncorrected charged particle distribution in $Cu + Cu$ collisions at $\sqrt{s_{NN}} = 62.4$ and 200 GeV.

Each centrality bin is associated with an average number of participating nucleons, N_{part} , and number of binary collisions, N_{coll} , using Glauber Monte Carlo calculations [44]. N_{part} and N_{coll} numbers are obtained from Glauber Monte Carlo calculations using the Woods-Saxon distribution for the nucleons inside the Cu nucleus. The systematic uncertainties on N_{part} and N_{coll} are determined by varying the Woods-Saxon parameters. Tables 6.1 and 6.2 list the percentage cross-section, the corresponding uncorrected charged particle multiplicity (N_{ch}) in the pseudo-rapidity region $-0.5 < \eta < 0.5$, the number of participating nucleons (N_{part}) and the number of binary collisions (N_{coll}) for $Cu + Cu$ collisions at $\sqrt{s_{NN}} = 62.4$ and 200 GeV, respectively.

6.1.1 Analysis Cuts

The analysis described in this chapter is based on the STAR data production P05id and P06ib for $Cu + Cu$ collisions at the center of mass energy of 62.4 GeV and 200 GeV, respectively, acquired during run V. Events are selected on the basis of quality cuts which are described below:

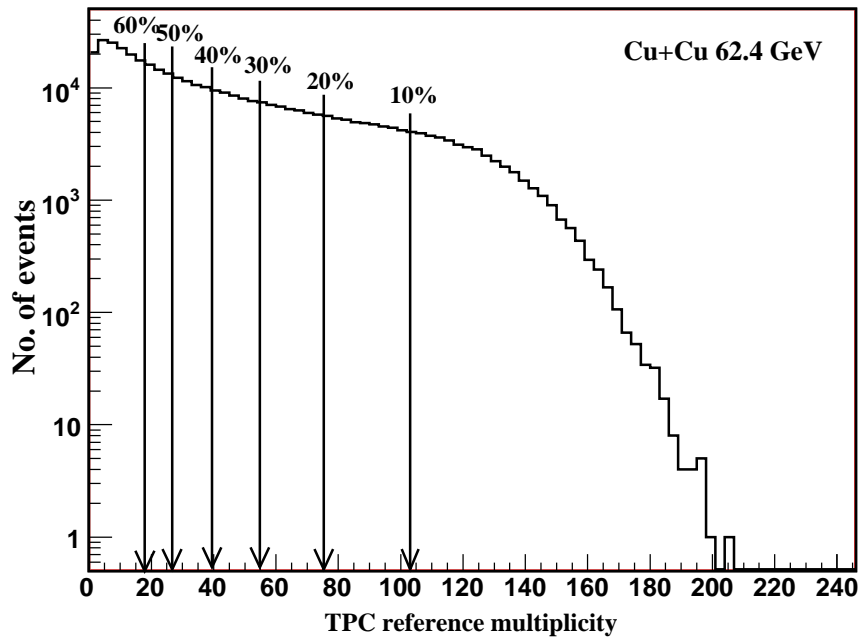


Figure 6.1: The TPC reference multiplicity within $-0.5 < \eta < 0.5$ from data for $Cu + Cu$ collisions at $\sqrt{s_{NN}} = 62.4$ GeV. Collision centralities or % cross-section are shown with the arrows in the plot.

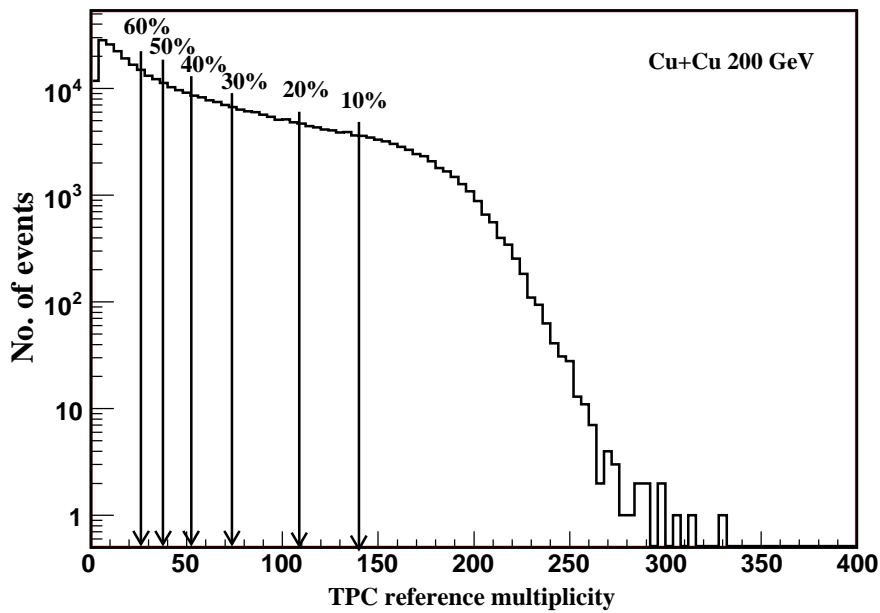


Figure 6.2: The TPC reference multiplicity within $-0.5 < \eta < 0.5$ from data for $Cu + Cu$ collisions at $\sqrt{s_{NN}} = 200$ GeV. Collision centralities or % cross-section are shown with the arrows in the plot.

Table 6.1: The percentage of cross-section, number of uncorrected charged particle multiplicity from the TPC within pseudo-rapidity $-0.5 < \eta < 0.5$, number of participating nucleons, N_{part} , and the number of binary collisions, N_{coll} , for $Cu + Cu$ collisions at $\sqrt{s_{NN}} = 62.4$ GeV.

% Cross-section	N_{ch}	$\langle N_{part} \rangle$	$\langle N_{coll} \rangle$
0-10%	>102	$95.59_{+1.0}^{-1.0}$	$160.64_{+5.4}^{-5.4}$
10-20%	74-102	$72.06_{+2.5}^{-2.1}$	$109.82_{+6.3}^{-6.1}$
20-30%	54-74	$52.27_{+3.0}^{-2.8}$	$71.42_{+6.1}^{-6.0}$
30-40%	39-54	$37.04_{+2.8}^{-3.1}$	$45.24_{+5.2}^{-4.8}$
40-50%	27-39	$25.43_{+2.0}^{-2.6}$	$27.71_{+3.1}^{-3.7}$
50-60%	18-27	$16.92_{+2.9}^{-2.9}$	$16.50_{+2.6}^{-3.2}$

Table 6.2: The percentage of cross-section, number of uncorrected charged particle multiplicity from the TPC within pseudo-rapidity $-0.5 < \eta < 0.5$, number of participating nucleons, N_{part} , and number of binary collisions, N_{coll} , for $Cu + Cu$ collisions at $\sqrt{s_{NN}} = 200$ GeV.

% Cross-section	N_{ch}	$\langle N_{part} \rangle$	$\langle N_{coll} \rangle$
0-10%	>140	$98.34_{+1.1}^{-1.1}$	$185.64_{+6.1}^{-5.6}$
10-20%	103-140	$74.47_{+2.1}^{-2.4}$	$125.92_{+6.8}^{-6.6}$
20-30%	74-103	$54.0_{+2.5}^{-2.8}$	$80.95_{+5.8}^{-6.9}$
30-40%	53-74	$38.56_{+2.4}^{-2.7}$	$51.07_{+4.7}^{-5.6}$
40-50%	37-53	$26.29_{+2.3}^{-3.0}$	$30.61_{+3.8}^{-3.9}$
50-60%	25-37	$17.61_{+2.6}^{-3.1}$	$18.16_{+3.5}^{-3.4}$

1. **Vertex Selection** : Events were selected for the analysis if the collision vertex position lied within 30 cm of the center of the TPC along the beam axis. The vertex position is determined using a fit involving all found tracks. Fig. 6.3 shows z-position of the vertex from data. Shaded portion shows the accepted vertex position along the beam direction. Such a cut is applied in order to minimize the need for corrections to account for the dependence of the TPC acceptance and reconstruction efficiency on the vertex position along the longitudinal direction. However, a relatively small percentage of events is lost with the vertex selection cut.

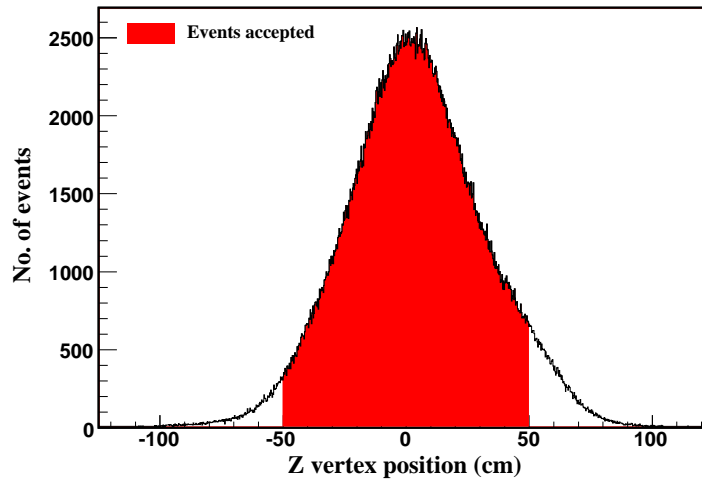


Figure 6.3: Distribution of z-position of the vertex in $Cu + Cu$ collisions at $\sqrt{s_{NN}} = 200$ GeV.

2. **Pseudo-rapidity** : As already mentioned before, with the narrow cut $-0.5 < \eta < 0.5$, the detection efficiency is rather insensitive to the position of the collision vertex. Figs. 6.4 and 6.5 show the efficiency uncorrected pseudo-rapidity η and ϕ distribution of all tracks produced within the TPC, respectively. The η distribution of the tracks is much smoother than the ϕ distribution. The reason for this is that the TPC consists of 24 anode sectors (12 per end) separated by finite gaps, where no charge detection is achieved. This produces a reduction of track reconstruction efficiency.
3. **Magnetic Field** : The magnetic field was set to 0.5 T for $Cu + Cu$ collisions at $\sqrt{s_{NN}} = 62.4$ and 200 GeV.
4. **Transverse momentum** : The transverse momentum, p_T , of a track is determined by fitting a circle through the x, y coordinates of the vertex and the points along the track. The net charge analysis was conducted with tracks from the TPC with transverse momentum in the range $0.2 < p_T < 5.0$ GeV/c with pseudo-rapidity $|\eta| < 0.5$.

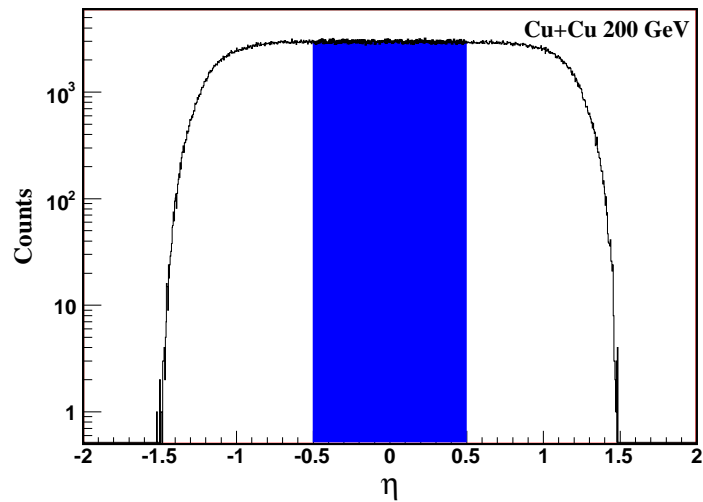


Figure 6.4: Uncorrected pseudo-rapidity distribution of all tracks produced within the TPC. Shaded portion shows the selected pseudo-rapidity range for the results presented in Section 4.2.

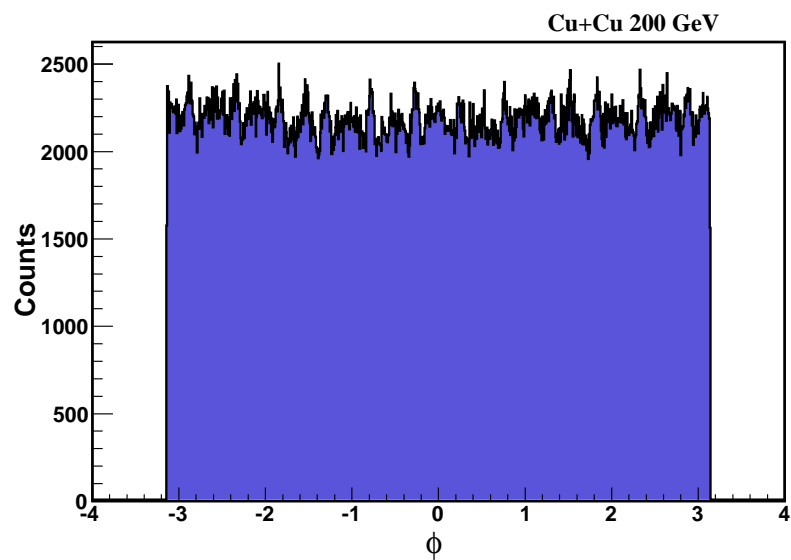


Figure 6.5: Uncorrected azimuthal angle distribution of all tracks produced within the TPC. Spikes and bumps structure result from reduced efficiency in the TPC sector boundary gaps.

Figs. 6.6 and 6.7 show the upper and the lower bound of the transverse momentum accepted for the analysis. The reason to limit the particle momenta to 5 GeV/c is that it ensures correct assignment of the particle charge. Given that the bulk of particle production takes place below 2 GeV/c, the inclusive analysis varies very little with the change in the upper bound. A finite magnetic field results in the track reconstruction efficiency of the TPC reducing progressively from a maximum value for $p_T > 200$ MeV/c to zero for $p_T < 100$ MeV/c. In order to minimize systematic effects due to varying efficiency, the lower bound in the transverse momentum of the tracks was restricted at 200 MeV/c.

5. **Track quality** : Good track quality was ensured by restricting the analysis to charged particle tracks producing more than 20 hits within the TPC where 50% of these hits were included in the final fit of the tracks. Tracks with at least 20 hits were accepted for the analysis in order to avoid track splitting. However, losing some percentage of tracks with this cut does not effect the present analysis.
6. **Distance of closest approach** : In order to minimize the contamination from secondary electron tracks and focus this analysis on primary tracks, i.e., particles produced at the $Cu + Cu$ collision vertex, tracks were accepted on the basis of their distance of closest approach (DCA) to the collision vertex. DCA is defined as the distance between the global partner of the track and the primary vertex position. A nominal cut of 3 cm was used for the results reported in this thesis. Fig. 6.8 shows the distance of closest approach distribution of the tracks.
7. **Dip angle cuts** : $Au + Au$ and $Cu + Cu$ data acquired during runs IV and V were subject to pile-up effects associated with large machine luminosity obtained during those years. The pile-up results in two collisions being mistaken as one and treated as such, thereby leading to excessive multiplicities and increased variances. Therefore, we carried out an extensive dip angle study in $Cu + Cu$ collisions at $\sqrt{s_{NN}} = 62.4$ and 200 GeV to understand the effect of luminosity and reject the pile-up events.

Dip angle is defined as the angle between the particle momentum and the drift direction, $\theta = \cos^{-1}(p_z/p)$. Figs. 6.9 and 6.10 together show average dip angle as a function of z-vertex position for all the six centralities in $Cu + Cu$ collisions at $\sqrt{s_{NN}} = 200$ GeV.

The dip angle is correlated with z-vertex position and features a width distribution which is a Gaussian at low luminosities. The width of the average dip angle distribution is narrow in central collisions but goes on becoming wider in peripheral collisions. Thus, we also study the mean and sigma of dip angle distribution with

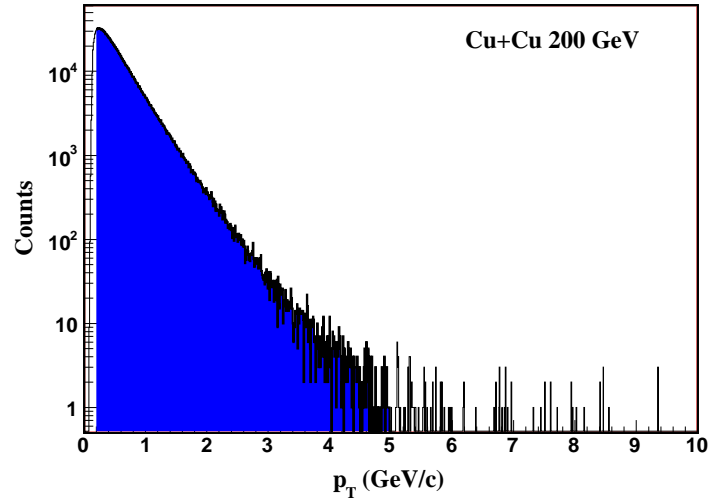


Figure 6.6: Transverse momentum distribution of the tracks from the TPC. Shaded portion shows the accepted upper bound of p_T .

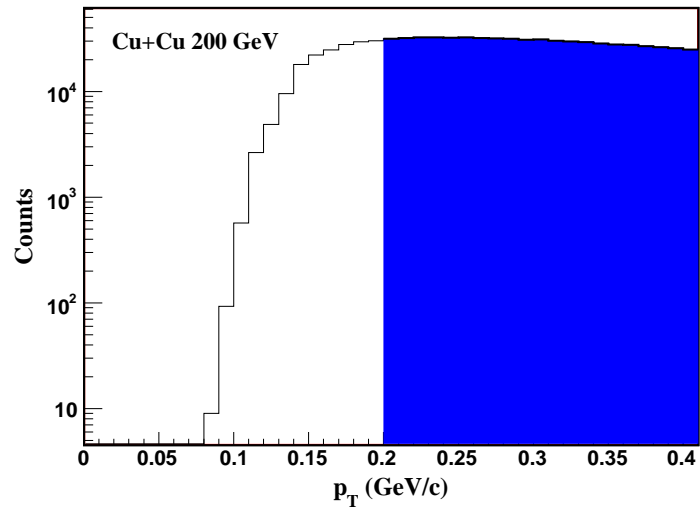


Figure 6.7: Zoom-in picture showing the lower bound of the transverse momentum of all tracks. Shaded portion shows the tracks were accepted with $p_T > 0.2$ GeV/c.

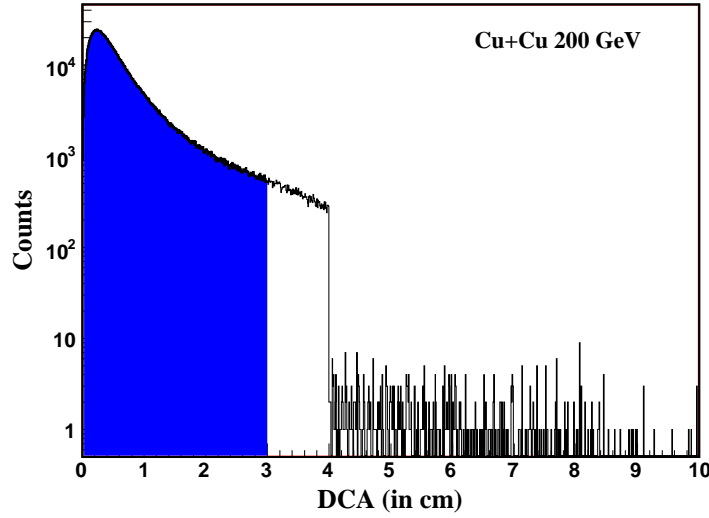


Figure 6.8: Distance of closest approach distribution of the all the tracks from TPC.

respect to z-vertex position. Mean and sigma values of the average dip angle distribution for each z-vertex position, for all centralities in $Cu + Cu$ collisions at $\sqrt{s_{NN}} = 200$ GeV can be seen in Fig. 6.11 and Fig. 6.12, respectively. Mean value of the average dip angle distribution varies from 0.05 radians to -0.05 radians for z-vertex position of -30 cm to 30 cm, respectively. In order to reject the pile-up events, we discard events which have mean value of the average dip angle more than two standard deviations from the mean at a particular z-vertex position. It is observed that the mean value of the average dip angle does not change with the centrality but the width of the distribution increases, Fig. 6.12. The value of σ increases from 0.02 to 0.08 from 0-10% (most central) to 50-60% (most peripheral) centrality.

Figs. 6.13(a) and 6.13(b) show primary multiplicity within $|\eta| < 1$ plotted as a function of the reference multiplicity before and after applying dip angle cuts in the data. Fig. 6.13(a) clearly shows a large number of low multiplicity events deviating away from the correlation band in the raw data set. However, despite cleaning the data using the dip angle cut, we observe a band labeled with a circle in Fig. 6.13(b) is still present. A closer look at primary multiplicity with $|\eta| < 1$ for all centralities in $Cu + Cu$ collisions at $\sqrt{s_{NN}} = 200$ GeV show residual tails strongest in most central collisions which are susceptible to pileup effects not correctible with the dip angle cut applied here. Figs. 6.14(a), 6.14(b), 6.14(c), 6.14(d), 6.14(e) and 6.14(f) show primary multiplicity distribution with $|\eta| < 1$ before and after applying dip angle cuts for various centrality selections. Dip angle cut was one of the source of systematic error in net charge fluctuations analysis (discussed in Section 6.2.1).

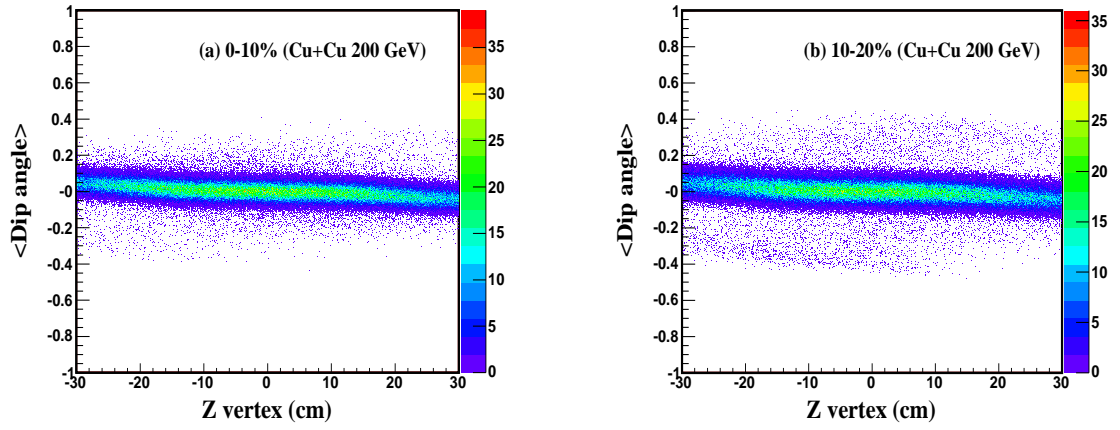
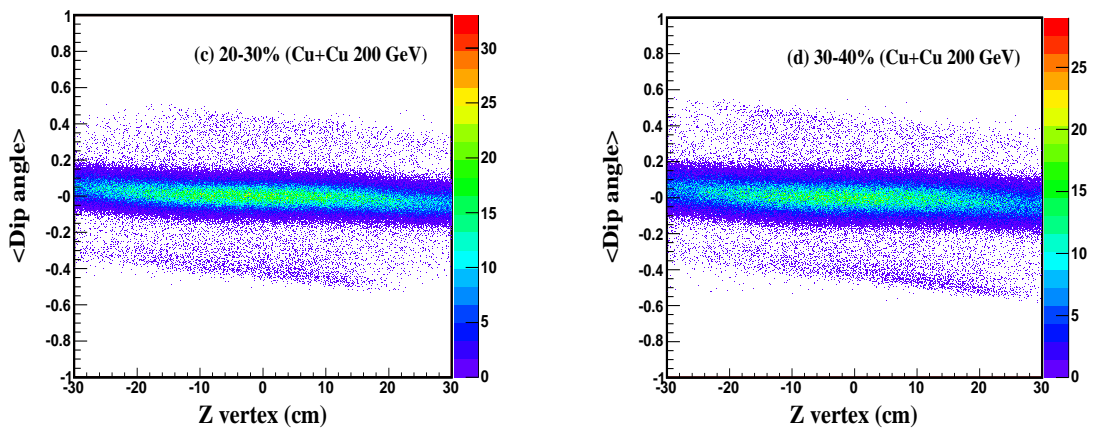


Figure 6.9: Average dip angle as a function of z-vertex position for (a) 0-10% centrality, (b) 10-20% centrality, in $Cu + Cu$ collisions at $\sqrt{s_{NN}} = 200$ GeV.



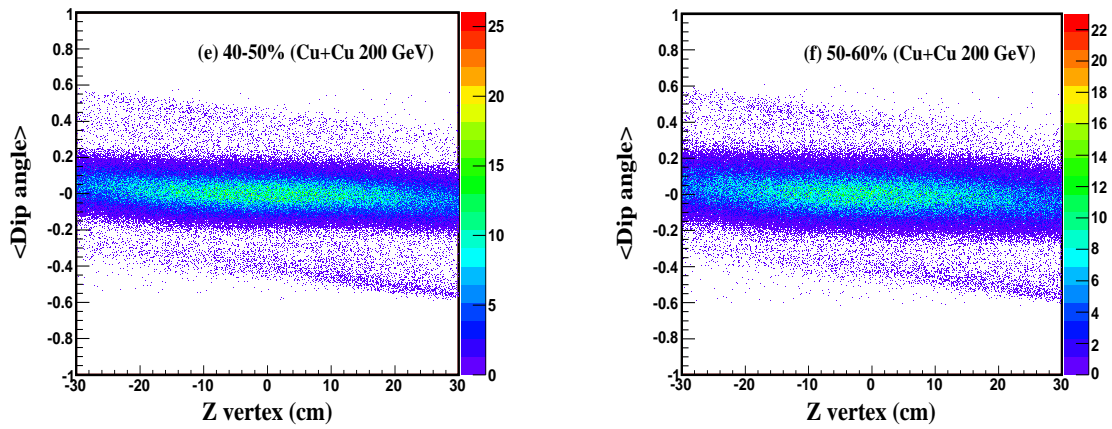
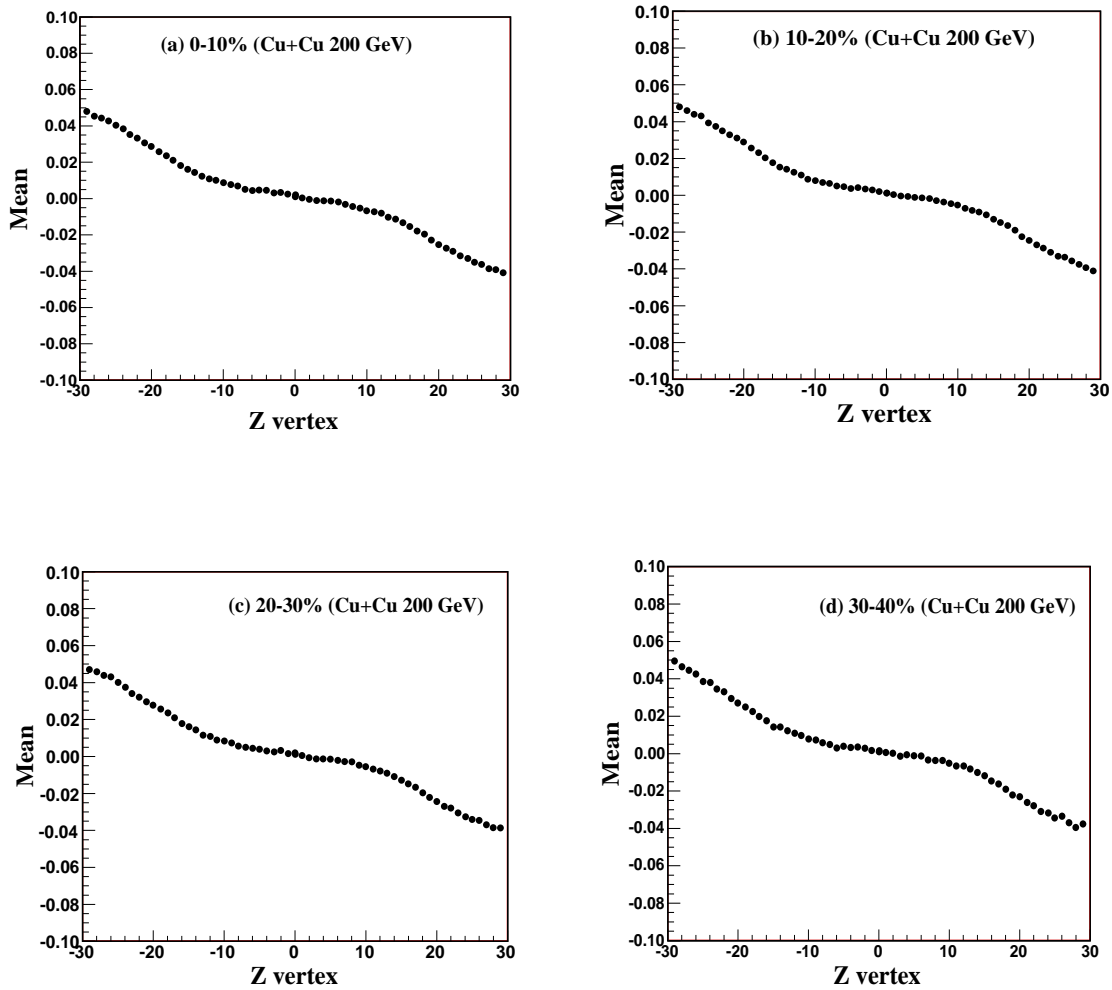


Figure 6.10: Average dip angle as a function of z-vertex position for (c) 20-30% centrality, (d) 30-40% centrality, (e) 40-50% centrality, and (e) 50-60% centrality, in $Cu + Cu$ collisions at $\sqrt{s_{NN}} = 200$ GeV.



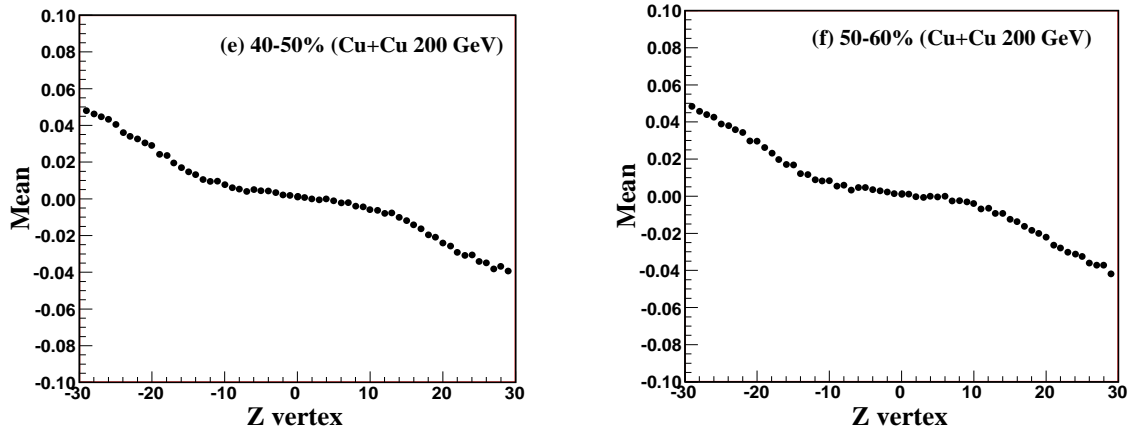
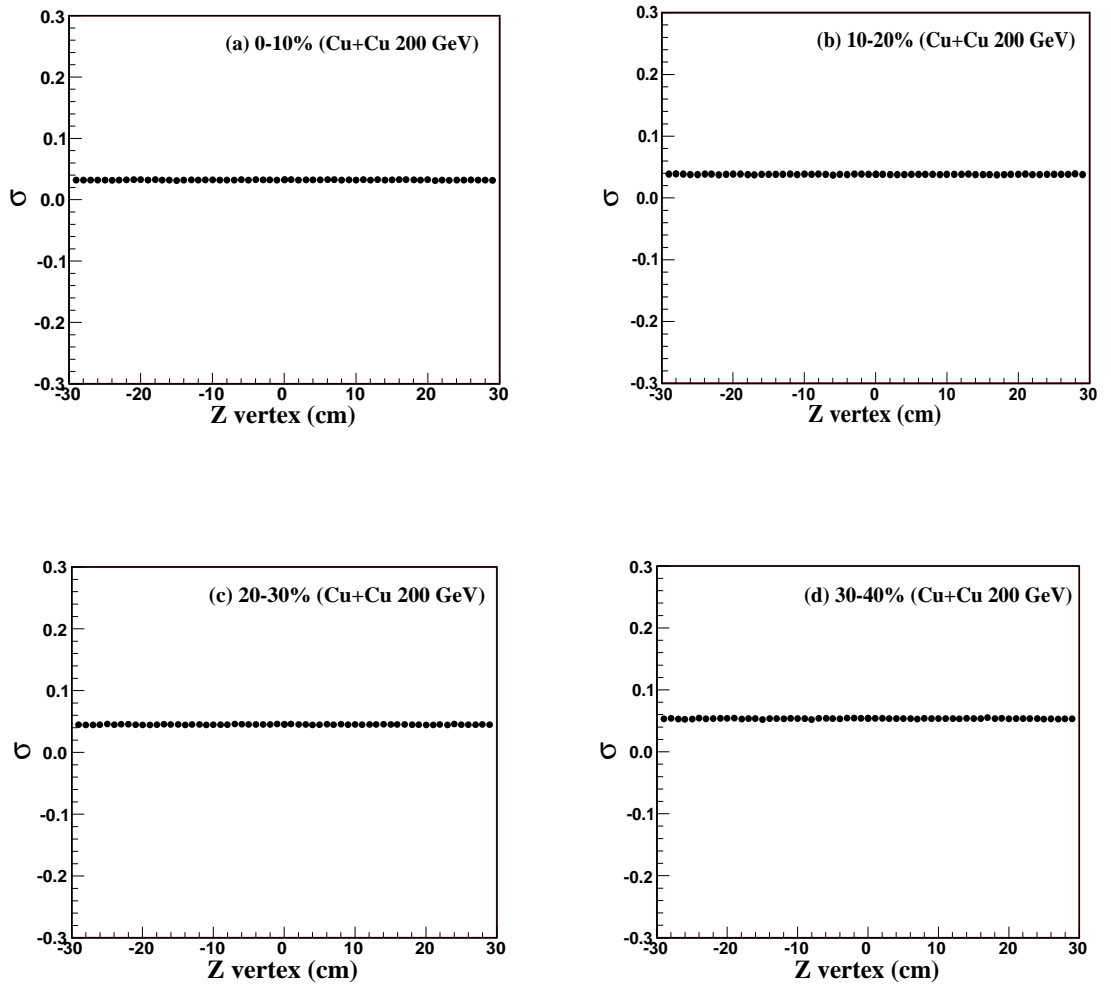


Figure 6.11: Mean values of the average dip angle distribution as a function of z -vertex position for (a) 0-10% centrality, (b) 10-20% centrality, (c) 20-30% centrality, (d) 30-40% centrality, (e) 40-50% centrality, and (e) 50-60% centrality, in $Cu + Cu$ collisions at $\sqrt{s_{NN}} = 200$ GeV.



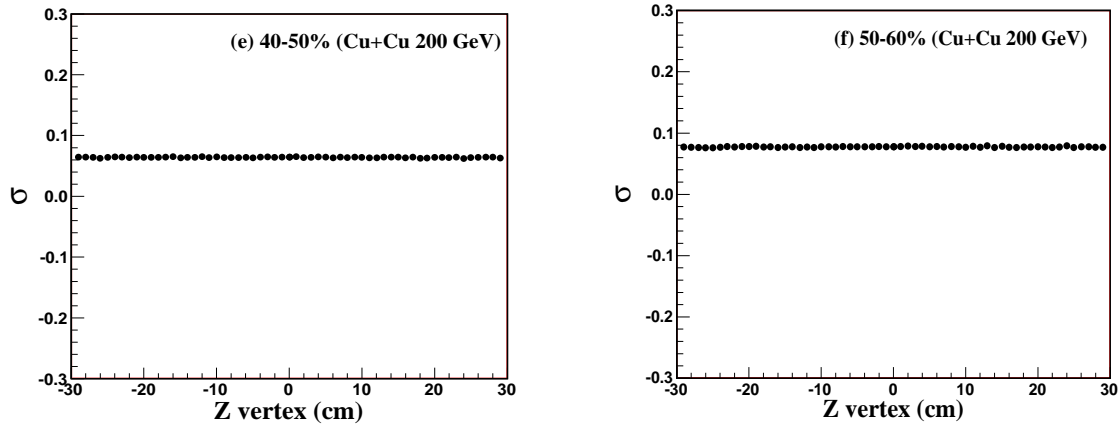


Figure 6.12: Sigma values of the average dip angle distribution as a function of z-vertex position for (a) 0-10% centrality, (b) 10-20% centrality, (c) 20-30% centrality, (d) 30-40% centrality, (e) 40-50% centrality, and (e) 50-60% centrality, in $Cu + Cu$ collisions at $\sqrt{s_{NN}} = 200$ GeV.

Further, to understand what causes some events to deviate away from the correlation band, we looked at the average reference multiplicity for a large number of different runs. Average reference multiplicity for all the run numbers analyzed are shown in Fig. 6.15 for $Cu + Cu$ collisions at the center of mass energy of 200 GeV. In principle, one expects all runs to have roughly the same average multiplicity. However, Fig. 6.15 shows some outlier runs either having large average reference multiplicity or having small average reference multiplicity. A total of 172 runs were studied for the present analysis and it was found that approximately 3% runs have average reference multiplicity more than three standard deviations away from the mean. Average reference multiplicity distribution for all these runs studied is shown in Fig. 6.16 for $Cu + Cu$ collisions at $\sqrt{s_{NN}} = 200$ GeV.

A similar study was also conducted for the TPC data in $Cu + Cu$ collisions at center of mass energy of 62.4 GeV. Pile-up events are not expected at this energy as the machine luminosity was not very high. Nevertheless, Fig. 6.17 shows a wide variation in the average reference multiplicity with respect to run number, for 349 runs analyzed at this energy. Interestingly a large number of run numbers on day 69 show two different values of the average reference multiplicity. Investigations showed that data were acquired using different combinations of trigger ID's on this day. At 62.4 GeV, ZDC alone was not efficient as a trigger detector. Therefore, a combined minimum bias trigger was put together from a combination of the ZDC and the BBC. The reason to use two detectors for trigger was that ZDC is efficient for low multiplicity events whereas BBC is efficient for central events, but inefficient for low multiplicity events. Some early runs on day 69 of data taking in run V were acquired with a combination of trigger ID's 76002 and 76011

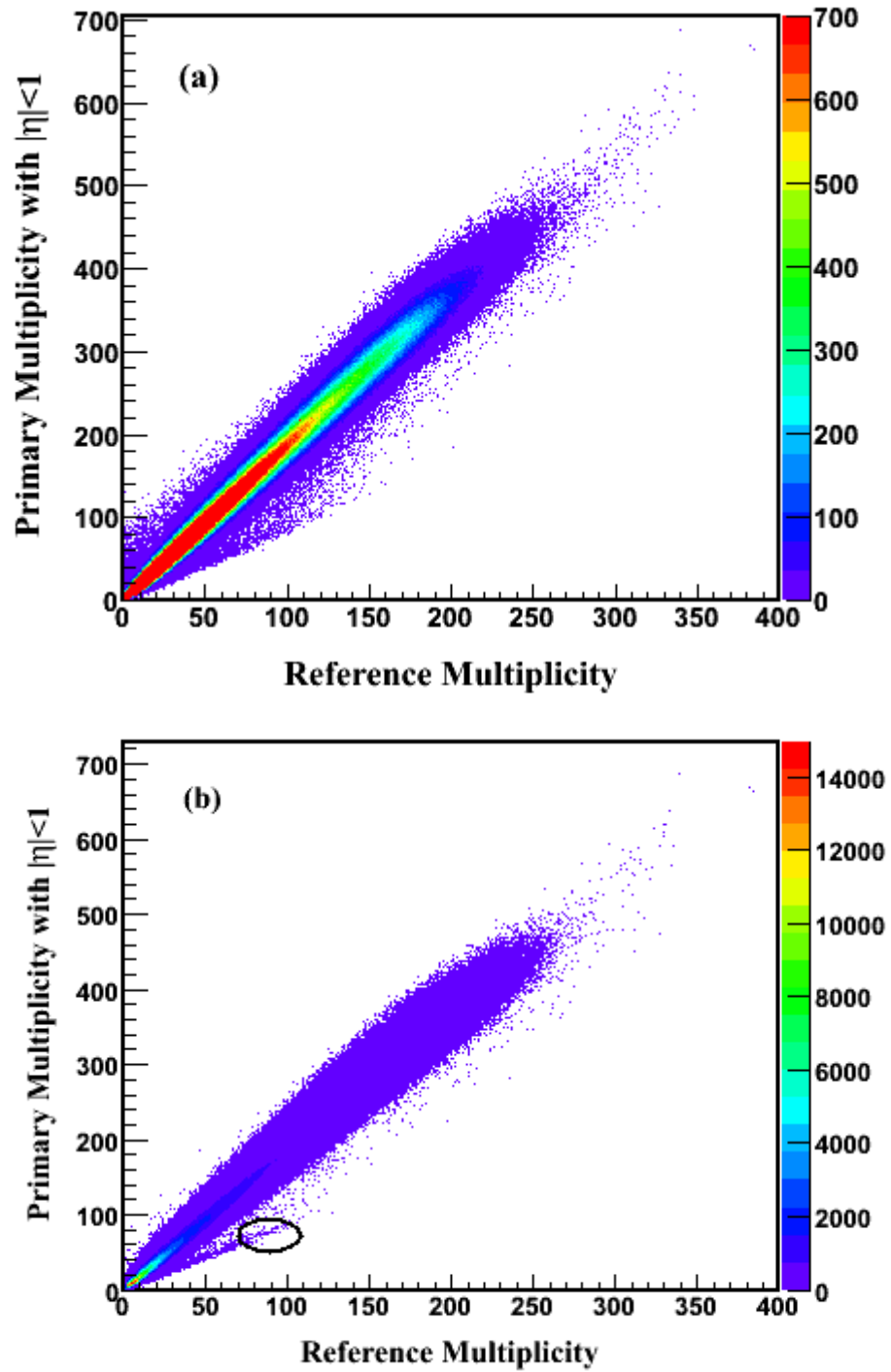
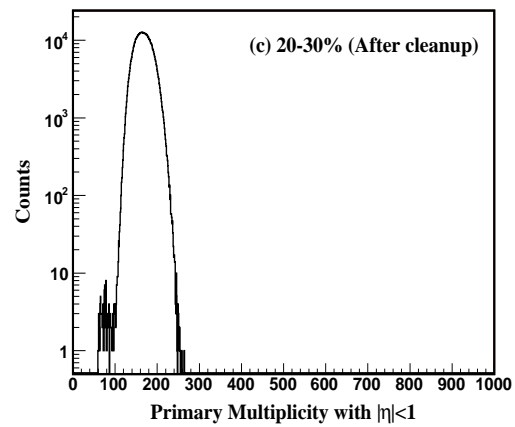
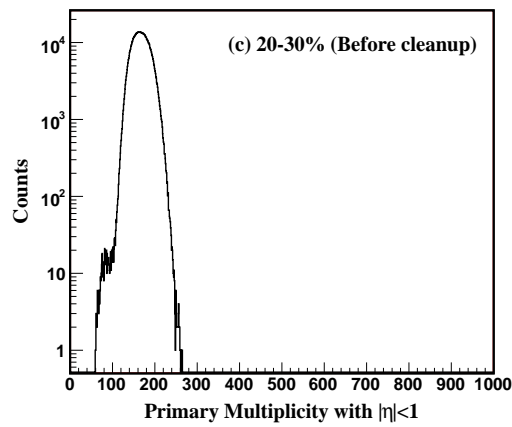
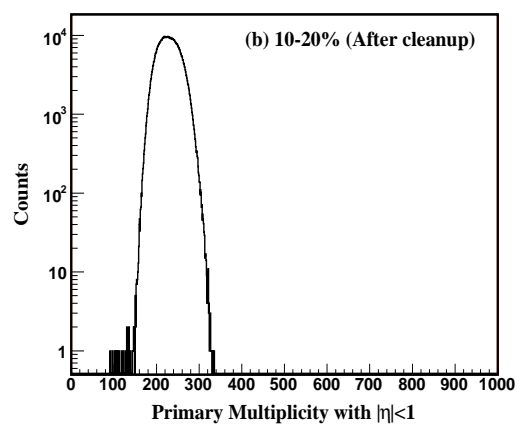
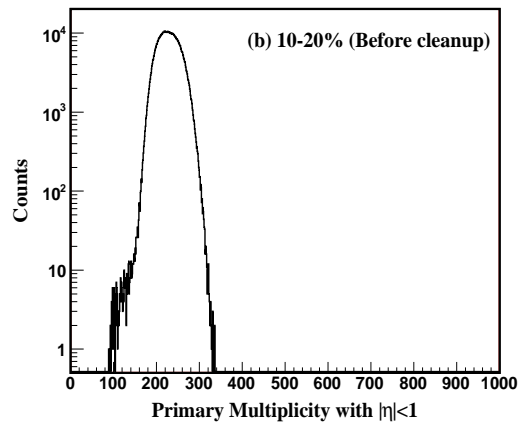
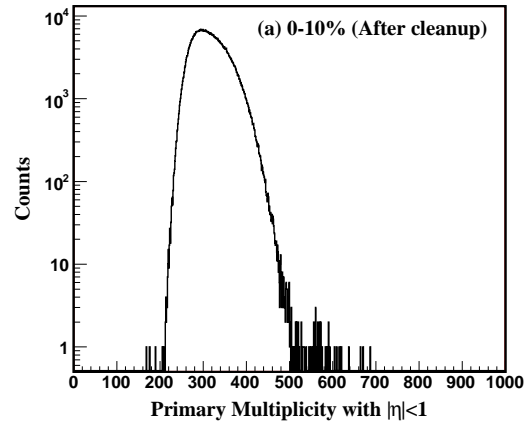
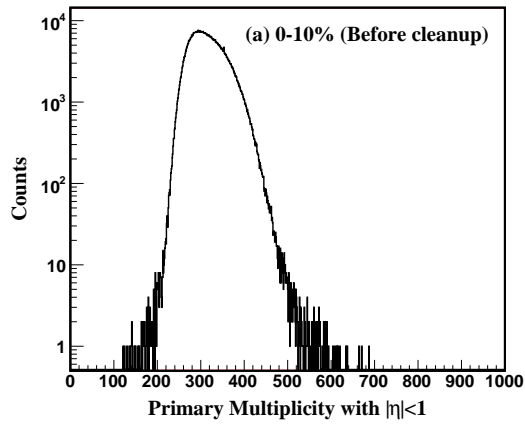


Figure 6.13: Primary multiplicity within $|\eta| < 1$ as a function of reference multiplicity (a) before applying dip angle cut, (b) after applying dip angle cuts for $Cu + Cu$ collisions at $\sqrt{s_{NN}} = 200$ GeV.



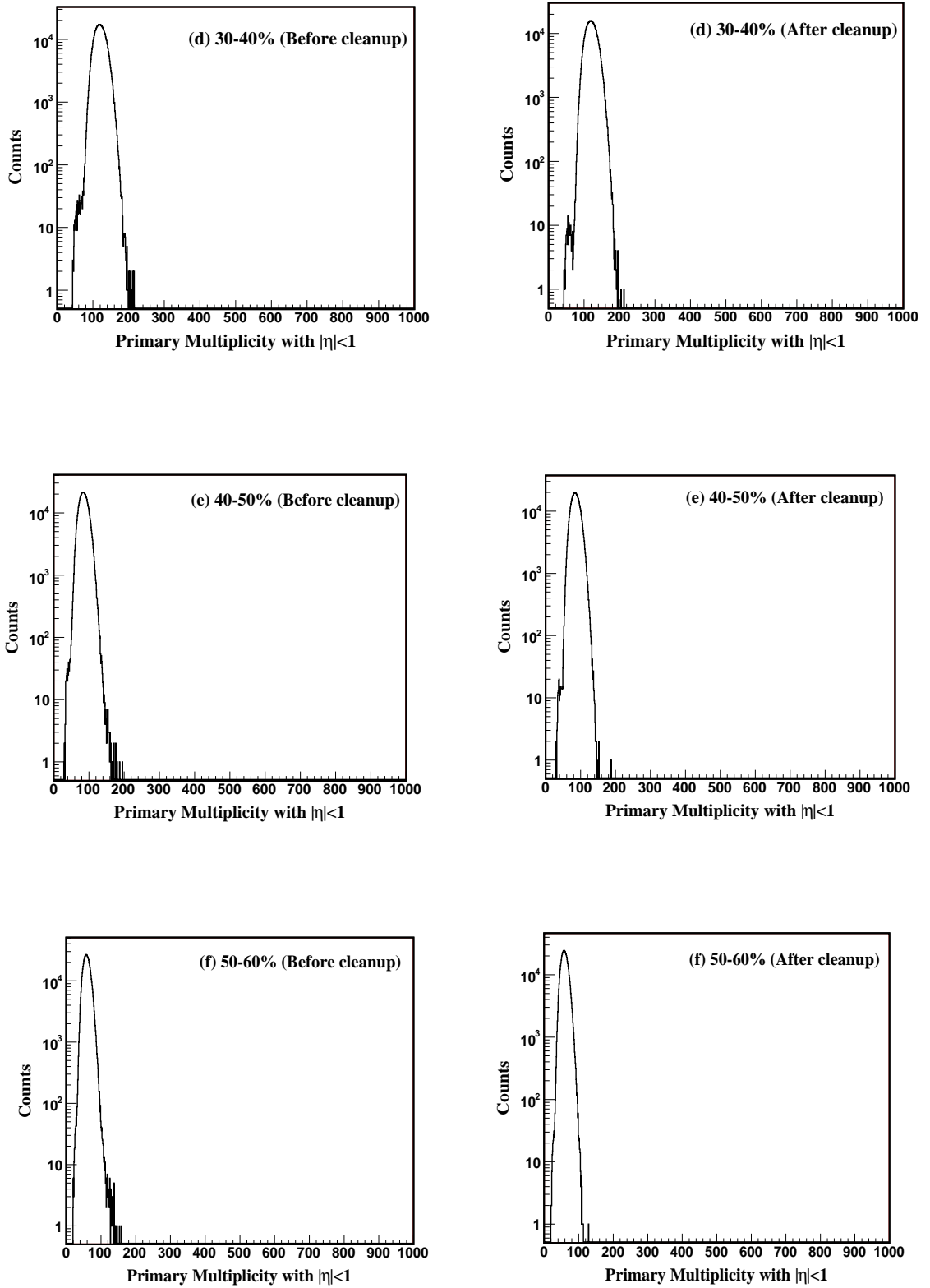


Figure 6.14: Primary multiplicity within $|\eta| < 1$ before and after cleanup (a) 0-10% centrality, (b) 10-20% centrality, (c) 20-30% centrality, (d) 30-40% centrality, (e) 40-50% centrality, and (e) 50-60% centrality, in $Cu + Cu$ collisions at $\sqrt{s_{NN}} = 200$ GeV.

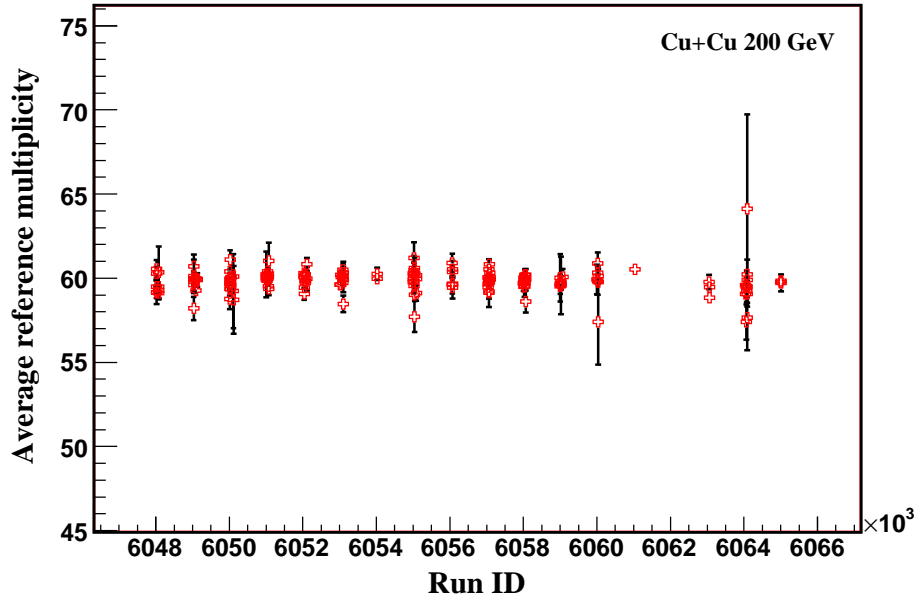


Figure 6.15: Average reference multiplicity as a function of run number for the TPC data in $Cu + Cu$ collisions at center of mass energy of 200 GeV.

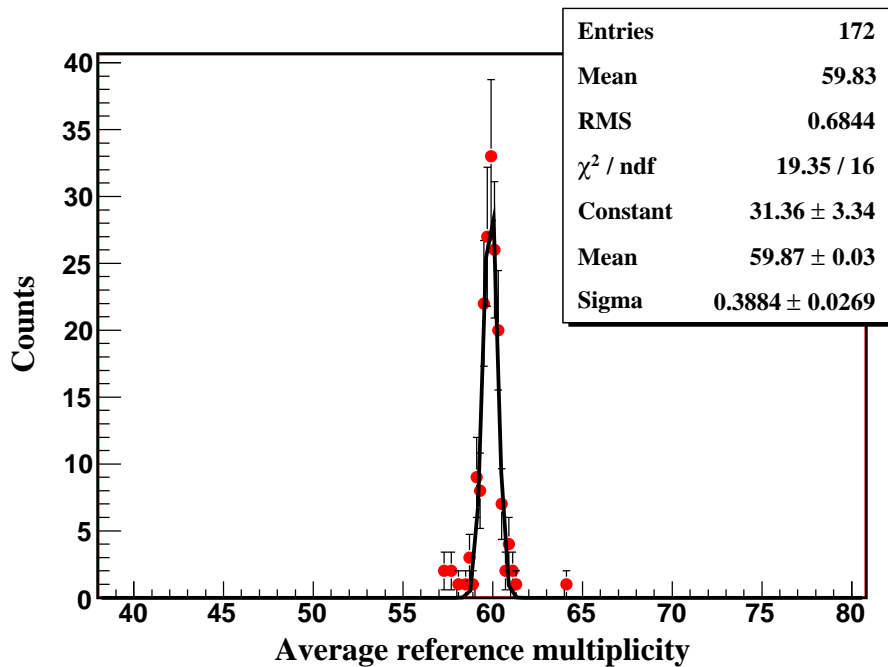


Figure 6.16: Average reference multiplicity distribution showing outlier runs for $Cu + Cu$ collisions at $\sqrt{s_{NN}} = 200$ GeV.

instead of 76007 and 76011. Trigger ID 76007 is cu-zdc-narrow (ZDC coincidence with 80 cm vertex cut), trigger ID 76011 is cu-bbc-narrow (BBC coincidence with 80 cm vertex cut) and trigger ID 76002 is cu-zdc-tacs (ZDC coincidence with no vertex cut). Thus, the reason for having two different values of average reference multiplicity is the use of the combination of trigger ID's 76002 and 76011 for run numbers before 6069077 instead of trigger ID's 76007 and 76011. This combination of trigger ID's 76007 and 76011 was used to acquire data in the minimum bias mode. Distribution of average reference multiplicity for 349 runs in $Cu + Cu$ collisions at 62.4 GeV is presented in Fig. 6.18. For the net charge fluctuations analyzes, we accepted runs with mean falling within three standard deviations of the mean for $Cu + Cu$ collisions at 62.4 and 200 GeV.

We studied primary multiplicity within $|\eta| < 1$ as a function of reference multiplicity after discarding these outlier runs. A comparison of primary multiplicity within $|\eta| < 1$ as a function of reference multiplicity before and after removing these outlier runs is shown in Fig. 6.19 and Fig. 6.20, respectively. We observe that removal of such runs only reduces the frequency but still doesn't remove all the events deviating away from the correlation band. Note that this is likely to have an effect on peripheral collisions only, i.e., 50-60% central collisions. Therefore, in order to evaluate the impact of finite pileup, we calculated $\nu_{+-,dyn}$ values obtained from $Cu + Cu$ collisions at $\sqrt{s_{NN}} = 62.4$ and 200 GeV with and without applying dip angle cuts. More details of such a study are listed in the subsequent section.

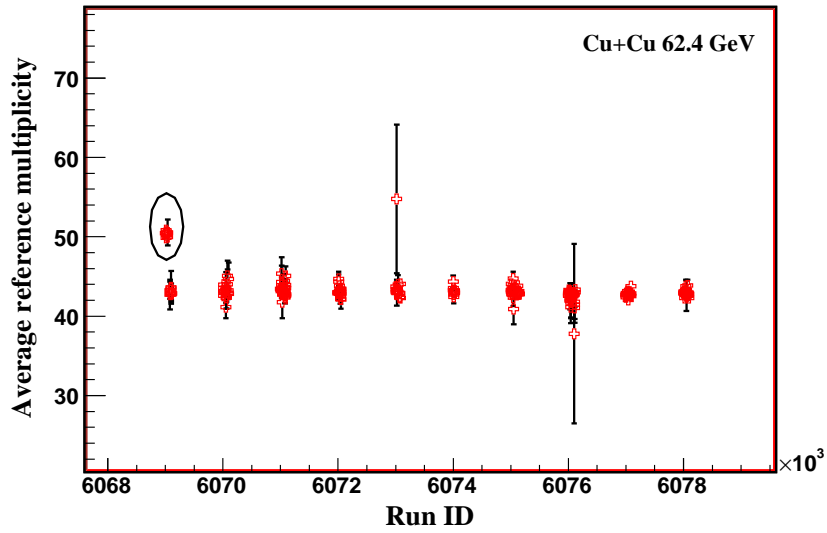


Figure 6.17: Average reference multiplicity as a function of run number for the TPC data in $Cu + Cu$ collisions at center of mass energy of 62.4 GeV.

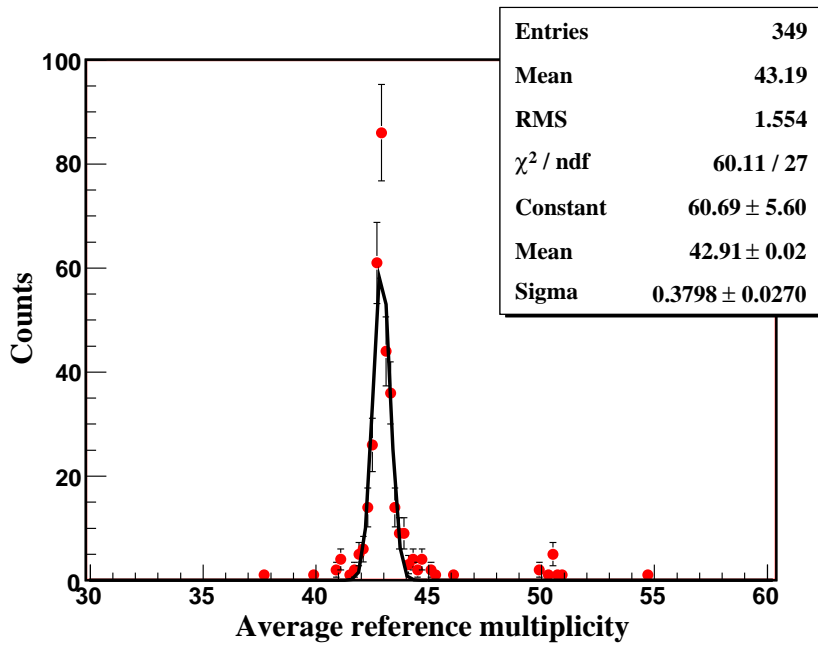


Figure 6.18: Average reference multiplicity distribution showing outlier runs for $Cu + Cu$ collisions at $\sqrt{s_{NN}} = 62.4$ GeV.

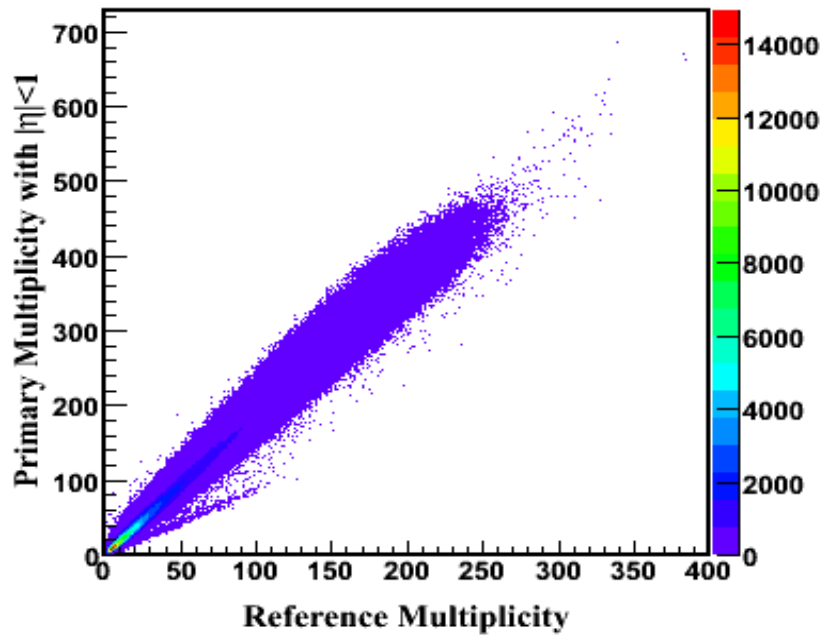


Figure 6.19: Primary multiplicity within $|\eta| < 1$ with respect to reference multiplicity in $Cu + Cu$ collisions at center of mass energy of 200 GeV obtained after applying the dip angle cuts, however outlier runs were not removed.

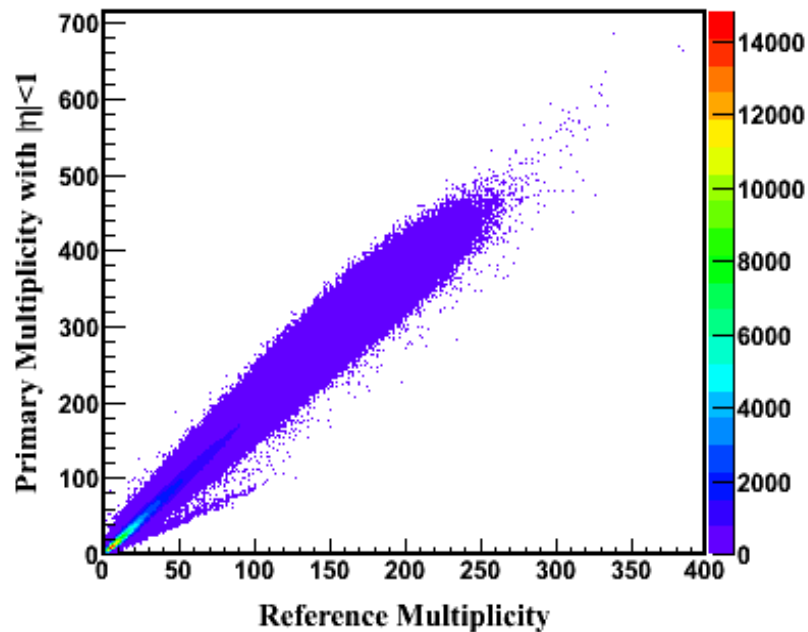


Figure 6.20: Primary multiplicity within $|\eta| < 1$ with respect to reference multiplicity in $Cu + Cu$ collisions at center of mass energy of 200 GeV obtained after applying the dip angle cuts as well as after removing the outlier runs.

6.2 Net Charge Fluctuation Results

Fig. 6.21 shows the measurements of the net charge dynamical fluctuations, $\nu_{+-,dyn}$, as a function of collision centrality in $Cu + Cu$ collisions at $\sqrt{s_{NN}} = 62.4$ and 200 GeV. Dynamical net charge fluctuations are finite at both energies and exhibit a similar decrease with the number of participating nucleons. The measured fluctuations also exhibit a modest dependence on beam energy, with $\nu_{+-,dyn}$ values being the largest at $\sqrt{s_{NN}} = 62.4$ GeV in peripheral collisions.

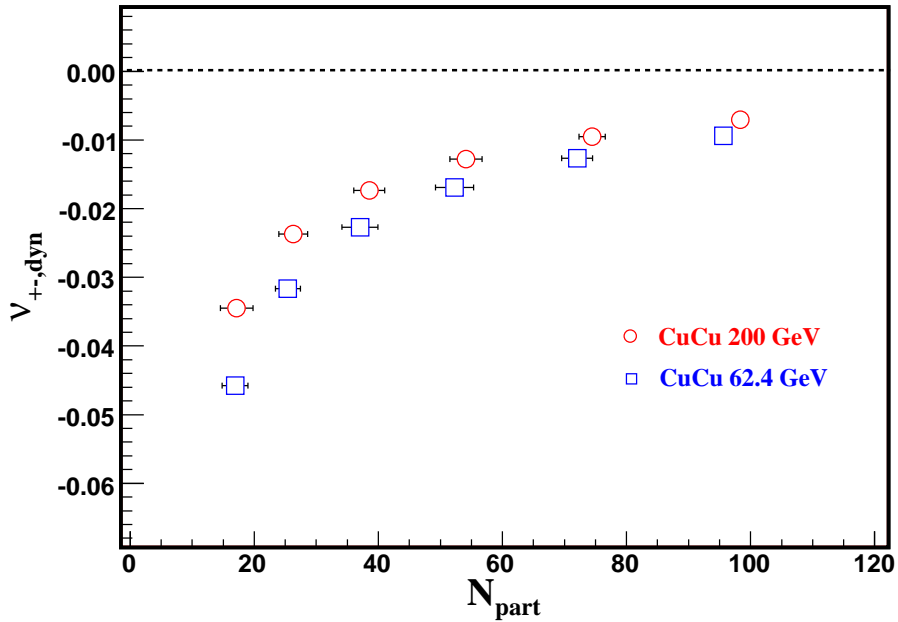


Figure 6.21: Net charge dynamical fluctuations, $\nu_{+-,dyn}$, of particles produced within pseudo-rapidity $|\eta| < 0.5$, as a function of the number of participating nucleons.

In order to study the system size dependence of net charge fluctuations, results from $Cu + Cu$ collisions at center of mass energy of 62.4 GeV and 200 GeV are compared with the results from $Au + Au$ collisions at center of mass energy of 20, 62.4, 130 [39] and 200 GeV, Fig. 6.22. Results of net charge fluctuation analysis in $Au + Au$ collisions at $\sqrt{s_{NN}} = 20, 62.4, 130$ [39] and 200 GeV and $p + p$ collisions at $\sqrt{s_{NN}} = 200$ GeV were obtained by C. Pruneau [45]. It is seen that $\nu_{+-,dyn}$ exhibits weak system size dependence.

We also studied the effect of calculating $\nu_{+-,dyn}$ values based on “wide bin method” and “unit bin method”. Wide bin method refers to calculating $\nu_{+-,dyn}$ values centrality wise whereas unit bin method refers to calculating $\nu_{+-,dyn}$ values at a fixed reference multiplicity with a binning of one. The weighted average of $\nu_{+-,dyn}$ was obtained for each centrality bin. The reason for carrying out such a study is that the factors like

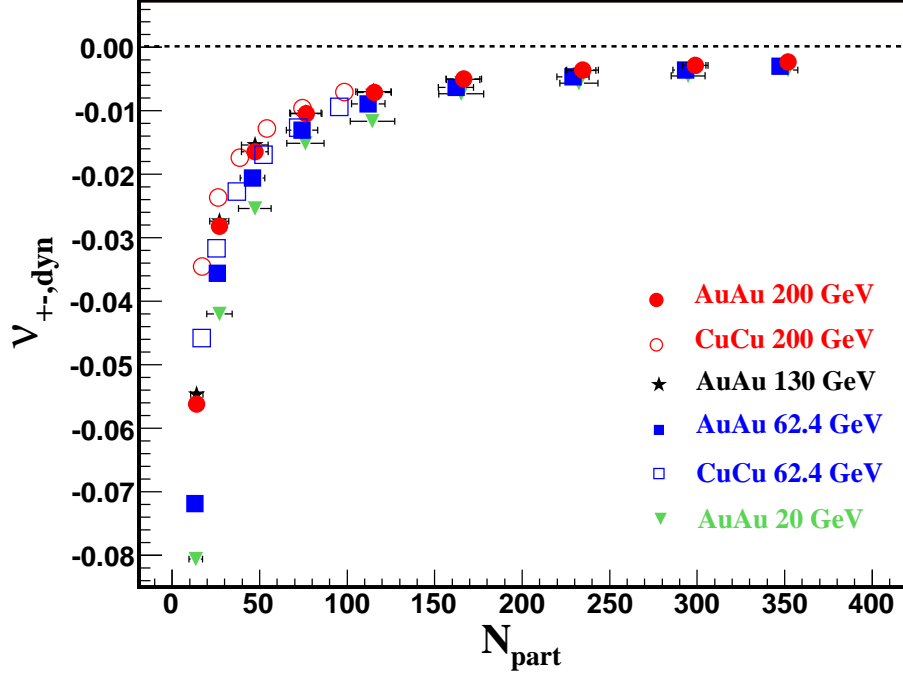


Figure 6.22: Comparison of net charge dynamical fluctuation, $\nu_{+-,dyn}$, results from $Cu + Cu$ collisions with $Au + Au$ collisions at various energies, of the particles produced within pseudo-rapidity $|\eta| < 0.5$, as a function of the number of participating nucleons.

$\langle N_+(N_+ - 1) \rangle$ are proportional to the variance of N_+ . So, when $\nu_{+-,dyn}$ values are calculated for a particular centrality bin, the width of the bin plays a significant role. In fact, the contribution from the width of a particular centrality bin may be so large that it can change the behavior of each term from sub-Poissonian to super-Poissonian. As a result, in order to eliminate the effect from the width of the bin and have contributions only from physics, the results shown in the Fig. 6.22 and in Table 6.5 are obtained from unit bin method and not from wide bin method. Independent emission of charged particles leads to a Poisson multiplicity distribution. Deviations from this shape, therefore, reveal correlations and dynamics in the production of final state particles. Positive correlations lead to a distribution wider than Poisson, whereas, negative correlations lead to a distribution narrower than Poisson [46][47]. Therefore, if the particle production in heavy-ion collisions is completely uncorrelated, then the three terms in Eq. 6.7 would be

unity, as shown in equations below.

$$Term\ I = \frac{\langle N_+(N_+ - 1) \rangle}{\langle N_+ \rangle^2} \quad (6.14)$$

$$Var(N_+) = \langle N_+ \rangle \quad (6.15)$$

$$\begin{aligned} \langle N_+ \rangle &= \langle N_+^2 \rangle - \langle N_+ \rangle^2 \\ \langle N_+ \rangle - \langle N_+^2 \rangle &= -\langle N_+ \rangle^2 \\ \langle N_+(N_+ - 1) \rangle &= \langle N_+ \rangle^2 \end{aligned} \quad (6.16)$$

Therefore using Eq. 6.16 in Eq. 6.14, we get

$$Term\ I = 1 \quad (6.17)$$

Thus, each term in Eq. 6.7 would be unity for a Poisson particle production.

Fig. 6.23 shows sub-Poissonian behavior of the individual terms in Eq. 6.7 for all centralities, based on unit bin method. For comparison, Fig. 6.24 shows super-Poissonian behavior of these terms based on wide bin method.

6.2.1 Systematic Error Studies

While $\nu_{+-,dyn}$ is a robust observable and shown to exhibit essentially no dependence of finite efficiencies, it may nonetheless be subject to finite systematic effects associated with the measurement process. We investigated dependencies of $\nu_{+-,dyn}$ on the longitudinal position of interaction vertex (z-vertex), the effect of resonance feed downs, event pile-up, track reconstruction and p_T resolution.

Table 6.3 and subsequent sub-sections give a detailed % systematic error contribution from all the sources for $Cu + Cu$ collisions at the center of mass energy of 200 GeV.

Table 6.3: Systematic error contribution from all sources for different centrality classes in $Cu + Cu$ collisions at the center of mass energy of 200 GeV.

Centrality	Vertex position	DCA	p_T	Electron	Dip angle
0-10%	0.89%	1.02%	1.37%	3.4%	0.009%
10-20%	2.0%	0.72%	0.768%	4%	0.08%
20-30%	2.3%	1.21%	1.19%	3.4%	0.05%
30-40%	0.44%	1.38%	1.582%	2.5%	0.05%
40-50%	0.92%	0.96%	2.82%	3.7%	0.05%
50-60%	0.77%	0.96%	1.55%	4.5%	0.02%

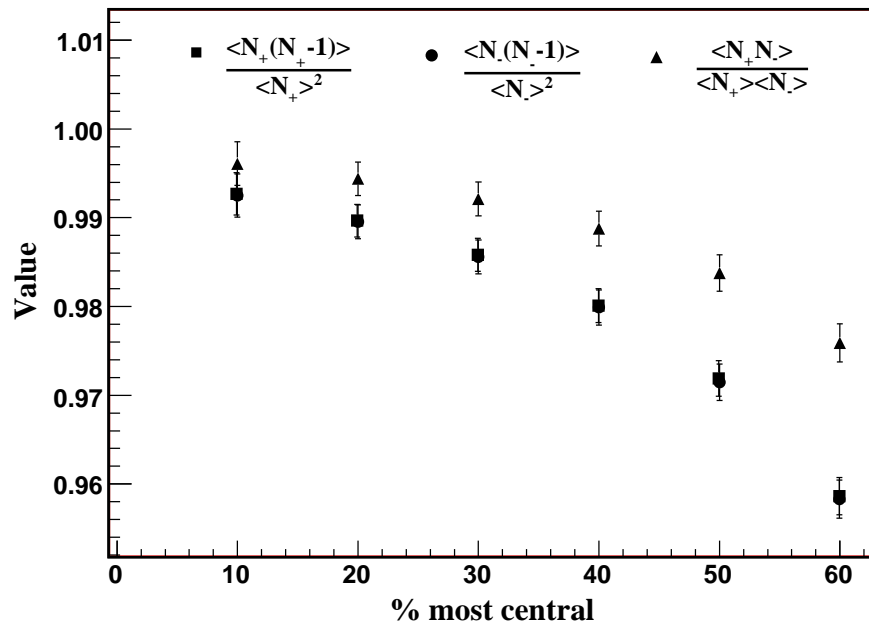


Figure 6.23: Individual terms in Eq. 6.7 obtained with unit bin method. With this method adopted the terms show sub-Poissonian behavior. The errors shown are statistical only.

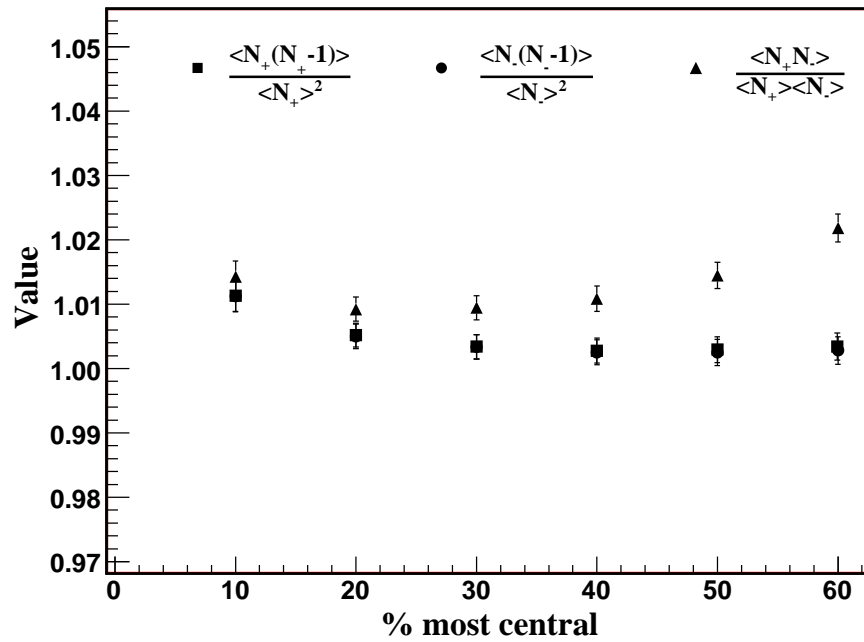


Figure 6.24: Individual terms in Eq. 6.7 obtained with wide bin method. With this method adopted the terms show super-Poissonian behavior. The errors shown are statistical only.

Acceptance in Z-vertex

Dependence of $\nu_{+-,dyn}$ on the longitudinal position of the interaction vertex might arise because of the finite acceptance of the Time Projection Chamber (TPC). We thus measured $\nu_{+-,dyn}$ by binning events according to the z-vertex in steps of 2.5 cm for positions varying from 30 to 5 cm. By construction $\nu_{+-,dyn}$ is expected to be robust against finite efficiency. However, the TPC presents a different η acceptance and reconstruction efficiency at different z-vertex positions. In order to verify the robustness of $\nu_{+-,dyn}$ on z-vertex position, we recalculated $\nu_{+-,dyn}$ values for every change in vertex position along the z-direction. Fig. 6.25 shows that $\nu_{+-,dyn}$ is indeed independent of z-vertex position. For better clarity the ratio of $\nu_{+-,dyn}$ value at a particular z-vertex value to $\nu_{+-,dyn}$ value at a z-vertex position of 30 cm w.r.t. z-vertex position is shown in Fig. 6.26. Results shown in Fig. 6.25 and 6.26 are obtained for 0-10% centrality in $Cu + Cu$ collisions at the center of mass energy of 200 GeV. The ratio is unity for any value of z-vertex position up to 5 cm. For z-vertex position less than 5 cm, the statistics reduces by a significant amount, so this study was not done. Our study clearly indicates that $\nu_{+-,dyn}$ is essentially independent of changes in acceptance is due to varying vertex position along the beam direction. Table 6.3 lists the systematic errors for different centralities due to z-vertex position.

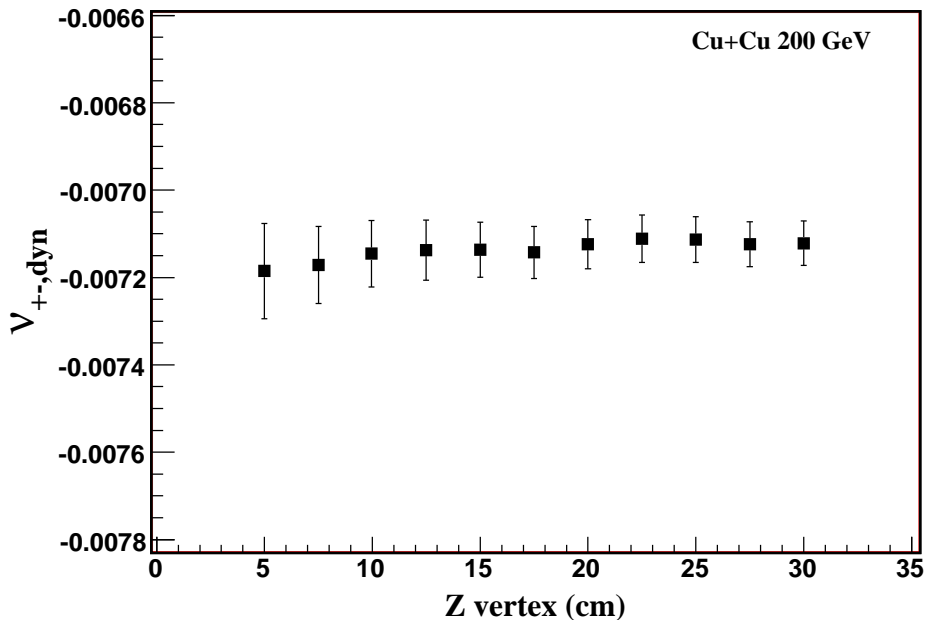


Figure 6.25: $\nu_{+-,dyn}$ as a function of vertex position along the beam direction in $Cu + Cu$ collisions at 200 GeV.

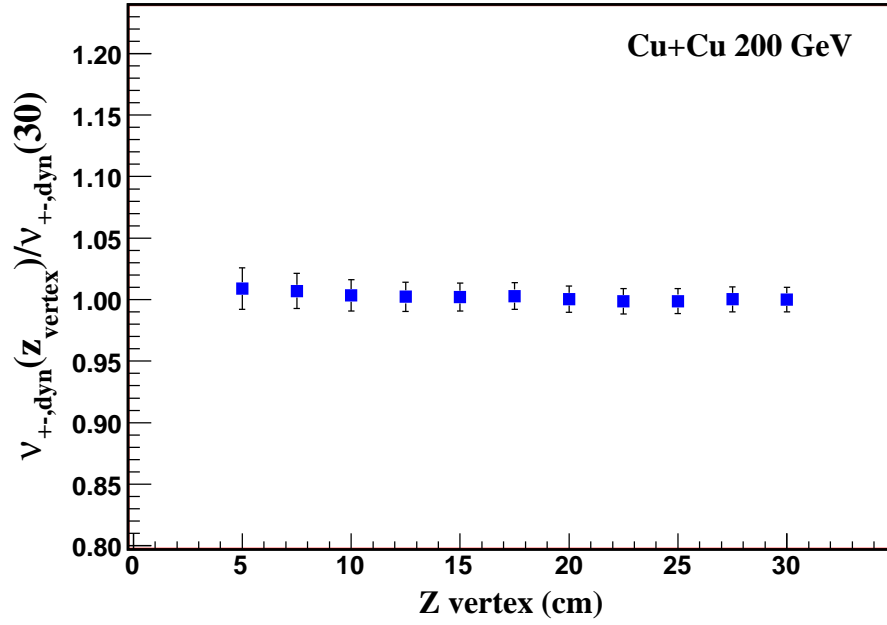


Figure 6.26: Ratio of $\nu_{+-,dyn}$ at a particular z-vertex to the $\nu_{+-,dyn}$ value at z-vertex position of 30 cm, w.r.t. z-vertex position..

Distance of Closest Approach

The $\nu_{+,dyn}$ measurement presented in this chapter is meant to be representative of particles produced in $Au + Au$, $Cu + Cu$ or $p + p$ collisions. By design, one thus seeks to eliminate effects from secondary decays (e.g., $\Lambda \rightarrow p + \pi^-$) or secondary particle production within the detector. This is accomplished by limiting the analysis to tracks that appear to originate from the collision vertex. Indeed a cut of 3 cm on the distance of closest approach of the tracks to the collision vertex selects primary particles and reduce those produced by decays and secondary interactions. A large value of DCA used in this analysis is chosen to account for finite DCA resolution and to maintain large track detection efficiency, needed especially for $\nu_{+-,dyn}$ analysis. However, with large value of DCA, one ends up counting particles produced by weak-decays (e.g., Λ or k_s^0) as primary particles. In particular with kaons (k_s^0) representing a finite fraction of all charged particle produced, one expects pions from such decays to increase the accepted charged particle multiplicity but with only a minor impact on the variance of the measured net charge. This implies $\nu_{+-,dyn}$ should be subject to a systematic decrease in magnitude when accepting weak-decays feed down. We thus studied $\nu_{+-,dyn}$ for smaller DCA cuts of 2 cm and found $|\nu_{+-,dyn}|$ value decreases by roughly 1% at all collision centralities thereby indicating feed-down from weak decays are of the order of one or a few percent, Table 6.3.

Effect of Secondary Particles

Another important source of secondary tracks not completely eliminated by DCA cut are electrons/positrons. While a finite electron primary yield is expected from decays of D-meson and B-mesons, from Dalitz decays of π^0 and η , the bulk of electrons/positrons observed in the STAR-TPC are from secondary interactions. Elimination of electrons/positrons is in principle partly achievable based on cuts on track dE/dx . However, because electrons and pions of low momenta experience similar energy loss in the TPC gas, a cut on the track dE/dx also eliminates a large amount of pions thereby effectively creating a “hole” in the pion acceptance (w.r.t. their momentum). We thus carried out the analysis by including the electrons/positrons. Again in this case, since electrons and positrons are typically created in pairs, this may lead to an increase in the integrated charged particle multiplicity with a little impact on the net charge variance. One thus expects inclusion of the electrons should produce a systematic shift in the magnitude of $\nu_{+,dyn}$. To verify this we carried out a measurement of $\nu_{+,-,dyn}$ when electrons (and consequently also pions) are eliminated on the basis of dE/dx cut. The dE/dx cut is accomplished on the basis of measurements of the truncated mean of the measured dE/dx samples along the track and the track momentum. Tracks were excluded whenever the measured dE/dx fell within two standard deviations of the mean value expected for electrons of a given momentum. We found that when electrons are eliminated, $|\nu_{+,-,dyn}|$ increases by as much as 3.5% in magnitude. This shift may, however, not be entirely due to the suppression of electrons. Indeed by eliminating electrons, one also reduce pion acceptance in transverse momentum. We have reported in Section 6.2.4 that $\nu_{+,-,dyn}$ exhibits finite dependence on the size of integrated longitudinal and azimuthal acceptances, similar (but weaker) dependence are expected on the transverse momentum. It is thus plausible that the shift by 3.5% may in part result from a reduction of pion acceptance. It is thus considered a source of systematic error as listed in Table 6.3 for different centralities.

Dip Angle

In order to estimate the effect of pileup, we calculated the $\nu_{+,-,dyn}$ values with and without the dip angle cuts. The values of net charge analysis measure, $\nu_{+,-,dyn}$, with and without dip angle cuts are listed in Tables 6.4 and 6.5 for $Cu + Cu$ collisions at the center of mass energies of 62.4 GeV and 200 GeV, respectively. We observe that $\nu_{+,-,dyn}$ is a robust variable and does not change appreciably with the dip angle cuts. We found that $\nu_{+,-,dyn}$ changes by less than 1% when dip angle cut is used for $Cu + Cu$ collisions at 62.4 as well as 200 GeV.

Table 6.4: The $\nu_{+-,dyn}$ values for with and without dip angle cuts for $Cu + Cu$ collisions at 62.4 GeV.

N_{part}	$\nu_{+-,dyn}$ without dip angle cuts	$\nu_{+-,dyn}$ with dip angle cuts	% difference
95.95	$-0.00940077 \pm 3.18e-05(stat)$	$-0.00939583 \pm 3.28e-05(stat)$	0.05%
74.47	$-0.0126273 \pm 3.38e-05(stat)$	$-0.0126001 \pm 3.45e-05(stat)$	0.21%
54.10	$-0.0168684 \pm 4.56e-05(stat)$	$-0.0169053 \pm 4.67e-05(stat)$	0.21%
38.56	$-0.0225939 \pm 6.28e-05(stat)$	$-0.022682 \pm 6.44e-05(stat)$	0.38%
26.29	$-0.0315162 \pm 9.07e-05(stat)$	$-0.0316475 \pm 9.29e-05(stat)$	0.41%
17.61	$-0.0456689 \pm 0.000137835(stat)$	$-0.0457942 \pm 0.000140628(stat)$	0.27%

Table 6.5: The $\nu_{+-,dyn}$ values for with and without dip angle cuts for $Cu + Cu$ collisions at 200 GeV.

N_{part}	$\nu_{+-,dyn}$ without dip angle cuts	$\nu_{+-,dyn}$ with dip angle cuts	% difference
98.34	$-0.0071222 \pm 3.49e-05(stat)$	$-0.00712153 \pm 3.58e-05(stat)$	0.009%
74.47	$-0.0096029 \pm 3.63e-05(stat)$	$-0.00961136 \pm 3.74e-05(stat)$	0.08%
54.10	$-0.0129442 \pm 4.90e-05(stat)$	$-0.0129516 \pm 5.03e-05(stat)$	0.05%
38.56	$-0.0176506 \pm 6.85e-05(stat)$	$-0.0176409 \pm 6.99e-05(stat)$	0.05%
26.29	$-0.0243281 \pm 9.78e-05(stat)$	$-0.0243401 \pm 9.97e-05(stat)$	0.05%
17.61	$-0.0350276 \pm 0.000146925(stat)$	$-0.0350359 \pm 0.000149658(stat)$	0.02%

Transverse Momentum

We also checked the effect of efficiency variation within the acceptance of interest. The efficiency is known, in particular, to progressively reducing from a maximum value for $p_T > 200$ MeV/c to zero for $p_T < 100$ MeV/c. We determined an upper bound of the effect of p_T dependence by measuring $\nu_{+-,dyn}$ with p_T thresholds of 150 MeV/c and 200 MeV/c. We found that the changes in $\nu_{+-,dyn}$ are typically negligible within the statistical accuracy of our measurement and amount to at the most 1.5%. The systematic errors on account of these are listed in Table 6.3.

6.2.2 Beam Energy Dependence

A study of the net charge fluctuation dependence on the beam energy is of interest as it can potentially reveal an increase or decrease in the magnitude of the fluctuations and signal of the formation of QGP. We have conducted our study primarily on the basis of the 0-5% and 0-10% most central collisions. Extensions to less central and peripheral collisions are possible but subject to additional uncertainties raised by finite systematic errors involved during the collision centrality determination.

As already stated in the introduction, charge conservation and the finite size of the colliding system intrinsically limit the magnitude of the net charge correlations. Intuitively, one expects charge conservation effects to become progressively smaller with increased produced charged particle multiplicity at higher energies. Charge conservation effects are nonetheless finite at all beam energies and produced multiplicities. Specifically, one estimates charge conservation implies a minimal value of order $\nu_{+-,dyn} = -4/N_{4\pi}$, where $N_{4\pi}$ is the *total* charged particles produced in an event in full azimuth [13]. This estimate is obtained for particle emission with uniform pseudorapidity distribution. Observed rapidity densities are however not uniform, charge conservation effects may therefore be stronger than the above minimal value. We nonetheless use the above expression to estimate the effects of charge conservation on the net charge fluctuations. Corrections for finite system size and charge conservation require knowledge of the total charged particle multiplicity. Although no experiment at RHIC actually measure particle production with complete coverage, but the PHOBOS experiment comes closest to the rapidity coverage of $|\eta| < 5.4$ over 2π azimuthal angles and a minimum transverse momentum of order of 100 MeV/c. The PHOBOS collaboration has published data on total measured charged particle multiplicities in $Au + Au$ collisions at $\sqrt{s_{NN}} = 20, 130$ and 200 GeV only [48–52]. The data for $Cu + Cu$ collisions at $\sqrt{s_{NN}} = 62.4$ and 200 GeV has been taken from Ref. [53]. We calculate charged particle multiplicities for $Au + Au$ collisions at $\sqrt{s_{NN}} = 62.4$ GeV based on charged particle multiplicity per participants reported by PHOBOS [54]. We correct for differences in collision centralities between the PHOBOS and STAR

measurements using a linear interpolation based on the two most central bins measured by PHOBOS. Collision centrality, adopted total multiplicities, uncorrected and charged conservation corrected values of $\nu_{+-,dyn}$ are listed in Table 6.6 for all four energies for $Au + Au$ collisions and two energies for $Cu + Cu$ collisions.

Table 6.6: Collision centrality, total multiplicity, uncorrected and corrected $\nu_{+-,dyn}$ values for four energies in $Au + Au$ collisions and two energies in $Cu + Cu$ collisions.

System & Energy	Centrality	N_{ch}	$\nu_{+-,dyn}$	$\nu_{+-,dyn}^*$
Au + Au 200 GeV	351.9	5092	-0.0024	-0.00163
Au + Au 130 GeV	351.6	4196	-0.0021	-0.00121
Au + Au 62.4 GeV	347.6	2788	-0.0029	-0.00146
Au + Au 20 GeV	351.9	1683	-0.0035	-0.00113
Cu + Cu 200 GeV	98.34	1410	-0.0071	-0.00426
Cu + Cu 62.4 GeV	95.59	790	-0.0093	-0.00423

The measured $\nu_{+-,dyn}$ and corrected $\nu_{+-,dyn}^{corr}$ values of the dynamical net charge fluctuations are shown in Fig. 6.27 as a function of beam energy for 0-5% central $Au + Au$ collisions with solid squares (in red color online) and for 0-10% central $Cu + Cu$ collisions with solid circles (in black color online). Displayed error bars include statistical errors involved in the measurement of $\nu_{+,dyn}$ and the total charged particle multiplicities as well as estimates of the systematic errors (shown by boxes) involved in the measurements of both quantities. Data from this work are compared to the corrected dynamical net charge fluctuation values by the PHENIX and CERES collaborations. The PHENIX point (triangle, in blue color online) is calculated from data published on the basis of ω_Q observable [36] and corrections based on total multiplicities measured by PHOBOS (as per values shown in Table 6.6). The CERES data points, obtained for $Pb + Au$ collisions, are extracted from their published results [55]. They include estimates of the systematic errors (open rectangles) as well as statistical errors (solid lines).

We first note that the PHENIX and STAR points measured at 130 GeV are in qualitative agreement as already reported in Ref. [39, 45]. The large error bar associated with the PHENIX measurement stems mainly from systematic uncertainties associated with corrections for finite detection efficiencies (see discussion in [39]). We observe additionally that STAR 20 GeV measurement is in agreement with a measurement by CERES at the same energy. Measurements at $Cu + Cu$ collisions show a sharp increase in magnitude, however, ν^* values at 62.4 and 200 GeV are identical within errors. This difference between $Cu + Cu$ and $Au + Au$ values can partly be attributed to the difference of number of participating nucleons in $Au + Au$ and $Cu + Cu$ collisions at 0-5% and 0-10%

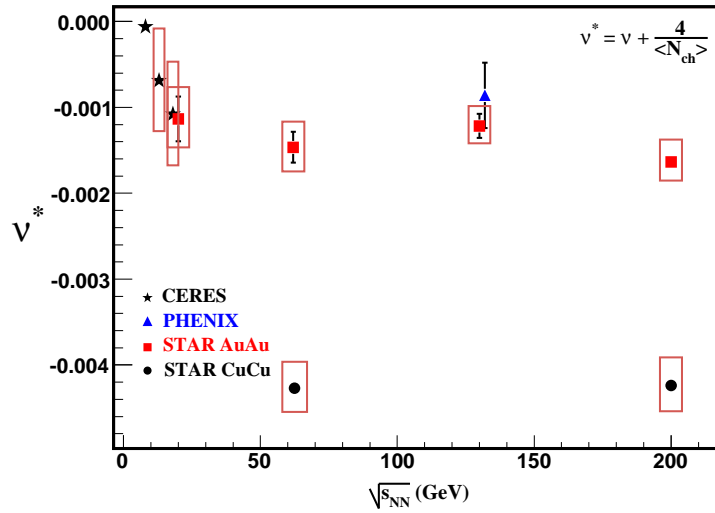


Figure 6.27: Corrected values of dynamical net charge fluctuations ($\nu_{+,-,dyn}^{corr}$) as a function of $\sqrt{s_{NN}}$ (in color online). See text for details.

centralities, respectively. However, the magnitude of corrected dynamical fluctuations in $Cu + Cu$ collisions when scaled by the ratio of number of participants in $Cu + Cu$ collisions to number of participants in $Au + Au$ collisions is $-0.00099521 \pm 1.645e-5(\text{stat}) \pm 6.17e-5(\text{sys})$ and $-0.00101422 \pm 1.63e-5(\text{stat}) \pm 8.21e-5(\text{sys})$ at $\sqrt{s_{NN}} = 62.4$ & 200 GeV, respectively. We note that CERES reports a dramatic reduction of the magnitude of the fluctuations at the lowest energy measured at SPS. We thus conclude that net charge fluctuations corrected for charge conservation show no obvious beam energy dependence in the range from 20 to 200 GeV but exhibits system size dependence. A sharp decrease in magnitude at the lowest SPS energies and an increase in $Cu + Cu$ collisions is worth noting.

Measurements at the SPS have shown that particle production at 5 GeV and lower energies are dominated by baryons while meson and resonance production become increasingly dominant at the energies above 20 GeV. This suggests the sharp change in dynamical net charge fluctuations below 20 GeV might be due to this shift in particle production dominance.

6.2.3 Collision Centrality Dependence

The observed monotonic reduction of the magnitude of $\nu_{+,-,dyn}$ with increasing number of participants, seen in Fig. 6.22, arises principally from the progressive dilution of two-particle correlation function when the number of particle sources is increased. In fact, one expects $\nu_{+,-,dyn}$ to be strictly inversely proportional to the number of participating nucleons or the produced particle multiplicity if $Au + Au$ collisions actually involve mutually

independent nucleon-nucleon interactions, and rescattering effects may be neglected. We investigate the possibility of such a scenario by plotting the dynamical fluctuations scaled by the measured particle multiplicity density ($dN/d\eta$) versus $dN/d\eta$ in Fig. 6.28(a). Data from $Au + Au$ collisions at various energies are shown with solid symbols while data from $Cu + Cu$ collisions at 62.4 and 200 GeV are shown with open symbols. Values of $dN/d\eta$ used for the scaling correspond to efficiency corrected charged particle multiplicities measured by STAR [56] and PHOBOS [48–53].

The first observation is the magnitude of $\nu_{+-,dyn}$ scaled by $dN_{ch}/d\eta$ for $Au + Au$ 200 GeV data is significantly different from the rest of the dataset. This could be attributed solely to multiplicity effects. We additionally observe that all four distributions exhibit the same qualitative behavior: the amplitude $|dN/d\eta \nu_{+-,dyn}|$ is smallest for peripheral collisions, and rises monotonically by 40% for central collisions. Clearly, the observed $|dN/d\eta * \nu_{+-,dyn}|$ is not invariant with increasing collision centrality. The dashed line in the figure corresponds to charge conservation effect and the solid line represents the prediction for a resonance gas. The charge conservation contribution for $Au + Au$ most central collisions at $\sqrt{s_{NN}} = 200$ GeV amounts to $-0.00078 \times 670.652 = 0.5264 \pm 0.05(\text{stat})$. Similarly, charge conservation contribution in $Cu + Cu$ most central collisions at $\sqrt{s_{NN}} = 200$ GeV amounts to $-0.0028 \times 156.689 = 0.56(\text{stat})$. The dashed line shown in the figure is for $Au + Au$ most central collisions at the center of mass energy of 200 GeV. The figure clearly indicates dynamical fluctuations are not only finite but rather large.

Further, we compare our measurements of the dynamical net charge fluctuations to the predictions based on the thermal models [43]. For this, we calculated D from $\nu_{+-,dyn}$ using Eq. 6.13. We observe that D decreases from $3.37 \pm 0.049(\text{stat})$ for the most peripheral collisions measured in $Au + Au$ collisions at $\sqrt{s_{NN}} = 200$ GeV to $2.96 \pm 0.05(\text{stat})$ in central collisions. The corresponding values of D for $Cu + Cu$ collisions at the center of mass energy of 200 GeV are 3.74 and 3.4 for the peripheral and central collisions, respectively. The value of D for most central $Au + Au$ collisions at 200 GeV approaches the value expected for a resonance gas [43]. It is worth noting that these values are much larger than expected for a quark-gluon gas undergoing fast hadronization and freeze-out [43]. However, it is not possible to draw a definite conclusion for the existence/non-existence of a deconfined phase during the collisions from these results. The reason for this is that incomplete hadronization could also lead to larger fluctuations than expected for a QGP.

Indeed, changes in the collision dynamics with increasing centrality are clearly manifest from these data. The PHOBOS collaboration has reported that the charged particle multiplicity per participant nucleon pair rises dramatically with increasing number of participants. They reported a value of $dN_{CH}/d\eta / (\langle N_{part} \rangle / 2)$ of order 3.9 in central 200 GeV $Au + Au$ collisions compared to a value of 2.5 in $p + p$ collisions at the same energy

[50]. This amounts to a 56% increase, similar in magnitude to that of $|dN/d\eta\nu_{+-,dyn}|$ measured in this work. We thus infer much of the centrality dependence of $|dN/d\eta\nu_{+-,dyn}|$ is due to the rise of $dN_{CH}/d\eta/(\langle N_{part} \rangle / 2)$ with increasing N_{part} . In order to validate this assertion, we plot in Fig. 6.28(b) the dynamical fluctuations scaled by the number of participants, $N_{part}\nu_{+-,dyn}$ as a function of the number of participants. Vertical bars represent statistical errors. Values of $N_{part}\nu_{+-,dyn}$ exhibit a small dependence on the collision centrality at all four measured energies for $Au + Au$ collisions and two energies for $Cu + Cu$ collisions. The measured data scaled by the number of participants (N_{part}) are thus consistent with either no or a very weak centrality dependence, however, there is a finite system size and energy dependence observed here. This implies that the strength of the (integrated) net charge two-particle correlation per participant is (quasi) invariant with collision centrality. We also scale $\nu_{+-,dyn}$ with the number of binary collisions, shown in Fig. 6.28(c). While we observe the datasets follow a common trend, $\nu_{+-,dyn}$ clearly exhibits dramatic collision centrality. Such a dependence is, however, expected given the measured fluctuations are dominated by low momentum particles with large cross-section for which binary scaling does not apply. $Au + Au$ and $p + p$ data presented in these results were courtesy of C. Pruneau [45].

6.2.4 Longitudinal and Azimuthal Dependences of the Dynamical Fluctuations

Pratt *et al.* [57, 58] have argued that the width of longitudinal charge balance function should significantly narrow in central $Au + Au$ collisions relative to peripheral collisions or $p + p$ collisions due to the delayed hadronization following the formation of a QGP. The STAR experiment has in fact reported this through the observation of narrowing of the balance function for central $Au + Au$ collisions relative to the peripheral collisions. We note, however, as already pointed by Pratt *et al.* and more recently by Voloshin [31], radial flow produced in heavy ion collisions induce large position-momentum correlations which manifest themselves in angular, transverse momentum, and longitudinal two-particle correlations. The observed narrowing of the longitudinal charge balance function therefore cannot be solely ascribed to delayed hadronization. It is thus important to gauge the change in two-particle correlations imparted by radial flow effects. As a first step towards this goal, we present studies of the net charge fluctuation dependence on the integrated (pseudo) rapidity and azimuthal ranges. We plot in Fig. 6.29(a) values of $\nu_{+-,dyn}(\eta)$ measured for different ranges of pseudo-rapidity, η . In order to compare data measured at different centralities, beam energies and system size, measured values are normalized by the magnitude of $|\nu_{+-,dyn}(\eta)|$ for a pseudorapidity range $|\eta| < 1$. Data shown are from $Au + Au$ collisions at $\sqrt{s_{NN}} = 62.4$ and 200 GeV, $Cu + Cu$ collisions

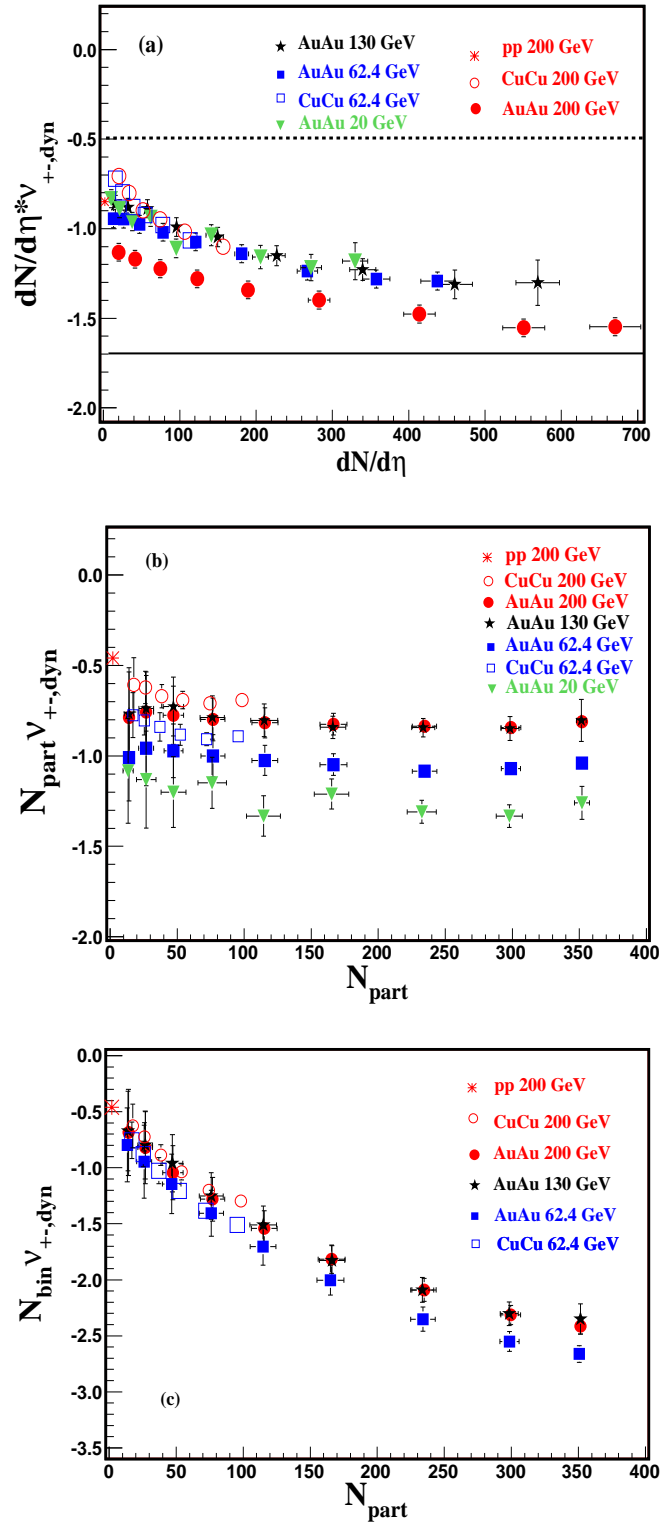


Figure 6.28: Net charge dynamical fluctuations, $\nu_{+-,dyn}$, of particles produced with pseudo-rapidity $|\eta| < 0.5$ scaled by (a) the produced multiplicity $dN/d\eta$, (b) the number of participants, and (c) the number of binary participants.

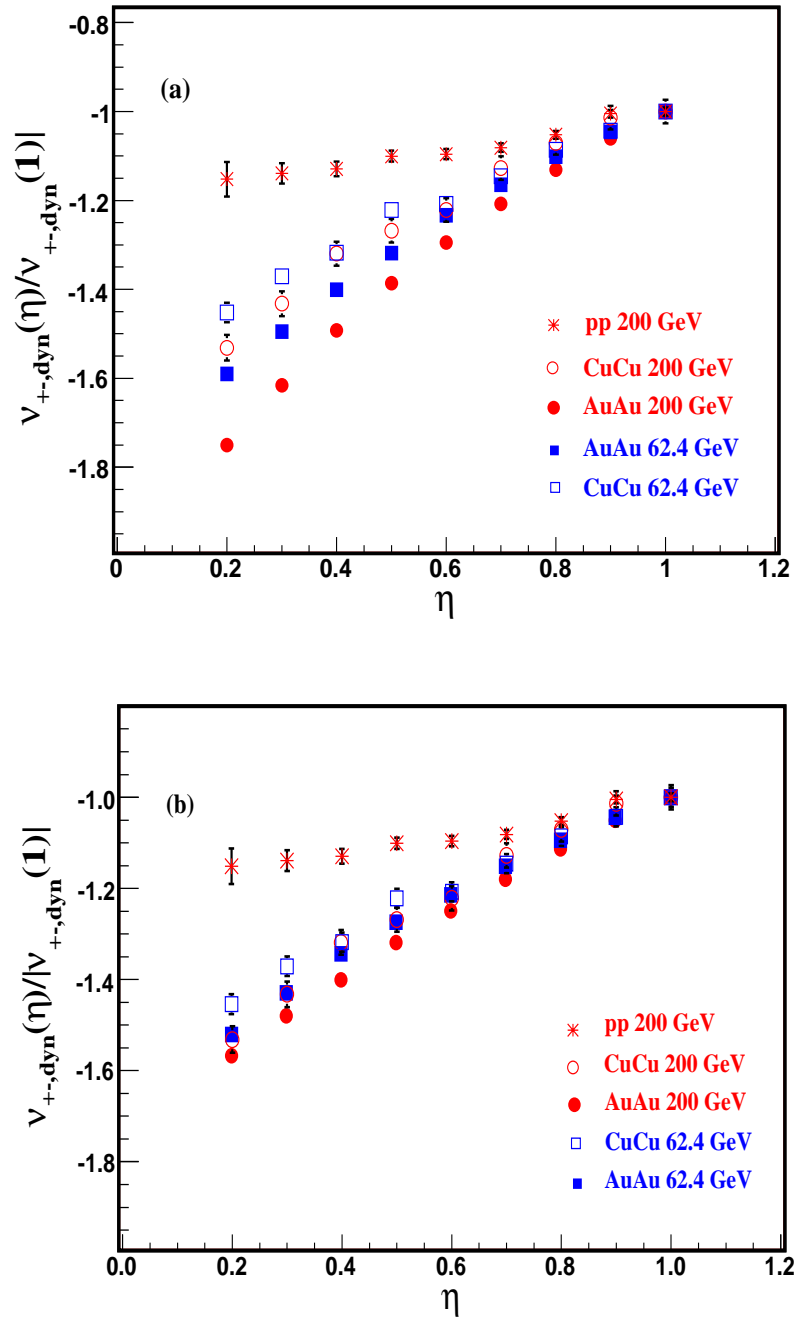


Figure 6.29: Dynamical fluctuations $\nu_{+,dyn}$, normalized to their value at $\eta = 1$, as function of the integrated pseudorapidity range. (a) Data for $Au + Au$ collisions at $\sqrt{s_{NN}} = 62.4, 200$ GeV (0-10%) along with data for $Cu + Cu$ collisions at $\sqrt{s_{NN}} = 62.4, 200$ GeV (0-10%), are compared to inclusive $p + p$ data at $\sqrt{s_{NN}} = 200$ GeV, and (b) Data for $Au + Au$ collisions at $\sqrt{s_{NN}} = 62.4, 200$ GeV (30-40%) along with data for $Cu + Cu$ collisions at $\sqrt{s_{NN}} = 62.4, 200$ GeV (0-10%), are compared to inclusive $p + p$ data at $\sqrt{s_{NN}} = 200$ GeV [45].

at 62.4 and 200 GeV, and $p + p$ data obtained at 200 GeV. One finds the magnitude of the normalized correlation is maximum for the smallest pseudorapidity ranges and decays monotonically to unity, at all energies and centralities, with increasing pseudorapidity range. The dynamical fluctuations being essentially a measure of two-particle correlation dominated by the R_{+-} term, one finds, as expected, that the correlation is strongest for small rapidity intervals, and is increasingly diluted (reduced) for larger intervals. One observes the magnitude of $|\nu_{+-,dyn}(\eta)/\nu_{+-,dyn}(1)|$ for $Cu + Cu$ collisions at 62.4 and 200 GeV are quite different from $Au + Au$ collisions at 62.4 and 200 GeV, respectively. This indicates that $Cu + Cu$ most central (0-10%) collisions are different from $Au + Au$ most central (0-5%) collisions. They are not the same as $p + p$ collisions either. We attribute these differences to the variation in collision dynamics. The relative magnitude of the correlations measured at $|\eta| < 0.5$ increases by nearly 30% for $Au + Au$ 200 GeV relative to those in $p + p$. Note in particular that the slope in $p + p$, $Cu + Cu$ and $Au + Au$ systems depends on the correlation length in pseudorapidity: the shorter the correlation, the larger the slope. The observed distributions then indicate that the correlation length is shorter for central collisions and for larger system, in agreement with the observed reduction of the charge balance function [22]. The larger values observed for most central collisions (as well as larger system) indicates correlated pairs of negative/positive particles tend to be emitted closer in rapidity than those produced in peripheral $Au + Au$ or $p + p$ collisions.

A comparison of $Au + Au$ collisions at $\sqrt{s_{NN}} = 62.4, 200$ GeV (30-40% central) has been made with $Cu + Cu$ collisions at the two energies for 0-10% centrality in Fig. 6.29(b), as these centralities correspond to approximately same number of participant nucleons. We observe that the magnitude of correlation is similar for the both systems at the same beam energy. Thereby indicating that the observed difference in $Au + Au$ and $Cu + Cu$ collisions (results shown in previous sections) is due to the difference in the number of participating nucleons in these collisions.

Authors of Ref. [57] have proposed that a reduction of the width of the balance function, and conversely a relative increase of short medium range ($\eta < 0.5$) correlations, could signal delayed hadronization. The observed increase in the correlation, reported here, might however also result from the strong radial flow believed to exist in central $Au + Au$ collisions. It is thus interesting to complement the above measurement with a study of the dependence of the dynamical fluctuation, $\nu_{+-,dyn}$, on the integrated azimuthal ranges. $Au + Au$ and $p + p$ data discussed in this section were obtained by C. Pruneau [45].

To understand the role of radial flow in net charge fluctuations measured in a finite azimuthal range (i.e. less than 2π), we first consider that the magnitude of $\nu_{+-,dyn}$ is in large part determined by the abundance of neutral resonances relative (such as the $\rho(770)$). The decay of neutral resonances into pairs of charged particles increases the

charged particle multiplicity without affecting the variance of the net charge. An increasing fraction of neutral resonances (relative to other particle production mechanisms) therefore leads to reduced magnitude of $\nu_{+-,dyn}$. Consider additionally that large radial flow should lead to a kinematical focusing of the decay products in a narrow cone. The width of the cone shall decrease with increasing radial velocity boost. One thus expects that while measuring $\nu_{+-,dyn}$ in a finite azimuthal wedge, the magnitude of the correlation should increase the level of kinematical focusing, i.e. the magnitude of the dynamical fluctuations (correlations) should increase with the magnitude of the radial flow. Azimuthal net charge correlations should therefore be rather sensitive to the magnitude of the radial flow velocity.

Fig. 6.30(a) and (b) display azimuthal net charge correlations integrated over azimuthal angle ranges from 10 to 360 degrees for $Au + Au$ and $Cu + Cu$ collisions at 200 GeV. Data are shown for seven collision centrality bins in $Au + Au$ collisions in 6.30(a) and for five centrality bins in $Cu + Cu$ collisions in 6.30(b). Note that the absolute magnitude of the correlation decreases from the most peripheral to the most central collisions as a result of progressive dilution of correlation with increasing number of participants. The variation of shape of the correlation function with the size of the azimuthal acceptance is perhaps of greater interest. One finds correlation functions measured in most central collisions decrease monotonically in magnitude with increasing azimuthal wedge size whereas they exhibit a more complicated behavior for most peripheral collisions. In general, one expects $\nu_{+-,dyn}$ to vanish for very small acceptance (azimuthal wedge), i.e., when the size of the acceptance is smaller than the typical correlation length. This explains why $|\nu_{+-,dyn}|$ decreases sharply for small angles in peripheral collisions. It is remarkable however to note this behavior is not observed in most central collisions with the angular ranges considered thereby indicating a change in the particle correlation length consistent with the reduction of the balance function in central collision already reported by STAR [22].

Fig. 6.31 shows a comparison of $Au + Au$ and $Cu + Cu$ collisions at similar number of participating nucleons. The magnitude of $\nu_{+-,dyn}$ w.r.t. ϕ is similar for similar number of participating nucleons in both systems. However the shape changes with collision centrality. The error bars shown here are statistical only. $Au + Au$ and $p + p$ data presented in these results were courtesy of C. Pruneau [45].

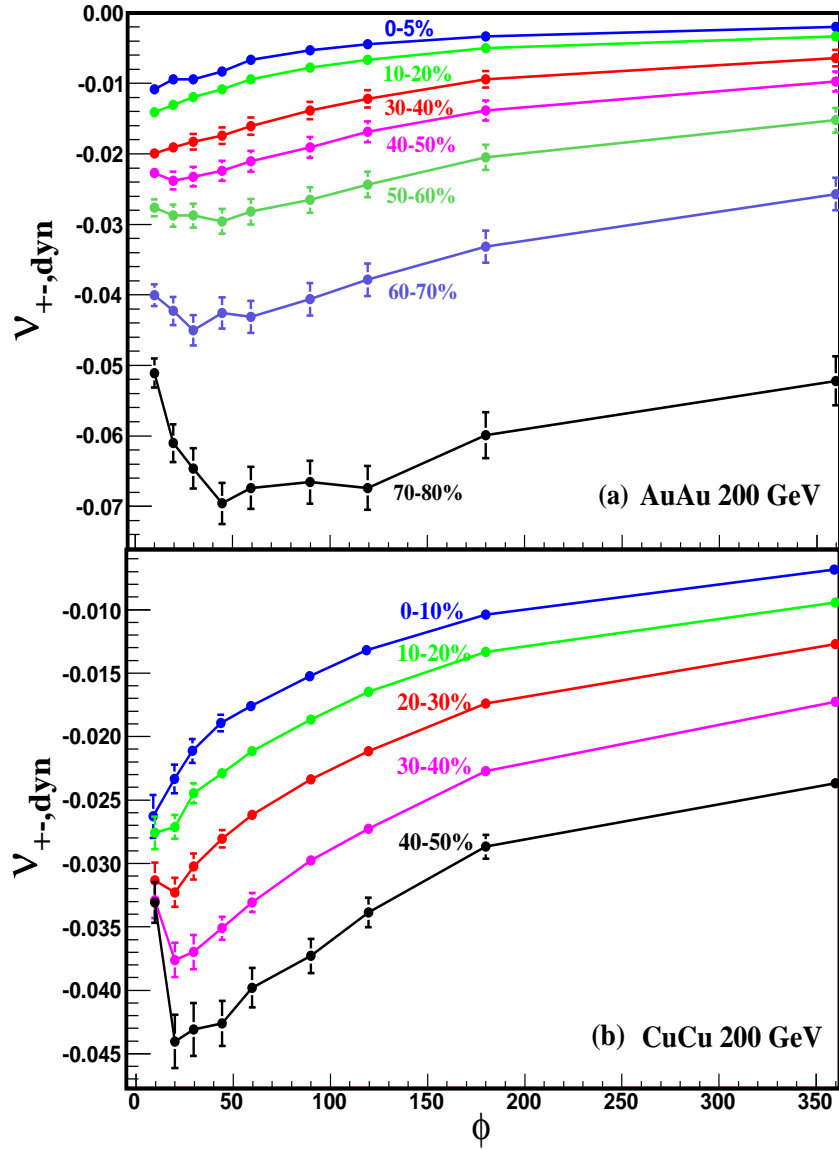


Figure 6.30: Dynamical fluctuations $\nu_{+-,dyn}$, as a function of the integrated azimuthal range ϕ for selected collision centralities for (a) $Au + Au$ 200 GeV [45], and (b) $Cu + Cu$ 200 GeV.

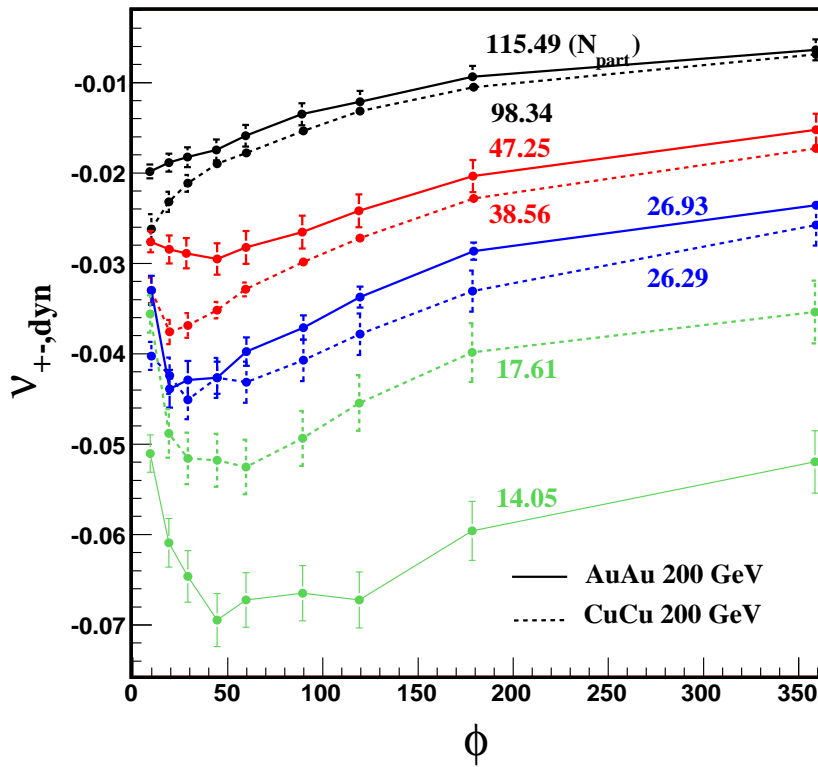


Figure 6.31: Dynamical fluctuations $\nu_{+-,dyn}$, as a function of the integrated azimuthal range ϕ for similar number of participating nucleons for $Au + Au$ 200 GeV [45] and $Cu + Cu$ 200 GeV.

Bibliography

- [1] J.W. Harris and B. Müller, *Ann. Rev. Nucl. Part. Sci.* **46** (1996) 71.
- [2] M. Stephanov, K. Rajagopal, and E. Shuryak, *Phys. Rev. Lett.* **81** (1998) 4816.
- [3] M. Stephanov, K. Rajagopal, and E. Shuryak, *Phys. Rev. D* **60** (1999) 114028.
- [4] S.A. Voloshin, V. Koch, and H.G. Ritter, *Phys. Rev. C* **60** (1999) 024901.
- [5] S.A. Bass, M. Gyulassy, H. Stöcker and W. Greiner, *J. Phys. G* **25** (1999) R1.
- [6] S. Jeon and V. Koch, *Phys. Rev. Lett.* **85** (2000) 2076.
- [7] M. Asakawa, U. Heinz and B. Müller, *Phys. Rev. Lett.* **85** (2000) 2072.
- [8] S.A. Bass, P. Danielewicz, and S. Pratt, *Phys. Rev. Lett.* **85** (2000) 2689.
- [9] H. Heiselberg, *Phy. Rep.* **351** (2001) 161.
- [10] Zi-wei Lin and C.M. Ko, *Phys. Rev. C* **64** (2001) 041901.
- [11] H. Heiselberg and A.D. Jackson, *Phys. Rev. C* **63** (2001) 064904.
- [12] E.V. Shuryak and M.A. Stephanov, *Phys. Rev. C* **63** (2001) 064903.
- [13] C. Pruneau, S. Gavin, and S.A. Voloshin, *Phys. Rev. C* **66** (2002) 044904.
- [14] M. Stephanov, *Phys. Rev. D* **65** (2002) 096008.
- [15] Q. Liu and T.A. Trainor, *Phys. Lett. B* **567** (2003) 184.
- [16] S. Gavin, (2003), [arXiv:nucl-th/0308067].
- [17] D. Adamova *et al.* [CERES Collaboration], *Nucl. Phys. A* **727** (2003) 97.
- [18] M.M. Aggarwal *et al.* [WA98 Collaboration], *Phys. Rev. C* **65** (2002) 054912.
- [19] H. Appelshauser *et al.* [NA49 Collaboration], *Phys. Lett. B* **459** (1999) 679.
- [20] J. Adams *et al.* [STAR Collaboration], [arXiv:nucl-ex/0308033].

- [21] J. Adams *et al.* [STAR Collaboration], [arXiv:nucl-ex/0307007].
- [22] J. Adams *et al.* [STAR Collaboration], Phys. Rev. Lett. **90** (2003) 172301.
- [23] K. Adcox *et al.* [PHENIX Collaboration], Phys. Rev. Lett. **89** (2002) 212301.
- [24] K. Adcox *et al.* [PHENIX Collaboration], Phys. Rev. C **6** (2002) 024901.
- [25] M Abdel Aziz, Sean Gavin, Phys. Rev. C **70** (2004) 034905.
- [26] B.I. Abelev *et al.* [STAR Collaboration], Phys. Rev. C **75** (2007) 054906.
- [27] A. Bialas, Phys. Lett. B **532** (2002) 249-251.
- [28] E. V. Shuryak, Phys. Lett. B **423** (1998) 9.
- [29] M. Abdel Aziz and S. Gavin, Phys. Rev. C **70** (2004) 034905.
- [30] S. Gavin, Phys. Rev. Lett. **92** (2004) 162301, [arXiv:nucl-th/0308067].
- [31] S. Voloshin, [arXiv:nucl-th/0312065].
- [32] C. Pruneau, *et al.*, (Star Collaboration), Proc. of 19th Nuclear Dynamics Conference at Breckenridge, Colorado, Feb, 2005 published in Heavy Ion Phys. **21** 261-266 (2004).
- [33] Q. H. Zhang, V. Topor Pop, S. Jeon and C. Gale, Phys. Rev. C **66** (2002) 014909.
- [34] M. Abdel Aziz, Ph.D. Thesis, Wayne State University, (2005).
- [35] F. W. Bopp and J. Ranft, Eur. Phys. J. **22** (2001) 171.
- [36] K. Adcox *et al.* (PHENIX Collaboration), Phys. Rev. Lett. **89** (2002) 082301, [arXiv:nucl-ex/0203014].
- [37] K. Adcox, *et al.* (PHENIX Collaboration), Phys. Rev. C **66** (2002) 024901.
- [38] G. Westfall, *et al.* (STAR Collaboration), Proc. 17th Nuclear Dynamic Conference, Breckenridge, Colorado, 2003.
- [39] J. Adams, *et al.* (STAR Collaboration), Phys. Rev. C **68** (2003) 044905.
- [40] C. Pruneau, *et al.*, (Star Collaboration), Proc. of 19th Nuclear Dynamics Conference at Breckenridge, Colorado, Feb 8-15, 2003 published in Heavy Ion Phys. **21**, 261-266 (2004).
- [41] J. Whitmore, Phys.Rep. **27** (1996) 187.

- [42] L. Foa, Phys. Rep. **22** (1975) 1.
- [43] V. Koch, M. Bleicher, and S. Jeon, Nucl. Phys. A **698** (2002) 261.
- [44] J. Adams, *et al.* (STAR Collaboration), [arXiv:nucl-ex/0311017].
- [45] C. Pruneau, Wayne State University, Detroit, USA. [Private communication].
- [46] G. J Alner, *et al.* (UA5 Collaboration), Phys. Lett. B **138** (1984) 304.
- [47] H. Müller, Proc. 25th Int. Conf. on High Energy Physics, eds. K.K. Phua and Y. Yamaguchi (South East Asia Theo. Phys. Assoc., Singapore, 1991) p.872.
- [48] B. B. Back, *et al.*, (PHOBOS Collaboration), Phys. Rev. Lett. **87** (2001) 102303.
- [49] B. B. Back, *et al.*, (PHOBOS Collaboration), Phys. Rev. Lett. **88** (2002) 022302.
- [50] B. B. Back, *et al.*, (PHOBOS Collaboration), Phys. Rev. C **65** (2002) 061901R.
- [51] B. B. Back, *et al.*, (PHOBOS Collaboration), Phys. Rev. C **70** (2004) 021902.
- [52] B. B. Back, *et al.*, (PHOBOS Collaboration), Phys. Rev. Lett. **91** (2003) 052303.
- [53] B. B. Back, *et al.*, (PHOBOS Collaboration), [arXiv:nucl-ex/0601026].
- [54] B.B. Back, *et al.*, (PHOBOS Collaboration), [arXiv:nucl-ex/0301017].
- [55] Adamova *et al.*, Nucl. Phys. A **727**, (2003) 97; H. Sako *et al.*, Quark Matter Conference Proceedings 2004.
- [56] C. Adler, *et al.*, (STAR collaboration), Phys. Rev. Lett. **87** (2001) 112303.
- [57] S. Bass, P. Danielewicz, and S. Pratt, Phys. Rev. Lett. **85** (2000) 2689; S. Cheng *et al.*, [arXiv:nucl-th/0401008].
- [58] S. Jeon, S. Pratt, Phys. Rev. C **65** (2002) 044902.

Chapter 7

Conclusions

One of the major goals of Relativistic Heavy Ion Collider at Brookhaven National Laboratory, Upton (New York), is to search for the formation of Quark Gluon Plasma in the heavy ion collisions. The RHIC was designed to study relativistic heavy ion collisions at the center of mass energies ($\sqrt{s_{NN}}$) ranging from 20 GeV to 200 GeV.

This thesis reports pseudo-rapidity density distribution of photons at forward rapidities in $Cu + Cu$ collisions at $\sqrt{s_{NN}} = 200$ GeV. PMD data was meticulously divided into various categories as cell-to-cell gain varied in time due to temperature, humidity etc. Furthermore, data had to be cleaned up to remove hot and noisy channels. Additionally, we observed that sometimes chains also fired abnormally high. Thus, one of the major task in the analysis was to clean and calibrate the data properly. Results were extracted from the data only after satisfactory gain calibration.

We observed that the pseudo-rapidity density distribution of photon is almost linear, however, its yield increases monotonically with the collision centrality. A finite increase in the slope with the increase in centrality was also observed. We compared our results with HIJING theoretical model and found that there is a qualitative agreement between data and HIJING.

Photons pseudo-rapidity density per participant pair is found to be invariant with respect to centrality. This sheds light on the particle production mechanism at forward rapidities. In general one expects the centrality dependence of charged particle pseudo-rapidity density ($dN_{ch}/d\eta$) as:

$$\frac{dN_{ch}}{d\eta} = \alpha N_{part} + \beta N_{col} \quad (7.1)$$

Particle production mechanism at mid-rapidity gets contributions both from N_{part} and N_{bin} . Whereas at forward rapidities, only soft processes dominate the particle production.

We carried out a study of variation of the number of photons normalized to the number of binary collisions as a function of pseudo-rapidity. We found that the data values

decrease from peripheral collisions to the most central collisions, thereby indicating that the contribution of hard processes to particle production at forward rapidity is small.

We compared pseudo-rapidity density per participant results for $Cu + Cu$ collisions at $\sqrt{s_{NN}} = 200$ GeV with $Au + Au$ collisions at $\sqrt{s_{NN}} = 62.4$ GeV for 0-5% (most central) and 40-50% (peripheral) collisions, $Cu + Cu$ collisions at $\sqrt{s_{NN}} = 62.4$ GeV for 0-10% (most central) collisions along with the WA98 data at $\sqrt{s_{NN}} = 17.3$ GeV and UA5 data for $p\bar{p}$ at $\sqrt{s_{NN}} = 540$ GeV. We found that the cross-section for different system sizes and energies remains constant at a particular pseudo-rapidity, however, the cross-section for $p\bar{p}$ data lies prominently different. One of the reason for this difference could be annihilation process which does not take place in heavy ion collisions. We conclude that inclusive photon production per participant pair follows universal limiting pseudo-rapidity distribution away from mid-rapidity which is independent of energy, system size and centrality.

Besides a study of pseudo-rapidity density distribution of photons, we also studied fluctuations in photon multiplicity at forward rapidities at RHIC energies. For this, we chose various 2% centrality bins in order to minimize the impact parameter fluctuations. We fitted different Gaussian distributions and fit parameters such as mean (μ), sigma (σ) and chi-square per degree of freedom (χ^2/ndf) were obtained for these centrality classes. We found that the values of χ^2/ndf remain more or less reasonable, i.e., around 1.0 - 1.5, whereas the values of mean and sigma decrease from 0-2% centrality to 40-42% centrality.

We compared experimental results of photon multiplicity fluctuations with with predictions of HIJING and participant models. We observed that the photon multiplicity fluctuations, $\omega_\gamma \sim 7$ in data are more or less constant within statistical errors. Whereas, HIJING model calculations show slightly large relative photon multiplicity fluctuations with a value of $\omega_\gamma \sim 8$. Participant model predictions with a value of $\omega_\gamma \sim 3$ fails to explain fluctuations observed in $Cu + Cu$ collisions at $\sqrt{s_{NN}} = 200$ GeV.

The net charge $Cu+Cu$ results were compared to results from $Au+Au$ collisions at $\sqrt{s_{NN}} = 20, 62.4, 130$ and 200 GeV (STAR experiment), and $p+p$ collisions at $\sqrt{s_{NN}} = 200$ GeV (STAR experiment). We find that the dynamical net charge fluctuations are finite at all energies and exhibit a similar monotonic dependence with the number of participating nucleons for all systems. We observe monotonic reduction in the magnitude of $\nu_{+-,\text{dyn}}$ with the increasing N_{part} . This arises in principle from the progressive dilution of two-particle correlation function when the number of particle sources is increased. Besides this, we also observe that at a given N_{part} the measured fluctuations also exhibit a modest dependence on beam energy. The magnitude of $\nu_{+-,\text{dyn}}$ is largest in $Au + Au$ collisions at center of mass energy of 20 GeV.

In order to study the magnitude of fluctuations and formation of a QGP, we studied the net charge fluctuation dependence on the beam energy. For such a study it is

important to take into account the role of charge conservation effects. Even though one expects charge conservation effects to become progressively smaller for increasing produced charged particles, this effect is finite at all beam energies and produced multiplicity. We thus estimate the effect of charge conservation by $\nu_{+-,dyn} = -4/N_{4\pi}$, where $N_{4\pi}$ is the *total* charged particles produced over 4π . We observe the net charge fluctuations corrected for charge conservation do not depend on beam energy in the range from 20 to 200 GeV for $Au + Au$ collisions. However, measurements at $Cu + Cu$ collisions show a sharp increase in magnitude. One could interpret this difference of magnitude of fluctuations on the basis of difference in the number of participating nucleons for most central collisions. However, the magnitude of corrected dynamical fluctuations in $Cu + Cu$ collisions when scaled by the ratio of number of participants in $Cu + Cu$ collisions is $-0.00099521 \pm 1.645e-5(\text{stat}) \pm 6.17e-5(\text{sys})$ and $-0.00101422 \pm 1.63e-5(\text{stat}) \pm 8.21e-5(\text{sys})$ at $\sqrt{s_{NN}} = 62.4$ & 200 GeV, respectively. This shows that there is a finite system size dependence between $Au + Au$ and $Cu + Cu$ systems. However, large difference in the corrected $\nu_{+-,dyn}$ values in the two systems basically comes from the difference in the N_{part} in the most central collisions.

We scaled dynamical fluctuations by various parameters like, the measured particle multiplicity density ($dN/d\eta$), the number of participating nucleons and binary collisions in order to check whether heavy ion collisions are a mere superposition of nucleon-nucleon collisions or not. Distributions of dynamical fluctuations scaled by $dN/d\eta$ exhibit similar qualitative behavior for all the energies at $Au + Au$ and $Cu + Cu$ collisions. However, we observe that $Au + Au$ data at 200 GeV lies prominently apart from the rest of the dataset. This could be partly attributed to multiplicity effects. Additionally, we observe that $|\nu_{+-,dyn}dN/d\eta|$ is not invariant with increasing centrality. The amplitude of $|\nu_{+-,dyn}dN/d\eta|$ is smallest for peripheral collisions in $Au + Au$ and $Cu + Cu$ collisions, and rises monotonically by 40% for central collisions. Similar rise in the pseudo-rapidity density per participant pair ($dN_{ch}/d\eta/(\langle N_{part} \rangle / 2)$) was also reported by the PHOBOS collaboration. They reported a value of 3.9 in central $Au + Au$ collisions at the center of mass energy of 200 GeV compared to a value of 2.5 in $p + p$ collisions at the same energy. We thus conclude that centrality dependence of $|\nu_{+-,dyn}dN/d\eta|$ is mostly due to the rise of ($dN_{ch}/d\eta/(\langle N_{part} \rangle / 2)$) with the increasing N_{part} . Further, we scale the data by N_{part} and observe that data shows no centrality dependence, however, no scaling is observed when it is scaled by N_{bin} . Since this analysis concentrates on particles with low momentum with large cross-section, we expect no scaling with the number of binary collisions.

We also compared our measurements of dynamical net charge fluctuations to the prediction based on the thermal models. We observed that the variable D decreases from $3.37 \pm 0.049(\text{stat})$ for the most peripheral collisions measured in $Au + Au$ collisions at $\sqrt{s_{NN}} = 200$ GeV to $2.96 \pm 0.05(\text{stat})$ in the central collisions. The corresponding

values of D for $Cu + Cu$ collisions at $\sqrt{s_{NN}} = 200$ GeV are 3.74 and 3.4 for peripheral and central collisions, respectively. The value of D for most central $Au + Au$ collisions approaches the prediction for a resonance gas. It is worth noting that these values are much larger than expected for a quark-gluon gas undergoing fast hadronization and freeze out. However, it is not possible to draw a definite conclusion for the existence/non-existence of a deconfined phase during the collisions from these results. The reason could be incomplete hadronization which lead to larger fluctuations than expected for a QGP.

In order to understand radial flow effects we carried out the net charge fluctuation analysis on the integrated pseudo-rapidity and azimuthal ranges. $\nu_{+-,dyn}$ was measured for nine different pseudo-rapidity ranges. In order to compare data measured at different centralities, beam energy and system size, the measured values are normalized by the magnitude of $|\nu_{+-,dyn}(\eta)|$ for a pseudo-rapidity range $|\eta| < 1$. By virtue of the charge conservation effects we expect $2R_{+-}$ to be larger than R_{++} and R_{--} . Since dynamical fluctuations are essentially a measure of two-particle correlation, we observe that the correlations are strongest for small rapidity intervals. Correlations monotonically dilute for larger intervals in pseudo-rapidity. We also compared the $Au + Au$ and the $Cu + Cu$ collisions at similar number of participants. The central (30-40%) $Au + Au$ collisions have approximately same number of N_{part} as 0-10% central $Cu + Cu$ collisions. At similar N_{part} we observe that the magnitude of correlation is similar for both the systems at the same beam energy.

We also studied the dependence of dynamical fluctuations on the azimuthal range of integration. The magnitude of $\nu_{+-,dyn}$ is largely driven by neutral resonances which further decay into pairs of charged particles. The increase in charged particle multiplicity due to the decay of neutral resonances does not effect the variance of net charge. However, increasing fraction of neutral resonances leads to the reduced magnitude of $\nu_{+-,dyn}$. Further, large radial flow leads to kinematical focusing of the decay products in a narrow cone. In other words, the magnitude of dynamical fluctuations or correlations should increase with the magnitude of radial flow. The azimuthal wedges selected for this analysis were from 10 to 360 degrees for $Au + Au$ and $Cu + Cu$ collisions at 200 GeV. Here again the correlation function measured for both the systems decreases monotonically for most central collisions. Interestingly we observe that $|\nu_{+-,dyn}|$ decreases sharply for small angles in peripheral collisions, whereas, this behavior is not shown in the most central collisions. This perhaps indicates a change in the particle correlation length consistent with the reduction of the balance function in central collisions reported by STAR.